LONDON'S GLOBAL UNIVERSITY

Nanoparticle Theranostics for Applications in Cancer Diagnostics and Cancer Therapy

Nicholas John Hobson

A thesis submitted in partial fulfilment of the requirements for the degree of
Doctor of Philosophy

of the
University College London
School of Pharmacy

2016

Declaration of Authorship

I, Nicholas John Hobson, confirm that the work presented in this thesis is my own. Where information has been derived from other sources, I confirm that this has been indicated in the thesis.

Signed: 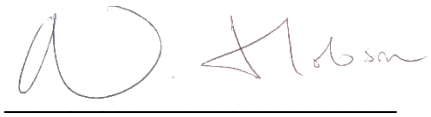

Date: 31.03.2017

Abstract

Traditionally, medicine has been conducted using a diagnostic procedure followed by an appropriate therapy and monitored were possible. On the whole, these steps have happened independently of each other. In recent years however many have started to question this independent approach and have asked whether technologies that seek to combine diagnostics and therapies would be more beneficial at treating diseases. This new medical discipline has been termed *theranostics*. The aim of this project was to design and synthesise a novel theranostic nanoparticle, using a micelle forming amphiphilic carbohydrate, with the overall hypothesis of determining whether using a nanomedicine that can simultaneously image and treat would improve the effectiveness of a cancer treatment.

Super paramagnetic iron oxide nanoparticles (IONPs) have gained considerable attention as an MRI contrast agent due to their unique magnetic properties and relatively inoffensive toxicity profile. Before IONPs may be used in a biological environment they must overcome several challenges, including being stable to aggregation and organ targeting. In this project a modified chitosan amphiphilic polymer was used to successfully formulate IONPs into colloidal stable aqueous dispersions using two different methods which produced *blackberry nanoparticles* and *raspberry nanoparticles*. The raspberry nanoparticles were extensively characterised *in vitro* and *in vivo* and were found to be highly effective as an MRI imaging probe for the liver and spleen. Following this, they were tested for their cancer imaging properties in an *in vivo* mouse tumour model. The drug loading capacity of the raspberry nanoparticles was investigated using lomustine, paclitaxel and methotrexate, however no effective drug encapsulation was determined in this project. Overall, a highly effective MRI probe was engineered and characterised, although its future success will be determined by its activity towards a disease target.

Publications, Awards and Conferences

Awards

Poster prize, Awarded at the Globalized Pharmaceutical Education Network (GPEN) Meeting. *Poster title: Design, Synthesis and Evaluation of Nanoparticle Diagnostics for Applications in Medical Imaging*. University of Kansas, USA. ***November 2016***

Best presentation award, UCL School of Pharmacy Research Day. *Presentation title: Design and Synthesis of Nanoparticle Theranostics for Applications in Cancer Diagnostics and Cancer Therapy*. University College London, UK. ***September 2015***

John Hopkins University Vredenburg Scholarship, Grant writing: The grant from this scholarship allowed a student from the John Hopkins University to visit the UCL School of Pharmacy to partake in a summer project entitled; *The Transdermal Delivery of Drug Loaded Magnetic Nanobeads*. Grant award: $5,500. ***Summer 2015***

Best poster prize runner up, UCL School of Pharmacy Research Day. Poster title: *Design and Synthesis of Nanoparticle Theranostics for Applications in Cancer Diagnostics and Cancer Therapy*. University College London, UK, ***September 2014***

Publications

Samuel E. F. Orubu, Nicholas J. Hobson, Abdul W. Basit, Catherine Tuleu. The Milky Way: paediatric milk-based dispersible tablets prepared by direct compression – a proof-of-concept study. *The Journal of pharmacy and pharmacology* ***2016***.

Nicholas J. Hobson, Xian Weng, Catarina Veiga, Bernard Siow, Marianne Ashford, Nguyen T.K. Thanh, Andreas G. Schatzlein, Ijeoma F. Uchegbu. Design and Synthesis of Self-Assembling Polymeric Iron Oxide Nanoparticle Theranostics for Applications in Cancer Diagnostics and Cancer Therapy. ***2017***. *(In progress)*

Conferences

American Association of Pharmaceutical Scientists Annual Meeting (AAPS). Poster title: Pharmacokinetics and Pharmacodynamics of Uniquely Clustered Superparamagnetic Iron Oxide Nanoparticles that can Drastically Improve Magnetic Resonance Contrast. Denver, Colorado, USA. ***November 2016***

Globalized Pharmaceutical Education Network biannual meeting (GPEN). Poster title: Design, Synthesis and Evaluation of Nanoparticle Diagnostics for Applications in Medical Imaging. University of Kansas, Kansas, USA. ***November 2016***

European University Consortium for Pharmaceutical Sciences (ULLA) Summer School. Poster title: The Biology Underpinning Post-Surgical Nanotheranostics. UCL School of Pharmacy, London, UK. ***July 2013***.

Acknowledgments

I would like to thank Professor Ijeoma F. Uchegbu, Professor Andreas G. Schätzlein, Professor Nguyen T.K. Thanh and Dr Marianne Ashford for their supervision throughout my PhD. Their knowledge and experience were crucial in the development of the project and in the progression of my own scientific thinking.

I would also like to thank the Targeted Therapeutics & Formulation Sciences Centre for Doctoral Training for giving me this opportunity as well as all the program's sponsors, especially AstraZeneca who was my individual sponsor.

This project has used a large range of techniques. It would not have been possible to utilise them all without the expertise from others in their relevant fields, therefore specific acknowledgements must be given to; David McCarthy (electron microscopy), Paul Southern (magnetometry), Lisa Godfrey and Steve Coppard (animal experimentation), Bernard Siow (MRI), Catarina Veiga (computational MRI) and Xian Weng (elemental analysis).

Of course a PhD would be a tortuous journey without the support of friends and colleges. So I would like to thank everyone in the departments and labs that I've had the fortune to meet throughout my time at UCL. Many of whom have become lifelong friends.

Lastly I'd like to mention my Grandparents for allowing me to live with them during my time in London, significantly reducing my financial burden. My Mother and Father, Liseby Hobson and John Hobson for their continued support and lastly my partner Anouk Schumacher, who has continually supported me and has had to endured a continuous fight for attention against my PhD.

Table of Contents

List of Figures

List of Tables

List of Schemes

List of Abbreviations

µm	micrometre *or* micron
^{1}H	proton
^{1}H-COSY	proton correlation spectroscopy
^{1}H-NMR	proton nuclear magnetic resonance
2θ	diffraction angle
Å	ångström
AcOD	deuterated acetic acid
ADME	absorption, distribution, metabolism, and excretion
AES	atomic emission spectroscopy
b.p.	boiling point
B_0	magnetic field
BBB	blood brain barrier
CMC	critical micelle concentration
CPP	critical packing parameter
D_2O	deuterated water
Da	dalton
dGC	degraded glycol chitosan
DLS	dynamic light scattering
DMSA	dimercaptosuccinic acid
DMSO	dimethyl sulfoxide
Dn/Dc	refractive index increment
DNA	deoxyribonucleic acid
EDTA	ethylenediaminetetraacetic acid
EE%	encapsulation efficiency
EMA	European Medicines Agency
emu	electromagnetic units
EPR	enhanced permeation and retention
EtOH	ethanol
FA	folic acid
FBS	fetal bovine serum

FDA	the U.S. Food and Drug Administration
Fe	iron
Fe^{2+}	iron ion in +2 oxidation state
Fe^{3+}	iron ion in +3 oxidation state
Fe_3O_4	magnetite
g	gramme
GC	glycol chitosan
GCPQ	quaternary ammonium palmitoyl glycol chitosan
Gd^{3+}	gadolinium ion in +3 oxidation state
GM-1	monosialotetrahexosylganglioside
GPC	gel permeation chromatography
h	hours
H_2O	water
HCl	hydrochloric acid
HFMA	2,2,3,4,4,4-hexafluorobutyl methacrylate
HPLC	high performance liquid chromatography
HTS	high-throughput screening
Hz	hertz
IC_{50}	half maximal inhibitory concentration
ICP	inductively coupled plasma
IONP	superparamagnetic iron oxide nanoparticles
K	kelvin
LOD	limit of detection
Lom	lomustine
M	molar
M vs H	field dependent magnetization
MALLS	multi angled laser light scattering
MeI	methyl iodide
MeOD	deuterated methanol
mg	milligrammes
mL	millilitre
mm	millimetre

MR	magnetic resonance
MRI	magnetic resonance imaging
MTX	methotrexate
mV	millivolts
Mw	relative molecular weight
MWCO	molecular weight cut off
M_x	vector x-axis component
M_y	vector y-axis component
M_z	vector z-axis component
n	replicate number
N_2	diatomic nitrogen
NaCl	sodium chloride
NaI	sodium iodide
NaOH	sodium hydroxide
nm	nanometre
NMP	N-Methyl-2-pyrrolidone
ns	nanoseconds
^{O}C	degrees Celsius
Oe	oersted
PBMA	Poly(isobutylene-alt-maleic anhydride)
PBS	phosphate buffer saline
PCL	poly(capro-lactone)
PdI	polydispersity index
PEG	poly(ethylene glycol)
PEO	poly(ethylene oxide)
PFP	perfluoropentane
PGC	palmitoylated glycol chitosan
pH	molar concentration of hydrogen ions
ppm	parts per million
PPO	poly(propylene oxide)
PTX	paclitaxel
PVA	polyvinyl acetate

r_1	longitudinal relaxivity
r_2	transverse relaxivity
rcf	relative centrifugal force
RF	radio frequency
s	seconds
s.d.	standard deviation
SDS	sodium dodecyl sulfate
SQUID	super quantum interference device
T	tesla *or* temperature
T1	longitudinal relaxation time
$t_{1/2}$	half-life
T2	transverse relaxation time
T_c	Curie temperature
TCL	thermally cross-linked
TE	echo time
TEM	transmission electron microscopy
TI	inversion time
TPES	D-α-tocopheryl polyethylene glycol 1000 succinate
TP-LENK	leucine-enkephalin
TR	repetition time
UV/Vis	ultra violet/visible spectroscopy
v/v	volume/volume
XRD	x-ray diffraction
δ	delta $_{or}$ solubility parameter
ΔE	change in energy
ΔG	change in Gibbs free energy
ΔH	change in enthalpy
ΔS	change in entropy
λ	wavelength
χ	Flory-Huggins parameter
ħ	Planck unit

Chapter 1

Introduction

1.1 Thesis Motivations

The aim of this project was to design and create a theranostic nanoparticle to test the hypothesis that using a nanomedicine that can simultaneously be imaged and used as a therapy will improve the effectiveness of a cancer treatment. Nanotechnology is a rapidly advancing discipline and it is now possible to create structures with more than one application and function. These kinds of multi-functional nanoparticles look particularly interesting in the field of medicine. Traditionally, medicine has been conducted using a diagnostic procedure to assess a pathological condition, followed by an appropriate therapy and then monitored where possible. On the whole, these steps are applied independently of each other. In recent years however, many have started to question this independent approach and have asked whether technologies that seek to combine diagnosis and therapy would be more beneficial at treating diseases.[1] This has become an increasingly interesting area and treatments that combine both diagnostics and therapies have been termed *theranostics*.[2] Theranostics is a relatively new area of science with some remarkable applications. A typical example of this can be explained as follows; a patient visits their doctor and after a consultation and a diagnostic procedure a tumour is detected. Their oncologist may make a decision to treat them with an appropriate drug based on general information about patients calculated from population averages (i.e. this chemotherapeutic drug has had an effect in 25% of cases). If the medication does not work after a period of time, the medication may be switched.[3] Of course treating a patient in this way is not desirable as it leads to a loss of time, adverse side effects, increased costs of treatment and patient dissatisfaction. In many circumstances, the reason why it has not worked is because not all diseases are the same and not all patients are the same. In fact, in recent years a rather complex picture has emerged where genetic variation in diseases and patients significantly contributes to the

response of a drug.[4] In light of this, it would seem that the future of medicine could rely heavily on the effective diagnosis of patients and diseases during every stage of their treatment. Creating treatments that fuse diagnostics and therapeutics together is at the centre of this new movement towards the personalisation of medicine.

There are many strategies for combining diagnostics and therapies, however two have gained considerable popularity; *companion diagnostics* and *nanotheranostics*. Companion diagnostics is the term given to a diagnostic procedure that when performed can predict whether a person will benefit from a particular treatment.[5,6] This type of technology has become more prevalent with the development of more specific drugs. The first commercial companion diagnostic was the HercepTest™, an immunohistochemical assay that could predict whether a cancer would be responsive to the chemotherapeutic Herceptin™.[7] Since its release in 1998, Herceptin™ has become a gold standard therapeutic as it is highly active against cancers that overexpress the HER2 receptor. It is widely believed however, that because only 15-20% of breast cancers over express the HER2 receptor, without the HercepTest™ the development of Herceptin™ may well have been discontinued in early clinical trials for lack of efficacy in large populations.[7,8] Designing medical treatments by carefully diagnosing the specific biology of a disease and then providing an appropriate treatment specific to the patients' needs has led to a new approach in healthcare that has been termed *personalised medicines*.[9] With the advances in biomedical technology the personalization of medicine is set to radically alter the landscape of healthcare over the coming years.

More recently, theranostics has come to encompass a branch of nanotechnology whereby nanoparticles are developed to simultaneously provide imaging and therapeutic effects.[10] These types of structures have been termed *nanotheranostics*.[11] Combining therapeutic and diagnostic elements into a single nanoparticle allows for

disease visualisation, treatment and real time monitoring of treatment progress. The issue can be illustrated as follows; when a patient presents them-selves with a disease they will be given a therapeutic based on general information about patients calculated from population averages. As explained previously, patients and diseases can be highly variable and there is a chance that the given medicine will have no effect. Usually a patient will have to wait until the end of a treatment to determine whether the medicine has been successful and this can lead to a loss of time, adverse side effects and patient dissatisfaction. By combining the therapeutic with an imaging agent, it can quickly be determined if the administered drug is reaching the diseased site by performing a simple diagnostic procedure. This extra information will improve the overall efficiency of disease treatment. It can be misleading to group both the companion diagnostic and the nanotheranostic strategies together under the single term “theranostics”, as they are both unique approaches each with their own individual advantages. However both strategies are united by their desire to combine the disciplines of diagnosis and therapy to improve the overall healthcare of a patient.

This project will focus on nanotheranostics as their clinical relevance has generally been less explored compared to its companion diagnostic counterpart. The hypothesis is that using a theranostic nanoparticle will improve the treatment of a disease compared to the separate use of its individual components (diagnostic and therapeutic). A scientific investigation into this prediction can be conducted by at first, designing and synthesising a suitable theranostic nanoparticle and then by evaluating its potential using *in vitro* and *in vivo* models. This project will aim to synthesise a theranostic nanoparticle by harnessing the MRI potential of superparamagnetic iron oxide nanoparticles and combining them with a therapeutic drug. The overall nanostructure will be held together within a micelle forming amphiphilic carbohydrate based polymer. The overall aim will be a biologically suitable MRI agent with cytotoxic effects against tumours.

1.2 Iron Oxide Nanoparticles as Magnetic Resonance Imaging Contrast agents

1.2.1 Magnetic resonance imaging

Magnetic resonance imaging (MRI) is a powerful imaging technique used to produce detailed anatomical images of organs and tissues within the body.[12] MRI specifically allows for the three-dimensional mapping of the hydrogen nuclei (or protons) in any given sample. As water is comprised of one oxygen nuclei coupled to two hydrogen nuclei it is responsible for the majority of an MRI signal. As the density and distribution of water molecules differs within each tissue type, MRI allows for the *in vivo* imaging of tissues and organs within a patient. The powerful imaging capability of MRI has led this technique to become common practice in modern hospitals. Strong super conducting magnets between 1.5 – 3.0 Tesla (T) are used to generate the strong magnetic fields needed for this particular technique.[13] MRI has the ability to provide anatomical information in any part of the body where there is difference in water concentration. Significantly, the concentration of water can change with disease or injury and this has led MRI to become commonly used in medical diagnostics. A number of other diagnostic techniques are available, these are summarised in Table 1.2.1.1.[14] Compared to its counterparts MRI is a technique with good spatial resolution and excellent tissue penetration. Another advantage is that MRI is the only deep tissue imaging technique that uses non-ionising radiation. Positron emission tomography (PET) usually uses radio isotopes that decay and release 511-keV positrons which have enough energy to damage biological structures. Low doses usually mean PET is relatively safe for patients, however technicians in nuclear medicine facilities can often receive more harmful levels of positron exposure.[15,16] Recently, a long term clinical study by *Matthews et al* has found that the radiation

used in a diagnostic X-Ray/CT procedure is likely to slightly increase the patient's risk of getting cancer in the future.[17] As MRI is considered the safest of the *in vivo* deep tissue imaging techniques it is often preferred in general situations.

	Source	Resolution	Molar Sensitivity	Tissue penetration	Time	Ionising
Magnetic resonance imaging (MRI)	Radio waves	10-100 μm	10^{-5}	No limit	Minutes-hours	No
X-ray computed tomography (CT)	X-rays	50-200 μm	10^{-6}	No limit	Minutes	Yes
Positron emission tomography (PET)	γ-rays	4-6 mm	10^{-12}	No limit	Minutes-hours	Yes
Single Photon Emission Computed Tomography (SPECT)	γ-rays	8-12 mm	10^{-11}	No limit	Minutes-hours	Yes
Ultrasound (US)	Sound waves	>2-3 mm	N/A	<10 cm	Seconds-minutes	No
Optical Imaging	Light	>0.3 μm	10^{-12}	<1 mm	Seconds-minutes	No

Table 1.2.1.1. A comparison of various imaging modalities.

1.2.2 The fundamentals of MRI

The MRI signal arises from the interaction of a proton with an external magnetic field. The phenomenon is founded in the quantum mechanical principle that sub-atomic particles possess *spin*.[12] Each spinning proton is associated with a magnetic dipole moment. In many atoms the spins of the protons are paired, annulling their effect and ultimately giving no overall dipole moment. Commonly known atoms include ^{12}C and ^{16}O. Other atoms, including hydrogen nuclei (^{1}H), do contain unpaired spinning protons and as a result they possess an overall dipole moment resulting in some impressive magnetic characteristics that can be exploited by MRI. In the absence of a magnetic field these dipole moments are randomly orientated. However when placed in the presence of an external magnetic field (B_0) the majority of these protons will seek to align their dipoles in the direction of B_0. The ratio of protons that align their dipoles with B_0 is governed by the Boltzmann distribution. A radiofrequency (RF)

pulse can then be applied to the sample, in turn exciting some protons into a new dipole orientation, offset from that of B_0. As the spinning protons relax back to their natural thermal equilibrium, determined by T1 and T2 relaxation, they produce a change in the magnetic field that can be measured by a receiver coil. The change in magnetism induced from a single proton relaxing back from one spin orientation to another is exceedingly small but fortuitously for medical science there are a large number of protons in biological samples (6.6 x10^{19} per mL of water) which overall give enough of an effect to be measured.[18] This process is illustrated in 1.2.2.1.

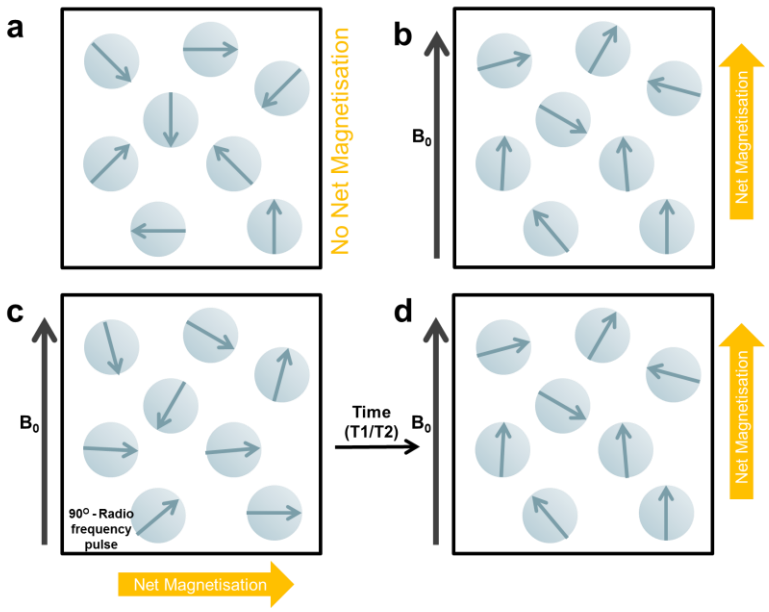

Figure 1.2.2.1. The physics of MRI. Principally all hydrogen nuclei or protons have an associated dipole moment; denoted by blue arrows in the schematic. (a); In the absence of a magnetic field the protons have randomly orientated magnetic dipole moments. (b); In the presence of an external magnetic field (B_0), the protons will seek to align their dipole moments with B_0, overall this creates a net magnetization in the direction of B_0. (c); A radio frequency (RF) pulse can be used to knock the proton's dipole moments out of alignment with B_0. (d); The spinning nuclei relax back to their original alignment and in doing so produce a change in voltage in the receiver coil that can be measured.

Understanding the mechanism of how the protons relax back to thermal equilibrium is an important principle of MRI. In 1946 Felix Bloch attempted to describe the origin of an MRI signal.[19] His mathematical interpretations are commonly known as the *Bloch equations* and they have provided the standard model for understanding the nature of an MRI signal to this day. The assumption is made that any proton in a sample can be represented by a single vector (m) precessing around the direction of an external magnetic field.[20] The rate of precession is determined by the *Larmor frequency.* Since m is a vector in space it can be resolved into 3 components m_x, m_y and m_z. m_x and m_y are known as the transverse components and m_z is known as the longitudinal component. Using a radiofrequency pulse the dipole moment of the proton can be knocked out of alignment with the external magnetic field (B_0). The proton will then seek to re-establish its alignment with B_0 and will do so by precessing around the longitudinal axis at the *Larmor frequency* as shown in Figure 1.2.2.2.c. This type of relaxation mechanism creates a change in net magnetism in both the transverse and longitudinal components. Understanding these mechanisms is important as MRI can make measurements in either component which can ultimately give very different effects.

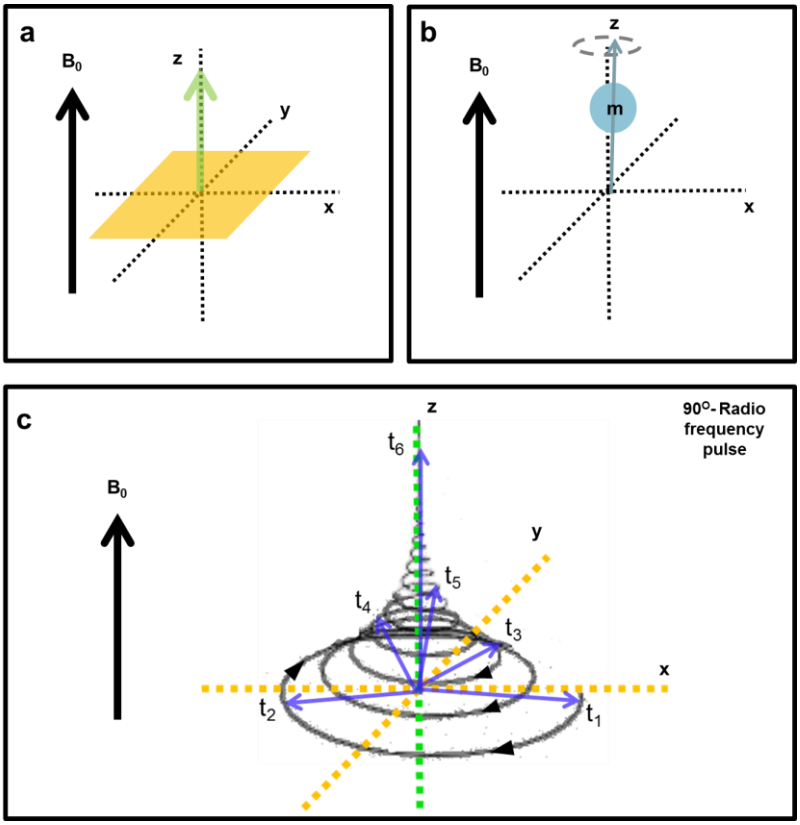

Figure 1.2.2.2. A mathematical interpretation of spinning nuclei in a magnetic field; (a), a representation of the 3-dimensional space of a proton: The z-axis is the longitudinal axis (green) and is always in the direction of the magnetic field (B_0). The x and y plane is the transverse plane (yellow) and is always perpendicular to B_0; (b), the proton is represented as a vector (m); (c), the relaxation pathway of a protons' dipole moment over a period of time (t_1-t_6) following a 90^O-radiofrequency pulse.

When the net magnetisation of relaxing protons is measured relative to the longitudinal axis it is termed *T1 relaxation* or *longitudinal relaxation* or *spin-lattice relaxation*. At equilibrium there is an overall net magnetisation in the longitudinal component as the majority of the dipoles are aligned with the magnetic field. After a RF pulse, the dipoles are flipped, overall reducing the net magnetization in the longitudinal component. As the dipoles of the protons relax back to their thermal equilibrium over a period of time the net magnetisation in the longitudinal component

increases until it is restored.[21] The restoration of the net magnetisation can be modelled as a simple exponential with T1 as the first order rate constant ($M_z = M_0(1-e^{-t/T1})$).[22] This process usually takes several seconds and is illustrated in Figure 1.2.2.3. The energy associated with T1 relaxation is lost into the surrounding environment which has led to the common synonym spin-lattice relaxation.

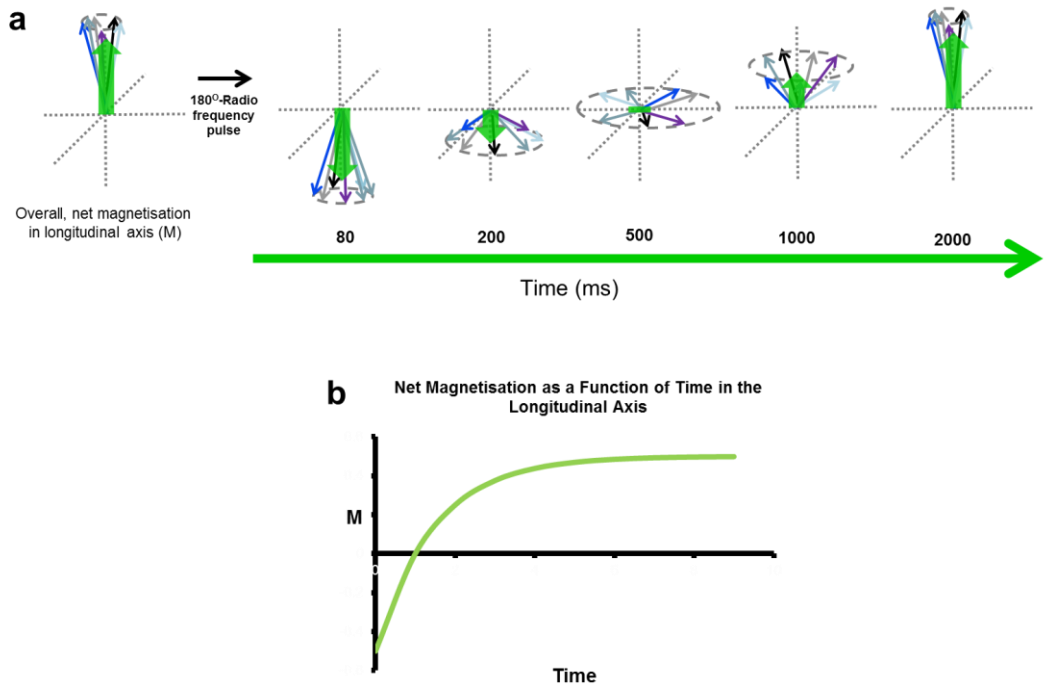

Figure 1.2.2.3. The origin of T1 relaxation; (a), hydrogen nuclei relaxing back to the equilibrium following a 180^O radiofrequency pulse over several seconds; (b), the net magnetisation (green) plotted as a function of time in the longitudinal axis.

When the net magnetisation of relaxing protons is measured in the transverse plane it is termed *T2 relaxation* or *transverse relaxation* or *spin-spin relaxation*. At equilibrium the precession of the protons is random overall creating no net magnetisation in the transverse plane. After a RF pulse, the dipole moments of the protons are flipped into the transverse plane. This results in the net magnetisation that was in longitudinal axis now being transferred into the transverse plane. As the protons precess at the Larmor frequency small magnetic inhomogeneities cause the

protons to precess at slightly different rates "*de-phase*", in turn reducing the net magnetisation in the transverse plane.[21] This can be modelled as a simple exponential decay with T2 as the first order rate constant ($M_{x,y} = M_0.e^{-t/T2}$)).[23] T2 relaxation is usually much faster than T1 relaxation and usually takes 10s of milliseconds and is illustrated in Figure 1.2.2.4. Magnetic inconsistences in the surrounding environment can change the T1 and T2 relaxations and overall give rise to contrast in an MR image and lead to the differentiation between different types of tissues and organs.

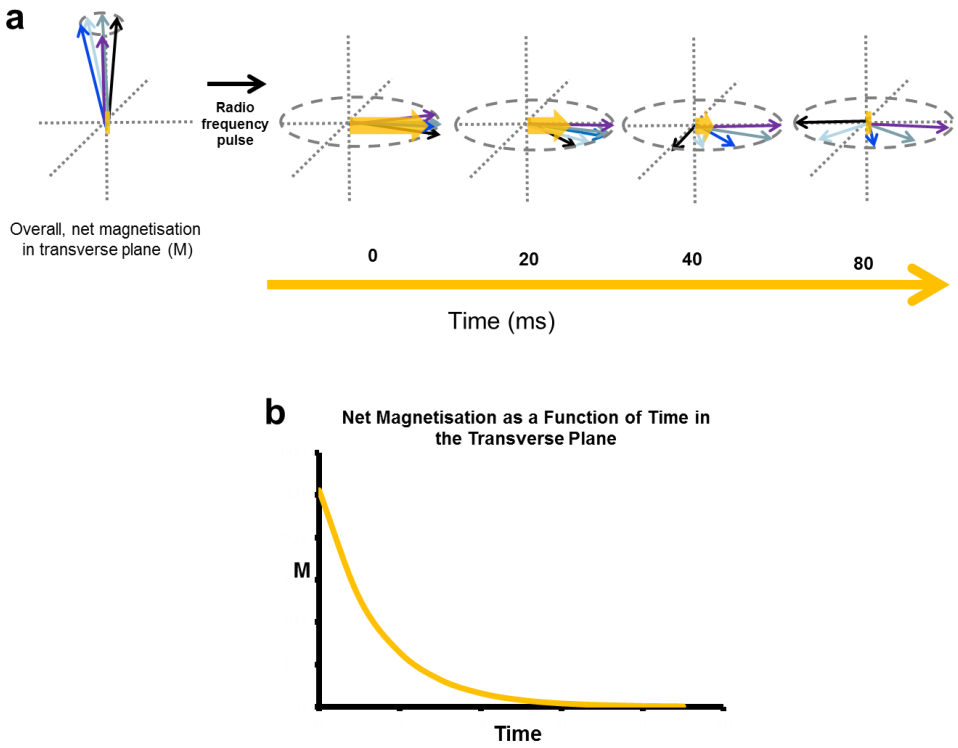

Figure 1.2.2.4. The origin of T2 relaxation; (a), hydrogen nuclei relaxing back to the equilibrium following a radiofrequency pulse over several milliseconds; (b), the net magnetisation (yellow) plotted as a function of time in the transverse axis.

1.2.3 Contrast agents

MRI can distinguish between tissue types as different tissue types contain different amounts of water. This said however, it can often be difficult to distinguish between healthy and unhealthy sites in the same tissue.[24] Contrast agents work by significantly changing the T1 and T2 relaxation times of the hydrogen nuclei in their vicinity, thus altering the MRI signal and allowing the protons to be differentiated more clearly in an MRI image. Currently, the majority of clinically available contrast agents affect the T1 signal and are called *positive contrast agents* due to the distinctive image brightening of the tissue in their vicinity (hyperintense contrast). These positive contrast agents are predominately made up of gadolinium chelates and the chemical structures of the commercially available products are shown in Figure 1.2.3.1.[25] Gadolinium (Gd^{3+}) is used owed to its high abundance of unpaired electrons in the 4f electron orbital and slow electron relaxation rate giving it greater magnetic properties compared to other atoms. For T1 relaxation to occur the gadolinium ion must exhibit field fluctuations near to the Larmor frequency which is achieved by the gadolinium ion rotating, colliding, bonding and diffusing with the surrounding environment in a phenomenon known as *Brownian motion*.[26] As a water molecule approaches and co-ordinately binds to a fluctuating gadolinium ion it can undergo a magnetic interaction that gives rise to *inner sphere relaxation*. Gadolinium ions can also magnetically interact with water molecules via a dipole-dipole interaction and this is known as *outer sphere relaxation*. As the interaction and the physical movement of a gadolinium ion has such an effect on relaxation, scientists have found that they can control T1 relaxivity effects by using various chelates that differ in size, molecular weight, hydrophobicity, number of hydrogen bonding donors/acceptors and co-ordination number.[27] Also, the distribution of the gadolinium species within the body can somewhat be controlled by the nature of the chelating agent used. The main complication with using gadolinium is that it is extremely toxic in its free form and so

these products are characteristically based around a gadolinium ion complexed to strong chelators.[28] By shielding the gadolinium from the biological environment its toxicity can be reduced. Nevertheless, these complexes are entropically unfavourable and strong thermodynamic driving forces are able to pull these complexes apart releasing free gadolinium into the body.[29] In recent years there has been an association made between free gadolinium and the debilitating disease nephrogenic systemic fibrosis.[30] The disease was first recognised in 1997 in patients with impaired renal function and typically causes hardening of the connective tissue throughout the body. Although gadolinium based contrast agents do raise safety concerns, for many, the risks are worth taking. Gadolinium based contrast agents are also limited by their non-specificity to a target, quick removal by renal elimination and a short window for contrast enhancement.[31] It is for these reasons that new MRI contrast agents need to be developed.

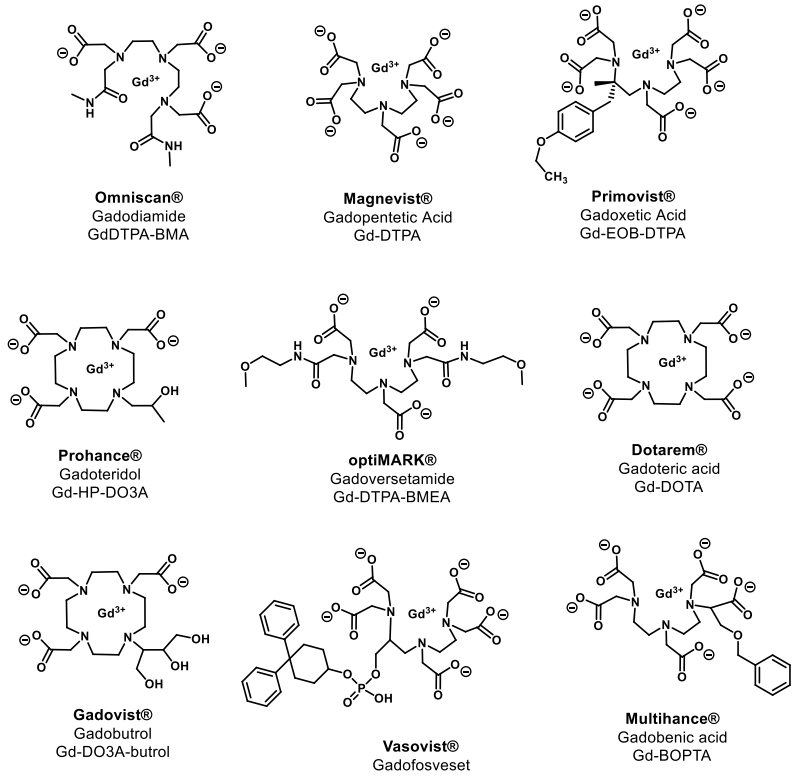

Figure 1.2.3.1. The chemical structure of the commercially available T1 gadolinium chelate contrast agents.

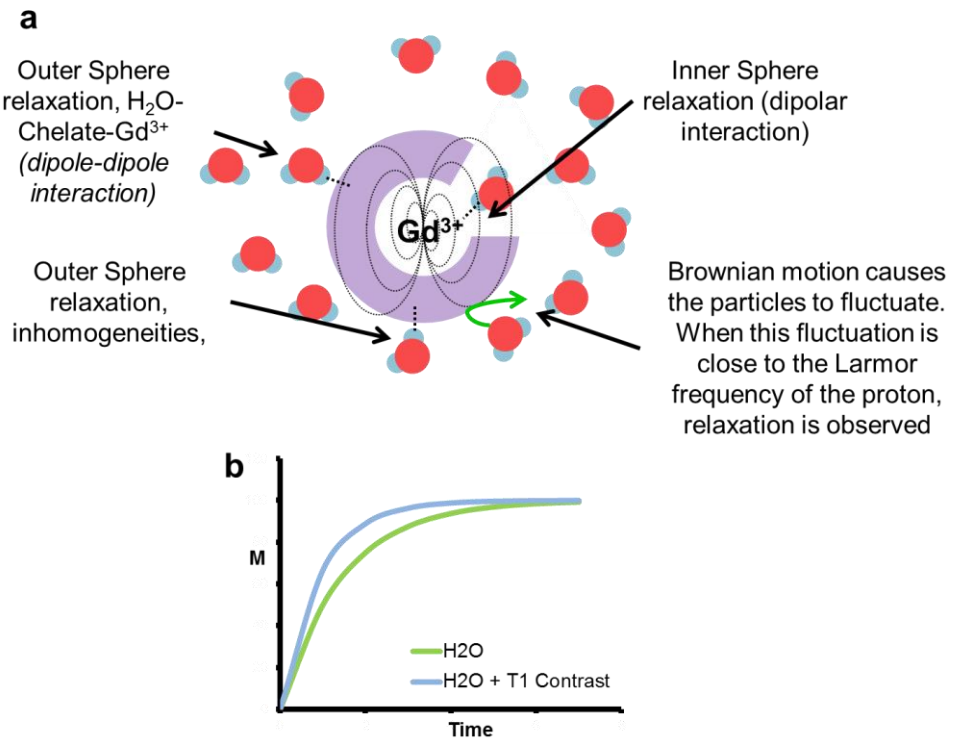

Figure 1.2.3.2. The origin of T1 contrast; (a), schematic illustration of a gadolinium contrast agent interacting with water molecules to induce T1 relaxation; (b), an example of the effect a T1 contrast agent has on the magnetisation over time. The T1 relaxation time is decreased providing contrast to protons in the vicinity of the contrast agent.

The next class of contrast agents are the *super paramagnetic iron oxide nanoparticle* (IONP) contrast agents.[32] The magnetic properties of IONPs enable it to affect T1 and T2 relaxation times on the surrounding protons. IONP research is predominately focused on their effect at decreasing the T2 relaxation times of protons. When the IONPs are placed in a magnetic field they become magnetised. These magnetic nanoparticles induce pockets of magnetic disruption into the system known as *in-field inhomogeneities*.[33] The inhomogeneities in the field cause the precession of the protons to de-phase at a much faster rate, in turn decreasing T2 relaxation time. IONPs can also act as a T1 contrast agent as the iron ions themselves have several

unpaired electrons (5 and 4 unpaired electrons for Fe^{3+} and Fe^{2+}, respectively) making them paramagnetic in nature. This gives the IONP's surface bound iron ions the ability to induce inner and outer sphere relaxation, albeit to a lesser extent that gadolinium.[34] The type and extent of contrast is predominantly determined by the size of the IONP.[35] Larger IONPs have larger magnetic fields and therefore, introduce larger inhomogeneities into the system. This increases T2 relaxation and makes T2 contrast the more dominant effect over T1 contrast. Smaller IONPs have smaller magnetic fields and therefore introduce less inhomogeneities into the system, additionally in relation to size, water molecules are able to diffuse between smaller IONPs at a much faster rate. Overall, both effects create a system that experiences less inhomogeneities. This reduces the T2 contrast effect for smaller IONPs, in some cases it is reduced to such an extent it makes T1 contrast the dominant effect.

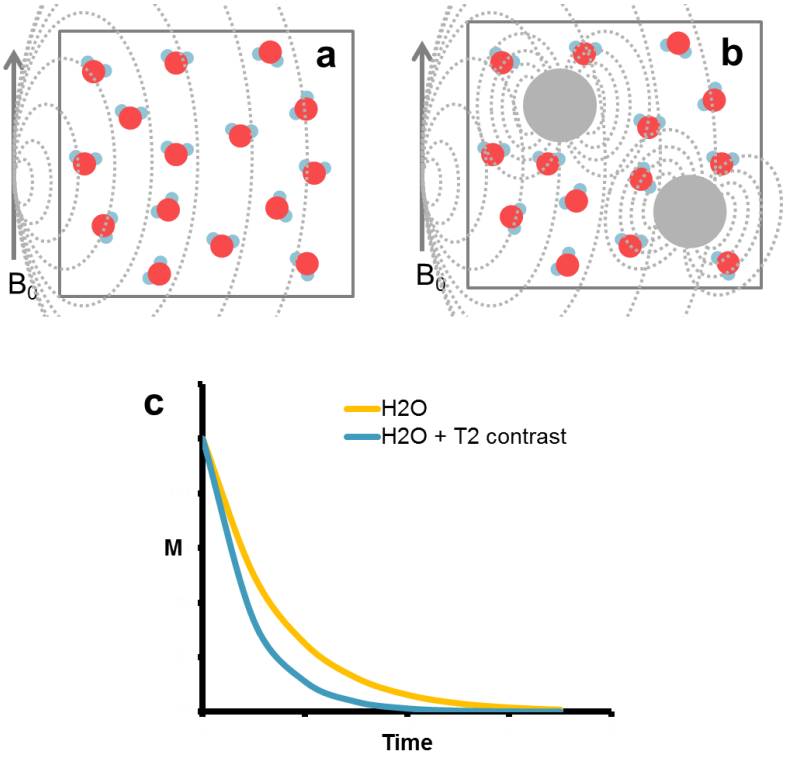

Figure 1.2.3.3. The origin of T2 contrast; (a), water molecules in the presence on an external magnetic field; (b), IONPs introducing local magnetic field inhomogeneities; (c), example of the effect a T2 contrast agent has on the magnetisation over time. The T2 relaxation time is decreased providing contrast to protons in the vicinity of the contrast agent.

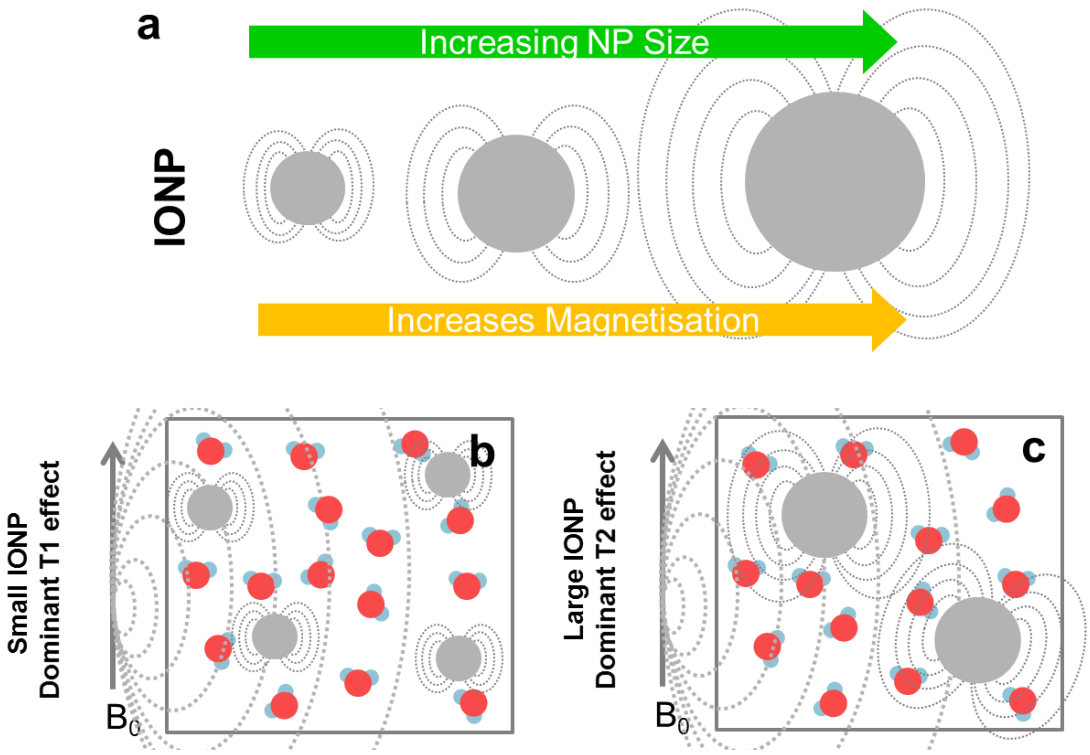

Figure 1.2.3.4. The effects of IONP size on contrast capability; (a), increase in IONP size increases the overall magnetization of the magnetic nanoparticle; (b), Smaller IONPs have smaller magnetic fields and therefore introduce less inhomogeneities into the system, also, in relation to size, water molecules are able to diffuse between smaller IONPs at a much faster rate. Overall, creating a system that experiences less inhomogeneities. (c), Larger IONPs have larger magnetic fields and therefore introduce larger inhomogeneities into the system.

Commercially available products have primarily focused on using IONPs as a T2 contrast agent.[36] IONP contrast agents are characteristically called *negative contrast agents* due to the distinctive image darkening of the tissue in their vicinity (hypointense contrast). These agents work by accumulating in healthy tissue and darkening its MRI signal enabling easier detection of the damaged or diseased tissue. There have been 6 licensed commercially available IONP products in the market

including; Feridex IV® (a.k.a. Endorem™), Resovist®, Sinerem® (a.k.a. Combidex®), Ferumoxytol®, Lumirem® (a.k.a. GastroMARK®) and Abdoscan®.[37] All the products have a core made from IONP crystals, however each are formulated with their own unique polymers and have varying hydrodynamic sizes, therefore yielding products with distinctive *in vivo* pharmacokinetic characteristics. The majority of these compounds (Feridex IV®, Resovist® and Sineren®) were all primarily used to provide contrast in large organs of the lymphatic system (liver, spleen, lymph nodes, bone marrow). Prior to the time of writing this thesis, 3 of the products have been discontinued; Feridex IV® in 2009, Sinerem® in 2007 and Abdoscan® in 2000.[38] Resovist® is only available in Japan and the USA. Ferumoxytol® is licensed for use as an anaemia medication only, however it has been reported that this formulation is used *off-label* as an MRI contrast agent.[39] Lumirem® is still currently licenced for providing contrast in the GI tract following oral administration. A table summarising the current status of contrast agents can be found in Table 1.2.3.1. Generally, the intravenously administered lymphatic IONP contrast products have now been discontinued. After a number of years in clinical use, companies ceased production of their IONP contrast agents largely attributing their withdrawal to the lack of demand in the market. The discontinuation of lymphatic IONP contrast agents was due to a number of factors: Firstly, a major reason for their withdrawal was highlighted in a pinnacle study on Sinerem®, reported by the EMA.[40] The EMA found that using Sinerem® gave no significant benefits in sensitivity and failed to confirm non-inferiority with regards to specificity. Overall clinicians were finding that these products were not sensitive or specific enough to consistently and reliably detect cancer as often as they should. Secondly, it is reported that clinicians and radiographers were finding that they could use gadolinium agents and other imaging techniques to provide better detection of liver lesions when compared to IONPs.[41] Lastly, a minor consideration was that although findings from many studies conclude that IONP contrast agents have an agreeable safety profile, individual case studies reveal that patients did not

relish large volumes of black liquid being intravenously administered which inevitably led to patient dissatisfaction.[42] Essentially, these points combined, largely left IONPs without a market. Their manufacture was no longer economically viable and so their production was discontinued. Although the clinical utility of the first generation of IONP contrast agents was not demonstrated, IONPs do have remarkable magnetic properties and low toxicities, leading many to still believe that the material has a promising future in medicine. The key to using IONPs as a contrast agent will largely revolve around engineering particles that are specific in function and nature and that have a greater contrasting ability.

Brand name	Structure	Hydrodynamic size (nm)	Avg. Core size (nm)	MRI classification	Relaxivity (B_0 = 1T, *B_0 = 0.5T)	r_2/r_1	Target	Company	Current license
Magnevist®	Gd-DTPA			T_1 agent	r_1 =3.4, r_2 =3.8	1.1	Extracellular	Bayer Schering	Currently licensed
Omniscan®	Gd-DTPA-BMA			T_1 agent	r_1 =3.9, r_2 =4.3	1.1	Extracellular	GE-healthcare	Currently licensed
Primovist®	Gd-EOB-DTPA			T_1 agent			Liver	Bayer Schering	Currently licensed
Multihance®	Gd-BOPTA			T_1 agent			Extracellular	Bracco	Currently licensed
Prohance®	Gd-HP-DO3A			T_1 agent	r_1 =3.7, r_2 =4.8	1.3	Extracellular	Bracco	Currently licensed
Vasovist®/Ablavar®	Gd-DTPA			T_1 agent			Extracellular	Lantheus Medical Imaging	Currently licensed
optiMARK®	Gd-DTPA-BMEA			T_1 agent			Extracellular	Mallinckrodt	Currently licensed
Gadavist®	Gd-DO3A-butrol			T_1 agent			CNS, Kidneys, Liver	Bayer Schering	Currently licensed
Dotarem®/Artirem®	Gd-DOTA			T_1 agent	r_1 =3.4, r_2 =4.8	1.4	Extracellular	Guerbet	Currently licensed
VoLumen®	Barium Sulphate			T_1 & T_2 agent			Bowel marking	Bracco	Currently licensed
Ferumoxides (Feridex IV®, Endorem™)	IONP-Dextran	120-180 nm	4.5 nm	T_2 agent	*r_1 = 10.1, r_2 =120	11.8	Recticuloendothelial system, liver	AMAG Pharma/ Bayer Schering	MRI - Product discontinued in 2009
Resovist®	IONP-Carboxy dextran	45-60 nm	4.2 nm	T_2 agent	*r_1 = 9.7, r_2 =189	19.5	Blood pool, liver	Bayer Schering/ FUJIFILM	Currently licensed for MRI in USA and Japan
Sineren®, Combidex®	IONP-Dextran	15-30 nm	4.6 nm	T_2 agent	*r_1 =9.9, r_2 =65	6.6	Blood pool, Lymphatic system	Guerbet/ AMAG Pharma	MRI - Product discontinued in 2007
Feraheme® (ferumoxytol)	IONP-Carboxylmethyl dextran	30 nm		T_2 agent	*r_1 =15, r_2 =89	5.9		AMAG Pharma	Currently licensed for anaemia
Lumirem®, GastroMARK®	IONP-Silicon	300 nm		T_2 agent	*r_1 =3.2, r_2 =72	22.5	GI tract, Stomach	AMAG Pharma	Currently licensed for MRI. Oral administration
Abdoscan®	cross-linked poly(ammonium styrenesulfonate) - IONP	>300nm		T_2 agent			Bowel marking	GE-healthcare	MRI - Product discontinued in 2000

Table 1.2.3.1. Current status of commercially available contrast agents.

1.2.4 Superparamagnetic iron oxide nanoparticles

Nanoparticles offer a great platform from which to build a biological device. They have controllable sizes ranging from a few nanometres to many hundreds of nanometres. As a result, they have comparable sizes to proteins, viruses, enzymes and other biological nanostructures.[18] The iron oxide family is probably the most popular family of nanoparticles to emerge in recent years. Out of the 16 types of iron oxide, Magnetite (Fe_3O_4) holds perhaps the most promising potential in biomedicine.[43] In its bulk form magnetite is somewhat uninteresting, but when its particle size is reduced to only a few nanometres it takes on some rather remarkable magnetic characteristics. These magnetic properties allow iron oxide nanoparticles (IONPs) to be used for MRI contrast imaging, hyperthermia treatment and magnetic targeting.[18] In addition to this, they are widely regarded as non-toxic and have already been approved by the FDA and EMA for use in MRI contrast applications and anaemia treatment.[44,45]

Magnetite's magnetic properties may be explained by looking into the material's structure. Magnetite has a cubic spinel structure with a general formula that can be written as $(Fe^{3+})_{tet}(Fe^{3+}Fe^{2+})_{oct}O_4$. A single unit cell consists of oxygen atoms found in a 'face centred cubic' arrangement.[46] This arrangement creates interstitial octahedral sites (2/3) and interstitial tetrahedral sites (1/3).[47] Half of the Fe^{3+} ions occupy the tetrahedral sites, while the Fe^{2+} ions and the remaining half of the Fe^{3+} ions occupy the octahedral sites.[48,49] The nuclei spins of the Fe^{3+} ions in the octahedral sites are aligned antiparallel to the Fe^{3+} ions in the tetrahedral sites, therefore contributing no effect to the overall net magnetisation, however, the nuclear spins of the Fe^{2+} ions are aligned parallel to the electron spins of the Fe^{3+} ions found in the tetrahedral sites thus, giving magnetite an overall net magnetic dipole.[49] This overall structure gives magnetite ferrimagnetic properties.

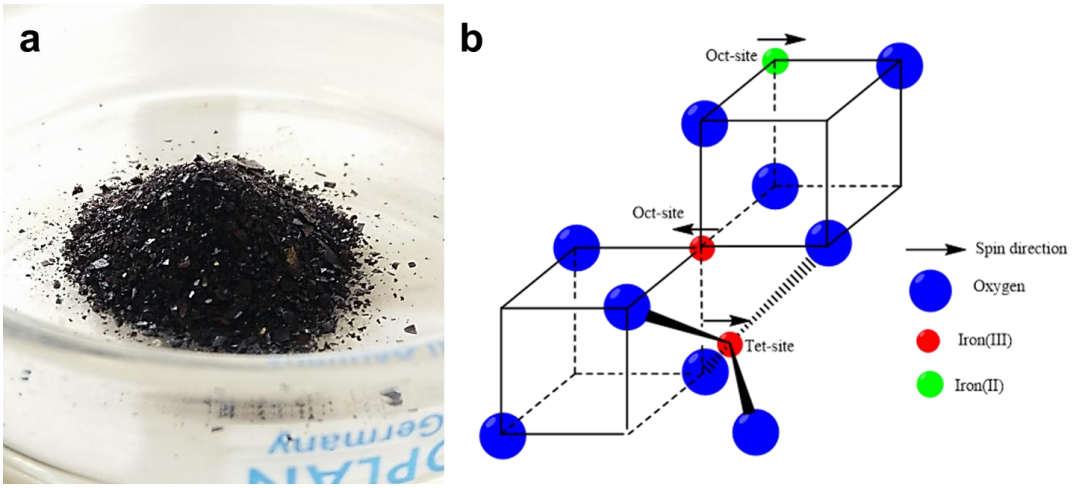

Figure 1.2.4.1. The structure of IONPs; (a), Macro image of magnetite iron oxide nanoparticles (IONPs); (b), A schematic representation of the crystal structure of magnetite.[49]

IONPs are interesting because of their unique magnetic properties. All compounds may be divided into 5 distinctive groups of magnetic materials largely governed by their atomic structure and arrangement:[50] 1. *Diamagnetism* is a phenomenon exhibited by all materials that possess paired electrons and is typically characterised by the material being slightly repelled by an external magnetic field. Diamagnetism is a weak force and is only observed if the material has no other competing magnetic properties; 2. *Paramagnetism* is a phenomenon exhibited by an atomic or molecular species that possess unpaired electrons and this gives the material an overall dipole moment. Paramagnetic materials are usually characterised by their slight positive magnetisation in the presence of an external magnetic field. The next three classifications of materials are observed when atoms are arranged in ordered structures termed *crystal lattices*: 3. *Ferromagnetism* arises when paramagnetic nuclei in ordered structures undergo long-range ordering and arrange their spins in a single direction giving the material an overall net magnetisation. Ferromagnetic materials are highly magnetic; 4. *Antiferromagnetism* is exhibited when paramagnetic

nuclei in ordered structures are arranged in equal and opposite directions cancelling out any contributions from their magnetic dipoles. A perfect antiferromagnetic material should have no overall net magnetisation, however small lattice defects usually result in these materials being weakly magnetic and often exhibit small paramagnetic or ferrimagnetic behaviour; 5. *Ferrimagnetism* is found when paramagnetic nuclei in ordered materials are arranged in opposite directions where the nuclei are not equal in dipole moment. This usually is observed for more complex crystal structures and results in a strong overall net magnetisation. The characterisation of all materials is usually determined by how they react in the presence on an external magnetic field. Measuring the magnetism of a material while cycling between positive and negative external magnetic fields usually results in a plot that is unique to each magnetic classification. These plots are termed *M-H curves* or *hysteresis loops* and are summarised in Figure 1.2.4.2.[18]

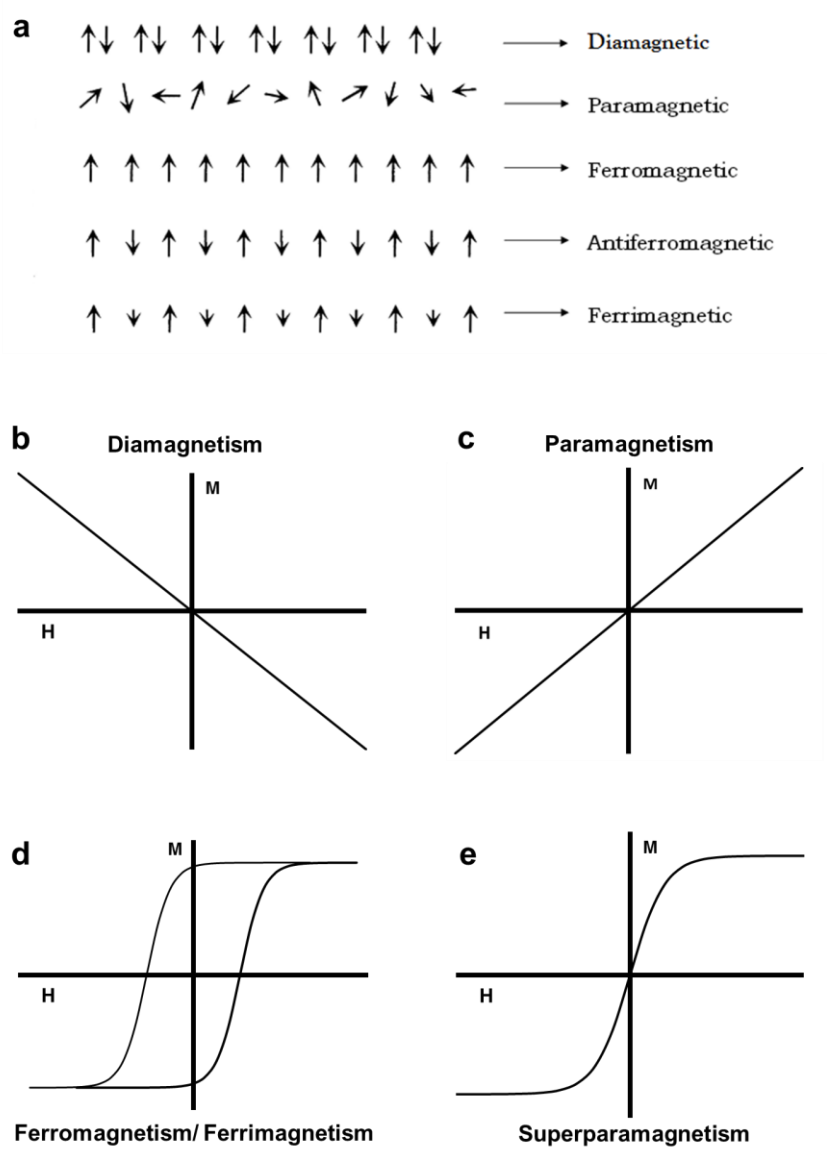

Figure 1.2.4.2. The origin of magnetism; (a), A schematic representation of the nuclei spin ordering that gives rise to the main types of magnetic material. Typical M-H curves for; (b), diamagnetic materials; (c), paramagnetic materials; (d), ferro-/ferri- magnetic materials and; (e), superparamagnetic materials.

Magnetite is a ferrimagnetic material. To reduce the internal energy in the bulk material, magnetite establishes small regions of uniform magnetisation termed *domains* which are often 10s of nanometres in diameter.[51] When the size of a magnetite particle falls below a threshold value it enters a single-domain state as it is

too small to set up multiple domains. This critical limit varies depending on source but is usually considered to be below 20 nm for magnetite.[52] When a particle of magnetite is reduced to below this critical value it behaves rather differently and is said to be *Superparamagnetic*. Superparamagnetic materials become magnetized in the presence of an external magnetic field however, unlike ferromagnetic and ferrimagnetic materials, superparamagnetic materials do not retain any magnetisation when the external magnetic field is removed. Superparamagnetic materials give distinct sigmoidal M-H curves, an example is given in Figure 1.2.4.2.e. The overall bulk properties resemble that of paramagnetic materials, the key differences being that they are highly ordered at the molecular level and usually have much greater magnetic moments. Gadolinium,[53] nickel[54] and cobalt[55] have also been used to make magnetic nanoparticles due to their paramagnetic atomic nuclei, however their use in medicine is somewhat limited due to their associated toxicities in humans. Iron oxide on the other hand is generally considered safe and non-toxic which therefore makes it an extremely promising nano-material for biomedical applications.

1.2.5 Engineering superparamagnetic iron oxide nanoparticles for biomedical applications

IONPs hold a high level of interest in the scientific community, as a result a considerable amount of attention has been devoted to the development of this material. Many methods for IONP synthesis exist each with their own unique advantages and shortcomings:

Chemical co-precipitation is by far the most popular way of synthesising IONPs. This method is a well-studied technique, relatively straight forward and can be performed at minimal cost.[56] The method is based on the precipitation of IONPs from Fe^{3+} and Fe^{2+} salts via the addition of a base.[57] The overall reaction may be written as: Fe^{2+} +

$2Fe^{3+} + 8OH^- \rightarrow Fe_3O_4 + 4H_2O$.[56] Although chemical co-precipitation is a widely used method it does have shortcomings. Firstly, nanoparticles made using chemical co-precipitation are extremely sensitive to their reaction conditions including; ionic strength, pH of the reaction, presence of oxygen, injection rates, presence of salts and counter ions, temperature and concentration of the alkali agent. This often leads to relatively polydisperse samples. A polydisperse sample could lead to batch to batch variation in stability, magnetism and biodistribution. Secondly, IONPs made via chemical co-precipitation tend to form large polydisperse aggregates which lead to sedimentation. Finally, naked magnetite nanoparticles made using chemical co-precipitation readily oxidise into a less magnetic form called maghemite, often with a loss of magnetisation, however this can be reduced by keeping the IONPs in an inert environment.[58]

High temperature thermal decomposition is a method that has considerably increased in popularity in recent years. This non-aqueous method utilises organometallic compounds, high boiling point organic solvents and long chained fatty acids to yield IONPs with highly controllable sizes and narrow size distributions.[59] The main drawback with these IONPs is that they are hydrophobic and can only be dispersed in organic solvents, therefore they are unsuitable for biological applications without further modification.

Hydrothermal synthesis is a process whereby IONPs are produced in aqueous conditions at high temperature and pressure using autoclaves and microwave reactors.[60] This technique can also be performed using organic solvents where it is referred to as *solvothermal synthesis*. Both strategies are known to produce IONPs with high crystallinity and recent publications have reported the synthesis of particles with varying shapes and morphologies including; rods, rings, and hollow nanoparticles.[61]

Sol-gel synthesis is a technique widely used to produce metal oxides and is commonly employed for the development of ceramics.[62] The '*sol'* is a colloidal suspension of precursor reagents. In IONP synthesis this usually involves iron alkoxides or iron salts (chlorides, nitrates and acetates). The '*gel*' is formed by the addition of gelators, catalysts and reagents. These additives form a gel like reaction mixture creating an integrated network between the precursors and gelators. This network plays a key role in influencing the type of structures formed and can be heavily influenced by temperature, pH, concentration of reagents, salts and solvents.[24] Heat treatment or high vacuum conditions are then used to remove the solvent yielding the final crystal product.

Sonochemical synthesis is a method that produces IONPs in the presence of high energy sounds waves (>20 mHz), a process more commonly known as *sonication*.[63] The negative and positive pressures of these high energy waves generate microbubbles. These microbubbles are thermodynamically unstable and as a result implode in a phenomenon known as *cavitation*.[64] The imploding nanoparticle releases energy into the environment as heat. This localised heating or '*hot spot*' can be used to facilitate processes where large amounts of energy are needed in small volumes.[65] This technique is frequently used in; chemical reactions, homogenation, mixing, cleaning and drug encapsulation. *Sonochemical synthesis* has been used to produce naked and functionalised IONPs. The energies involved in sonication are usually large enough to force species together that have a high activation energy for mixing. The major drawback is that the high energies used can often damage delicate molecules and biologics. This however, can be reduced by using cooling systems such as an ice bath.

Microbial synthesis is a remarkable process that exploits biological organisms to synthesise near perfect IONPs.[66] *Thermoanaerobacter ethanolicus* and *Shewanella*

loihica are two strains of bacteria that have been shown to reproducibly produce IONPs under anaerobic conditions. The main drawback with microbial synthesis was the small scale of IONP production, however recently *Moon et al*, have been seeking to address this issue by using large scale fermentation processes.[67]

The most widely used IONP synthesis methods have been discussed, however many more methods exist including; polyol synthesis, microwave synthesis, electron beam lithography, gas-phase deposition, flow reactors, electrochemical synthesis, nano-reactors and supercritical fluid synthesis. In depth reviews of each of these synthesis processes may be found in recent publications by *Reddy et al* and *Wu et al*.[68,69] Considerable effort has been placed into synthesising IONPs, however the methods discussed rarely make IONPs that are suitable for biomedical applications. Due to their small size, *bare* or *naked IONPs* have large surface energies and to reduce this effect IONPs have a tendency to agglomerate.[58] These aggregates are often several microns in size which sediment under their own gravitational mass. In this aggregated state IONPs are largely unsuitable for biomedical applications.[58] IONPs synthesised using organic solvents are usually functionalised with long chained fatty acids making these particles extremely hydrophobic and again not suitable for biomedical applications.[70]

Traditionally, polymers have been used to overcome many of the challenges faced with the delivery of IONPs.[24] Polymers provide stabilisation via two key mechanisms; firstly, *steric stabilisation* which is founded in the quantum mechanical principle that clouds of electrons cannot occupy the same space (Pauli's exclusion principle).[71] The resulting effect is that large bulky molecules tend to repel each other and act as a barrier against agglomeration; secondly, *electrostatic stabilisation* which originates from the electronic repulsion experienced by two species of the same charge.[72] As a result, introducing highly charged polymers onto the surface of nanoparticles

promotes colloidal stabilisation. Polymers may promote colloidal stabilisation by a single or combined effect (Figure 1.2.5.1). Many hundreds of polymers have been used to stabilise IONPs, though the most common include; polyethylene glycol (PEG), polyvinyl acetate (PVA), dextran (and its derivative carboxymethyl dextran) and chitosan, with dextran being the most widely used in the first generation of IONP contrast agents (Figure 1.2.5.2). Additional, the nature of polymer not only provides stabilisation but also determines properties such as size, morphology, charge and has a large impact on the resulting pharmacokinetic profile.

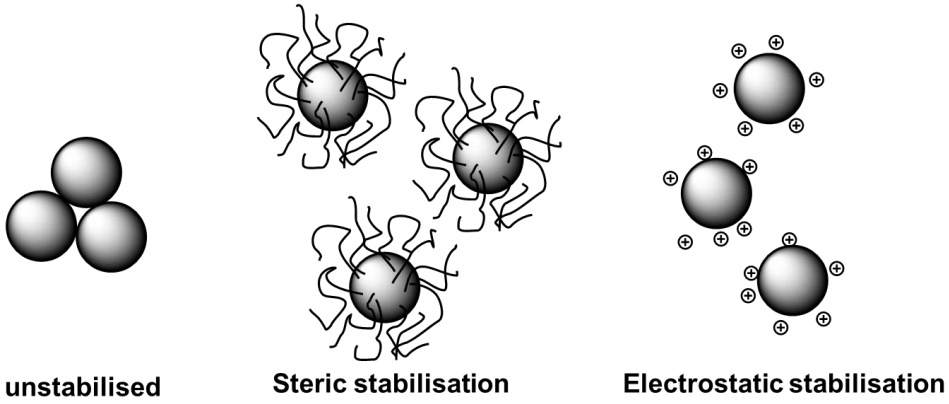

Figure 1.2.5.1. *Steric stabilisation* and *electrostatic stabilisation*.

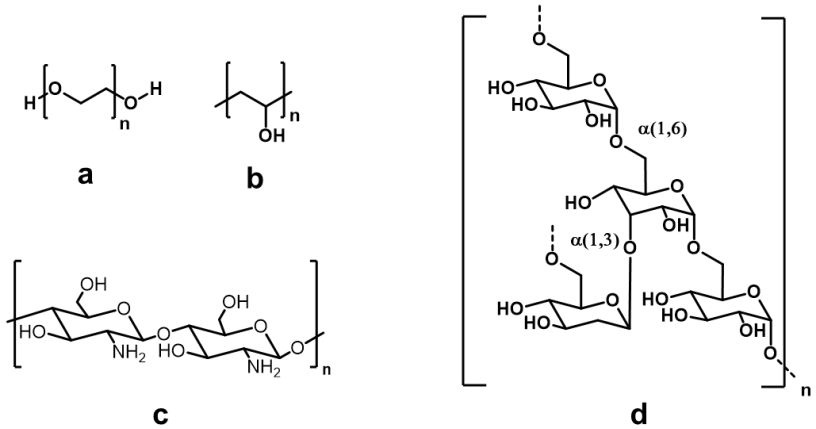

Figure 1.2.5.2. Structure of common IONP stabilising polymers: (a), polyethylene glycol (PEG); (b), polyvinyl acetate (PVA); (c), chitosan and (d), dextran

Research has shown, that as an IONP enters the body it is exposed to a rich environment of proteins that bind to the material and label it as “foreign”, a process known as *opsonisation*.[73] The tagged material is then taken up by phagocytic cells (macrophages and monocytes) where they are processed and broken down.[74] This process makes it very difficult to engineer long circulating nanoparticles for medical treatment. The key advantage of using IONPs is due to their favourable toxicity profile in humans, however iron is also a valuable mineral vital for healthy human function.[74] As a result, the body is extremely good at scavenging IONPs and recycling them to obtain the valuable iron mineral where it is stored in ferritin to later be used in the production of haemoglobin in red blood cell synthesis.[74,75] The body has an efficient and effective clearance system for IONPs making engineering long surviving IONPs very difficult. The blood half-life of these compounds varies considerably depending on the nature of the nanoparticle species, however one key aspect that scientists can easily control is the selection of polymer.[76] A common example is given by the stealth polymer *polyethylene glycol* (PEG). A PEGylated IONP was created under the trade name Clariscan®. It has widely been reported that Clariscan® has an increased blood half-life compared to its dextran counterparts, however it did not reach the clinic and was discontinued in the late development stages.[32] It should also be considered, that it may not be appropriate for a diagnostic nanoparticle to have too long a circulation time. Ideally, a diagnostic agent should be cleared from the body as soon as the imaging procedure is performed, although this may not be true for a theranostic nanoparticle. Another major factor that is believed to play a role in the pharmacokinetics and biodistribution of IONPs is the effect of hydrodynamic size. Classically, clinical IONP contrast agents which had a mean hydrodynamic diameter <50 nm where categorised as ultra-small superparamagnetic iron oxide contrast agents (such as Clariscan® and Combidex®).[77] The general size trend is that larger IONPs have shorter blood half-lives as they are more quickly taken up by the macrophage rich organs whereas, the ultra-small IONPs have longer circulation times

and better tissue penetration. The importance of size is debated, but what is generally accepted is that nanoparticles larger than 200 nm are usually filtered out by the liver and spleen, whereas particles smaller than 6 nm are usually quickly excreted renally.[78] Of course, these values are not absolute and do vary depending on the nature of the nanoparticle. Overall, it seems that quite a complex picture is emerging where IONP synthesis technique and the polymer stabiliser all have a crucial impact on the resulting contrast agent.

1.3 Polymer Micelles as Delivery Vectors for Biomedical Applications

1.3.1 Amphiphilic polymers as drug carriers

Polymeric micelles have been widely used in industrial processes and commercial products over the years. Micelles are formed from the aggregation of amphiphiles and provide a particularly useful strategy for the delivery of medicines in biomedical applications. An amphiphile is a species that is composed of both a hydrophilic region, termed the *head group* and a hydrophobic region, termed the *tail group*.[79] When an amphiphile is placed in an aqueous environment it will seek to minimise the high energy interactions between its hydrophobic moieties and the surrounding water molecules. Consequently, this causes the amphiphiles to rearrange to form a secondary structure which shields the hydrophobic moieties from the surrounding aqueous environment.[80] Several secondary structures exist and their architecture is usually determined by the amphiphile geometry. In 1976, Israelachvili described the relationship between the amphiphile and its secondary structure mathematically and summarised it using the *critical packing parameter* (CPP).[81]

$$CPP = \frac{V}{a_0.l_c} \qquad (1.3.1.1)$$

Where: $\boldsymbol{l_c}$, is the length of hydrocarbon chain. $\boldsymbol{v}$, the volume of the hydrocarbon chain and $\boldsymbol{a_0}$, the area of the head group. CPP values allow for the prediction of a secondary structure from the geometry of a specific amphiphile: values of approximately 1 give planar bilayer secondary structures; a CPP between 0.5-1 forms bilayer vesicles commonly known as liposomes, a CPP of 0.3-0.5 produces cylindrical nanofibers and

a CPP of less than 0.3 tends to create micelles. An example of these structures can be found in Figure 1.3.1.1.[82]

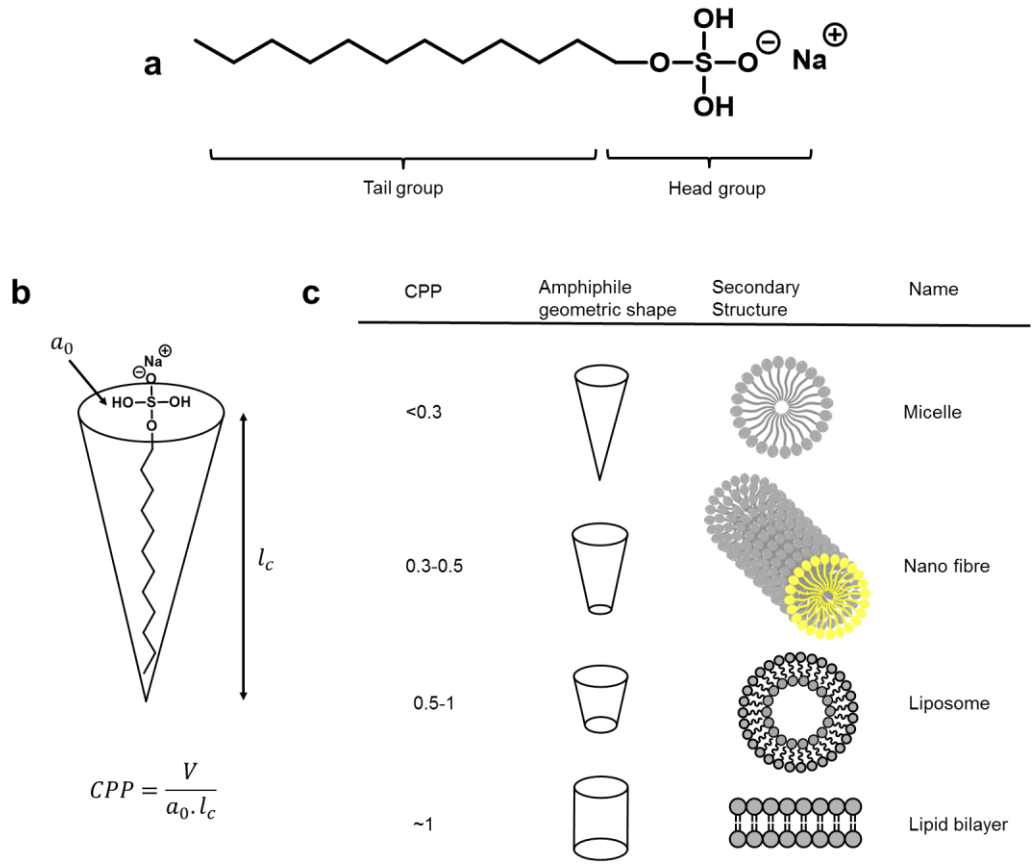

Figure 1.3.1.1. The origin of amphiphilic nanoparticles; (a), chemical structure of the common amphiphile *sodium dodecyl sulphate* highlighting the hydrophobic tail group and hydrophilic head group; (b), Geometric structure of an amphiphile modelled by Israelachvili's crystal packing parameter (CPP); (c), table summarising the relationship between CPP and aqueous secondary structure.

Micelles are typically used as industrial solubilizers and cleaning agents, however they have become particular interesting for medical applications.[83,84] Overall micelle structures are stable in aqueous conditions while still maintaining a hydrophobic core making them promising vectors for the delivery of challenging medicines, mostly hydrophobic drug molecules.[85] The delivery of hydrophobic drugs poses a

considerable challenge for formulation scientists as they are incredibly hard to deliver via traditional *solid oral dosage forms* or by *intravenous injection*. In recent years, industrial techniques such as *high-throughput screening* (HTS) have led to the development pipeline being dominated by highly hydrophobic new chemical entities.[86] These potential drugs usually have promising *in vitro* results but are often let down by their poor aqueous solubility leading to a poor bioavailability in a patient.[87] Micelles have gained considerable attention as aqueous vectors for hydrophobic drugs, especially for the delivery of poorly soluble anticancer drugs.[88] Despite a large focus on micelle technology no commercial products are available, yet. However, a number of promising potential candidates are in clinical trials and they are summarised in Table 1.3.1.1.[89]

Name	Polymer	Drug	Company	Status
NK105	PEG-polyaspartic acid	Paclitaxel	Nippon Kayaku	*Phase II/III
NK012	PEG-polyglutamic acid	Irinotecan metabolite	Nippon Kayaku	Phase II
NK911	PEG-polyaspartic acid	Doxorubicin	Nippon Kayaku	Phase II
NC-6004	PEG-polyglutamic acid	Cisplatin	Nanocarrier	Phase III
NC-4016	PEG-polyglutamic acid	Oxaliplatin	Nanocarrier	Phase I
NC-6300	PEG-polyaspartate hydrazone	Epirubicin	Nanocarrier	Phase I
NM0127	GCPQ	LENK	Nanomerics	Preclinical
NM0133	GCPQ	Cyclosporine A	Nanomerics	Preclinical

*July 2016, Nippon Kayaku published that their phase III breast cancer trial for NK105 did not achieve its primary endpoints. NK105 is now in a phase II stomach cancer trial.

Table 1.3.1.1. Current status of some promising commercial micelle products.

At very low concentrations amphiphiles have an affinity for liquid-air or liquid-solid interfaces in an attempt to minimise their unfavourable interactions with the water. When amphiphile concentrations become large enough, the interfaces become saturated and the amphiphiles begin to agglomerate within the aqueous solution to form micelles.[90] The concentration at which this phenomenon is observed is known

as the *critical micelle concentration* (CMC).[90] The CMC is considered one of the most important features of a micelle and is associated with structural stability. The lower the CMC value the less polymer is needed to create the micellar structure. Low CMC amphiphiles are favoured for biomedical applications as they are less sensitive to changes in concentration, this is especially significant in pharmacology where dilution with the blood or stomach contents could result in the deaggregation of micelles held together by weaker forces, resulting in the premature release and precipitation of the drug contents.[85] Research has found that large polymeric amphiphiles often have a CMC several orders of magnitude lower than their small molecular counterparts. These larger polymer amphiphiles can also be composed of more biocompatible materials like carbohydrates or PEGylated species. Furthermore, small molecule amphiphiles can be associated with toxicities as the amphiphiles can interact with biological membranes and disrupt their function.[91] Polymeric amphiphiles used for formulation and delivery applications are often considered in terms such as *biocompatible* or *non-biocompatible*. These terms are often derived from the ability of a polymer to be able to successfully deliver an agent (therapeutic or diagnostic) without inducing significant negative responses (toxic, thrombogenic, immunogenic or carcinogenic effects).[92] Of course, one must always consider the contextual application of a polymeric material, as a single polymer may be applicable in one circumstance but may not be suitable in another. For example, a particular polymer may have virtually no side effects when used orally but may have significantly larger side effects when administered intravenously. Therefore, polymers may only truly be regarded as biocompatible with regards to a specific application. This has led to the contemporary scientific understanding of *biocompatibility* to be defined as "*the ability of a material to perform with an appropriate host response in a specific application*".[93]

Various polymer amphiphiles have been reported and they can be categorised into groups depending on their chemical structure (Figure 1.3.2).[85] These polymers

include repeating units of hydrophilic and hydrophobic segments that give rise to their amphiphilic characteristics. The orders and proportions of hydrophilic and hydrophobic segments can usually be controlled to yield micelles with the appropriate thermodynamic properties for stability, drug loading and pharmacokinetic profile.

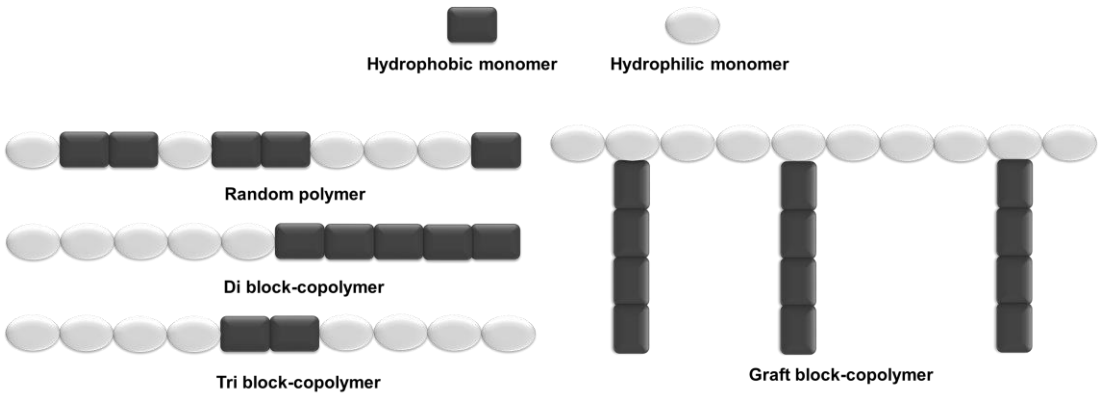

Figure 1.3.1.2. Main structural types of micelle forming amphiphile polymers.

1.3.2 Amphiphile interactions

There is a large volume of publications describing micelle formation, mostly due to the large resources of the detergent industries that sought to understand the underlying mechanisms of their amphiphiles in order to maximise efficiency and profits. The traditional way of understanding the self-assembly of amphiphiles can be described thermodynamically using the Gibbs-Helmholtz equation:

$$\Delta G_m = \Delta H_m - T\Delta S_m \qquad (1.3.2.1)$$

Where: ΔG_m, is the change in Gibbs free energy for micellisation; ΔH_m, the enthalpy change for micellisation; T, temperature and ΔS_m, the entropy change for micellisation. Micellisation is driven by the minimisation of ΔG_m. The enthalpy change for micellisation is made up of two competing factors: Firstly, upon micellisation there

is a favourable solvent interaction which arises from increased number of hydrogen bonding between water molecules. The second, but competing component is that large, bulky, often charged head groups have to be bought into close proximity to one another during micelle formation and this is an unfavourable interaction. These two competing enthalpy contributions largely cancel each other out, making ΔH_m not significant in the process of micellisation. As a result, this leaves entropy as the major driving factor behind micellisation. At first this may seem surprising as the entropy change associated with the aggregation of colloidal stable particles is usually an unfavourable process, however it is the entropy change of the solvent that drives the micellisation process.[79] This favourable change in entropy is associated with the *hydrophobic effect.*[81] To solubilise an amphiphile in an aqueous environment water molecules must organise them-selves into highly structured arrays that promote hydrogen bonding but reduce interaction with the hydrophobic tail group. This arrangement forms “lattice like cages” termed *iceberg arrays*.[90] This structuring is remarkably effective in stabilising hydrophobic moieties, however are highly unfavoured entropically. Micellisation reduces the need for these iceberg arrays, freeing water molecules and allowing them to adopt their more favoured disordered arrangements, in turn giving a large increase in entropy.[94] It is not too much of a jump to appreciate that an increase in the size of the hydrophobic tail group would increase the iceberg arrays around the amphiphile resulting in a more favourable entropy gain upon micellisation. As micelle formation would be more favourable with a larger hydrophobic moiety, it would result in less amphiphile needed to undergo micellisation or in other words, a reduction in CMC. This effect was first published by Traube in 1891 and he proposed that small changes in hydrophobic moieties have considerable impacts on the activity of an amphiphile.[90] It could be imagined that all amphiphile chemists would simply just increase the hydrophobic potions of their polymers indefinitely to obtain favourable activities. However if the hydrophobic portion becomes disproportionally large, it will result in precipitation making the amphiphile

largely redundant for aqueous applications. These effects have been extensively studied in the detergent industry, where amphiphile chemists attempt to maximise hydrophobicity while maintaining adequate stability in aqueous environments. In these industries small changes in chemical structure can have large financial implications.

The structural nature of micelles have made them particularly interesting as vectors to transport poorly water soluble materials. This has overwhelmingly led to their success as detergents, mainly due to their ability of removing poorly soluble materials like grease, fats and oils.[84] For a number years now, biomedicine has also looked into using micelles as delivery vectors for hydrophobic drugs, which also suffer from poor solubility in water, usually leading to poor bioavailability.[95] For a material to be incorporated into the core of a micelle there has to be a favourable interaction. When any material is placed into an aqueous solution with an amphiphile it primarily has three fates: Firstly, it may have a favourable interaction with the water molecules and simply form an aqueous suspension of drug independent of the amphiphile. Secondly, it may undergo an unfavourable interaction with the water molecules and a favourable interaction with the amphiphile, resulting in micellisation or, lastly, it could have an unfavourable interaction with the water molecules and an unfavourable interaction with the amphiphile, overall resulting in material precipitation. It can therefore be assumed that a key driving force behind drug encapsulated micellisation is the favourable interaction between the drug and the amphiphile. Interestingly, this has been modelled by the Flory-Huggins theory.[85,96] The interaction between a polymer and a drug species is given by the Flory-Huggins parameter χ and is typically considered a measure of compatibility between a polymer and a drug species.

$$\chi = \frac{\left(\delta_{drug} - \delta_{polymer}\right)^2 V_{drug}}{RT} \qquad (1.3.2.2)$$

Where: χ is the Flory-Huggins parameter; δ_{drug}, is the solubility parameter of the drug; $\delta_{polymer}$, is the solubility parameter of the polymer; V_{drug}, is volume of drug, R, is the ideal gas constant and T, the temperature.

δ_{drug} is the Hilderbrand-Scatchard solubility parameter and is defined by:

$$\delta = \frac{\sqrt{\Delta E_{vap}}}{V} \qquad (1.3.2.3)$$

Where: ΔE_{vap}, is the energy change for evaporation and V, is the volume of solvent. Interaction is maximised between the drug and polymer when χ is minimised. Values <0.5 are generally considered favourable and will most likely result in a positive amphiphile-drug interaction. Overall this can be summarised in an assumption that "like interacts with like", or in other words drugs that are similar in nature to the hydrophobic core of a micelle will probably be easier to load and have higher drug encapsulation efficiencies.[97] In summary, the main driving force behind micellisation is the entropy driven hydrophobic effect, where hydrophobic moieties of an amphiphile will seek to minimise interactions with the water molecules and create a hydrophobic core, aligning its hydrophilic regions towards the aqueous environment. If a species is similar enough in nature to the hydrophobic core, then the micelle may act as a delivery vector for that particular species.

1.3.3 N-palmitoyl,N-monomethyl-N,N-dimethyl-N,N,N-trimethyl-6-O-glycolchitosan (GCPQ)

The amphiphilic polymer selected for this project was a chitosan based polymer named N-palmitoyl,N-monomethyl-N,N-dimethyl-N,N,N-trimethyl-6-O-glycolchitosan (GCPQ).[98] Chitosan, α (1-4) 2-amino β-D glucan, is a heterogeneous polymer produced by the deacetylation of chitin, of which, is an abundant material produced by an array of living organisms making it one of the most abundant natural polymers

on the planet.[99] This hydrophilic polymer is widely considered to have an inoffensive toxicity profile making it particularly interesting for biomedical applications.[100] In addition to this, chitosan also contains amino and hydroxyl side groups that allow for additional functionalization meaning polymer chemists can manipulate the properties of this polymer giving chitosan some truly remarkable characteristics.[101] As a result, chitosan has been used in a number of areas in science including; tissue engineering, gene delivery, wound dressing and hydrogel technologies.[102] Our group, has used chitosan as a platform to synthesise a particularly interesting amphiphile named GCPQ, a relatively non-toxic polymer which has been shown to enhance the delivery and bioavailability of a number of drug molecules.[98] GCPQ consists of a glucosamine sugar backbone where, a fraction of the amine groups have been functionalised with either a long chained hydrophobic pendant group or a quaternary ammonium cation. Functionalisation in this way creates an amphiphilic polymer which exhibits some interesting properties.

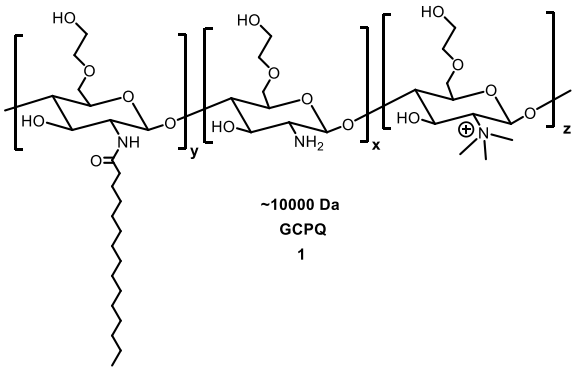

Figure 1.3.3.1. N-palmitoyl,N-monomethyl-N,N-dimethyl-N,N,N-trimethyl-6-O-glycolchitosan (GCPQ).

Upon addition to water the polymer self-assembles into nano-sized micelles usually between 20-40 nm in diameter as determined by electron microscopy.[103] The GCPQ micelles are considered suitably stable and have a CMC in the μM range when

measured by isothermal calorimetry. The hypothesis behind micelle formation is that the long chained hydrophobic pendant groups rearrange to form an inner hydrophobic core, whilst the positively charged sugar backbone faces outwards towards the aqueous environment shielding the core. The polymer has an IC_{50} of 1.28 mg/mL against the A431 cell line which compares favourably with other cationic polymers including; poly-l-lysine (0.007 mg/ml) and poly-l-ornithine (0.004 mg/ml) against the same cell line.[103] Furthermore, when measured for haemolytic activity, polyoxyethylene (20) sorbitan a common amphiphile, gave around 80% haemolysis at a concentration of 1 mg/mL, were as GCPQ gave no haemolysis at the same concentration and only 20% haemolysis at a concentration of 10 mg/mL.[79] Characteristically, GCPQ micelles appear to have rather favourable properties and so they have been employed in a number of drug transport applications. GCPQ has been used to encapsulate cyclosporine A, a poorly water soluble cyclic peptide used as an immunosuppressant.[104] The GCPQ nanoparticle formulation has been shown to increase the bioavailability by 3-fold and the C_{MAX} by 5-fold against cyclosporine alone in water. In addition to this, GCPQ has also been loaded with leucine-enkephalin (TP-LENK) a pro-drug used for the treatment of chronic pain.[105,106] The study showed that the GCPQ micelle did not cross the blood brain barrier but did facilitate the delivery of the peptide to the brain, improving the pharmacokinetic activity and sustaining its pharmacological effect. It is likely that this is a result of the micelle protecting the peptide from plasma degradation and promoting blood brain barrier (BBB) adhesion. Furthermore, at a sufficiently large doses the GCPQ-LENK nanoparticles could also be delivered via the oral route. A particularly interesting result as peptides are often quickly degraded in the gastrointestinal tract. In a study by *Lalatsa et al*, they found that GCPQ did not accumulate in the liver following intravenous administration. This is quite a significant result for a polymeric nanoparticle, as it may be evidence that GCPQ has a stealth effect allowing it evade the immune system. Intravenously administrated IONPs have primarily been used as

imaging agents for the lymphatic system and therefore it can be hypothesised that a GCPQ micellar IONP may not share the same fate and possibly lead to new modalities for imaging and diagnostics. Overall, GCPQ is an interesting amphiphile and may provide a good strategy to facilitate IONP and drug delivery.

1.3.4 Polymer micelles as vectors for iron oxide nanoparticles

This project will use the amphiphilic polymer GCPQ as the scaffold to engineer the proposed nanotheranostic. It is therefore worth reviewing the literature to evaluate strategies that have already been attempted in this area. The earliest known IONP micelle was published was in 2003 by *Euliss et al*.[107] Aqueous stability was provided to hydrophobic IONPs using a peptide based polymer known as polypeptide(EG)-(asp). No function for these particles was investigated, however it was the first evidence to show that IONPs could be encapsulated within micellar architecture.

Ai et al, used a common micelle forming polymer named poly(capro-lactone)-b-poly(ethylene glycol) (PCL-PEG).[108] In their study they were able to synthesis IONPs with a high degree of control and subsequently encapsulated them within their PCL-PEG micelles. In this study, they found that by increasing the size of the IONP core they could increase the T2 contrast of their nanoparticles. *Cheng et al* went a step further and produced a targeted IONP micelle by conjugating folic acid to the end of the PCL-PEG polymer, yielding PCL-PEG-Folate.[109] They did form an IONP micelle and they could accurately control the size of the nanoparticle by altering the molecular weight of the PCL polymer. They subsequently tested their particles in an *in vivo*, flank tumour, mouse model and found that their folate targeted micelles did accumulate at the site of the tumour to a larger extend than the non-targeted micelles. *Pöselt et al* used a branched ethylene imine PCL-PEG (PEI-PCL-PEG) to synthesise nanoparticles with a high degree of control over micelle size and IONP loading.[35] They took the opportunity to investigate the relationship between particle size and relaxivity

and surprisingly found their results had been predicted by the computer simulations of *Gillis et al*, who attempted to model IONP aggregation and its effects on T2 relaxation a decade earlier.[110] PCL-PEG is widely considered non-toxic, while the outer PEG corona can act as a stealth coating, shielding the nanoparticle form the immune system and prolonging residence time.[111] PCL-PEG is a good micelle forming polymer, however alternative polymers and strategies should also be investigated.

Li et al, created polymeric micelles composed of 2,2,3,4,4,4-hexafluorobutyl methacrylate - methoxy poly(ethylene glycol) monomethacrylate (HFMA-g-PEGMA) and encapsulated hydrophobic IONPs to yield “magnetomicelles”.[112] They employed an emulsification method using hexane and probe sonication to formulate their structures and then removed the organic solvent using a stream of N_2. Cyctoxicity studies demonstrated a cell viability of over 90% at a concentration of 250 μg/mL in a Hela cell line, suggesting average cytocompatibility. In an *in vivo* mouse model study they found that the majority of their nanoparticles quickly accumulated in the liver and spleen significantly reducing their T2 MRI signal.

Su et al, synthesised a unique “star like” amphiphile by conjugating β-cyclodextrins to a branched dextran polymer that had been modified with stearic acid.[113] Adding the β-cyclodextrins reduced the CMC of their polymers by 10-fold, making them more stable for biomedical applications. They then used their star micelles as a platform to encapsulate IONPs and then went on to produce a nanotheranostic by incorporating doxorubicin into the nanoparticles structure.

Paquet et al used sodium dodecyl sulfate (SDS) to make their IONP micelles, an amphiphile widely found in detergents.[114] They could control the size of their IONP micelles with high precision and made particles ranging between 40-200 nm. The main drawback with these simple amphiphiles is that they may result in toxicity issues if used for biomedical applications due to their interaction with biological membranes.

Choo et al synthesised an interesting polymer using Poly(isobutylene-alt-maleic anhydride) (PBMA) as the main backbone and then decorated it with hydrophobic pendant groups made from 1-dodecylamine and fluoresceinamine.[115] Upon addition to water it formed micelles and the author was successfully able to load these structures with IONPs using an emulsification technique. They were able to strictly control IONP loading and were able to model the relationship between magnetic saturation and relaxivity in simple aqueous environments.

Lin et el, have recently engineered an IONP loaded within a chitosan polymer.[116] Chitosan is not an amphiphile, however the structures produced do resemble micelle like nano-spheres. As chitosan is not an amphiphile, the group had to use the crosslinking agent ethylenediaminetetraacetic acid (EDTA) to hold the nanoparticle together in aqueous conditions. Crosslinking is often an effective strategy for stabilising nanoparticles. However, such cross-linked nanoparticles may become too stable and not be efficiently broken down by biological clearance mechanisms. The nanoparticles synthesised had a large effect on T2 contrast and did produce a contrast effect at a tumour site in an *in vivo* mouse model.[116]

As discussed a variety of IONP micelles have been engineered using a number of amphiphiles and strategies and they are summarised in Table 1.3.4.1.[117-119] The micelle nanoparticles produced have been shown to be relatively magnetic and produce good T2 contrast *in vitro* testing. This said, there is a lack of truly novel polymers, with the majority relying on PEG and hydrocarbon chains. This produces micellar species that are limited in properties such as surface composition and surface charge. These properties are considered important as the nanoparticle will interact with its environment using these surface characteristics. Also, it is of the author's opinion that the translation from the bench to *in vivo* investigation is relatively weak and clinical relevance has largely not been explored. Interestingly, none of the

particles discussed above have been tested for stability in biologically relevant media. This is often a key experiment for amphiphilic systems as charge screening from electrolytes, protein adsorption and pH can all have destabilising effects on polymeric nanoparticles. It is predicted that the positively charged, carbohydrate based polymer GCPQ will generate some novel applications in this area, while also providing a platform to further build a nanotheranostic.

Amphiphile	IONP core size (nm)	Micelle size (nm)	Relaxivity (r_2) (Fe mM^{-1} S^{-1})	Encapsulation method	Clinical applications	Reference
Poly(EG-lys)-b-poly(asp)	6	20	-	stirring	-	Euliss et al, 2003
PCL-b-PEG	16	110	169	Sonication	-	Ai et al, 2005
PCL-b-PEG-FA	6	28-125	58-121	Solvent evaporation	Tumour	Cheng et al, 2010
PS-b-PAA	5	150-200	10.-176	Solvent dialysis	-	Niu et al, 2010
PDMAEA-g-C18	6	96	333	Emulsion evaporation	Tumour	HJ Lee et al, 2010
PBMA-g-(C12/Flu)	6	158-250	101-439	Emulsion evaporation	-	Choo et al, 2011
SDS	9	53-94	394-505	Emulsion evaporation	-	Paquett et al, 2011
HFMA-g-PEGMA	10	138	134	Emulsion evaporation	Liver, spleen	Li et al, 2012
PEI-b-PCL-b-PEG	4-13	30-200	220-480	Solvent evaporation	-	Pöselt et al, 2012
β-CD-Dex-g-SA	8	118	437	Solvent evaporation	-	Su et al, 2013
PCL-b-PEG	10	169	196	Solvent evaporation	-	Qi et al, 2014
Chitosan	9	200-351	101-439	Sonication-chemical crosslinking	Tumour, liver, intestine	Lin et al, 2015

Table 1.3.4.1. A summary of published IONP micelles.

1.4 Nanotheranostics: Drug Delivery with Iron Oxide Nanoparticles

1.4.1 Engineering drug loaded iron oxide nanoparticles

The hydrophobic core of a micelle is not limited to the encapsulation of a single entity, but can incorporate any number of species as long as they are compatible. This allows for the design of quite exotic nanoparticle species that could have more than one function. Multifunctional nanoparticles which comprise both an imaging element and a drug payload are termed *nanotheranostics*. In recent years, a large number of publications have emerged where groups have engineered nanotheranostics using a variety of different strategies. The majority of the nanoparticles published have mainly been engineered for the treatment of cancer. This is because cancer is not only widely considered an important disease target for scientists today, but also because nanoparticles have a proven track record in this field. IONPs are widely used when engineering nanotheranostic platforms as they have a favourable toxicity profile compared to other nanomaterials and they can also be used for several applications including localised magnetic heating (hyperthermia) and selective accumulation via the use of an external magnetic field (magnetic guidance). Many hundreds of drug loaded IONP based nanotheranostics have been developed and a small number of the most cited examples can be found in Table 1.4.1.1.[120-132]

Polymer	Drug	Reference
LCP-PEG-PLA	Doxorubicin	Guthi et al, in 2010
PLGA-PEG	Docetaxel	Ling et al, in 2011
FA-PEG-PLA-PEG-acrylate (nano worms)	Doxorubicin	yang et al, in 2010
Pluronic F-127	Doxorubicin/ Paclitaxel	Jain et al, in 2008
β-CD-Pluronic F-127	Curcumin	Yallapu et al, in 2011
MPEG-*b*-PMAA-*b*-PGMA	Adriamycin	Guo et al, in 2008
PVA	Doxorubicin	Purushotham et al, in 2009
PCL-PEG-FA	Doxorubicin	Yang et al, in 2008
PLA	Doxorubicin/ cucumin	Wang et al, in 2016
APS-MTX	Methotrexate	Kohler et al, in 2005
Chitosan	Doxorubicin	Yuan et al, in 2008
PTMC-PGA	Doxorubicin	Sanson et al, in 2011

Table 1.4.1.1. A summary of some of the most widely cited IONP and drug nanotheranostics. Hundreds more have been published showing the true scale and interest in this area.

Overwhelmingly the majority of the nanotheranostics have been designed around incorporating IONPs with doxorubicin. This is most likely due to the fact that doxorubicin has already been formulated into a commercially available nanoparticle product, Doxil®. Although many nanotheranostics have been synthesised their translation into *in vivo* studies has been relatively low, leading to the biological relevance of many of these nanotheranostics remaining unexplored.

1.4.2 In vivo studies using nanotheranostics

There have been a small number of recent publications where a nanotheranostic has been tested *in vivo*. These studies are highly valued as they are the first to illustrate how these species could be used to treat disease.

In an impressive study by *Maeng et al*, they synthesised a new vesicle forming polymer composed of poly(ethylene oxide)-trimellitic anhydride chloride-folate (PEO-TMA-FA) and loaded it with IONPs and doxorubicin.[133] Their nanoparticles had an average diameter of 88 nm and contained 2.1 mg/mL of doxorubicin. Their dissolution results suggested that the rate of doxorubicin release was much larger in acidic conditions than in neutral conditions. This could be advantageous as the tumour environment is often slightly acidic, therefore the toxic payload would be preferentially released at the disease site minimising off target side effects. An MRI studied confirmed that the nanoparticle was accumulating in the liver and this led them in develop an *in vivo* liver tumour study using VX2-implanted rabbits. When studied for tumour efficiency the nanotheranostic group gave a decreased tumour volume when compared to the free doxorubicin control group. This is a good example that shows the effectiveness of a dual imaging and therapeutic nanoparticle.

Wang et al, used a PEGylated dextran to encapsulated IONPs and doxorubicin forming structures roughly 116 nm in diameter.[128] They tested their nanotheranostic in an *in vivo* tumour model and monitored their distribution via MRI. It was found that after 15 min the nanotheranostic had accumulated in the liver and tumour site reducing their signal by 84.4% and 42.7%, respectively. As the nanotheranostic did accumulate in the tumour tissue they decided to conduct an anti-tumour study. It was found that after 21 days the tumour volume in the nanotheranostic group was half that of the control group (49%) and impressively when an external magnetic field was placed at the site of the tumour its volume was one third that of the control group

(32%). This is strong evidence that by adding a magnetic component to a drug species you can markedly increase the efficiency of the treatment.

Yu et al used their anti-biofouling polymer coated, thermally cross-linked IONPs (TCL-IONP) to encapsulate doxorubicin.[134] Their hypotheses was that their nanoparticle could accumulate and treat cancer purely based on size without the need to magnetically target. An MRI study conducted on tumour bearing mice showed that their nanotheranostic did accumulate at the tumour site over a 4.5 h period. An anti-tumour efficiency study was conducted and found that the nanotheranostic group gave a significant reduction in tumour growth (approximately 63 % relative to the control). The health of the animals was monitored by weight, the control group treated with doxorubicin alone showed a drop in weight, however the nanotheranostic treatment group increased in the same manner as the non-treatment group suggesting they may not be suffering from as many off target side effects.

Chen et al used a temperature responsive poly(ethyleneimine)-modified poly(ethylene oxide)−poly(propylene oxide)−poly(ethylene oxide) (PEO−PPO−PEO) block copolymer to encapsulate IONPs.[135] Using this nanoparticle they were successfully able to encapsulate hydrophobic drugs (ibuprofen) and hydrophilic drugs (Eosin Y and monosialotetrahexosylganglioside(GM-1)). GM-1 is a drug that can be used to treat spinal cord injury. Their hypothesis was that GM-1 is a hydrophilic compound and upon injection into the spinal cavity the drug quickly flows away as a result of fluid exchange. If GM-1 could be loaded into a nanoparticle it may prolong the drugs residence time and improve treatment. This was tested in an *in vivo* model where their GM-1-IONPs were injected into the damaged spinal cords of living Sprague−Dawley rats. 4 weeks after treatment the rats were sacrificed and their spinal cords were analysed. They found that the group treated with the GM-1-IONPs displayed significant spinal cord recovery, whereas the GM-1 control group displayed

no significant recovery. Although the MRI experimentation was not conducted in this study, one could monitor the drug in the spinal cord cavity using MRI allowing for evaluation of GM-1 retention and therefore personalised dosing regimens.

1.4.3 Hyperthermia treatment and magnetic targeting

As briefly highlighted earlier in the report, IONPs are not limited to purely being an MRI diagnostic probe. The studies described above give clear examples of how a nanotheranostic (imaging and drug therapy) can be used to improve the efficiency of a cancer treatment and reduced the rate of tumour growth. This said however, in many of the examples highlighted, generally there is still a slow increase in tumour size throughout the experiment. Some of the most impressive data being published in recent years uses all the functions of IONPs to go beyond simply slowing the progression of the tumour, but actually causing tumour remission. These approaches involve: *magnetic guidance* and *hyperthermia therapy*.[18] As IONP theranostics are magnetic by nature they can be guided and held at the site of disease via an external magnet, this increases nanoparticle accumulation and residence time leading to an increased bioavailability. Hyperthermia therapy involves the IONP theranostic being subjected to an alternating magnetic field used to induce nanoparticle heating. Cancer cells are particularly sensitive to heat and it have been found that If the cancer is subjected to a temperature of 42 ^{O}C for 30 min it will be destroyed, whereas the healthy cells will survive.[18,136] In addition to this, many publications have highlighted a synergistic effect of having a drug present, which significantly increased the efficiency of the hyperthermia treatment.[137] The most impressive examples of multi-functional therapeutic nanotheranostics are evaluated here, although a comprehensive review has recently been published by *Ulbrich et al*:[138]

Tietze et al, used chemical co-precipitation to synthesise IONPs and then coated them in lauric acid.[139] This most likely created a lipid bilayer, confirmed by the

negative zeta potential of their particles. They could subsequently load these nanoparticles with mitoxantrone to yield a nanoparticle that was less than 200 nm in diameter. To study the therapeutic effect of these nanoparticles an, *in vivo* study was conducted using tumour bearing rabbits. The nanoparticles were injected directly into the tumours and an external magnetic field was used to hold the nanoparticles at the site of the tumour. Half of the treated animals experienced complete tumour remission (8 of 16) and the other half experienced a reduction in growth rate, even when the injected drug dose in the nanoparticle group was 10% that of the drug dose used in the control group. Intravenous results were not as impressive, this could be to do with plasma instability or poor distribution to the tumour site. Overall, this experiment displays the advantage of using an external magnetic field.

Hu et al, used PVA to create IONP emulsions which were later loaded with doxorubicine and paclitaxel.[140] This formulation was injected directly into the solid tumours of nude mice. It was measured that the nanoparticles were cleared from the site after 4 h, most likely as a result of fluid exchange. To evaluate the therapeutic effect, an alternating magnetic field was applied for 10 min following administration of the nanoparticles. Treatments were carried out every 3 days. Impressively the tumours went into complete remission during treatment over a 30 day period, and by the end of the experiment the tumours were barely visible.

Peiris et al, developed some remarkable “nano-chains” that were composed of three IONPs and one doxorubicin filled liposome organised in a linear arrangement.[141] The authors cleverly engineered the liposome portion of the nanoparticle to release the doxorubicin when exposed to a radio frequency of 10 kHz. Its rate of release could be modulated by varying the dissipation power (1-50 W). A pharmacokinetic study was conducted and the authors found that the doxorubicin had a blood half-life of c.a. 26 h, which compared favourably to a commercially available liposomal formulation

which had a blood half-life of 18 h. The therapeutic effect of the nanoparticles was investigated in tumour bearing rats. The nanoparticles were intravenously injected followed by the application of a radio frequency pulse. After just one treatment on day 6, a significant reduction in tumour growth rate was observed. Additionally, when a second treatment was applied on day 8 the development of the tumour arrested and did not continue to grow for the remainder of the 17 day experiment.

Finally, another high performing IONP was engineered by *Huang et al*. IONP perfluoropentane (PFP) vapour "nanobubble" emulsions were engineered using temperature-sensitive Pluronic F127 and high-polarity polyacrylic acid (PEO–PPO–PEO, F127).[142] The nanobubbles were loaded with carmustine which is a toxic chemotherapeutic DNA alkylying agent. To test the therapeutic efficiency the nanobubbles were injected into tumour bearing mice and an external magnetic field was placed on the tumour for 30 s. MRI studies confirmed the presence of the nanobubbles in the tumour up to two hours after administration. Over a 13 day study, mice were administered with the nanobubbles and subjected to magnetic targeting combined with the high-intensity focused ultrasound, by the end of the experiment the treatment group displayed complete remission of tumour growth.

1.4.4 Summary and future prospects

Over the past decade there has been an unprecedented increases in the engineering of nanotheranostics for biomedical applications. Due to the advances in nanoparticle and polymer synthesis these nanotheranostics are becoming complex systems, which have led to some remarkable applications. Due to their versatility, IONPs have been an influential component in the design of many of these nanotheranostics, most notably because they are widely considered as a safe material and can be used as an imaging probe within MRI. The clinical utility of the first generation of IONP contrast agents was simply not demonstrated, however this does not mean that IONP research is a fruitless pursuit. Magnetic materials have truly revolutionised our modern society and are considered a valuable material in many disciplines. Data storage, domestic appliances, entertainment systems, computing, particle physics and even planet earth all have magnetic materials at the core of their function, in fact it would be hard to imagine a world without magnetic materials. Medicine is not far behind and as this review has highlighted, there are many that still dedicate large resources to IONP research believing they could be beneficial in the treatment of many of society's most difficult diseases. Of course, the key to using IONPs in biomedicine heavily depends on their polymeric architecture and therefore finding new polymers is of high importance. Combining IONPs with therapeutic drugs offers a unique opportunity to overcome many of the challenges faced with the delivery of medicines and it is a technology worth investigating. The aim of this project is to design and synthesise a novel theranostic nanoparticle, using a positively charged micelle forming amphiphilic carbohydrate (GCPQ), with the overall hypothesis of determining whether using a nanomedicine that can simultaneously image and treat would improve the effectiveness of a cancer treatment.

(1) Jørgensen, J. T. Companion diagnostics: the key to personalized medicine. *Expert Review of Molecular Diagnostics* **2015**, *15*, 153-156.

(2) Kelkar, S. S.; Reineke, T. M. Theranostics: Combining Imaging and Therapy. *Bioconjugate Chemistry* **2011**, *22*, 1879-1903.

(3) Paving the Way for Personalized Medicine *U.S. Food and Drug Administration* **2013**, *1*, 1-62.

(4) Chan, I. S.; Ginsburg, G. S. Personalized Medicine: Progress and Promise. *Annual Review of Genomics and Human Genetics* **2011**, *12*, 217-244.

(5) Olsen, D.; Jørgensen, J. T. Companion Diagnostics for Targeted Cancer Drugs – Clinical and Regulatory Aspects. *Frontiers in Oncology* **2014**, *4*, 105.

(6) Agarwal, A.; Ressler, D.; Snyder, G. The current and future state of companion diagnostics. *Pharmacogenomics and Personalized Medicine* **2015**, *8*, 99-110.

(7) Hans Christian Pedersen, J. T. J. Immunohistochemical Staining Methods Education Guide: Companion Diagnostics *Dako*, *1*, 132-143.

(8) Wolff, A. C.; Hammond, M. E. H.; Hicks, D. G.; Dowsett, M.; McShane, L. M.; Allison, K. H.; Allred, D. C.; Bartlett, J. M. S.; Bilous, M.; Fitzgibbons, P.; Hanna, W.; Jenkins, R. B.; Mangu, P. B.; Paik, S.; Perez, E. A.; Press, M. F.; Spears, P. A.; Vance, G. H.; Viale, G.; Hayes, D. F. Recommendations for Human Epidermal Growth Factor Receptor 2 Testing in Breast Cancer: American Society of Clinical Oncology/College of American Pathologists Clinical Practice Guideline Update. *Journal of Clinical Oncology* **2013**, *31*, 3997-4013.

(9) Schork, N. J. Personalized medicine: Time for one-person trials. *Nature* **2015**, *520*, 609-611.

(10) Mura, S.; Couvreur, P. Nanotheranostics for personalized medicine. *Advanced Drug Delivery Reviews* **2012**, *64*, 1394-1416.

(11) Crawley, N.; Thompson, M.; Romaschin, A. Theranostics in the Growing Field of Personalized Medicine: An Analytical Chemistry Perspective. *Analytical Chemistry* **2014**, *86*, 130-160.

(12) Edelman , R. R.; Warach , S. Magnetic Resonance Imaging. *New England Journal of Medicine* **1993**, *328*, 708-716.

(13) McRobbie, D. W., .; et al.: *MRI from Picture to Proton*; Cambridge University Press, 2006.

(14) Cheon, J.; Lee, J.-H. Synergistically Integrated Nanoparticles as Multimodal Probes for Nanobiotechnology. *Accounts of Chemical Research* **2008**, *41*, 1630-1640.

(15) Dell, M. A. Radiation safety review for 511-keV emitters in nuclear medicine. *Journal of nuclear medicine technology* **1997**, *25*, 12-17; quiz 33.

(16) Bixler, A.; Springer, G.; Lovas, R. Practical aspects of radiation safety for using fluorine-18. *Journal of nuclear medicine technology* **1999**, *27*, 14-16.

(17) Mathews, J. D.; Forsythe, A. V.; Brady, Z.; Butler, M. W.; Goergen, S. K.; Byrnes, G. B.; Giles, G. G.; Wallace, A. B.; Anderson, P. R.; Guiver, T. A.; McGale, P.; Cain, T. M.; Dowty, J. G.; Bickerstaffe, A. C.; Darby, S. C. Cancer risk in 680 000 people exposed to computed tomography scans in childhood or adolescence: data linkage study of 11 million Australians. *BMJ : British Medical Journal* **2013**, *346*.

(18) Pankhurst, Q. A.; Connolly, J.; Jones, S. K.; Dobson, J. Applications of magnetic nanoparticles in biomedicine. *Journal of Physics D: Applied Physics* **2003**, *36*, R167.

(19) Bloch, F. Nuclear Induction. *Physical Review* **1946**, *70*, 460-474.

(20) de Graaf, R. A.: *In Vivo NMR Spectroscopy: Principles and Techniques*; Wiley, 2007.

(21) Pooley, R. A. Fundamental Physics of MR Imaging. *RadioGraphics* **2005**, *25*, 1087-1099.

(22) What is T1 relaxation? http://mri-q.com/what-is-t1.html. (accessed 10/01/2017 2016).

(23) What is T2 relaxation? http://mri-q.com/what-is-t2.html (accessed 10/01/2017 2016).

(24) Laurent, S.; Forge, D.; Port, M.; Roch, A.; Robic, C.; Vander Elst, L.; Muller, R. N. Magnetic Iron Oxide Nanoparticles: Synthesis, Stabilization, Vectorization, Physicochemical Characterizations, and Biological Applications. *Chemical Reviews* **2008**, *108*, 2064-2110.

(25) Caravan, P.; Ellison, J. J.; McMurry, T. J.; Lauffer, R. B. Gadolinium(III) Chelates as MRI Contrast Agents: Structure, Dynamics, and Applications. *Chemical Reviews* **1999**, *99*, 2293-2352.

(26) De Leon-Rodriguez, L. M.; Martins, A. F.; Pinho, M. C.; Rofsky, N. M.; Sherry, A. D. Basic MR relaxation mechanisms and contrast agent design. *Journal of magnetic resonance imaging : JMRI* **2015**, *42*, 545-565.

(27) Caravan, P. Strategies for increasing the sensitivity of gadolinium based MRI contrast agents. *Chemical Society Reviews* **2006**, *35*, 512-523.

(28) Idée, J.-M.; Port, M.; Raynal, I.; Schaefer, M.; Le Greneur, S.; Corot, C. Clinical and biological consequences of transmetallation induced by contrast agents for magnetic resonance imaging: a review. *Fundamental & Clinical Pharmacology* **2006**, *20*, 563-576.

(29) Cacheris, W. P.; Quay, S. C.; Rocklage, S. M. The relationship between thermodynamics and the toxicity of gadolinium complexes. *Magn Reson Imaging* **1990**, *8*, 467-481.

(30) Marckmann, P.; Skov, L.; Rossen, K.; Dupont, A.; Damholt, M. B.; Heaf, J. G.; Thomsen, H. S. Nephrogenic systemic fibrosis: suspected causative role of gadodiamide used for contrast-enhanced magnetic resonance imaging. *Journal of the American Society of Nephrology : JASN* **2006**, *17*, 2359-2362.

(31) Bellin, M. F.; Van Der Molen, A. J. Extracellular gadolinium-based contrast media: an overview. *European journal of radiology* **2008**, *66*, 160-167.

(32) Corot, C.; Robert, P.; Idée, J.-M.; Port, M. Recent advances in iron oxide nanocrystal technology for medical imaging. *Advanced Drug Delivery Reviews* **2006**, *58*, 1471-1504.

(33) Roch, A.; Muller, R. N.; Gillis, P. Theory of proton relaxation induced by superparamagnetic particles. *The Journal of Chemical Physics* **1999**, *110*, 5403-5411.

(34) Kim, B. H.; Lee, N.; Kim, H.; An, K.; Park, Y. I.; Choi, Y.; Shin, K.; Lee, Y.; Kwon, S. G.; Na, H. B.; Park, J.-G.; Ahn, T.-Y.; Kim, Y.-W.; Moon, W. K.; Choi, S. H.; Hyeon, T. Large-Scale Synthesis of Uniform and Extremely Small-Sized Iron Oxide Nanoparticles for High-Resolution T1 Magnetic Resonance Imaging Contrast Agents. *Journal of the American Chemical Society* **2011**, *133*, 12624-12631.

(35) Pöselt, E.; Kloust, H.; Tromsdorf, U.; Janschel, M.; Hahn, C.; Maßlo, C.; Weller, H. Relaxivity Optimization of a PEGylated Iron-Oxide-Based Negative Magnetic Resonance Contrast Agent for T2-Weighted Spin–Echo Imaging. *ACS Nano* **2012**, *6*, 1619-1624.

(36) Wang, Y.-X. J.; Hussain, S. M.; Krestin, G. P. Superparamagnetic iron oxide contrast agents: physicochemical characteristics and applications in MR imaging. *European Radiology* **2001**, *11*, 2319-2331.

(37) Wang, Y.-X. J. Superparamagnetic iron oxide based MRI contrast agents: Current status of clinical application. *Quantitative Imaging in Medicine and Surgery* **2011**, *1*, 35-40.

(38) Wang, Y.-X. J. Current status of superparamagnetic iron oxide contrast agents for liver magnetic resonance imaging. *World journal of gastroenterology* **2015**, *21*, 13400-13402.

(39) Muehe, A. M.; Feng, D.; von Eyben, R.; Luna-Fineman, S.; Link, M. P.; Muthig, T.; Huddleston, A. E.; Neuwelt, E. A.; Daldrup-Link, H. E. Safety Report of Ferumoxytol for Magnetic Resonance Imaging in Children and Young Adults. *Invest Radiol* **2016**, *51*, 221-227.

(40) Withdrawal Assessment Report for Sinerem. *European Medicines Agency* **2008**, *1*, 1-18.

(41) Kim, Y. K.; Kim, C. S.; Kwak, H. S.; Lee, J. M. Three-dimensional dynamic liver MR imaging using sensitivity encoding for detection of hepatocellular carcinomas: comparison with superparamagnetic iron oxide-enhanced mr imaging. *Journal of magnetic resonance imaging : JMRI* **2004**, *20*, 826-837.

(42) Whatever happened to Feridex®? Aren't iron-containing contrast agents useful for liver MRI? http://mriquestions.com/feridex-and-iron-oxides.html. (accessed 06/09/2016 2016).

(43) Thanh, N. T. K.: *Magnetic Nanoparticles: From Fabrication to Clinical Applications*; Taylor & Francis, 2012.

(44) Bourrinet, P.; Bengele, H. H.; Bonnemain, B.; Dencausse, A.; Idee, J. M.; Jacobs, P. M.; Lewis, J. M. Preclinical safety and pharmacokinetic profile of ferumoxtran-10, an ultrasmall superparamagnetic iron oxide magnetic resonance contrast agent. *Invest Radiol* **2006**, *41*, 313-324.

(45) Schwenk, M. H. Ferumoxytol: a new intravenous iron preparation for the treatment of iron deficiency anemia in patients with chronic kidney disease. *Pharmacotherapy* **2010**, *30*, 70-79.

(46) Cornell, R. M.; Schwertmann, U.: *The Iron Oxides: Structure, Properties, Reactions, Occurrences and Uses*; Wiley, 2003.

(47) Schwertmann, U.; Cornell, R. M.: The Iron Oxides. In *Iron Oxides in the Laboratory*; Wiley-VCH Verlag GmbH, 2007; pp 5-18.

(48) Nadoll, P.; Angerer, T.; Mauk, J. L.; French, D.; Walshe, J. The chemistry of hydrothermal magnetite: A review. *Ore Geology Reviews* **2014**, *61*, 1-32.

(49) Lakay, E. M. Superparamagnetic iron-oxide based nanoparticles for the separation and recovery of precious metals from solution. University of Stellenbosch, 2009.

(50) Spaldin, N. A.: *Magnetic Materials: Fundamentals and Applications*; 2 ed.; Cambridge University Press: Cambridge, 2010.

(51) Lu, A.-H.; Salabas, E. L.; Schüth, F. Magnetic Nanoparticles: Synthesis, Protection, Functionalization, and Application. *Angewandte Chemie International Edition* **2007**, *46*, 1222-1244.

(52) Wahajuddin; Arora, S. Superparamagnetic iron oxide nanoparticles: magnetic nanoplatforms as drug carriers. *International journal of nanomedicine* **2012**, *7*, 3445-3471.

(53) Park, J. Y.; Baek, M. J.; Choi, E. S.; Woo, S.; Kim, J. H.; Kim, T. J.; Jung, J. C.; Chae, K. S.; Chang, Y.; Lee, G. H. Paramagnetic Ultrasmall Gadolinium Oxide Nanoparticles as Advanced T1 MRI Contrast Agent: Account for Large Longitudinal Relaxivity, Optimal Particle Diameter, and In Vivo T1 MR Images. *ACS Nano* **2009**, *3*, 3663-3669.

(54) Yuanzhi, C.; Dong-Liang, P.; Dongxing, L.; Xiaohua, L. Preparation and magnetic properties of nickel nanoparticles via the thermal decomposition of nickel organometallic precursor in alkylamines. *Nanotechnology* **2007**, *18*, 505703.

(55) Yang, H. T.; Su, Y. K.; Shen, C. M.; Yang, T. Z.; Gao, H. J. Synthesis and magnetic properties of ε-cobalt nanoparticles. *Surface and Interface Analysis* **2004**, *36*, 155-160.

(56) Gupta, A. K.; Gupta, M. Synthesis and surface engineering of iron oxide nanoparticles for biomedical applications. *Biomaterials* **2005**, *26*, 3995-4021.

(57) Massart, R. Preparation of aqueous magnetic liquids in alkaline and acidic media. *IEEE Transactions on Magnetics* **1981**, *17*, 1247-1248.

(58) Wu, W.; He, Q.; Jiang, C. Magnetic Iron Oxide Nanoparticles: Synthesis and Surface Functionalization Strategies. *Nanoscale Research Letters* **2008**, *3*, 397-415.

(59) Park, J.; An, K.; Hwang, Y.; Park, J.-G.; Noh, H.-J.; Kim, J.-Y.; Park, J.-H.; Hwang, N.-M.; Hyeon, T. Ultra-large-scale syntheses of monodisperse nanocrystals. *Nat Mater* **2004**, *3*, 891-895.

(60) Khollam, Y. B.; Dhage, S. R.; Potdar, H. S.; Deshpande, S. B.; Bakare, P. P.; Kulkarni, S. D.; Date, S. K. Microwave hydrothermal preparation of submicron-sized spherical magnetite (Fe3O4) powders. *Materials Letters* **2002**, *56*, 571-577.

(61) Wu, W.; Xiao, X.; Zhang, S.; Zhou, J.; Fan, L.; Ren, F.; Jiang, C. Large-Scale and Controlled Synthesis of Iron Oxide Magnetic Short Nanotubes: Shape Evolution, Growth Mechanism, and Magnetic Properties. *The Journal of Physical Chemistry C* **2010**, *114*, 16092-16103.

(62) Lu, Y.; Yin, Y.; Mayers, B. T.; Xia, Y. Modifying the Surface Properties of Superparamagnetic Iron Oxide Nanoparticles through A Sol−Gel Approach. *Nano Letters* **2002**, *2*, 183-186.

(63) Bang, J. H.; Suslick, K. S. Applications of Ultrasound to the Synthesis of Nanostructured Materials. *Advanced Materials* **2010**, *22*, 1039-1059.

(64) Santos, H. M.; Lodeiro, C.; Capelo-Martínez, J.-L.: The Power of Ultrasound. In *Ultrasound in Chemistry*; Wiley-VCH Verlag GmbH & Co. KGaA, 2009; pp 1-16.

(65) Adewuyi, Y. G. Sonochemistry: Environmental Science and Engineering Applications. *Industrial & Engineering Chemistry Research* **2001**, *40*, 4681-4715.

(66) Narayanan, K. B.; Sakthivel, N. Biological synthesis of metal nanoparticles by microbes. *Advances in Colloid and Interface Science* **2010**, *156*, 1-13.

(67) Moon, J.-W.; Rawn, C. J.; Rondinone, A. J.; Love, L. J.; Roh, Y.; Everett, S. M.; Lauf, R. J.; Phelps, T. J. Large-scale production of magnetic nanoparticles using bacterial fermentation. *Journal of Industrial Microbiology & Biotechnology* **2010**, *37*, 1023-1031.

(68) Reddy, L. H.; Arias, J. L.; Nicolas, J.; Couvreur, P. Magnetic Nanoparticles: Design and Characterization, Toxicity and Biocompatibility, Pharmaceutical and Biomedical Applications. *Chemical Reviews* **2012**, *112*, 5818-5878.

(69) Wei, W.; Zhaohui, W.; Taekyung, Y.; Changzhong, J.; Woo-Sik, K. Recent progress on magnetic iron oxide nanoparticles: synthesis, surface functional strategies and biomedical applications. *Science and Technology of Advanced Materials* **2015**, *16*, 023501.

(70) Na, H. B.; Lee, I. S.; Seo, H.; Park, Y. I.; Lee, J. H.; Kim, S.-W.; Hyeon, T. Versatile PEG-derivatized phosphine oxide ligands for water-dispersible metal oxide nanocrystals. *Chemical Communications* **2007**, 5167-5169.

(71) Pinter, B.; Fievez, T.; Bickelhaupt, F. M.; Geerlings, P.; De Proft, F. On the origin of the steric effect. *Physical Chemistry Chemical Physics* **2012**, *14*, 9846-9854.

(72) Studart, A. R.; Amstad, E.; Gauckler, L. J. Colloidal Stabilization of Nanoparticles in Concentrated Suspensions. *Langmuir* **2007**, *23*, 1081-1090.

(73) Thode, K.; Lück, M.; Semmler, W.; Müller, R. H.; Kresse, M. Determination of Plasma Protein Adsorption on Magnetic Iron Oxides: Sample Preparation. *Pharmaceutical Research* **1997**, *14*, 905-910.

(74) Almeida, J. P. M.; Chen, A. L.; Foster, A.; Drezek, R. In vivo biodistribution of nanoparticles. *Nanomedicine* **2011**, *6*, 815-835.

(75) Levy, M.; Luciani, N.; Alloyeau, D.; Elgrabli, D.; Deveaux, V.; Pechoux, C.; Chat, S.; Wang, G.; Vats, N.; Gendron, F.; Factor, C.; Lotersztajn, S.; Luciani, A.; Wilhelm, C.; Gazeau, F. Long term in vivo biotransformation of iron oxide nanoparticles. *Biomaterials* **2011**, *32*, 3988-3999.

(76) Moghimi, S. M.; Hunter, A. C.; Murray, J. C. Long-Circulating and Target-Specific Nanoparticles: Theory to Practice. *Pharmacological Reviews* **2001**, *53*, 283-318.

(77) Geraldes, C. F.; Laurent, S. Classification and basic properties of contrast agents for magnetic resonance imaging. *Contrast media & molecular imaging* **2009**, *4*, 1-23.

(78) Arami, H.; Khandhar, A.; Liggitt, D.; Krishnan, K. M. In vivo delivery, pharmacokinetics, biodistribution and toxicity of iron oxide nanoparticles. *Chemical Society Reviews* **2015**, *44*, 8576-8607.

(79) Uchegbu, I. F.; Schätzlein, A. G.; Cheng, W. P.; Lalatsa, A.: *Fundamentals of Pharmaceutical Nanoscience*; Springer New York, 2013.

(80) Torchilin, V. P. Micellar Nanocarriers: Pharmaceutical Perspectives. *Pharmaceutical Research* **2006**, *24*, 1-16.

(81) Israelachvili, J. N.: *Intermolecular and Surface Forces: With Applications to Colloidal and Biological Systems*; Academic Press, 1985.

(82) Salim, M.; Minamikawa, H.; Sugimura, A.; Hashim, R. Amphiphilic designer nano-carriers for controlled release: from drug delivery to diagnostics. *MedChemComm* **2014**, *5*, 1602-1618.

(83) Gong, J.; Chen, M.; Zheng, Y.; Wang, S.; Wang, Y. Polymeric micelles drug delivery system in oncology. *Journal of Controlled Release* **2012**, *159*, 312-323.

(84) Falbe, J.: *Surfactants in Consumer Products: Theory, Technology and Application*; Springer Berlin Heidelberg, 2012.

(85) Biswas, S.; Vaze, O. S.; Movassaghian, S.; Torchilin, V. P.: Polymeric Micelles for the Delivery of Poorly Soluble Drugs. In *Drug Delivery Strategies for Poorly Water-Soluble Drugs*; John Wiley & Sons Ltd, 2013; pp 411-476.

(86) Hoelder, S.; Clarke, P. A.; Workman, P. Discovery of small molecule cancer drugs: Successes, challenges and opportunities. *Molecular Oncology* **2012**, *6*, 155-176.

(87) Khadka, P.; Ro, J.; Kim, H.; Kim, I.; Kim, J. T.; Kim, H.; Cho, J. M.; Yun, G.; Lee, J. Pharmaceutical particle technologies: An approach to improve drug solubility, dissolution and bioavailability. *Asian Journal of Pharmaceutical Sciences* **2014**, *9*, 304-316.

(88) Oerlemans, C.; Bult, W.; Bos, M.; Storm, G.; Nijsen, J. F. W.; Hennink, W. E. Polymeric Micelles in Anticancer Therapy: Targeting, Imaging and Triggered Release. *Pharmaceutical Research* **2010**, *27*, 2569-2589.

(89) Cabral, H.; Kataoka, K. Progress of drug-loaded polymeric micelles into clinical studies. *Journal of Controlled Release* **2014**, *190*, 465-476.

(90) Berg, J. C.: *An Introduction to Interfaces & Colloids: The Bridge to Nanoscience*; World Scientific, 2010.

(91) Buckton, G.: *Interfacial Phenomena in Drug Delivery and Targeting*; Taylor & Francis, 2000.

(92) Naahidi, S.; Jafari, M.; Edalat, F.; Raymond, K.; Khademhosseini, A.; Chen, P. Biocompatibility of engineered nanoparticles for drug delivery. *Journal of Controlled Release* **2013**, *166*, 182-194.

(93) Williams, D. F. On the mechanisms of biocompatibility. *Biomaterials* **2008**, *29*, 2941-2953.

(94) Tadros, T. F.: Physical Chemistry of Surfactant Solutions. In *Applied Surfactants*; Wiley-VCH Verlag GmbH & Co. KGaA, 2005; pp 19-51.

(95) Uchegbu, I. F.; Schatzlein, A. G.: *Polymers in Drug Delivery*; Taylor & Francis, 2006.

(96) Narang, A. S.; Mahato, R. I.: *Targeted Delivery of Small and Macromolecular Drugs*; CRC Press, 2010.

(97) Du, A.; Stenzel, M. Polymer Micelles for Drug Delivery. *Polymeric Drug Delivery Techniques-Sigma-Aldrich* **2015**, *1*, 1-62.

(98) Uchegbu, I. F.; Sadiq, L.; Arastoo, M.; Gray, A. I.; Wang, W.; Waigh, R. D.; Schätzleinä, A. G. Quaternary ammonium palmitoyl glycol chitosan—a new polysoap for drug delivery. *International Journal of Pharmaceutics* **2001**, *224*, 185-199.

(99) Garcia-Fuentes, M.; Alonso, M. J. Chitosan-based drug nanocarriers: where do we stand? *J Control Release* **2012**, *161*, 496-504.

(100) Ravi Kumar, M. N. V. A review of chitin and chitosan applications. *Reactive and Functional Polymers* **2000**, *46*, 1-27.

(101) Uchegbu, I. F.; Carlos, M.; McKay, C.; Hou, X.; Schätzlein, A. G. Chitosan amphiphiles provide new drug delivery opportunities. *Polymer International* **2014**, *63*, 1145-1153.

(102) Jayakumar, R.; Menon, D.; Manzoor, K.; Nair, S. V.; Tamura, H. Biomedical applications of chitin and chitosan based nanomaterials—A short review. *Carbohydrate Polymers* **2010**, *82*, 227-232.

(103) Qu, X.; Khutoryanskiy, V. V.; Stewart, A.; Rahman, S.; Papahadjopoulos-Sternberg, B.; Dufes, C.; McCarthy, D.; Wilson, C. G.; Lyons, R.; Carter, K. C.; Schätzlein, A.; Uchegbu, I. F. Carbohydrate-Based Micelle Clusters Which Enhance Hydrophobic Drug Bioavailability by Up to 1 Order of Magnitude. *Biomacromolecules* **2006**, *7*, 3452-3459.

(104) Siew, A.; Le, H.; Thiovolet, M.; Gellert, P.; Schatzlein, A.; Uchegbu, I. Enhanced Oral Absorption of Hydrophobic and Hydrophilic Drugs Using Quaternary Ammonium Palmitoyl Glycol Chitosan Nanoparticles. *Molecular Pharmaceutics* **2012**, *9*, 14-28.

(105) Lalatsa, A.; Lee, V.; Malkinson, J. P.; Zloh, M.; Schätzlein, A. G.; Uchegbu, I. F. A Prodrug Nanoparticle Approach for the Oral Delivery of a Hydrophilic Peptide, Leucine5-enkephalin, to the Brain. *Molecular Pharmaceutics* **2012**, *9*, 1665-1680.

(106) Lalatsa, A.; Garrett, N. L.; Ferrarelli, T.; Moger, J.; Schätzlein, A. G.; Uchegbu, I. F. Delivery of Peptides to the Blood and Brain after Oral Uptake of

Quaternary Ammonium Palmitoyl Glycol Chitosan Nanoparticles. *Molecular Pharmaceutics* **2012**, *9*, 1764-1774.

(107) Euliss, L. E.; Grancharov, S. G.; O'Brien, S.; Deming, T. J.; Stucky, G. D.; Murray, C. B.; Held, G. A. Cooperative Assembly of Magnetic Nanoparticles and Block Copolypeptides in Aqueous Media. *Nano Letters* **2003**, *3*, 1489-1493.

(108) Ai, H.; Flask, C.; Weinberg, B.; Shuai, X. T.; Pagel, M. D.; Farrell, D.; Duerk, J.; Gao, J. Magnetite-Loaded Polymeric Micelles as Ultrasensitive Magnetic-Resonance Probes. *Advanced Materials* **2005**, *17*, 1949-1952.

(109) Cheng, D.; Hong, G.; Wang, W.; Yuan, R.; Ai, H.; Shen, J.; Liang, B.; Gao, J.; Shuai, X. Nonclustered magnetite nanoparticle encapsulated biodegradable polymeric micelles with enhanced properties for in vivo tumor imaging. *Journal of Materials Chemistry* **2011**, *21*, 4796-4804.

(110) Gillis, P.; Moiny, F.; Brooks, R. A. On T2-shortening by strongly magnetized spheres: A partial refocusing model. *Magnetic Resonance in Medicine* **2002**, *47*, 257-263.

(111) Gong, C. Y.; Shi, S.; Dong, P. W.; Yang, B.; Qi, X. R.; Guo, G.; Gu, Y. C.; Zhao, X.; Wei, Y. Q.; Qian, Z. Y. Biodegradable in situ gel-forming controlled drug delivery system based on thermosensitive PCL–PEG–PCL hydrogel: Part 1—synthesis, characterization, and acute toxicity evaluation. *Journal of Pharmaceutical Sciences* **2009**, *98*, 4684-4694.

(112) Li, X.; Li, H.; Liu, G.; Deng, Z.; Wu, S.; Li, P.; Xu, Z.; Xu, H.; Chu, P. K. Magnetite-loaded fluorine-containing polymeric micelles for magnetic resonance imaging and drug delivery. *Biomaterials* **2012**, *33*, 3013-3024.

(113) Su, H.; Liu, Y.; Wang, D.; Wu, C.; Xia, C.; Gong, Q.; Song, B.; Ai, H. Amphiphilic starlike dextran wrapped superparamagnetic iron oxide nanoparticle

clsuters as effective magnetic resonance imaging probes. *Biomaterials* **2013**, *34*, 1193-1203.

(114) Paquet, C.; de Haan, H. W.; Leek, D. M.; Lin, H.-Y.; Xiang, B.; Tian, G.; Kell, A.; Simard, B. Clusters of Superparamagnetic Iron Oxide Nanoparticles Encapsulated in a Hydrogel: A Particle Architecture Generating a Synergistic Enhancement of the T2 Relaxation. *ACS Nano* **2011**, *5*, 3104-3112.

(115) Guang Choo, E. S.; Tang, X.; Sheng, Y.; Shuter, B.; Xue, J. Controlled loading of superparamagnetic nanoparticles in fluorescent nanogels as effective T2-weighted MRI contrast agents. *Journal of Materials Chemistry* **2011**, *21*, 2310-2319.

(116) Lin, Y.; Wang, S.; Zhang, Y.; Gao, J.; Hong, L.; Wang, X.; Wu, W.; Jiang, X. Ultra-high relaxivity iron oxide nanoparticles confined in polymer nanospheres for tumor MR imaging. *Journal of Materials Chemistry B* **2015**, *3*, 5702-5710.

(117) Niu, D.; Ma, Z.; Li, Y.; Shi, J. Synthesis of Core–Shell Structured Dual-Mesoporous Silica Spheres with Tunable Pore Size and Controllable Shell Thickness. *Journal of the American Chemical Society* **2010**, *132*, 15144-15147.

(118) Qi, H.; Li, Z.; Du, K.; Mu, K.; Zhou, Q.; Liang, S.; Zhu, W.; Yang, X.; Zhu, Y. Transferrin-targeted magnetic/fluorescence micelles as a specific bi-functional nanoprobe for imaging liver tumor. *Nanoscale Research Letters* **2014**, *9*, 1-9.

(119) Lee, H. J.; Jang, K.-S.; Jang, S.; Kim, J. W.; Yang, H.-M.; Jeong, Y. Y.; Kim, J.-D. Poly(amino acid)s micelle-mediated assembly of magnetite nanoparticles for ultra-sensitive long-term MR imaging of tumors. *Chemical Communications* **2010**, *46*, 3559-3561.

(120) Guthi, J. S.; Yang, S.-G.; Huang, G.; Li, S.; Khemtong, C.; Kessinger, C. W.; Peyton, M.; Minna, J. D.; Brown, K. C.; Gao, J. MRI-Visible Micellar Nanomedicine for Targeted Drug Delivery to Lung Cancer Cells. *Molecular Pharmaceutics* **2010**, *7*, 32-40.

(121) Ling, Y.; Wei, K.; Luo, Y.; Gao, X.; Zhong, S. Dual docetaxel/superparamagnetic iron oxide loaded nanoparticles for both targeting magnetic resonance imaging and cancer therapy. *Biomaterials* **2011**, *32*, 7139-7150.

(122) Yang, X.; Grailer, J. J.; Rowland, I. J.; Javadi, A.; Hurley, S. A.; Steeber, D. A.; Gong, S. Multifunctional SPIO/DOX-loaded wormlike polymer vesicles for cancer therapy and MR imaging. *Biomaterials* **2010**, *31*, 9065-9073.

(123) Jain, T. K.; Richey, J.; Strand, M.; Leslie-Pelecky, D. L.; Flask, C.; Labhasetwar, V. Magnetic Nanoparticles with Dual Functional Properties: Drug Delivery and Magnetic Resonance Imaging. *Biomaterials* **2008**, *29*, 4012-4021.

(124) Yallapu, M. M.; Othman, S. F.; Curtis, E. T.; Gupta, B. K.; Jaggi, M.; Chauhan, S. C. Multi-functional Magnetic Nanoparticles for Magnetic Resonance Imaging and Cancer Therapy. *Biomaterials* **2011**, *32*, 1890-1905.

(125) Guo, M.; Yan, Y.; Zhang, H.; Yan, H.; Cao, Y.; Liu, K.; Wan, S.; Huang, J.; Yue, W. Magnetic and pH-responsive nanocarriers with multilayer core-shell architecture for anticancer drug delivery. *Journal of Materials Chemistry* **2008**, *18*, 5104-5112.

(126) Purushotham, S.; Chang, P. E.; Rumpel, H.; Kee, I. H.; Ng, R. T.; Chow, P. K.; Tan, C. K.; Ramanujan, R. V. Thermoresponsive core-shell magnetic nanoparticles for combined modalities of cancer therapy. *Nanotechnology* **2009**, *20*, 305101.

(127) Yang, X.; Chen, Y.; Yuan, R.; Chen, G.; Blanco, E.; Gao, J.; Shuai, X. Folate-encoded and Fe3O4-loaded polymeric micelles for dual targeting of cancer cells. *Polymer* **2008**, *49*, 3477-3485.

(128) Wang, X.; Jing, X.; Zhang, X.; Liu, Q.; Liu, J.; Song, D.; Wang, J.; Liu, L. A versatile platform of magnetic microspheres loaded with dual-anticancer drugs for drug release. *Materials Chemistry and Physics* **2016**, *177*, 213-219.

(129) Kohler, N.; Sun, C.; Wang, J.; Zhang, M. Methotrexate-Modified Superparamagnetic Nanoparticles and Their Intracellular Uptake into Human Cancer Cells. *Langmuir* **2005**, *21*, 8858-8864.

(130) Yuan, Q.; Venkatasubramanian, R.; Hein, S.; Misra, R. D. K. A stimulus-responsive magnetic nanoparticle drug carrier: Magnetite encapsulated by chitosan-grafted-copolymer. *Acta Biomaterialia* **2008**, *4*, 1024-1037.

(131) Sanson, C.; Diou, O.; Thevenot, J.; Ibarboure, E.; Soum, A.; Brulet, A.; Miraux, S.; Thiaudiere, E.; Tan, S.; Brisson, A.; Dupuis, V.; Sandre, O.; Lecommandoux, S. Doxorubicin loaded magnetic polymersomes: theranostic nanocarriers for MR imaging and magneto-chemotherapy. *ACS Nano* **2011**, *5*, 1122-1140.

(132) Wang, L.; Wang, W.; Rui, Z.; Zhou, D. The effective combination therapy against human osteosarcoma: doxorubicin plus curcumin co-encapsulated lipid-coated polymeric nanoparticulate drug delivery system. *Drug delivery* **2016**, 1-9.

(133) Maeng, J. H.; Lee, D.-H.; Jung, K. H.; Bae, Y.-H.; Park, I.-S.; Jeong, S.; Jeon, Y.-S.; Shim, C.-K.; Kim, W.; Kim, J.; Lee, J.; Lee, Y.-M.; Kim, J.-H.; Kim, W.-H.; Hong, S.-S. Multifunctional doxorubicin loaded superparamagnetic iron oxide nanoparticles for chemotherapy and magnetic resonance imaging in liver cancer. *Biomaterials* **2010**, *31*, 4995-5006.

(134) Yu, M. K.; Park, J.; Jon, S. Targeting Strategies for Multifunctional Nanoparticles in Cancer Imaging and Therapy. *Theranostics* **2012**, *2*, 3-44.

(135) Chen, S.; Li, Y.; Guo, C.; Wang, J.; Ma, J.; Liang, X.; Yang, L.-R.; Liu, H.-Z. Temperature-Responsive Magnetite/PEO−PPO−PEO Block Copolymer Nanoparticles for Controlled Drug Targeting Delivery. *Langmuir* **2007**, *23*, 12669-12676.

(136) Rudolf, H.; Silvio, D.; Robert, M.; Matthias, Z. Magnetic particle hyperthermia: nanoparticle magnetism and materials development for cancer therapy. *Journal of Physics: Condensed Matter* **2006**, *18*, S2919.

(137) Hervault, A.; Thanh, N. T. K. Magnetic nanoparticle-based therapeutic agents for thermo-chemotherapy treatment of cancer. *Nanoscale* **2014**, *6*, 11553-11573.

(138) Ulbrich, K.; Holá, K.; Šubr, V.; Bakandritsos, A.; Tuček, J.; Zbořil, R. Targeted Drug Delivery with Polymers and Magnetic Nanoparticles: Covalent and Noncovalent Approaches, Release Control, and Clinical Studies. *Chemical Reviews* **2016**, *116*, 5338-5431.

(139) Tietze, R.; Lyer, S.; Dürr, S.; Struffert, T.; Engelhorn, T.; Schwarz, M.; Eckert, E.; Göen, T.; Vasylyev, S.; Peukert, W.; Wiekhorst, F.; Trahms, L.; Dörfler, A.; Alexiou, C. Efficient drug-delivery using magnetic nanoparticles — biodistribution and therapeutic effects in tumour bearing rabbits. *Nanomedicine: Nanotechnology, Biology and Medicine* **2013**, *9*, 961-971.

(140) Hu, S. H.; Liao, B. J.; Chiang, C. S.; Chen, P. J.; Chen, I. W.; Chen, S. Y. Core-shell nanocapsules stabilized by single-component polymer and nanoparticles for magneto-chemotherapy/hyperthermia with multiple drugs. *Adv Mater* **2012**, *24*, 3627-3632.

(141) Peiris, P. M.; Bauer, L.; Toy, R.; Tran, E.; Pansky, J.; Doolittle, E.; Schmidt, E.; Hayden, E.; Mayer, A.; Keri, R. A.; Griswold, M. A.; Karathanasis, E. Enhanced Delivery of Chemotherapy to Tumors Using a Multicomponent Nanochain with Radio-Frequency-Tunable Drug Release. *ACS Nano* **2012**, *6*, 4157-4168.

(142) Huang, H.-Y.; Hu, S.-H.; Hung, S.-Y.; Chiang, C.-S.; Liu, H.-L.; Chiu, T.-L.; Lai, H.-Y.; Chen, Y.-Y.; Chen, S.-Y. SPIO nanoparticle-stabilized PAA-F127 thermosensitive nanobubbles with MR/US dual-modality imaging and HIFU-triggered drug release for magnetically guided in vivo tumor therapy. *Journal of Controlled Release* **2013**, *172*, 118-127.

Chapter 2

Design, Synthesis and Characterisation of an Iron Oxide Nanoparticle Formulation using Amphiphilic Chitosan Based Polymers for MRI applications

2.1 Introduction

It has long been a goal for scientists to have complete synthetic control over nanoparticle size and shape and as a result, iron oxide nanoparticles (IONPs) have been prepared using a variety of methods including: chemical co-precipitation, high temperature thermal decomposition, sono-chemical synthesis, hydrothermal synthesis, sol-gel synthesis and microbial synthesis.[1,2] Each method inevitably comes with advantages and challenges and so choosing an appropriate IONP synthesis method could be essential to the success of this project. By far the most conventional way for synthesising IONPs is via *chemical coprecipitation,* this well-studied method allows for the production of large volumes of nano-sized magnetic iron oxide particles at low cost and using relatively non-toxic materials.[3] Chemical co-precipitation is based on the precipitation of IONPs from Fe^{3+} and Fe^{2+} salts in the presence of a base, were black IONPs are usually seen when the pH of the reaction mixture reaches pH 9-14.[4] Although chemical coprecipitation is a widely used method it does have a number of shortcomings: The first main challenge is that IONPs made using chemical coprecipitation are extremely sensitive to their reaction conditions. This sensitivity often leads to relatively polydisperse products that could result in batch to batch variation in; levels of stability, magnetism and biodistribution. Secondly, by their nature nanoparticles have a high surface to volume ratio often leading to particles with high surface energies.[5] To minimise this effect naked IONPs have a tendency to agglomerate which in turn leads to sedimentation, consequentially making them largely unsuitable for use in biological applications.[5] In addition to this, magnetite (Fe_3O_4) nanoparticles can readily oxidise into maghemite (Fe_2O_3) unless kept in inert conditions, often with a loss of magnetisation and this could have an effect on the sensitivity of the final contrast agent. To overcome many of the challenges discussed, IONPs made via chemical coprecipitation are often formulated with polymers or

surfactants to stop agglomeration and reduce oxidation. Many examples have been published, however dextran, carboxymethyl dextran, poly ethylene glycol (PEG) and polyvinyl alcohol (PVA) are amongst the most reported with a dextran-IONP being one of the first iron oxide based MRI contrast agents to become commercially available (Feridex I.V. ®).[6]

In more recent years, synthesis of IONPs via *high temperature thermal decomposition* has considerably gained in popularity.[7] This non-aqueous method utilises organometallic compounds, high boiling point organic solvents and long chained fatty acids to yield IONPs with highly controllable sizes and narrow size distributions. One of the most commonly used fatty acids is oleic acid, a fatty acid that is often used in pharmaceutical formulations to improve the bioavailablilty of poorly soluble drugs. In addition to this, scientists have also been able to use this method to prepare IONPs with various shapes by varying the reaction conditions, altering the ratio of reagents and by the introduction of seeding and capping agents.[8,9] Although these oleic acid coated iron oxide nanoparticles (IONPs) exhibit more desirable properties, their drawback is that they are hydrophobic and can only be dispersed in organic solvents making them unsuitable for biological applications without further modification.[10]

The aim of this work was to create a multifunctional nanotheranostic using IONPs as the main diagnostic component. As mentioned previously formulating IONPs into a colloidal suspension that is suitable for *in vivo* MRI applications is often challenging. In this project it was believed that many of these complications could be overcome by using a chitosan based amphiphilic polymer named N-palmitoyl-N-monomethyl-N,N-dimethyl-N,N,N-trimethyl-6-O-glycolchitosan (GCPQ). This polymer was selected as it has previously demonstrated to be rather effective at formulating challenging drug species, as well as having a reasonable toxicity profile. This chapter will explore the design, synthesis and formulation of a polymer-IONP formulation utilising IONPs

formed from the chemical coprecipitation and high temperature thermal decomposition processes. Chemical coprecipitation is the most widely used method for IONP synthesis. This method has been used for many years and so it was deemed a reasonable place to begin. The formation of hydrophobic IONPs made from the high temperature thermal decomposition was also explored as an alternative method as it was postulated that by talking advantage of the polymer's ability to undergo micellisation it may allow for effective IONP encapsulation within the micelle's hydrophobic core. To gain a deeper knowledge about nanoparticles and their potential for an application, comprehensive characterisation must be conducted. In a nanoparticle system one is usually interested in; colloidal stability, surface charge, size, aggregation, surface area and shape.[11] Fortunately, in the last few decades the field of nanoscience has rapidly grown and a number of characterisation techniques have now been developed. This chapter will cover the characterisation of the two newly formed IONP formulations and will seek to evaluate their potential as an MRI contrast agent.

2.2 Materials

Chemical	Purity	Supplier
1,10-phenanthroline	>99.5%	Sigma-Aldrich
Acetone		
Amberlite IRA-96		Sigma-Aldrich
Ammonia hydroxide	35% v/v	Fisher
Dextrose	20% w/v	Martindale Pharmaceuticals
Dialysis membrane		Medicell
Diethyl ether	>99.5%	Sigma-Aldrich
Dimercaptosuccinic acid	98%	Sigma-Aldrich
Dimethyl sulfoxide	>99.7%	Sigma-Aldrich
Diphenyl ether	>99%	Alfa Aesar
Ethanol	>99.5%	Fisher
$FeCl_2.4H_2O$	98%	Sigma-Aldrich
$FeCl_3.6H_2O$	>99%	Sigma-Aldrich
Glycol chitosan		WAKKO
Hexane	>99.5%	Sigma-Aldrich
Hydrochloric acid	32%	Fisher

Chemical	Purity	Supplier
Hydroxylamine hydrochloride	>99%	Alfa Aesar
Methanol		
Methyl iodide	>99%	Sigma-Aldrich
Nitrogen		BOC
N-methyl-2-pyrrolidone	>99%	Sigma-Aldrich
Oleic acid	>85%	CRODA
Oleyl alcohol	>85%	Sigma-Aldrich
Palmitic acid N-hydrosuccinimide		Toronto Research Chemicals
Polystyrene size standard (200 nm)	(0.2 ± 0.03) μm	Sigma-Aldrich
Polystyrene zeta standard	(-42 ± 4.2) mV	Malvern
Sodium acetate	>99%	Sigma-Aldrich
Sodium chloride	>99.8%	Fisher
Sodium hydroxide	>97%	Sigma-Aldrich
Sodium iodide	>99%	Sigma-Aldrich
Sodium oleate	97%	TCI chemicals
Toluene	>99.5%	Fisher

2.3 Methods

2.3.1 Synthesis of the modified chitosan amphiphilic polymer — N-palmitoyl-N-monomethyl-N,N-dimethyl-N,N,N-trimethyl-6-O-glycolchitosan (GCPQ)

GCPQ was synthesised as described previously.[12] Briefly, glycol chitosan (5 g, M_w ~120 kDa, WAKO) was dissolved in 4M HCl (380 ml). The solution was heated to 50 ^oC and stirred for 24 h. The resulting solution was dialysed exhaustively against water (MWCO – 3.5 kDa) and then lyophilised to obtain degraded glycol chitosan (dGC) as a white fibrous solid in a yield of 46%, ~7000 Da.

The degraded glycol chitosan (1 g) and $NaHCO_3$ (0.75 g) were dissolved into a mixture of ethanol and water (24:76). Palmitic acid N-hydrosuccinimide (1.58 g, Toronto Research Chemicals) was dissolved in ethanol (300 mL) and was added drop wise. The reaction was left to stir for 72 h protected from light. Ethanol was removed under vacuo and then extracted using diethyl ether. The aqueous phase was dialysed exhaustively against water (MWCO – 3.5 kDa) and then lyophilised to obtain palmitoylated glycol chitosan (PGC) as a white fibrous solid.

The palmitoylated glycol chitosan (300 mg) was dispersed in N-methyl-2-pyrrolidone (25 mL) and stirred vigorously overnight. Sodium hydroxide (40 mg) dissolved in ethanol (2mL) and sodium iodide (45 mg) dissolved in ethanol (2 mL) was added to the solution and the mixture was heated to 36 ^OC. Methyl iodide (0.45 mL) was added and the reaction was stirred under a N_2 environment for 3 h. The product was precipitated using diethyl ether and left over night. The resulting precipitate was washed x3 with diethyl ether (50 mL) and dissolved in water (100 mL) and then was dialysed exhaustively against water (MWCO – 3.5 kDa). The dialysate was passed

through an amberlite IRA-96 column to remove iodide and then lyophilised to obtain GCPQ in a white fibrous solid with a total synthetic yield of 30%.

2.3.2 Synthesis of iron oxide nanoparticles made via coprecipitation

IONPs (Fe_3O_4) were made via co-precipitation using ferrous complexes and NH_4OH as the base. Briefly, solutions of $FeCl_3.6H_2O$ (0.389 M) and $FeCl_2.4H_2O$ (0.195 M) [Fe^{3+}: Fe^{2+} = 2:1] were made using deoxygenated water and mixed in a round bottom flask under a N_2 atmosphere. 25% NH_4OH was added rapidly resulting in a dark black precipitate forming. The reaction was allowed to proceed for 30 mins whilst vigorously stirring. The black precipitate was isolated with a strong magnet and washed with de-oxygenated water until a neutral pH was obtained. De-oxygenated water was obtained by purging distilled H_2O with a stream of N_2 for several hours. The particles were stored wet under deoxygenated conditions.

2.3.3 Polymer stabilised iron oxide 'blackberry' nanoparticles

The GCPQ polymer stabilised IONPs were prepared via sonication. Usually, 1 mL of IONP (10 mg mL^{-1}) was added to 4 mL of polymer solution. The resulting formulation was probe sonicated for 10 mins (2 x 5 mins, 7 micron amplitude) to yield a black formulation.

2.3.4 Synthesis of iron oxide nanoparticles via high temperature thermal decomposition

Iron oxide nanoparticles were synthesised in a procedure outlined by *Kim et al*.[13] In a typical reaction, $FeCl_3.6H_2O$ (3 g) and sodium oleate (10.2 g) were dissolved in a solvent mixture of: 17 mL water, 23 mL ethanol and 40 mL hexane. The resulting mixture was stirred for 4 h at 70 ^{O}C. After 4 h the reaction mixture was allowed to cool to room temperature and the hexane layer was extracted and washed x3 with distilled

water (30 mL). The hexane was then evaporated under vacuo to yield the iron oleate complex as a waxy orange oil.

For synthesis of the iron oxide nanoparticles, iron-oleate complex (1.8 g), oleic acid (0.57 g) and oleyl alcohol (1.61 g) were dissolved in diphenyl ether (10 g). The reaction mixture was heated to 250 ^{O}C and then kept at this temperature for 20 mins under a N_2 blanket. The mixture was then rapidly cooled to room temperature and acetone (50 mL) was added to precipitate out the nanoparticles. Nanoparticles were collected via centrifugation (3000 rcf, 10 min), the supernatant was discarded and replaced with acetone (40 mL), and this procedure was repeated x3. The washed nanoparticles were finally dispersed and stored in hexane. To obtain dry nanoparticles for characterisation; hexane was removed under vacuo. Acetone was added and the nanoparticles could be gently be collected with a spatula and dried overnight under vacuum. From here, the particles could be weighed and made up to the desired concentration in hexane or chloroform.

2.3.5 Formulation of iron oxide polymeric 'raspberry' nanoparticles

In a small vial, iron oxide nanoparticles in hexane (2 mL, 4 mg/mL) were added to a GCPQ solution (5 mL, 1 mg/mL). The solution was then sonicated using probe sonication (2 x 5 min, 7 micron amplitude, Soni Prep 150, MSE, UK) at the interface between the organic and aqueous phases, creating a brown emulsion. This emulsion was left to separate over 48 h. The aqueous layer was then extracted and any residual hexane was allowed to evaporate overnight. The product was frozen and lyophilised to obtain a dry product which rapidly dispersed when added to water (5 mL). For the *in vivo* investigations a formulation with a higher yield of iron oxide nanoparticles was made by increasing the IONPs and polymer concentration by a factor of 15; iron oxide nanoparticles in hexane (2 mL, 60 mg/mL) were added to a GCPQ solution (5 mL, 15 mg/mL) and then processed as described above.

2.3.6 Ligand exchange of hydrophobic iron oxide nanoparticles with meso-2,3-dimercaptosuccinic acid (DMSA)

This ligand exchange protocol was followed as described previously by *Palma et al.*[14] Briefly, iron oxide nanoparticles (20 mg) were precipitated from hexane (1 mL) by the addition of ethanol and were collected via centrifugation (9000 rcf, 10 min), the supernatant was discarded and replaced with ethanol and this procedure was repeated twice. The final precipitate was re-dispersed in toluene. DMSA (36 mg) in DMSO (2 mL) was added to the toluene mixture and the reaction was bath sonicated (10 min) and left to stir at room temperature for 48 h. After 48 h a sediment was observed, this was collected via centrifugation (9000 rcf, 10 min), the supernatant was discarded and replaced with ethanol and this procedure was repeated twice. The final precipitate was re-dispersed in water, titrated to pH 10 using NaOH and then filtered through a 0.22 μm membrane.

2.3.7 ^{1}H-Nuclear magnetic resonance

All ^{1}H-NMR experiments were recorded on Brüker AMX 400 MHz spectrometers in deuterated solvents and processed using MestreNova software with calibration on residual solvent peaks. Chemical shifts (δ) are quoted in ppm. The level of palmitoylation was estimated by comparing the ratio of palmitoyl methyl protons (δ ~ 0.9 ppm) to the sugar protons (δ ~ 3.5 – 4.5 ppm) and the level of quarternisation was calculated by comparing the ratio of quaternary ammonium (δ ~ 3.45 ppm) to the sugar protons.

2.3.8 Gel permeation chromatography – multi angled laser light scattering

The molecular weight of DGC and GCPQ was determined by GCP-MALLS equipped with DAWN® EOS™ MALLS (λ = 690 nm), Optilab DSP Interferometric Refractometer (λ = 690 nm) and QELS detectors (Wyatt Technology Corporation, USA), using as a

mobile phase an acetate buffer (0.3 M CH_3COONa/0.2 M CH_3COOH, pH 4.5) for DGC and a mixture of the acetate buffer:methanol (35:65) for GCPQ. Filtered samples (0.2 µm, 200 µL) were injected using a Waters 717plus Autosampler into a POLYSEP TM-GFC-P guard column (35.0 x 7.8 mm, Phenomenex, UK) attached to a POLYSEP TM-GFC-P 4000 column (300.0 x 7.8 mm, exclusion limit for PEG =200,000 Da, Phenomenex, UK) at a concentration of 5 mg mL^{-1}. The experiments were performed at room temperature. The data was processed using ASTRA for Windows version 4.90.08 software (Wyatt Corporation, USA).

The specific refractive index increment (dn/dc) of DGC and GCPQ were measured with an Optila DSP Interferometric Refractometer (λ=690nm). Filtered samples (0.2 µm, 33 mm Millex GP syringe driven filter unit, PES membrane for sterilisation of aqueous solutions) of 5 concentrations ranging from 0.1-0.5 mg mL^{-1} were manually injected using an Injection System (Wyatt Technology Corporation, USA) at a flow rate of 0.3 ml min^{-1} at room temperature. The data was processed using DNDC for Windows version 5.90.03 software (Wyatt Corporation, USA).

2.3.9 Transmission electron microscopy

Images were collected using a FEI CM120 BioTwin Transmission Electron Microscope (Ex. Philips, Eindhoven, Netherlands). Digital images were captured using an AMT digital camera. A drop of the sample was placed on Formvar©/Carbon Coated Grid (F196/100 3.05 mm, mesh 300, Tab Labs Ltd, England). Samples were stained with 1 % aqueous uranyl acetate where indicated.

2.3.10 Dynamic light scattering

Particle size was determined by dynamic light scattering (DLS) on a Malvern Zetasizer 3000HS (Malvern Instruments, UK) using a laser wavelength of 633 nm. Samples were inverted several times and then left to equilibrate for 10 seconds before

particle sizing was carried out. The accuracy of the instrument was assessed periodically using latex beads (polystyrene, mean size: 0.2 μm) in a 50 mM sodium chloride dispersant phase.

2.3.11 Manual zeta potential and size – pH titration

Zeta potential was measured using a Malvern Zetasizer 3000HS (Malvern Instruments, UK). Nanoparticles were manually titrated to various pH values using 0.1 M HCl and 0.1 M NaOH. Measurements were carried out in gold plated disposable capillary cells (Malvern Instruments, UK). The accuracy of the instrument was assessed periodically using a polystyrene zeta standard (Malvern Instruments, UK).

2.3.12 Automatic zeta potential and size – pH titration

Zeta potential was measured using a Malvern Zetasizer 3000HS (Malvern Instruments, UK) paired with an MPT-2 automatic titrator (Malvern Instruments, UK). Prior to any titration the pH probes were calibrated using pH 4, pH 7 and pH 10 standards. Nanoparticles were manually titrated to pH 4. The instrument then automatically titrated the sample and measured size and zeta potential between pH 4 and 11. Reservoirs were filled with HCl and NaOH at concentrations of 0.05 M. Measurements were carried out in gold plated disposable capillary cells (Malvern Instruments, UK). Accuracy of the instrument was assessed periodically using a polystyrene zeta standard (Malvern Instruments, UK).

2.3.13 Magnetic properties

Magnetization curves were carried out in a Quantum Design hybrid Superconducting Quantum Interference Device-Vibrating Sample Magnetometer (SQUID-VSM) at 300 K, with applied fields up to 7 T. Samples were lyophilised to obtain a dry product.

Weighed samples of the dry product were placed into plastic capsules and measured in a straw sample holder.

2.3.14 X-ray diffraction

X-ray diffraction patterns were collected on an X-ray diffractometer (PanAlytical, UK) using CoKα radiation λ = 1.79 Å. Samples were prepared by pressing dried powders on a zero background silicon wafer and diffraction patterns were collected within 20–100 2θ (degrees) range.

2.3.15 *In vitro relaxivity measurements*

Relaxivity measurements for the iron oxide blackberry nanoparticles were performed at the ICPMS (Campus de Cronenbourg, Strasbourg, France) on a contrast agent analyzer (minispec mq 60, Bruker, Germany) at 1.5T at 37 ^{O}C. T2 values were collected using a spin-echo sequence. T1 values were obtained using an inversion recovery sequence. The relaxivities were plotted against the iron concentration of a series of blackberry nanoparticle formulations and the relaxivities was determined from the gradient of the slope. Iron concentration was measured using the 1,10-phenanthroline iron quantification assay.

2.3.16 MR relaxivity measurements

MR relaxivities for the raspberry nanoparticles and the DMSA.IONPs were measured using a 1T benchtop MRI scanner (ICON^{TM}, Bruker, UK) at 37 ^{O}C. For T2 relaxation a spin echo sequence was used with the following parameters; TE: 6-100 ms, TR: 1845 ms. The T2 relaxivities were determined by curve fitting the echo times (TE) using MATLAB (Mathworks, UK). The relaxivities were plotted against the iron concentration of a series of iron oxide polymeric raspberry nanoparticles samples and the T2 was determined from the gradient of the slope. T1 relaxivity was measured

using an inversion recovery sequence with the follow parameters; TI: 35-7500 ms, TR: 15000. The T1 relaxivities were determined by curve fitting several inversion times (TI). The relaxivities were plotted against a series of samples and the T1 was determined from the gradient of the slope.

2.4 Results

2.4.1 Amphiphilic polymer synthesis

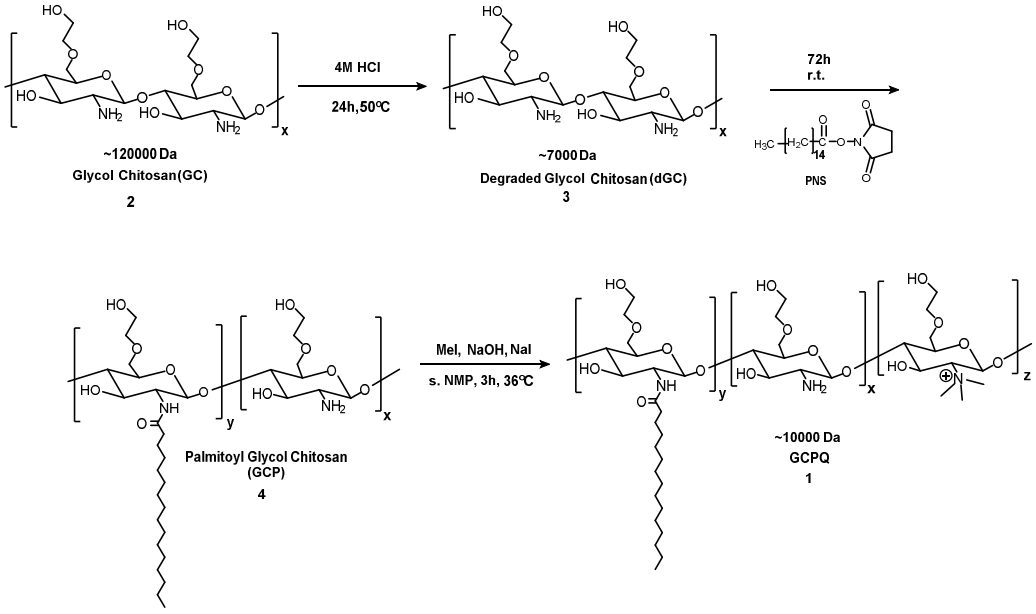

Scheme 2.4.1.1. Synthesis of the amphiphilic chitosan based polymer (GCPQ).

2.4.2 *Nuclear magnetic resonance characterisation*

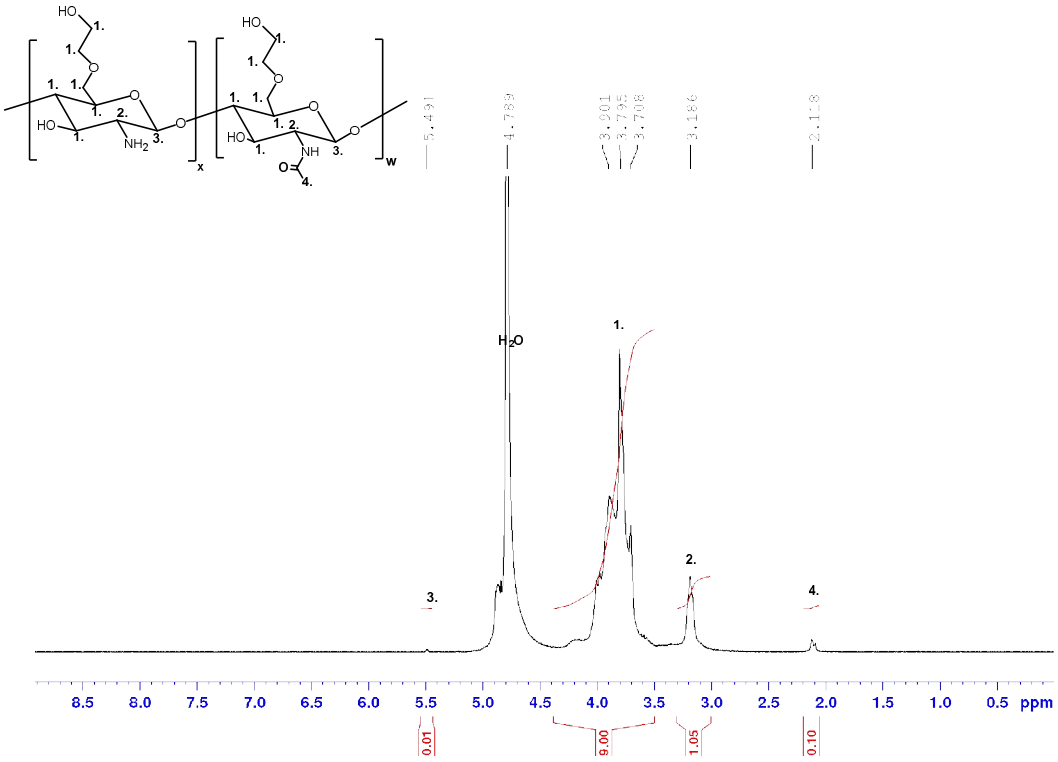

Figure 2.4.2.1. ^{1}H-NMR of degraded glycol chitosan (dGC) in D_2O. An acetyl group was present in small amounts at position 4. This is an inherited feature from chitin, which is the acetylated polymer that glycol chitosan is originally derived from. ^{1}H NMR (400 MHz, D_2O, 298 K): δ 2.1 (3H, s, H_4), δ 3.3 (1H, m, H_2), δ 3.5-4.5 (9H, m, H_1), δ 5.5 (1H, s, H_3).

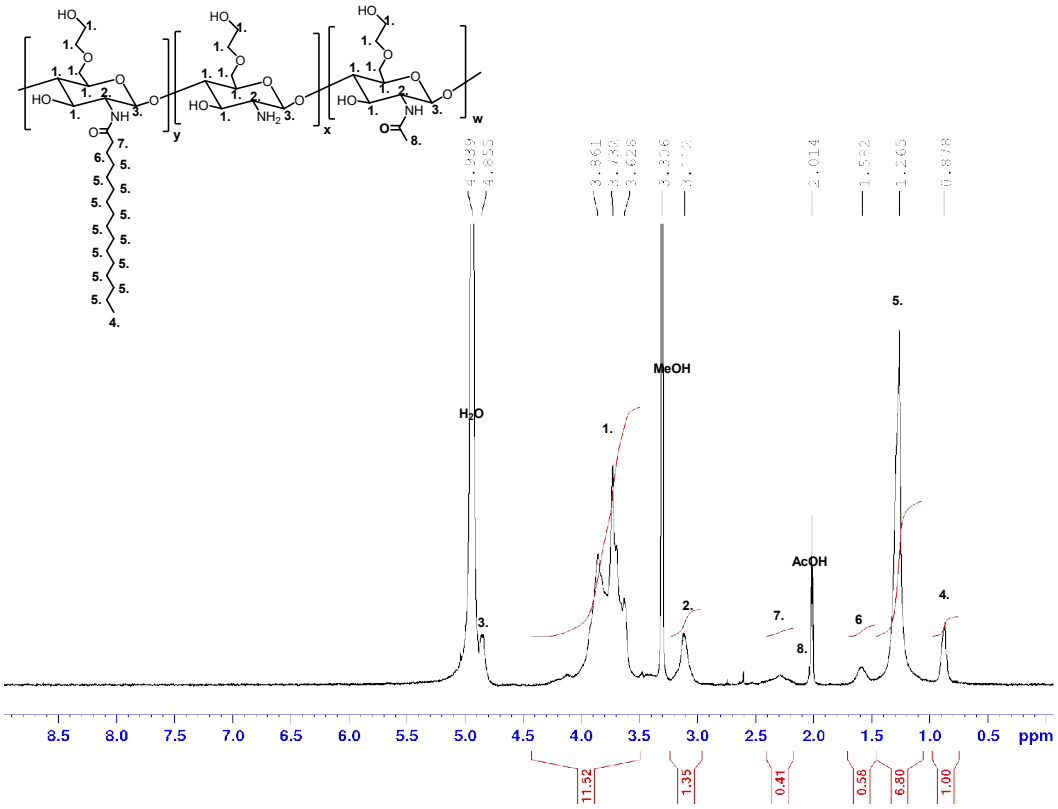

Figure 2.4.2.2. ^{1}H-NMR of palmitoylated glycol chitosan (PGC) in D2O:MeOD:AcOD (8:4:1). The order of protons found at positions 6 and 7 can only be determined by 1H-COESY reported in Figure 2.4.2.4. ^{1}H NMR (400 MHz, D2O:MeOD:AcOD (8:4:1), 298 K): δ 0.9 (3H, t, H_4), δ 1.3 (24H, m, H_5), δ 1.6 (2H, m, H_6), δ 2.0 (3H, s, H_8), δ 2.3 (2H, m, H_7), δ 3.2 (1H, m, H_2), δ 3.5-4.5 (9H, m, H_1), δ 4.9 (1H, m, H_3).

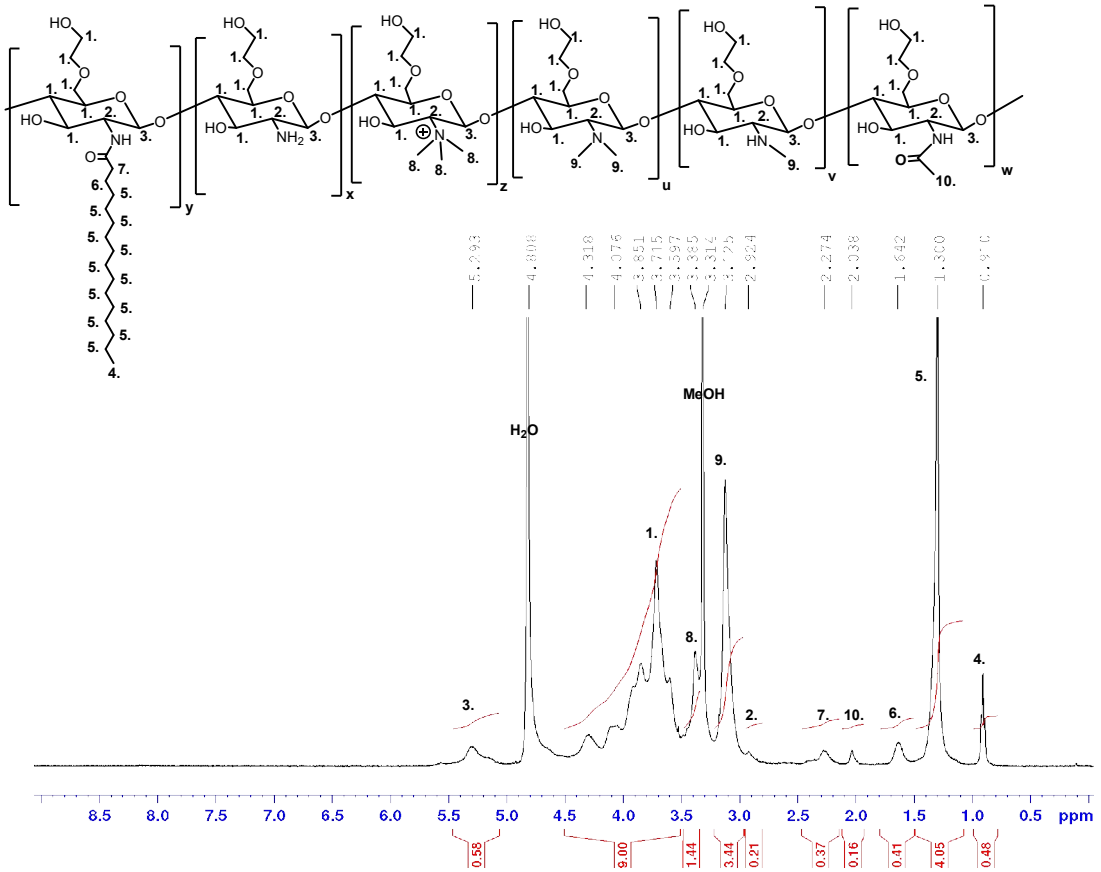

Figure 2.4.2.3. ^{1}H-NMR of N-palmitoyl-N-monomethyl-N,N-dimethyl-N,N,N-trimethyl-6-O-glycolchitosan (GCPQ) in MeOD. The newly formed quaternary ammonium group can be found at position 8. Di and mono substituted methylation can be found at position 9. ^{1}H NMR (400 MHz, MeOD, 298 K): δ 0.9 (3H, t, H_4), δ 1.3 (24H, m, H_5), δ 1.6 (2H, m, H_6), δ 2.0 (3H, s, H_{10}), δ 2.3 (2H, m, H_7), δ 3.0 (1H, m, H_2), δ 3.2 (9H, s, H_9), δ 3.4 (9H, s, H_8) δ 3.5-4.5 (9H, m, H_1), δ 5.3 (1H, m, H_3).

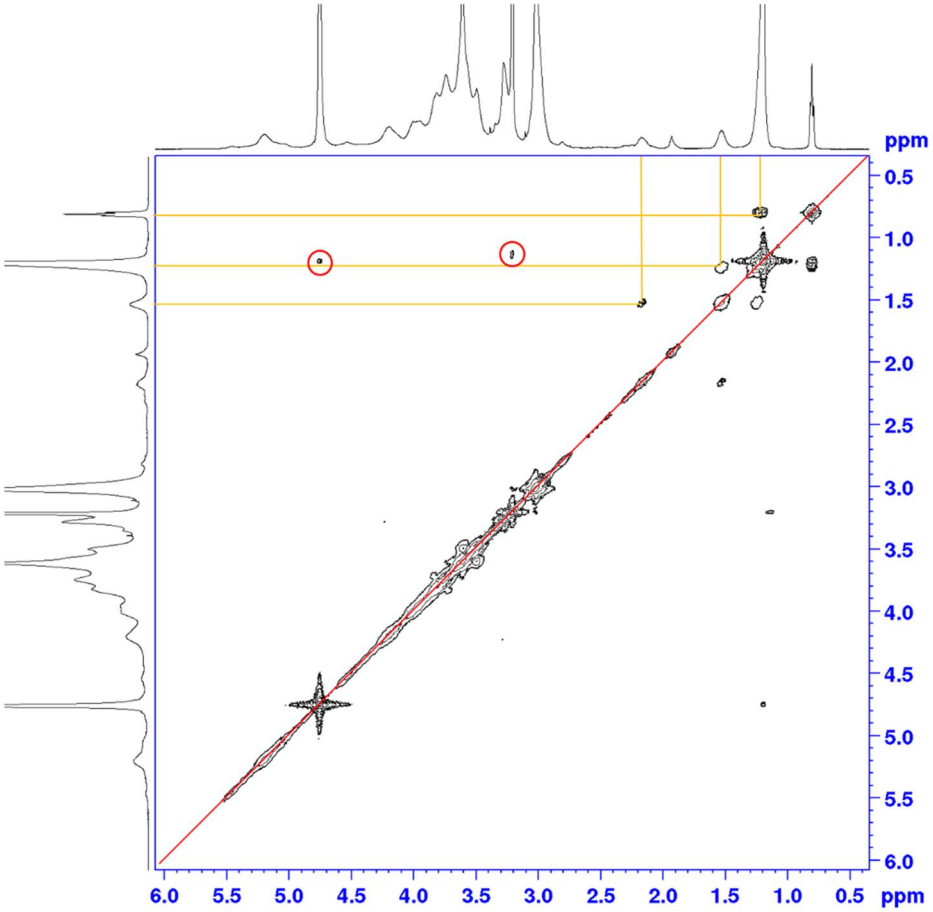

Figure 2.4.2.4. COSEY of N-palmitoyl-N-monomethyl-N,N-dimethyl-N,N,N-trimethyl-6-O-glycolchitosan (GCPQ) in MeOD. A proton-proton correlation experiment (COSEY) was used to differentiate between the protons found at positions 6 and 7. Solvent coupling between MeOH and H_2O was observed (circled in red).

GCPQ batch No.	*% palmitoylation*	*%* quarternisation
GCPQ 1	17.3	18.4
GCPQ 2	13.0	18.2
GCPQ 3	9.7	20.9
GCQP 4	16.0	16.0
GCPQ 5	11.0	9.1
GCPQ 6	13.3	10.7

Table 2.4.2.1. Table summarising the degree of functionalisation of the GCPQ polymer between batches determined by NMR giving a palmitoyl functionalisation of (13.4 ± 2.9)% and a trimethyl functionalisation of (15.6 ± 4.7)%.

2.4.3 *Gel permeation chromatography*

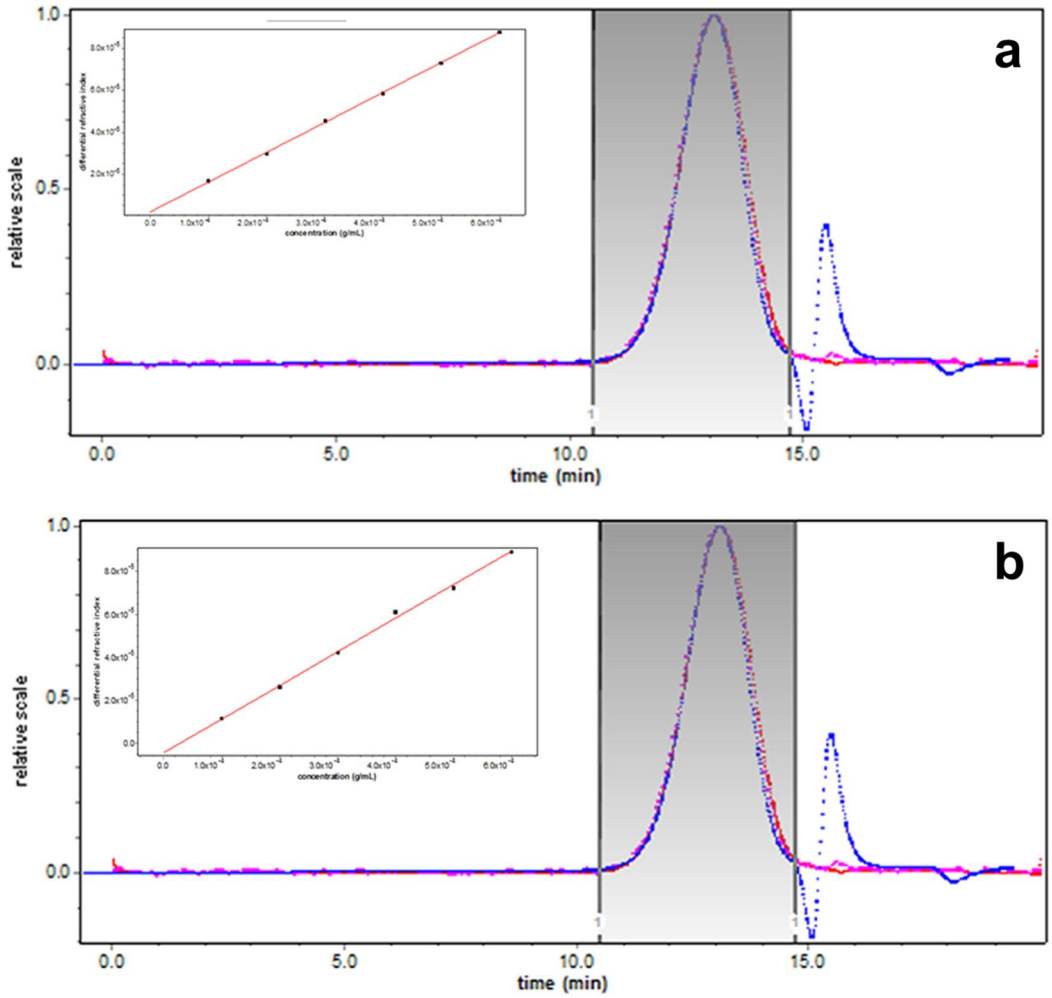

Figure 2.4.3.1. Gel permeation chromatography coupled to a multi angled laser light scatting detector was used to determine the molecular weights of the polymers; (a) GPC chromatogram of dGC; 7081 Da; M_w/M_n, 1.011 (2%). *(Inset),* the dn/dc; 0.1418 ±0.0016 mL/g; (b) GPC chromatogram of GCPQ; 10250 Da; M_w/M_n, 1.032 (3%). *(Inset),* the dn/dc; 0.1561±0.0039 mL/g.

2.4.4 Formulation 1 using IONPs made via coprecipitation: iron oxide "blackberry" nanoparticles

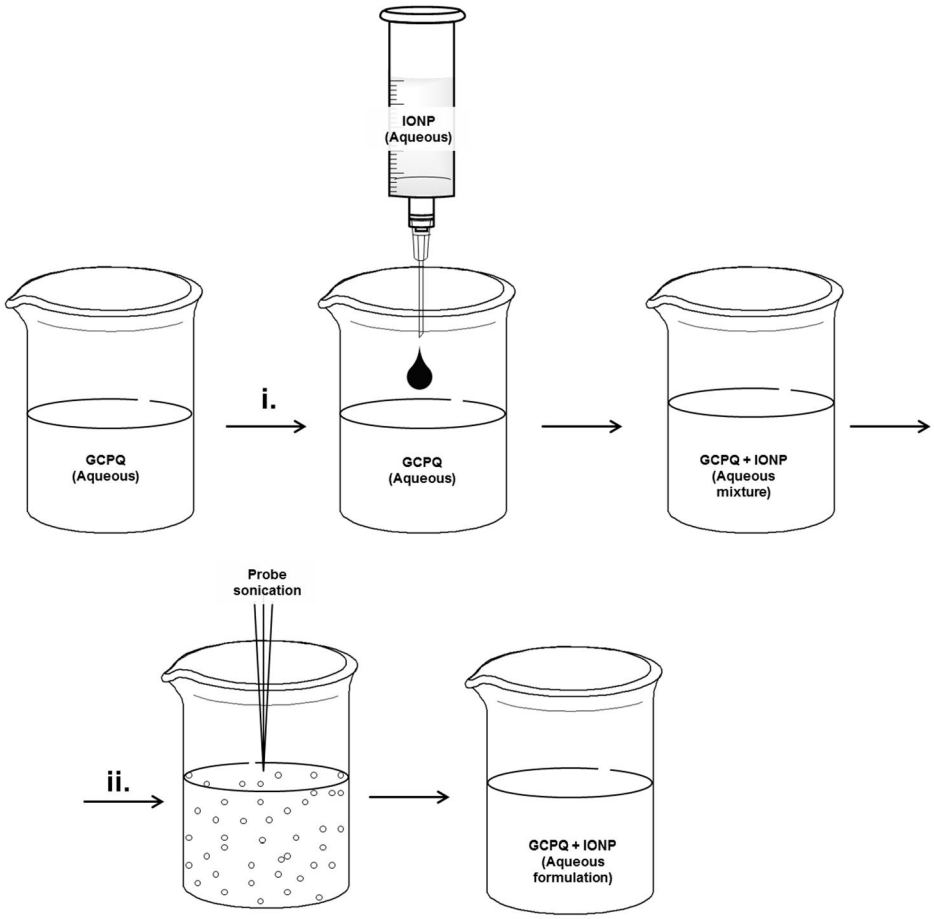

Scheme 2.4.4.1. The preparation procedure and work up for the polymer stabilised iron oxide "blackberry" nanoparticles. This formulation was made using the naked IONPs formed from chemical co-precipitation reaction: i, addition of naked IONPs; ii, probe sonication.

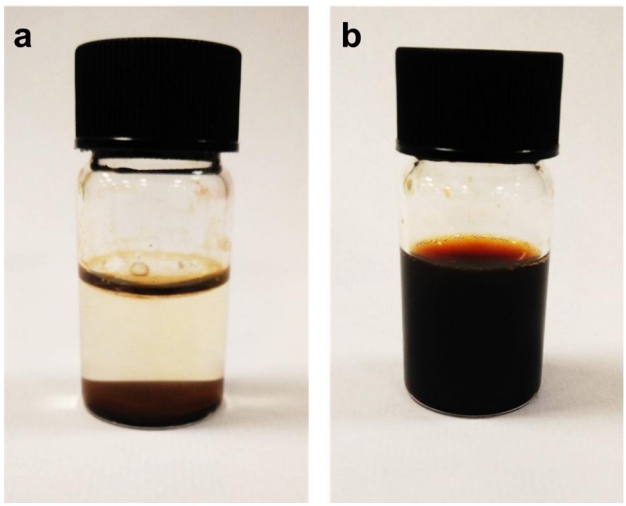

Figure 2.4.4.2. Blackberry nanoparticles macro images: (a) an image of the formulation before processing and (b) the IONP formulation after probe sonication with the amphiphilic polymer. Before processing the naked IONPs form a sediment on the bottom of the vial however after processing, the IONPs appear to have an improved colloidal stability.

2.4.5 Formulation 2 using IONPs made via high temperature thermal decomposition: iron oxide "raspberry" nanoparticles

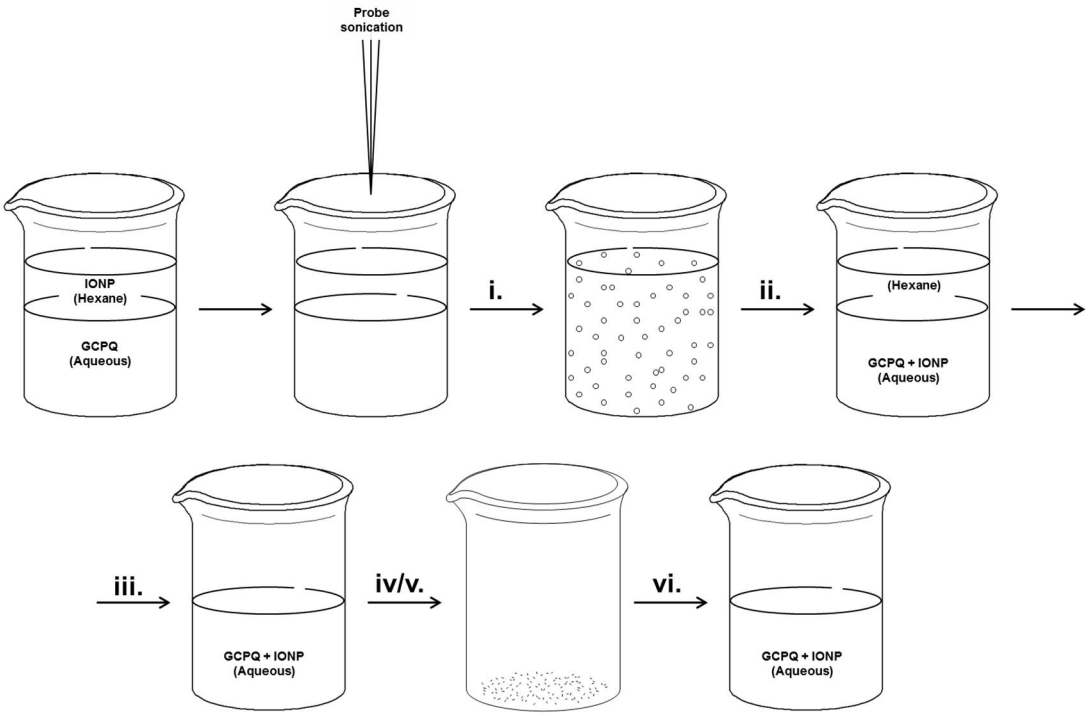

Scheme 2.4.5.1. The preparation procedure and work up for the polymer modified iron oxide "raspberry" nanoparticles. This formulation was made using the IONPs formed from the high temperature thermal decomposition method: **i**, emulsification via probe sonication; **ii**, separation; **iii**, extraction; **iv**, evaporation; **v**, lyophilisation; **vi**, reconstitution in aqueous medium.

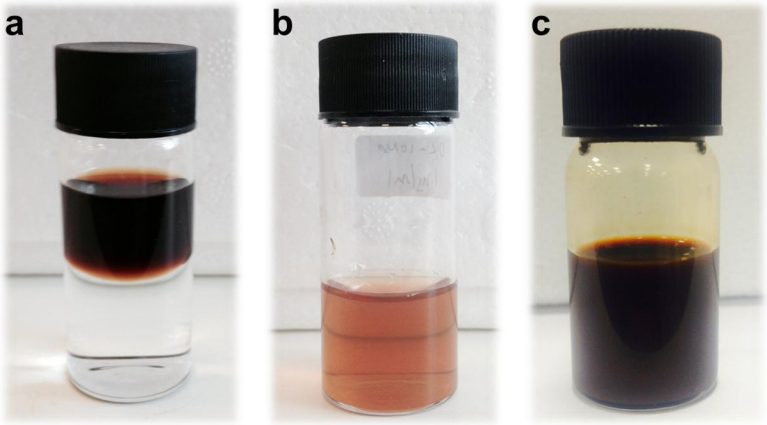

Figure 2.4.5.2. Raspberry nanoparticles macro images: (a) an image of the formulation before processing. The hydrophobic IONPs sit the upper organic layer (hexane), the polymer micelles sit in the lower aqueous layer (water); (b) an image of the iron oxide raspberry nanoparticle formulation at a concentration of 0.45 mg Fe/mL; (c) an image of the iron oxide raspberry nanoparticle formulation at a concentration of 6.5 mg Fe/mL.

2.4.6 Transmission electron microscopy

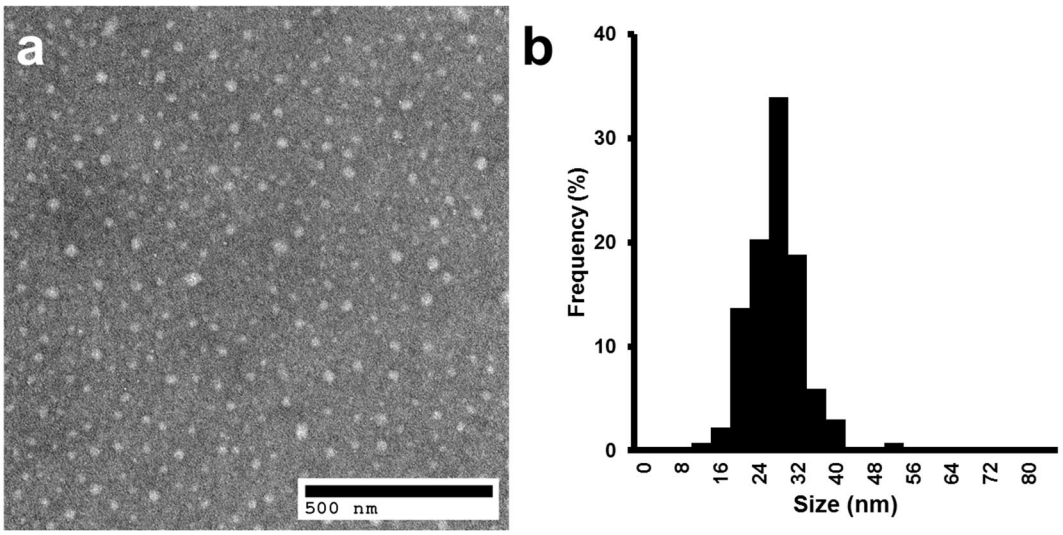

Figure 2.4.6.1. (a) TEM image of the amphiphilic polymer (GCPQ) with a 1% uranyl acetate stain. The amphiphilic nature of GCPQ allows the polymer to self-assemble into nano-sized micelles; (b) size distribution of the polymer nanoparticles with an average size of (29.6 ± 5.7) nm. Data are means ± s.d., n >250.

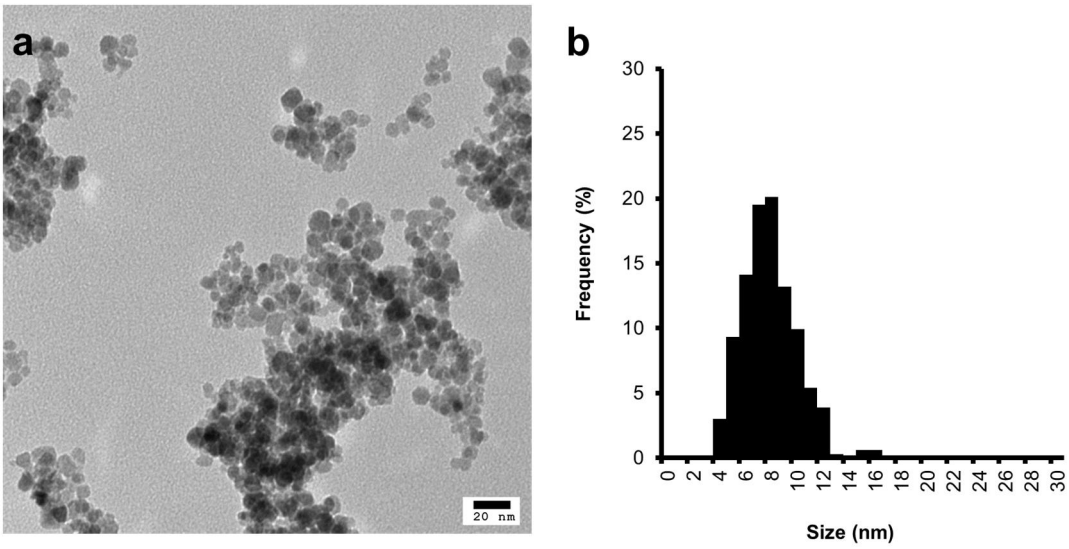

Figure 2.4.6.2. (a) TEM image of the naked IONPs made via chemical co-precipitation. The high surface energy causes the nanoparticles to cluster into large aggregates; (b) size distribution of the naked IONPs with an average size of (8.4 ± 2.1) nm. Data are means ± s.d., n >300.

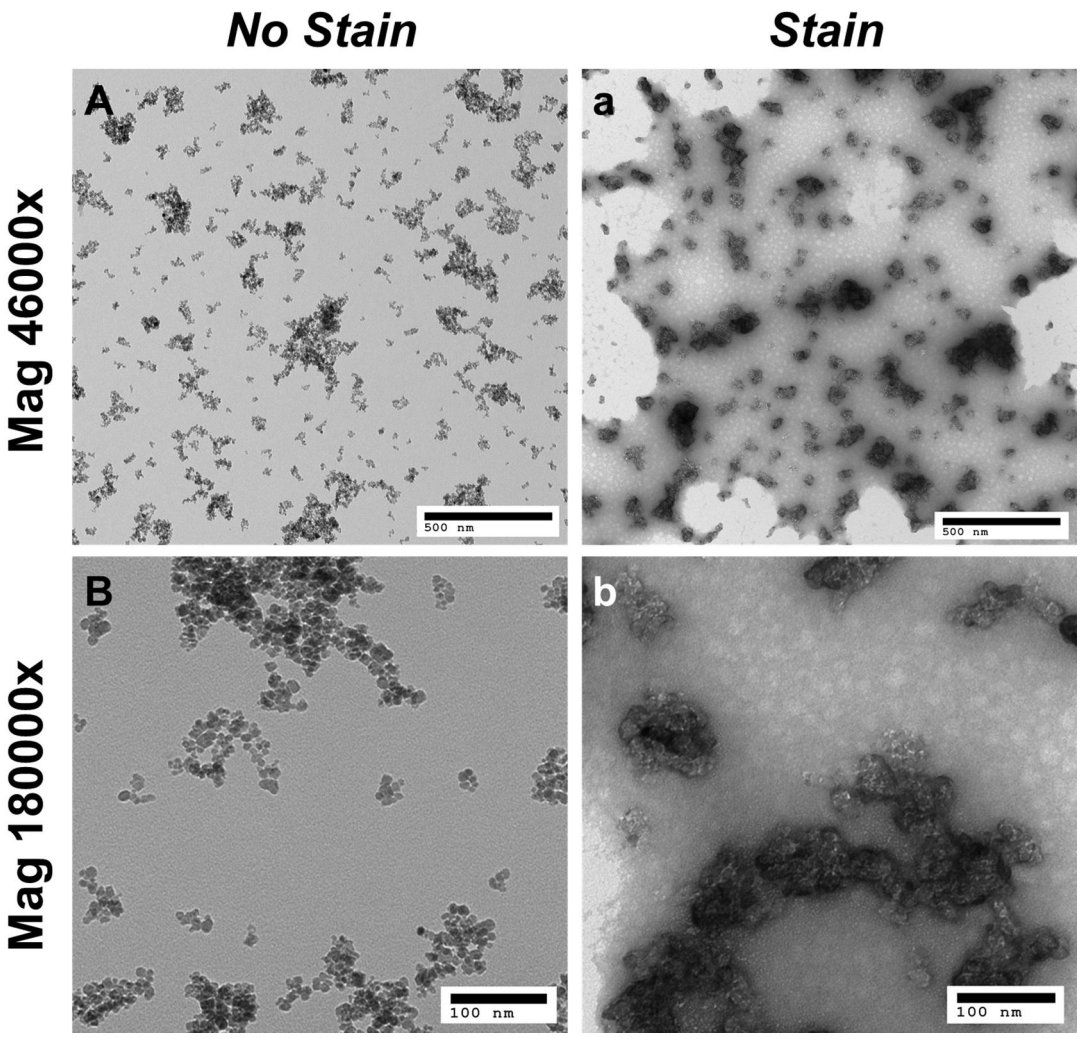

Figure 2.4.6.3. (A) TEM image of formulation 1 made using co-precipitation IONPs and stabilised using the amphiphilic chitosan based polymer (GCPQ). Nano sized "clusters" of IONPs with varying morphology are observed; (a) with a 1% uranyl acetate stain; (B) TEM images of the cluster nanoparticles at 180000x magnification without a stain and (b) with a 1% uranyl acetate stain. These structures will be referred to as 'blackberry nanoparticles'.

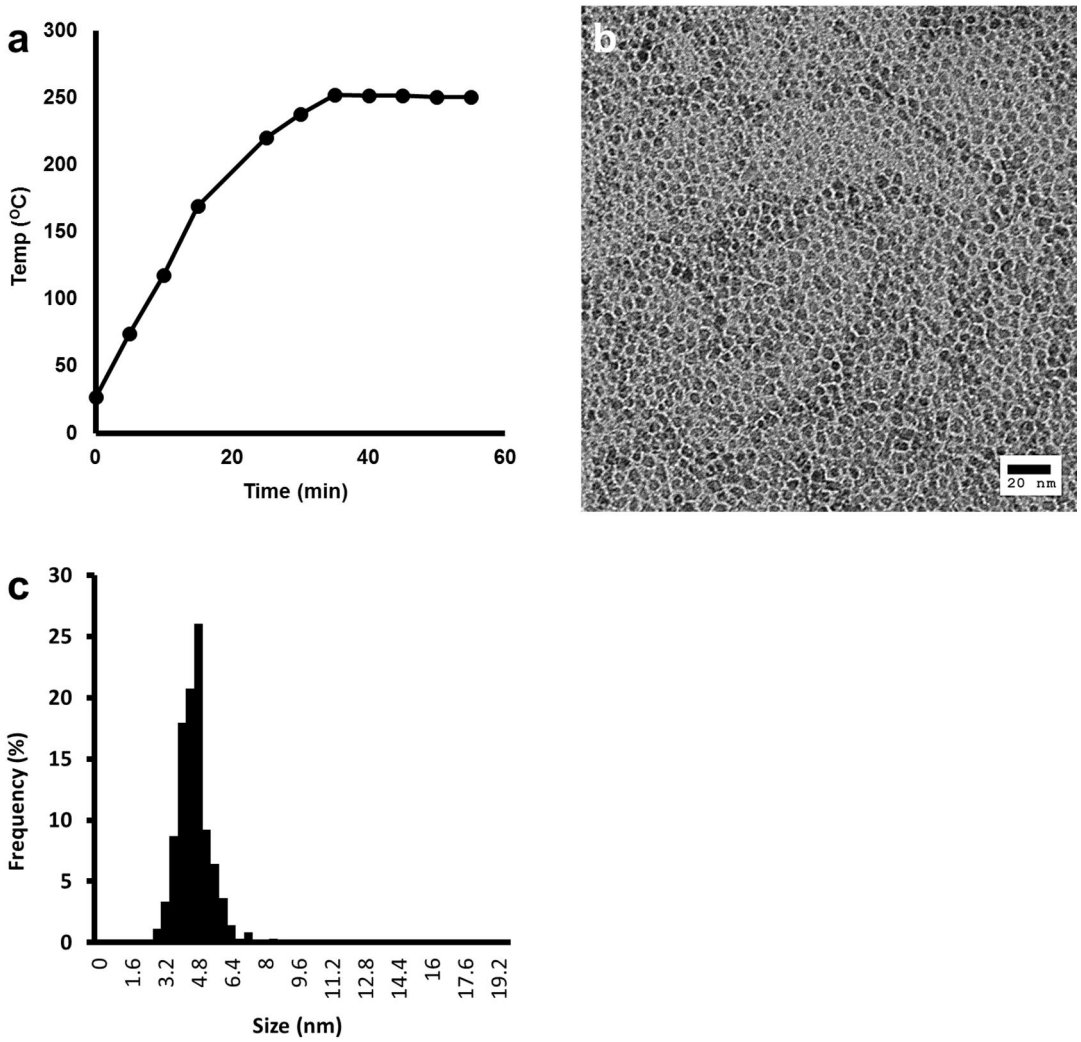

Figure 2.4.6.4. (a) Heating profile for a typical IONP reaction. These reactions are heated at 10 ^{O}C/min and then maintained at 250 ^{O}C for 20 mins. Size and morphology of the iron oxide crystals have a relationship to the rate of heating and reaction temperature they are grown in; (b) TEM image of the resulting hydrophobic IONPs; (c) size distribution of IONPs with an average size of (4.8 ± 0.8) nm. Data are means ± s.d., n >300.

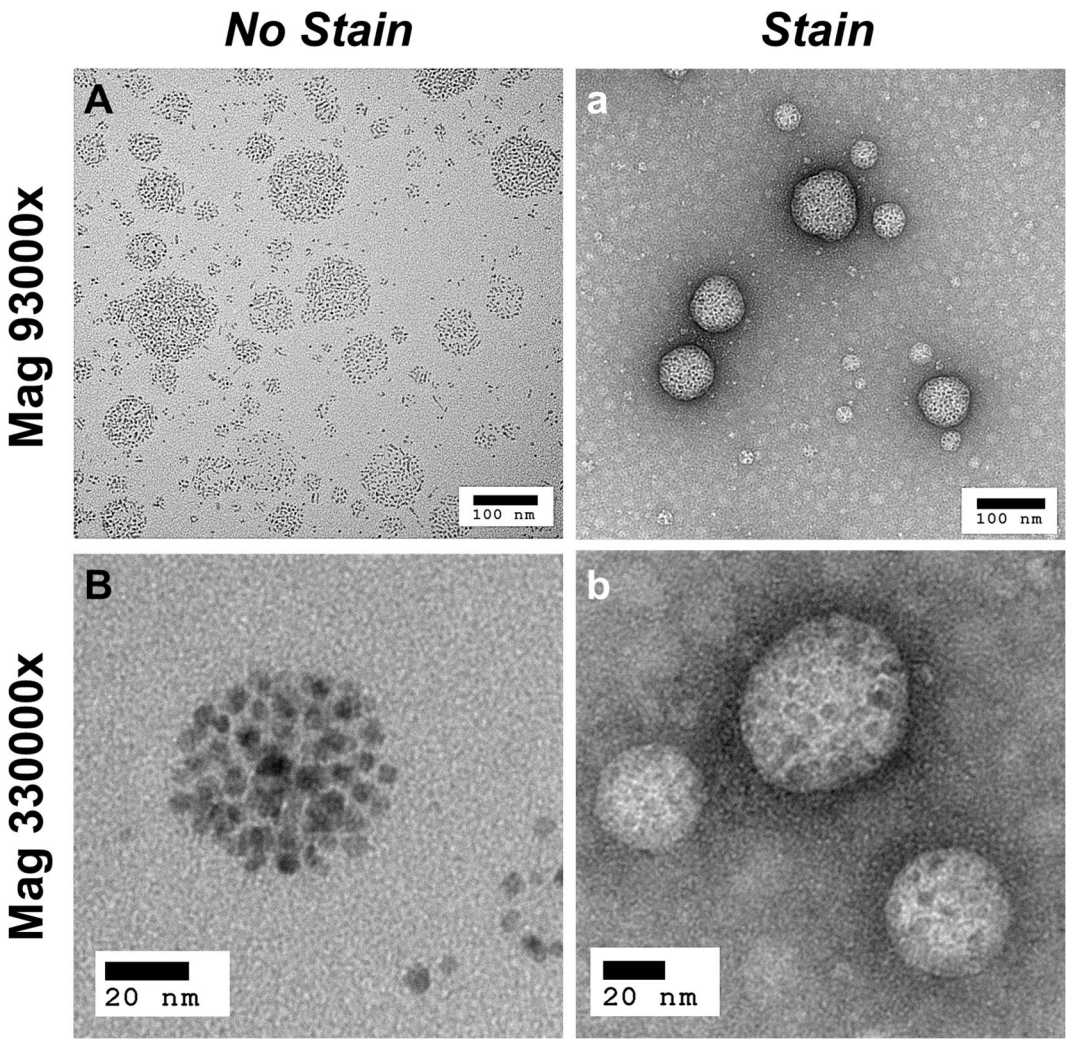

Figure 2.4.6.5. (A) TEM image of formulation 2 made using high temperature thermal decomposition IONPs and encapsulated within a GCPQ polymeric micelle, forming “raspberry” like nanostructures without stain and; (a) with a 1% uranyl acetate stain; (B) TEM images of the nanoparticles at 330000x magnification without a stain and (b) with a 1% uranyl acetate stain. These structures will be referred to as ‘raspberry nanoparticles’.

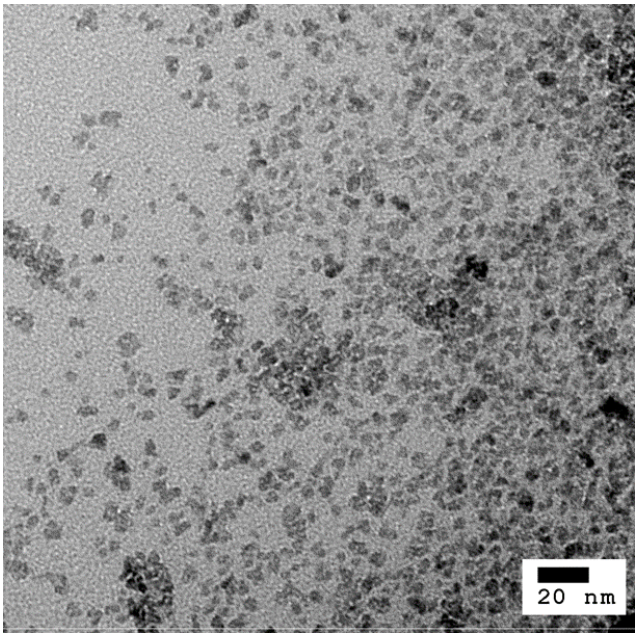

Figure 2.4.6.6. TEM image of the commercially available IONP negative MRI contrast agent Ferucarbotran® (Resovist®). IONPs are stabilised using a carboxymethyl dextran polymer. IONPs (average c.a. 5 nm) are polydisperse in size and morphology.

2.4.7 *Dynamic light scattering*

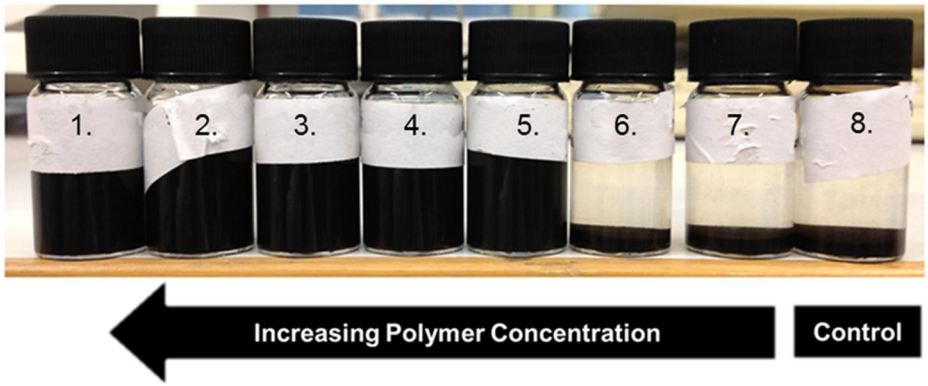

Sample No.	*IONP:polymer ratio*
1	1:2
2	1:0.4
3	1:0.2
4	1:0.04
5	1:0.02
6	1:0.004
7	1:0.002
8	No polymer

Figure 2.4.7.1. Macro image of the blackberry nanoparticle formulation and stability study. Various concentrations of polymer were used to stabilise 10 mg of Naked IONPs. At low polymer concentrations IONP sedimentation was observed, however at higher polymer concentrations colloidal stabilisation did appear to improve.

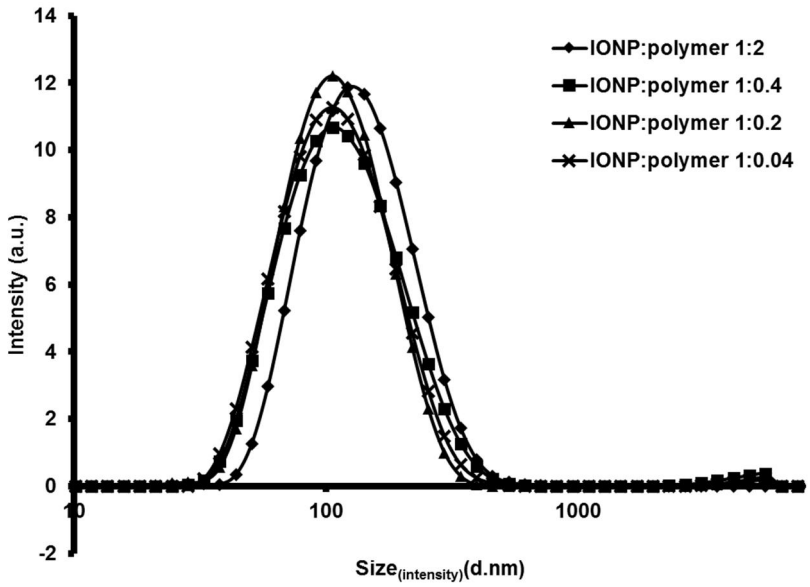

Figure 2.4.7.2. Dynamic light scattering was used to determine the average size of the nanoparticles in the formulation. Measurements of blackberry nanoparticle formulations containing different weight ratios of naked IONP:polymer; 1:2, 1:0.4, 1:0.2 and 1:0.04. IONP:polymer formulations have sizes (and polydispersity indexes) of 148 nm (0.19), 183 nm (0.22), 141 nm (0.19) and 152 nm (0.22), respectively. Formulations with less polymer than 1:0.04 (IONP:polymer) did not stabilise IONPs and gave erroneous results with high polydispersity indexes. The size results between formulations are not statistically significant suggesting that the ratio of IONP:polymer has no effect on the size of the blackberry nanoparticles formed. Data are means ± s.d., n=3, (p <0.05, 1-way ANOVA).

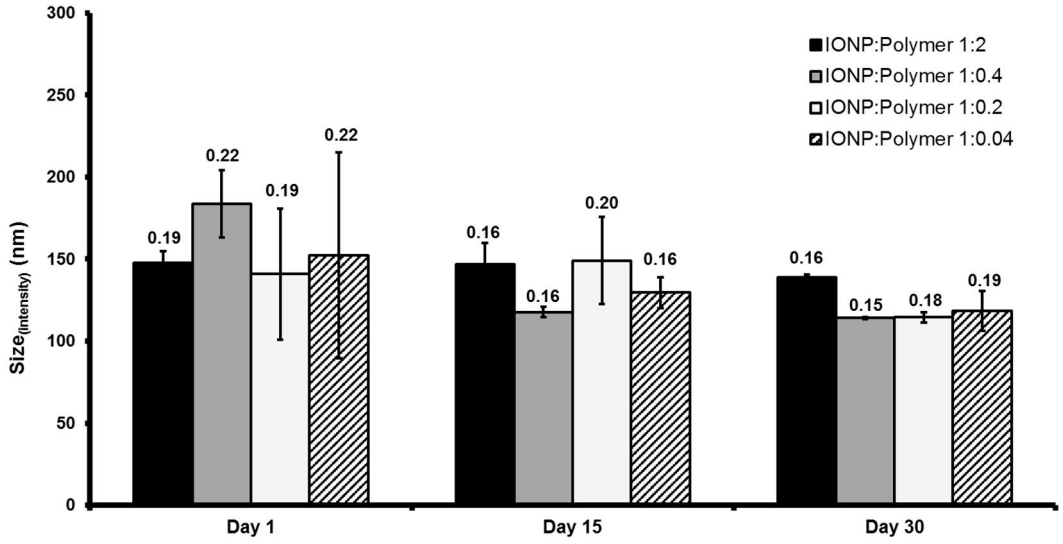

Figure 2.4.7.3. Blackberry nanoparticle stability was investigated by dynamic light scattering in water over 30-days at 5 ^{O}C. Polydispersity values given in labels above each column. No significant difference to the formulation on day 1 was observed in any of the formulations studied over the time period, suggesting good blackberry nanoparticle stability in aqueous conditions. Data are means ± s.d., n=3, (p <0.05, 1-way ANOVA, Games-Howell post hoc test).

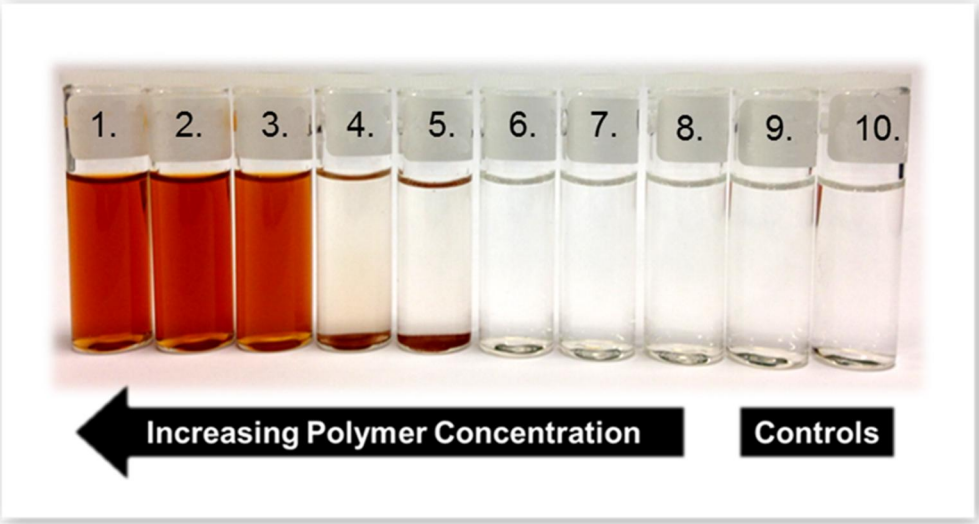

Sample No.	*IONP:polymer ratio*
1	1:2.5
2	1:0.5
3	1:0.25
4	1:0.005
5	1:0.0025
6	1:0.0005
7	1:0.00025
8	1:0.0000.5
9	IONP control
10	Polymer control

Figure 2.4.7.4. Macro image of the raspberry nanoparticle formulations and stability study. Various concentrations of polymer were used to stabilise 8 mg of hydrophobic IONPs. At low polymer concentrations no IONP stabilisation was observed, however at higher polymer concentrations colloidal stabilisation did appear improved.

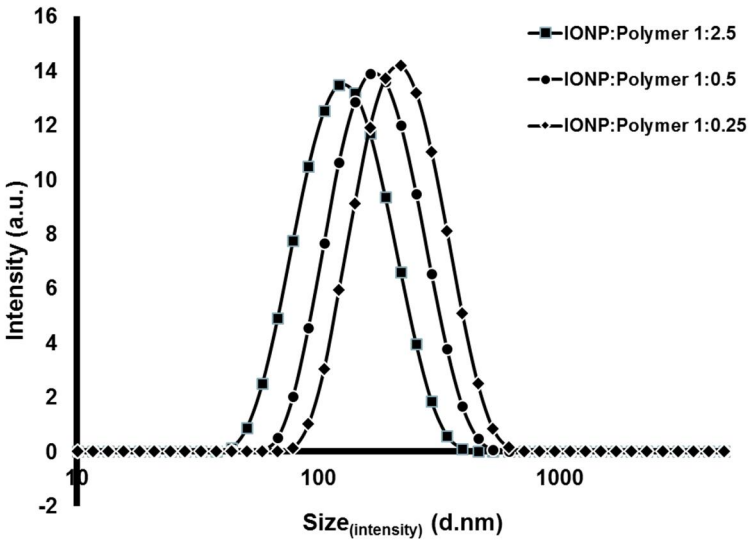

Figure 2.4.7.5. DLS measurements of the raspberry nanoparticle formulations containing different weight ratios of IONP:polymer; 1:2.5, 1:0.5 and 1:0.25. IONP:polymer formulations have sizes (and polydispersity indexes) of 120 nm (0.15), 190 nm (0.14) and 230 nm (0.14), respectively. Formulations with less polymer than 1:0.25 (IONP:polymer) did not encapsulate IONPs. There was a statistical difference between each formulation suggesting that raspberry nanoparticle size can be controlled by manipulation of IONP:polymer ratio. Data are means ± s.d., n=3, (p <0.05, 1-way ANOVA, Tukey post hoc test).

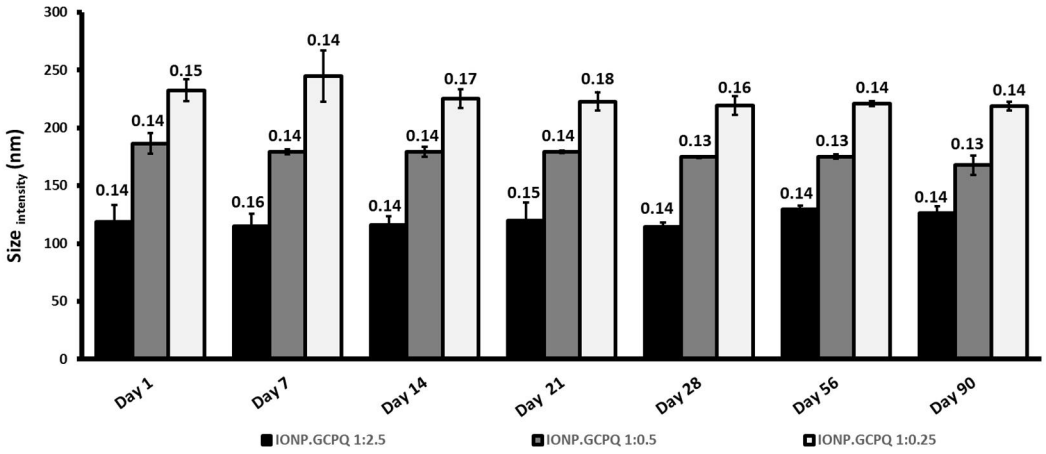

Figure 2.4.7.6. Raspberry nanoparticle stability was investigated by dynamic light scattering in water over 90-days at 5 ^{O}C. Polydispersity values given in labels above each column. No significant difference to the formulation on day 1 was observed in any of the formulations studied over the time period, suggesting good raspberry nanoparticle stability in aqueous conditions. Data are means ± s.d., n=3, (p <0.05, 1-way ANOVA, Games-Howell post hoc test).

2.4.8 Zeta surface charge and size - pH titrations

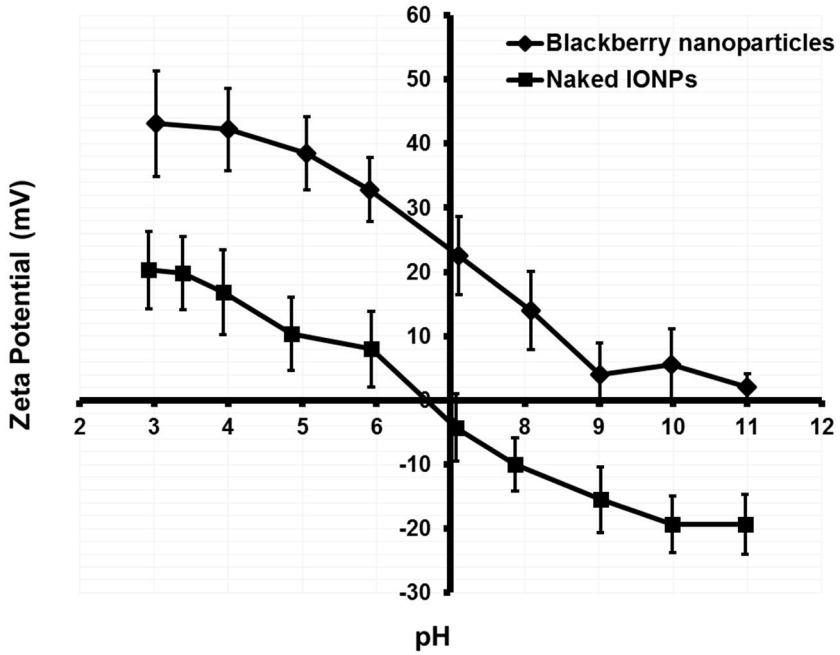

Figure 2.4.8.1. Blackberry nanoparticle manual zeta potential pH titration. These experiments are conducted to measure the surface charge of a nanoparticle in acidic and alkaline environments: Blackberry nanoparticles are shown to be positively charged in nature and have a surface zeta potential of (+22.5 ±6.1) mV in neutral conditions (pH 7.1). The surface characteristics of the naked IONPs are highly dependent on the pH of its environment and therefore display effectively no charge in neutral conditions; (-4.3 ±5.2) mV at pH 7.1. Data are means ± s.d., n=3.

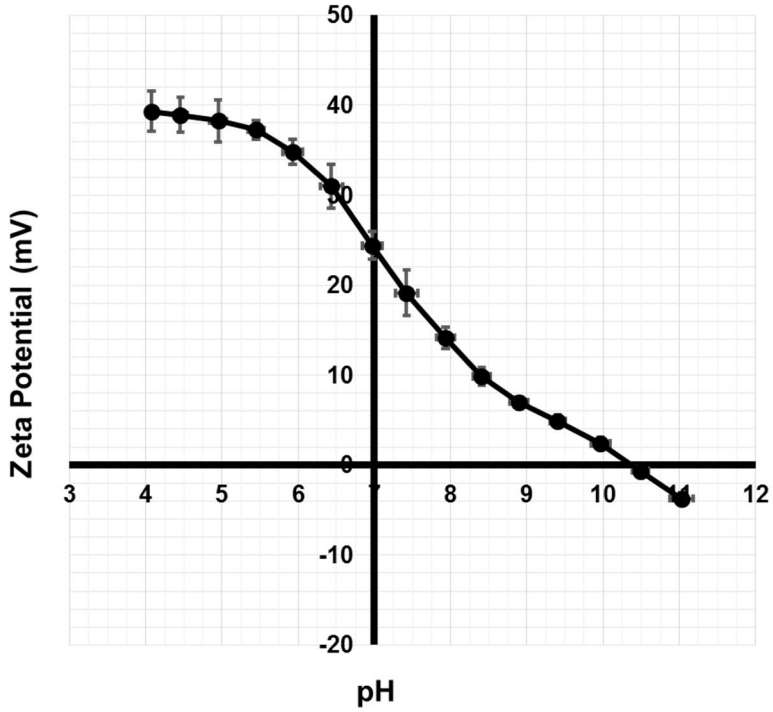

Figure 2.4.8.2. Raspberry nanoparticle automatic zeta potential pH titration. Raspberry nanoparticles are positively charged having a (+24.4 ±1.5) mV in neutral conditions (pH 7.0). Data are means ± s.d., n=3.

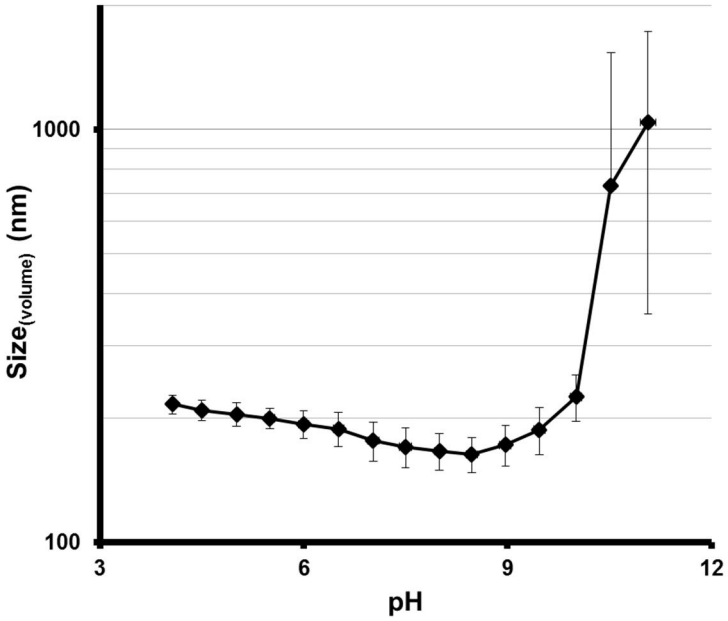

pH	*Size* ± S.D.	*Polydispersity index (PdI)*
4.1	216.0 ± 11.4	0.10
4.5	208.9 ± 11.8	0.10
5.0	204.3 ± 13.6	0.10
5.5	199.8 ± 11.4	0.09
6.0	193.2 ± 14.9	0.10
6.5	188.4 ± 17.6	0.11
7.0	176.4 ± 19.1	0.10
7.5	170.4 ± 19.1	0.11
8.0	166.4 ± 17.0	0.11
8.5	163.5 ± 16.1	0.12
9.0	172.2 ± 19.4	0.11
9.5	187.4 ± 24.2	0.11
10.0	224.9 ± 28.9	0.15
10.5	730.1 ± 804.9	0.20
11.1	1040.7 ± 683.0	0.22

Figure 2.4.8.3. Raspberry nanoparticle automatic dynamic light scattering pH titration. Conducted to study the effect of pH on raspberry nanoparticle size. In strongly basic conditions (pH >9) large aggregation is observed, indicated by an increase in particle size and PdI. These results suggest the raspberry nanoparticles are not stable in strongly basic conditions. Data are means ± s.d., n=3.

2.4.9 *X-ray diffraction*

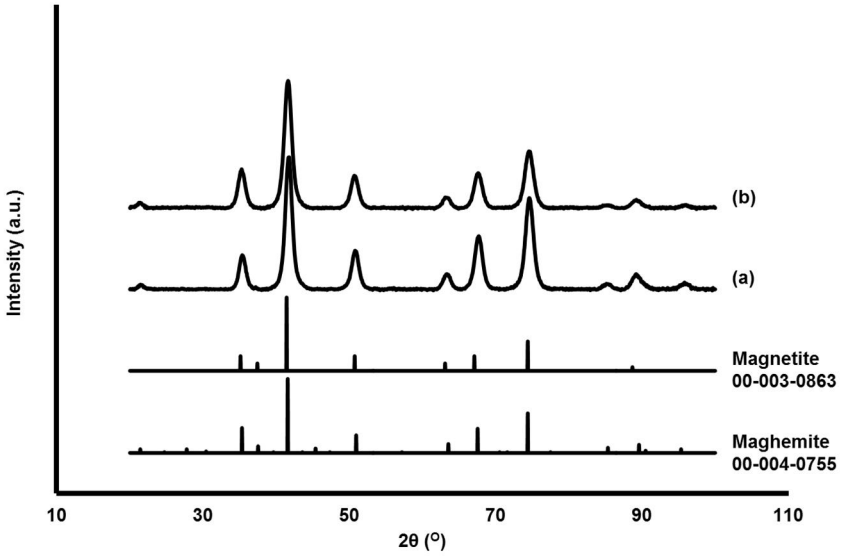

(a) Blackberry nanoparticles	2θ (°)	Relative intensity (A.U.)	d-spacing (Å)	Miller indices (h k l)	Identification material
1	21.5	3.5	4.79	1 1 1	Fe_3O_4/Fe_2O_3
2	35.4	27.1	2.95	2 2 0	Fe_3O_4/Fe_2O_3
3	41.7	100.0	2.51	3 1 1	Fe_3O_4/Fe_2O_3
4	50.8	29.7	2.08	4 0 0	Fe_3O_4/Fe_2O_3
5	63.2	4.3	1.70	4 2 2	Fe_3O_4/Fe_2O_3
6	67.7	15.3	1.61	5 1 1	Fe_3O_4/Fe_2O_3
7	74.6	26.7	1.48	4 4 0	Fe_3O_4/Fe_2O_3
8	84.9	4.2	1.32	6 2 0	Fe_3O_4/Fe_2O_3
9	89.1	3.9	1.28	6 2 2	Fe_3O_4/Fe_2O_3
10	95.7	1.6	1.20	4 4 4	Fe_3O_4/Fe_2O_3

(b) Naked IONPs	2θ (°)	Relative intensity (A.U.)	d-spacing (Å)	Miller indices (h k l)	Identification material
1	21.4	3.8	4.82	1 1 1	Fe_3O_4/Fe_2O_3
2	35.2	30.1	2.96	2 2 0	Fe_3O_4/Fe_2O_3
3	41.6	100.0	2.52	3 1 1	Fe_3O_4/Fe_2O_3
4	50.7	25.6	2.09	4 0 0	Fe_3O_4/Fe_2O_3
5	63.0	7.1	1.71	4 2 2	Fe_3O_4/Fe_2O_3
6	67.5	27.3	1.61	5 1 1	Fe_3O_4/Fe_2O_3
7	74.6	44.4	1.48	4 4 0	Fe_3O_4/Fe_2O_3
8	85.3	2.1	1.32	6 2 0	Fe_3O_4/Fe_2O_3
9	89.1	6.0	1.28	6 2 2	Fe_3O_4/Fe_2O_3
10	96.1	1.9	1.2	4 4 4	Fe_3O_4/Fe_2O_3

Figure 2.4.9.1. X-ray diffraction patterns of (a) the blackberry nanoparticles and (b) the naked IONPs (8 nm). Both patterns indicate the presence of magnetic iron oxide.

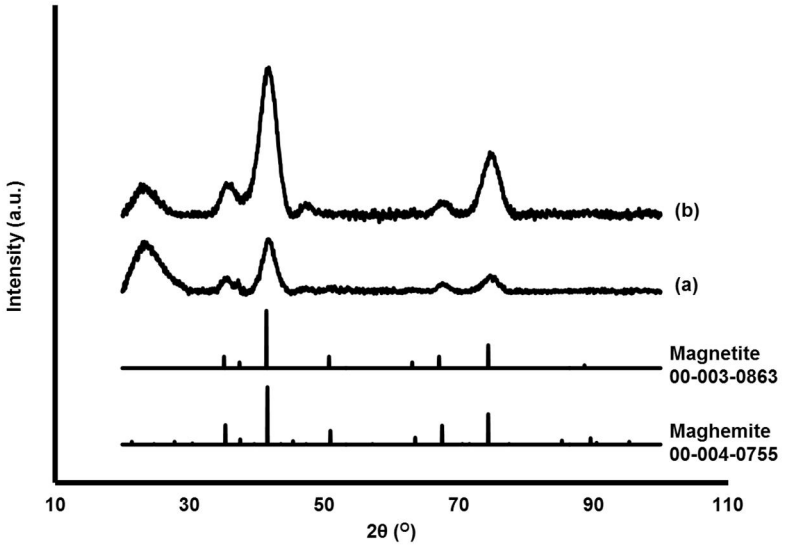

(a) Raspberry nanoparticles	2θ (°)	Relative intensity (A.U.)	d-spacing (Å)	Miller indices (h k l)	Identification material
1	22.93	73.34730833	4.5	1 1 1	Polymer
2	35.58	24.12647006	2.93	2 2 0	Fe_3O_4/Fe_2O_3
3	41.71	100	2.51	3 1 1	Fe_3O_4/Fe_2O_3
4	67.15	11.99853595	1.62	5 1 1	Fe_3O_4/Fe_2O_3
5	74.64	29.14416063	1.48	4 4 0	Fe_3O_4/Fe_2O_3

(b) Hydrophobic nanoparticles	2θ (°)	Relative intensity (A.U.)	d-spacing (Å)	Miller indices (h k l)	Identification material
1	22.5	13.4	4.59	1 1 1	Fe_3O_4/Fe_2O_3
2	35.2	15.4	2.96	2 2 0	Fe_3O_4/Fe_2O_3
3	41.8	100.0	2.51	3 1 1	Fe_3O_4/Fe_2O_3
4	47.6	8.2	2.22	4 0 0	Fe_3O_4/Fe_2O_3
5	67.8	9.8	1.6	5 1 1	Fe_3O_4/Fe_2O_3
6	74.9	43.6	1.47	4 4 0	Fe_3O_4/Fe_2O_3

Figure 2.4.9.2. X-ray diffraction patterns of (a) the raspberry nanoparticles and (b) the hydrophobic IONPs (5 nm). Both patterns indicate the presence of magnetic iron oxide.

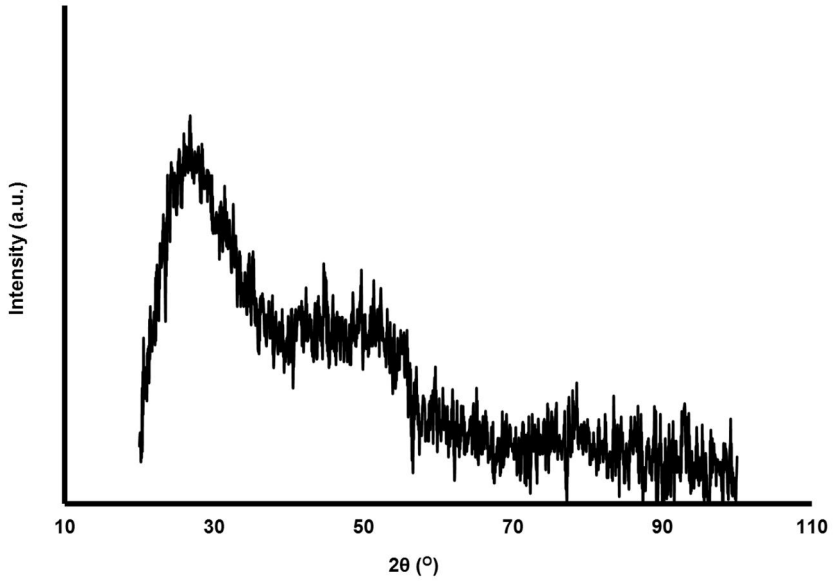

Figure 2.4.9.3. X-ray diffraction pattern of GCPQ alone. Broad and weak scattering observed between 20^{O}- 55^{O} (2θ) with the most intense scattering seen at a 26.9^{O}. This type of scattering is characteristic of an amorphous polymeric material.

2.4.10 Magnetic characterisation

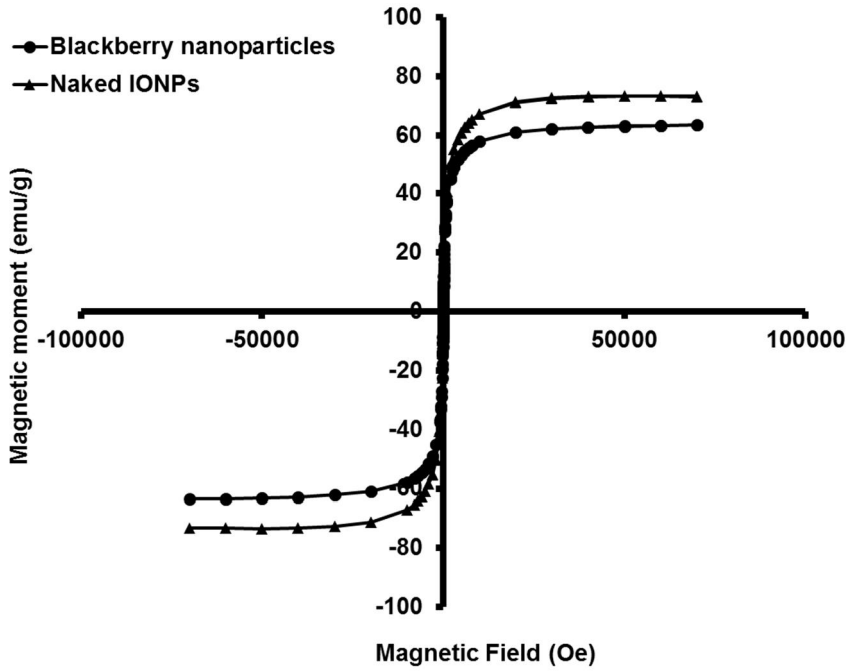

Figure 2.4.10.1. M vs H plot at 300 K comparing the blackberry nanoparticles and the naked IONPs (8 nm). The blackberry nanoparticles retain their superparamagnetic behaviour after formulation with the GCPQ polymer. The magnetic saturation of the naked IONP and the blackberry nanoparticles were found to be (73.3 ± 1.1) emu/g and (63.5 ± 1.3) emu/g, respectively showing that the blackberry nanoparticles are slightly less magnetic per gram of material. Data are means ± s.d., n=3, (p <0.05, Student's t-test).

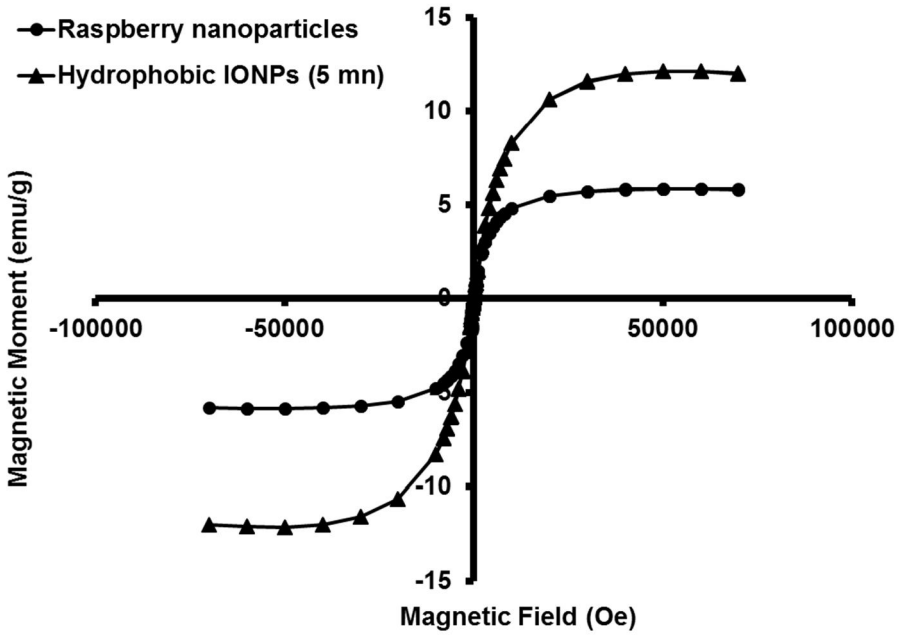

Figure 2.4.10.2. M vs H plot at 300 K comparing raspberry nanoparticles and the hydrophobic IONPs (5 nm). Raspberry nanoparticles retain their superparamagnetic behaviour after encapsulation within the polymeric GCPQ nanoparticle. The magnetic saturation of the hydrophobic IONP and raspberry nanoparticles were found to be (13.4 ± 1.9) emu/g and (5.5 ± 0.3) emu/g, respectively, showing that the raspberry nanoparticles are less magnetic per gram of material. Data are means ± s.d., n=3, (p <0.05, Student's t-test).

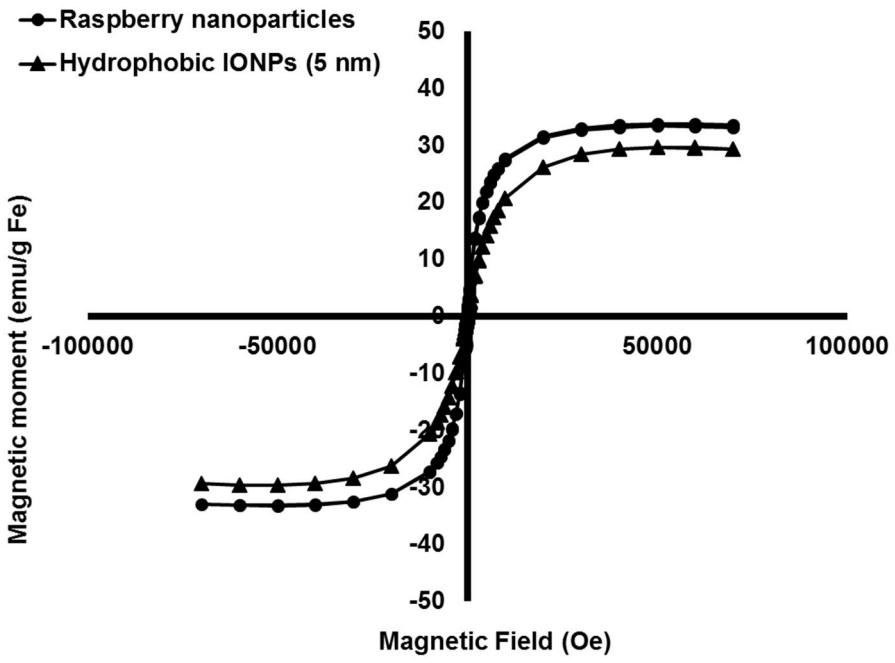

Figure 2.4.10.3. M vs H plot at 300 K comparing the magnetic iron content of the raspberry nanoparticles and the hydrophobic IONPs. Samples of hydrophobic IONPs and raspberry nanoparticles were measured for iron content and then plotted against their magnetisation profile. This yielded a magnetic saturation value of (29.6 ± 3.7) emu/g Fe and (33.8 ± 1.8) emu/g Fe for the hydrophobic IONPs and raspberry nanoparticles, respectively. There is no significant change in magnetisation between the two curves, showing that modification using the polymer has little to no effect on the IONPs magnetisation. Data are means ± s.d., n=3, (p <0.05, Student's t-test).

2.4.11 *Relaxometry*

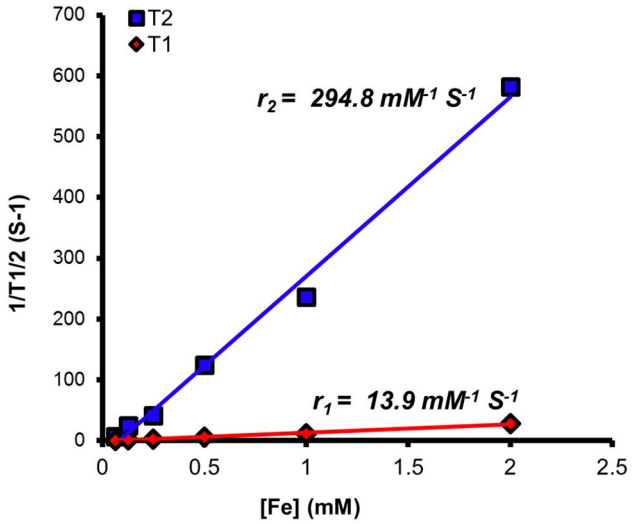

Figure 2.4.11.1 Relaxivity plot of the blackberry nanoparticles conducted on a Bruker Mq 60 Minispectrometer (Bruker, Germany). Plot of $1/T_1$ S^{-1} and $1/T_2$ S^{-1} against the concentration of a series of blackberry nanoparticles in [Fe]. The relaxivities (r_1 and r_2) can be determined from the slope of the plots.

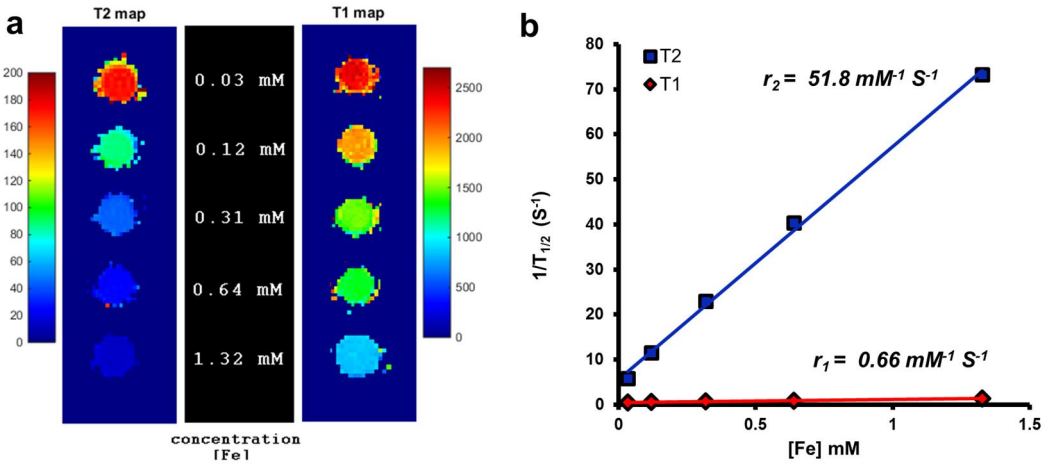

Figure 2.4.11.2. (a) Phantom T1 and T2 maps of raspberry nanoparticles conducted on a 1T benchtop MRI scanner (ICON^{TM}, Bruker, UK) and (b), Plot of $1/T_1$ S^{-1} and $1/T_2$ S^{-1} against the concentration of a series of raspberry nanoparticles in [Fe].

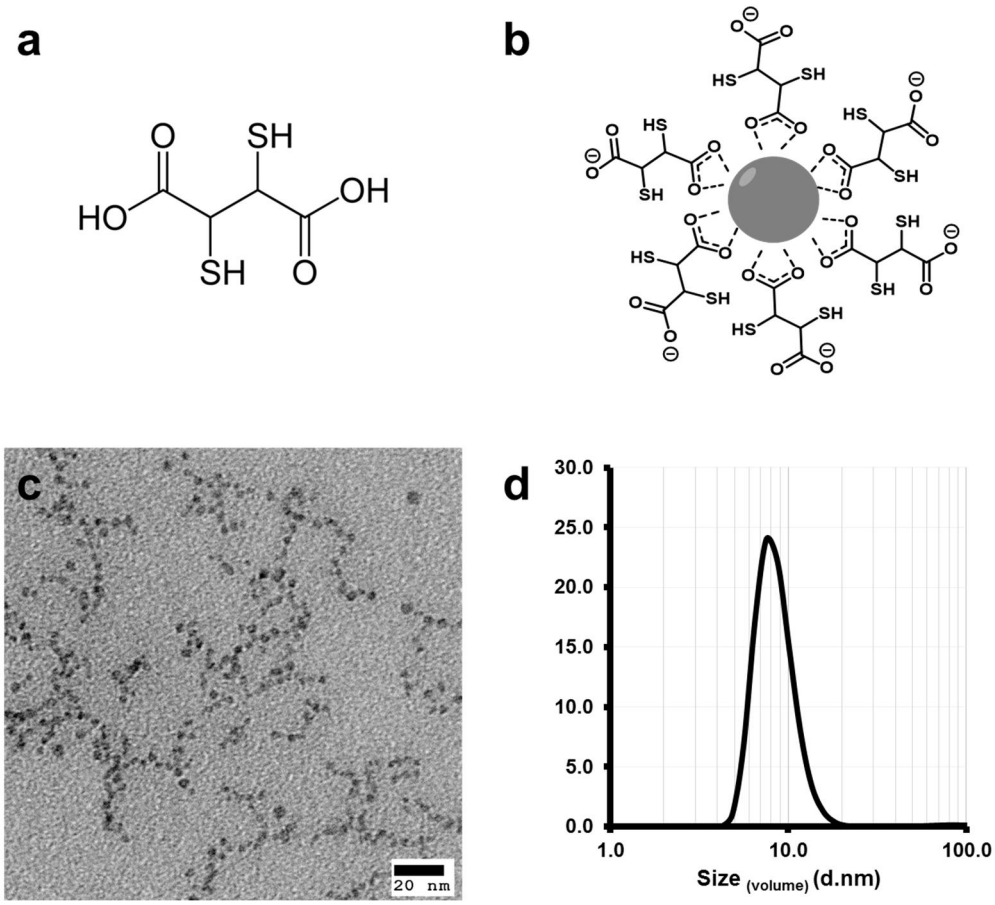

Figure 2.4.11.3 To investigate the effects of clustering on relaxivity a single crystal IONP was made using dimercaptosuccinic acid (DMSA): (a), molecular structure of DMSA; (b), schematic of the resulting DMSA.IONP produced via ligand exchange; (c), TEM of the DMSA.IONP; (d), DLS of the DMSA.IONP with an average hydrodynamic size by volume of 9 nm.

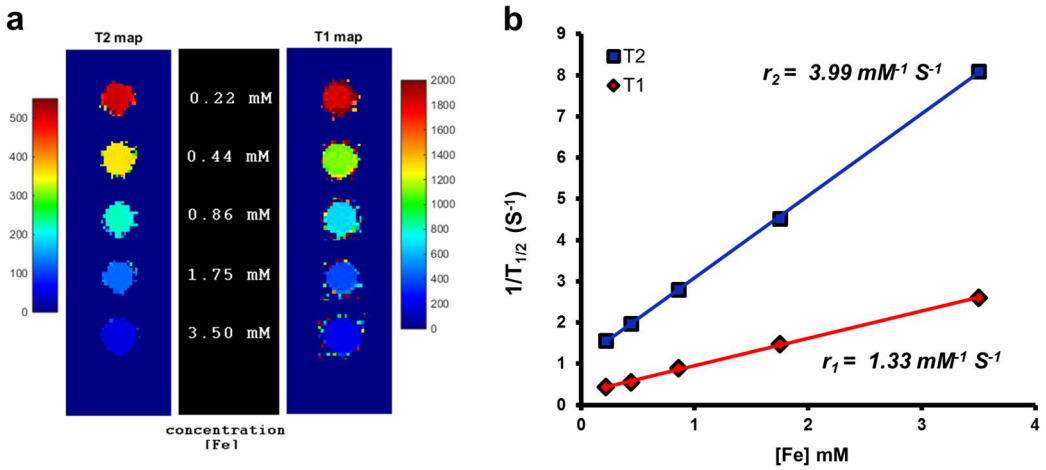

Figure 2.4.11.4 (a) Phantom T1 and T2 maps of DMSA.IONPs conducted on the 1T benchtop MRI scanner (ICON^{TM}, Bruker, UK)and (b), Plot of $1/T_1$ S^{-1} and $1/T_2$ S^{-1} against the concentration of a series of DMSA.IONP in [Fe].

2.5 Discussion

2.5.1 Synthesis of the modified chitosan amphiphilic polymer (GCPQ)

The synthesis of GCPQ began with a commercially available derivative of chitin named glycol chitosan (GC). The commercially available polymer is far too large (120,000 Da) to be of use, as using the final polymer at this size would often lead to gelation in the formulation, as a result its size had to be reduced. This is achieved via acid hydrolysis in the presence of 4M HCl to yield a polymer with an average mass of 7,000 Da measured by gel permeation chromatography coupled to a multi angled laser light scatting detector (GPC-MALLS) (Figure 2.4.2.1 and 2.4.3.1.a). The polymers amphiphilic nature was added by introducing a long chained hydrophobic alkyl chain to the amine position in the sugar backbone using palmitic acid N-hydroxysuccinimide (Figure 2.4.2.2). The palmitoylated GC was only sparingly soluble in aqueous environments and so a quaternary ammonium cation was introduced to increase it aqueous solubility in a process known as methylation using methyl iodide as the main reagent (Figure 2.4.2.3). The final polymer (GCPQ) was obtained as a white fibrous solid with a total synthetic yield of 30%. Only a number of the sugar units in the polymer backbone were functionalised and the degree of palmitoylation was estimated via ^{1}H NMR (Figure 2.4.2.3). This was done by comparing the integration values of the methyl peak (from the alkyl chain) found at δ 0.9 ppm and that of the sugar unit peak found at δ 3.5-4.5 ppm and placing them into Equation 2.5.1.1.

$$\%\ palmitoylation = \frac{Integration\ value\ of\ methyl\ protons/3}{Integration\ value\ of\ sugar\ protons/9} \times 100 \qquad (2.5.1.1)$$

The degree of quarternisation was again calculated using ^{1}H NMR (Figure 2.4.2.3). This was done by comparing the integration values of the trimethyl protons from the quaternary amine found at 3.4 ppm and that of the sugar unit peak and placing them into Equation 2.5.1.2.

$$\%\ quaternisation = \frac{Integration\ value\ of\ trimethyl\ protons/9}{Integration\ value\ of\ sugar\ protons/9} \times 100 \qquad (2.5.1.2)$$

From the ^{1}H NMR data the average degree of palmitoylation and the average degree of quarternisation between batches is summarised in Table 2.4.2.1. Palmitoylation gave an average functionalisation of (13.4 ± 2.9)%, while quarternisation gave an average functionalisation of (15.6 ± 4.7)%. Synthesising GCPQ polymers with highly reproducible functionalisation was difficult, to minimise variation large batches were produced. The average molecular weight of the final GCPQ polymer was often found to be approximately 10,000 Da as determined by GPC-MALLS (Figure 2.4.3.1.b). The amphiphilic nature of GCPQ allows the polymer to self-assemble into nano-sized micelles of around 32 nm in diameter which could be seen via electron microscopy (TEM), these nanoparticles were stable at low polymer concentrations without the need for further crosslinking (Figure 2.4.6.1.a and b).

2.5.2 Formulation and nanoparticle morphology

The naked IONPs were prepared via the chemical co-precipitation of $FeCl_3.6H_2O$ and $FeCl_2.4H_2O$ (Fe^{3+}:Fe^{2+}, 2:1) using 25% NH_4OH. To minimise oxidation of the resulting nanoparticles the reaction was carried out in oxygen free conditions by purging all aqueous reagents with $N_{2\ (g)}$ for several hours. After the addition of NH_4OH a black precipitate was immediately formed which could be isolated with a strong magnet and washed with de-oxygenated water until a neutral pH was obtained. Electron

microscopy (TEM) confirmed the presence of nanoparticles which where spherical in nature and had an average diameter of (8.4 ± 2.1) nm (Figure 2.4.6.2.a and b). TEM images also show that these IONPs formed irregular size and shaped agglomerates which can largely be attributed to the IONPs clustering together to minimise their high surface energies.[4] The prepared naked IONPs had a tendency to sediment in aqueous conditions making them unsuitable for biological applications. In order to stabilise the nanoparticles in aqueous conditions the naked IONP aggregates and the modified chitosan polymer (GCPQ) were formulated together with the aid of probe-sonication (Scheme 2.4.4.1). This method yielded a formulation which was observed to have improved colloidal properties compared to the naked IONPs alone (Figure 2.4.4.2.a and b). Electron microscopy revealed that the polymer modified formulation was composed of irregular size and shaped agglomerates and a 1% uranyl acetate stain provided evidence that these structures were coated by a hydrophilic layer as, by its nature, this stain likes to accumulate in regions of hydrophilicity (Figure 2.4.6.3). A reasonable hypothesis for the structures observed is that the energy provided by sonication was enough to fragment the large naked IONP agglomerates into much smaller clusters, their high surface energies could then be stabilised by the GCPQ polymer and in doing so reduce their tendency to re-aggregate. These structures will now be referred to as ‘blackberry nanoparticles’.

Uniform iron oxide nanocrystals were synthesised via high temperature thermal decomposition of an iron-oleate complex in the presence of oleic acid, oleyl alcohol and diphenyl ether in a method reported by *kim et al*.[13] Diphenyl ether turned out to be the most suitable high temperature solvent tested (b.p. 258 ^{O}C) as the nanoparticles were easily purified by washing with acetone. Octadecene was also investigated as a potential solvent, however purification of these nanoparticles from the solvent was troublesome. The reaction was heated at a rate of approximately 10

^{O}C/min and then kept at the desired temperature for 20 min (Figure 2.4.6.4.a). Electron microscopy (TEM) confirmed the presence of nanoparticles which had an average diameter of (4.8 ± 0.8) nm and were spherical in nature (Figure 2.4.6.4.b and c). Compared to the IONPs prepared by aqueous co-precipitation these were considerably more uniform and would easily disperse in organic solvents (hexane and chloroform). The prepared nanoparticles were coated in a layer of oleic acid making them extremely hydrophobic and not suitable for biological applications. In order to stabilise these nanoparticles in aqueous conditions the modified amphiphilic chitosan based polymer (GCPQ) was used. The hydrophobic oleic acid coated nanoparticles can be incorporated into the micelle core by a system of emulsification with the aid of ultra-sonication and then removal of the solvent (Scheme 2.4.5.1). Dry nanoparticles could then be reconstituted into aqueous based solvents at the desired concentration. This method yielded impressive 'raspberry' like nanostructures which can be seen via TEM. Interestingly, the hydrophobic nanoparticles seem to situate themselves inside the hydrophobic core of the polymer micelle which can be seen via electron microscopy (Figure 2.4.6.5). It is predicted that the driving force behind this structure formation is from the hydrophobic IONPs trying to avoid high energy interactions with the aqueous media.[15] These structures will now be referred to as 'raspberry nanoparticles'.

2.5.3 Nanoparticle size and aqueous stability

Several blackberry nanoparticle formulations, containing different weight ratios of IONP:polymer; 1:2, 1:0.4, 1:0.2 and 1:0.04 were formulated and monitored via dynamic light scattering (DLS) over a 30-day period in water.[16] Formulations made with less polymer than 1:0.04 (IONP:polymer) showed ineffective stabilisation from day 1 (Figure 2.4.7.1). DLS is a technique used to measure the size of nanoparticles in a collodial suspension. DLS is a light scattering technique that measures

fluctuations in scattered light from nanoparticles undgergoing bownian motion. The fluctuations are directly related to the movement of a nanoparticle through the solvent, which in turn, is related to the particles' hydrodynamic size. The various blackberry nanoparticle formulations have sizes (and polydispersity indexes) of 148 nm (0.19), 183 nm (0.22), 141 nm (0.19) and 152 nm (0.22), respectively. (Figure 2.4.7.2). A monodisperse sample will have polydispersity index (PdI) values around 0.05 whereas, a polydisperse sample has values close to 1.0 (values over 0.5 are usually considered polydisperse). The formulations remained colloidally stable and did not display any significant change in size over the time period (Figure 2.4.7.3). This data suggests that at least an IONP:polymer ratio of 1:0.04 is needed to create a colloidally stable formulation and that manipulating the IONP:polymer ratio has no significant effect on the overall size of the blackberry nanoparticles formed.

Several raspberry nanoparticle formulations, containing different weight ratios of IONP:polymer; 1:2.5, 1:0.5 and 1:0.25 were formulated and monitored via DLS over a 90-day period in water. Formulations made with less polymer showed ineffective stabilisation (Figure 2.4.7.4). A reasonable hypothesis for this observation is that polymer concentrations lower than the ones used for the IONP:polymer; 1:2.5 formulation are below the critical micelle concentration (CMC) of the polymer. One can see that the IONP:polymer formulations have sizes (and polydispersity indexes) of 120 nm (0.15), 190 nm (0.14) and 230 nm (0.14), respectively (Figure 2.4.7.5). This result remains relatively unchanged throughout the 90-day period indicating that the raspberry nanoparticles have good aqueous colloidal stability and that the size can be controlled by varying polymer concentrations (Figure 2.4.7.6). It is worth mentioning that nanoparticles did settle over prolonged periods of time, it is thought that this effect was probably caused by the large density of the raspberry nanoparticles however, these would easily re-disperse with gentle agitation with no

effect on the nanoparticle size. This effect was also observed by *Lin et al* with their chitosan-IONP.[17]

2.5.4 Nanoparticle pH titrations

The surface chemistry of a nanoparticle system is an important feature to understand as it is at this solid-liquid interface where the nanoparticle will interact with its environment. Surface charge is considered one of the most important features and many believe it plays an important role in colloidal stability and many biological mechanisms.[18,19] It is very difficult to measure the exact surface charge of a nanoparticle in solution, however it is possible to measure the electrostatic charge at the particle's *slipping plane*. The slipping plane is a term used to describe the point at which counter ions strongly adsorbed to the nanoparticles surface meet with loosely bound counter ions in the bulk phase.[20] The electrostatic charge at the point is called the *zeta potential* and it can be measured via electrophoretic light scattering. Nanoparticle surface charge usually has a direct correlation with environmental pH and so it is important to investigate the zeta potential in a range of acidic and basic conditions.[21] The zeta potential of the blackberry nanoparticle was monitored over a pH range in a manual titration experiment and then compared to the naked IONPs (Figure 2.4.8.1). Distinctive sigmoidal curves are observed for both nanoparticle systems where, the blackberry nanoparticles are shown to be positively charged and have a surface zeta potential of (+22.5 ±6.1) mV in neutral conditions (pH 7.1). The surface characteristics of the naked IONPs are highly dependent on the pH of its environment and therefore display effectively no charge in neutral conditions; (-4.3 ±5.2) mV at pH 7.1. The positively charged zeta potential of the blackberry nanoparticle can be attributed to the quaternary ammonium cationic functional group found on the polymer which has a pKa of 5.99 ±0.15.[22] This is a good indication that the polymer is bound to the surface of the IONPs. The zeta potential of the polymer

alone was difficult to measure and usually resulted in damage to the cell most likely due to its high ionic strength.

The zeta potential of the raspberry nanoparticle was measured whilst varying the pH in an automatic titration experiment (Figure 2.4.8.2). It was found, like many other nanoparticles of this nature, the zeta potential of the raspberry nanoparticles displayed a strong dependence with pH. Typically, the raspberry nanoparticles are positively charged having a positive zeta potential of (+24.4 ± 1.5) mV in neutral conditions (pH 7.1). Again, the positively charged nature of the nanoparticle can be attributed quaternary ammonium cationic functional group found on the polymer. Hydrophobic IONPs made via high temperature thermal decomposition could not be measured as they were not dispersible in aqueous media. From recent studies it has become clear that surface charge plays a key role in the adsorption of surface proteins, a process known as *opsonisation*, and it is often these surface bound agents that will dictate how a nanoparticle will behave in a biological environment.[23,24] An additional advantage is that positively charged nanoparticles appear to have enhanced penetration in tumour tissue than their neutral or negatively charged equivalents, this is most likely a result of the slight negative charge of the cell membrane.[25,26] A few examples include *Jiang et al* who have comprehensively investigating the effects of polystyrene nanoparticle surface charge on mesenchymal stem cells and have found that cationic nanoparticles (>100 nm) show much greater cellular internalization. Additionally, *Angeles et al* found that positively charged IONPs showed significantly better internalisation within human cervical carcinoma cell lines (HeLa) than their neutral or negatively charged counterparts.[27-29] Although positively charged nanoparticles may be preferred for their greater tissue penetration a number of studies have shown that positively charged nanoparticles could actually reduce

systemic blood circulation times and so may actually hinder the nanoparticle from getting to the diseased site.[30,31]

The size of the raspberry nanoparticles was also monitored with pH (Figure 2.4.8.3). It was found that the size of the raspberry nanoparticles displayed a slight reduction in size from acid to neutral pH however, once the nanoparticles were placed in a basic environment (pH >9) a large increase in particle size was observed, which is a strong indication of aggregation and instability.

2.5.5 X-ray diffraction

X-ray diffraction (XRD) is a technique used to measure the crystallinity of a material. Arrays of atoms are able to scatter x-rays primarily through their electronic configuration. Regular arrays of atoms produce regular arrays of scattering that result in a diffraction pattern. A typical XRD pattern from a crystalline material provides a unique “fingerprint” of the crystals present in the sample. When properly interpreted this fingerprint allows for identification of the crystalline material present. X-ray diffraction patterns were collected from the naked IONPs and the blackberry nanoparticles which confirm the presence of magnetic iron oxide (Figure 2.4.9.1). The addition of polymer to the formulation has little effect on the crystallinity of the IONPs. The average crystal size of the naked IONPs calculated by the Scherrer equation (Equation 2.5.5.1) was (8.8 ± 0.2) nm which is a very similar to the value obtained from TEM (8.4 ± 2.1) nm.

$$D_p = \frac{0.93\lambda}{\beta_{1/2} cos\theta} \qquad (2.5.5.1)$$

Where: Dp, average crystallite size; β, line broadening in radians; θ, bragg angle; λ, X-ray wavelength

X-ray diffraction (XRD) patterns from the raspberry nanoparticles and the hydrophobic IONPs (Figure 2.4.9.2) correspond to the patterns previously reported for super paramagnetic IONPs made via the high temperature thermal decomposition method.[8,32,33] One noticeable difference observed is that some of the peaks are weaker in intensity resulting in some of the smaller peaks being lost in the background, most likely indicating the XRD is measuring a less crystalline material caused by the increase in oleic acid and polymer content which is amorphous is nature. The average crystal size of the hydrophobic IONPs calculated by the Scherrer equation was (3.6 ± 0.1) nm. The small decrease in measured size compared to TEM (4.8 ± 0.8) nm and could be due to the *spin canting effect*. The spin canting effect is the term given to a small, non-crystalline layer of iron oxide often found at the surface of IONPs.[34]

2.5.6 Magnetic characterisation

A super quantum interference device (SQUID) is an instrument used to measure small variations in magnetic field flux. A SQUID device usually comprises of a superconducting loop separated by a number of non-superconducting junctions called *Josephson Junctions* or *weak links*. As the temperature of the device is cooled to below the material's *Curie Temperature* (T_c) all the material's magnetic flux is expelled. When a current is delivered through the device the measured voltage oscillates, this oscillation is extremely sensitive to the magnetic flux passing through the loop. Consequently, any material that has an effect on the loop's magnetic flux can be measured. A SQUID can be used to conduct a number of experiments but in this project it has been used to construct *M-H curves* or *hysteresis loops*. The magnetic behaviour of the newly created nanoparticles was investigated by collecting field dependant magnetization plots (M vs H plots). The magnetic characteristics of the nanoparticles is an important feature to understand as it is the magnetic

interaction with a proton relaxing back to the ground state that will fundamentally give contrast in an MRI procedure. Both the naked IONPs and the blackberry nanoparticles display superparamagnetic behaviour with no observable remnant magnetisation (Figure 2.4.10.1). This superparamagnetic behaviour means the nanoparticles will only become magnetised in the presence on an external magnetic field. The magnetic saturation of the naked IONP and the blackberry nanoparticles were found to be (73.3 ± 1.1) emu/g and (63.5 ± 1.3) emu/g, respectively. The small reduction in magnetisation is most likely due to the increase of the non-magnetic polymer within the sample which will contribute to the overall mass but not the magnetisation of the material.

Both the hydrophobic IONPs and the raspberry nanoparticles display superparamagnetic behaviour with no observable remnant magnetisation (Figure 2.4.10.2). The magnetic saturation of the hydrophobic IONPs was found to be (13.4 ± 1.9) emu/g. When comparing this result to the naked IONPs the hydrophobic IONPs have a much lower magnetic saturation which is most likely due to their smaller core size (5 nm compared to 8 nm for hydrophobic IONPs and naked IONPs, respectively) and the fact that the hydrophobic IONPs also contain a layer of non-magnetic oleic acid. The magnetic saturation of the raspberry IONPs were found to be (5.5 ± 0.3) emu/g. The reduction in magnetisation is most likely due to the increase in the non-magnetic polymer within the sample. To get a direct comparison between the magnetic component of the nanoparticle systems, the amount of iron in the samples was measured and plotted against the magnetisation which yielded a magnetic saturation value of (29.6 ± 3.7) emu/g Fe and (33.8 ± 1.8) emu/g Fe for the hydrophobic IONPs and raspberry nanoparticles, respectively (Figure 2.4.10.3). The polymer modified raspberry nanoparticles do exhibit a small increase in magnetic saturation, however this result was not statistically significant (p >0.05) suggesting that encapsulation within the polymer micelle has little to no effect on the magnetic

behaviour of the IONPs. Overall both nanoparticle systems display superparamagnetic characteristics. The larger magnetic saturation observed for the blackberry nanoparticles over the raspberry nanoparticles is likely to be a result of the increased crystallinity of the IONPs (as shown in the X-ray diffraction data). Both nanoparticle formulations are appropriately magnetic making them potentially suitably candidates for MRI contrast applications.

2.5.7 Relaxometry

A fundamental property of any MRI contrast agent will be its ability to alter the spin-lattice relaxation (r_1) and their spin-spin relaxation (r_2) of protons in their vicinity. To investigate the MRI contrast ability of the blackberry nanoparticles their r_1 and their r_2 was measured as a function of iron concentration using a contrast agent analyser (minispec mq 60, Bruker, Germany) at 1.5T at 37 ^{O}C (Figure 2.4.11.1). Overall, there was good correlation between concentration and relaxivity resulting in an r_1 value of 13.9 μM^{-1} S^{-1} and an r_2 value of 294.8 μM^{-1} S^{-1} hence, giving an r_2/r_1 of 21.1. Values of $r_2/r_1 < 10$ are generally considered to be positive contrast agents and $r_2/r_1 > 10$ are typically considered to be negative contrast agents.[35,36] This high r_2/r_1 value indicates that the blackberry nanoparticles are an effective negative contrast agent. When compared to commercially available negative contrast agents the blackberry nanoparticles have comparable relaxivity ratios and so could be considered to be just as effective for MRI contrast applications.

To investigate the MRI contrast ability of the raspberry nanoparticles their r_1 and their r_2 was measured as a function of iron concentration using a 1T bench top MRI scanner (ICON^{TM}, Bruker, UK) (Figure 2.4.11.2). Overall, there was good correlation between concentration and relaxivity resulting in an r_1 value of 0.66 μM^{-1} S^{-1} and an r_2 value of 51.8 μM^{-1} S^{-1} hence, giving an r_2/r_1 of 79.1. This high r_2/r_1 value indicates that an effective negative contrast agent has been created and is much larger than

any other commercially available negative contrast agent. As this was a unique result it was deemed necessary to investigate the effect of encapsulating the IONPs within a micelle further by measuring the IONPs in their single crystal form. This was achieved by coating the surface of the hydrophobic IONPs with dimercaptosuccinic acid (DMSA) via a ligand exchange procedure outlined by *Palma et al*.[14] The DMSA.IONPs were colloidally stable in aqueous conditions and gave an average hydrodynamic size of 9 nm by DLS (Figure 2.4.11.3). When measured in the MRI scanner they gave an r_1 value of 1.33 μM^{-1} S^{-1} and an r_2 value of 3.99 μM^{-1} S^{-1} therefore, giving an r_2/r_1 of 3.0 (Figure 2.4.11.4). This large reduction in the r_2/r_1 value suggests that the DMSA.IONPs are a much weaker negative contrast agent and possibly a more favourable positive contrast agent.[13,35] The data suggests that by encapsulating the IONPs within a micellar architecture one is able to reduce the spin-lattice relaxation and greatly improve the spin-spin relaxation. The reasoning behind these observations can be explained as follows; particles encapsulated within the polymeric micelle undergo the clustering effect, a well-documented phenomenon in which large clusters of packed IONPs are much more effective at generating magnetic field inhomogeneities and therefore, increase the spin-spin relaxation of the neighbouring water protons.[37-39] The IONP's ability to affect the spin-lattice relaxation is a less well understood mechanism although a compelling hypothesis is that encapsulation within the hydrophobic core of the micelle inhibits the water's dipolar interactions with the paramagnetic iron ions, a key interaction in the mechanism of spin-lattice relaxation, overall reducing its effect.[40,41] The data collected here shows that encapsulation within the polymeric micelle can greatly enhance the IONPs ability to act as a potent negative contrast agent.

2.6 Conclusions

In conclusion, the chitosan based amphiphilic polymer N-palmitoyl-N-monomethyl-N,N-dimethyl-N,N,N-trimethyl-6-O-glycolchitosan (GCPQ) has successfully been synthesized and characterised via NMR and GPC-MALLS. The amphiphilic nature of the polymer has caused it to form micelles of around 32 nm confirmed by TEM. Highly crystalline IONPs were successfully formed via chemical co-precipitation (c.a. 8 nm) and via high temperature thermal decomposition (c.a. 5 nm) which have given IONP products with very different properties. The naked IONPs made via chemical co precipitation were made colloidally stable in aqueous conditions by coating their surface with the GCPQ polymer, reducing their tendency to aggregate and sediment. These structures were dubbed 'blackberry' nanoparticles. The blackberry nanoparticles had an average size of 156 nm by DLS and were found to be positively charged in neutral conditions. XRD confirmed the presence of crystalline magnetic iron oxide and magnetometer experimentation found that the IONPs were still superparamagnetic even after modifying their surface with the polymer. Relaxometry found that the blackberry nanoparticles had a high r_2 value of 294.8 μM^{-1} S^{-1} and an r_2/r_1 of 21.1 giving it a comparable relaxivity profile to a number of known commercially available IONP based negative MRI contrast agents.

The hydrophobic IONPs were made colloidally stable in aqueous conditions by encapsulating them within a polymeric micelle (GCPQ) via a process of emulsification-evaporation that yielded highly ordered spherical nanostructures that were dubbed 'raspberry' nanoparticles. The size of the raspberry nanoparticle could be controlled by adjusting the ratio of IONP:polymer and had averages sizes between 120 – 230 nm by dynamic light scattering. The polymer modified raspberry nanoparticles were found to be positively charged and displayed instability in highly

basic conditions. XRD confirmed that the raspberry nanoparticles contained crystalline magnetic iron oxide and from magnetometer experimentation it was found that the IONPs retained their superparamagnetism even after encapsulation within the polymeric micelle. MR experimentation has shown that encapsulating IONPs within this polymeric nanoparticle greatly enhances the r_2 relaxivity and decreases the r_1 relaxivity compared to the single crystals alone overall, giving an effective negative contrast agent (r_2, 51.8 μM^{-1} S^{-1} and r_2/r_1, 79.1). The data presented in this chapter has shown that IONPs and GCPQ have been formulated into a stable polymeric nanoparticles using two distinctive strategies yielding very different nanoparticle structures. Both the blackberry nanoparticles and the raspberry nanoparticles have shown to be affective as a negative contrast agent for MR imaging applications. This said however, the only way to truly evaluate their suitability as an MRI contrast agent for biological applications will be through tougher *in vivo* investigations.

(1) Reddy, L. H.; Arias, J. L.; Nicolas, J.; Couvreur, P. Magnetic Nanoparticles: Design and Characterization, Toxicity and Biocompatibility, Pharmaceutical and Biomedical Applications. *Chemical Reviews* **2012**, *112*, 5818-5878.

(2) Wu, W.; He, Q.; Jiang, C. Magnetic Iron Oxide Nanoparticles: Synthesis and Surface Functionalization Strategies. *Nanoscale Research Letters* **2008**, *3*, 397-415.

(3) Laurent, S.; Forge, D.; Port, M.; Roch, A.; Robic, C.; Vander Elst, L.; Muller, R. N. Magnetic Iron Oxide Nanoparticles: Synthesis, Stabilization, Vectorization, Physicochemical Characterizations, and Biological Applications. *Chemical Reviews* **2008**, *108*, 2064-2110.

(4) Gupta, A. K.; Gupta, M. Synthesis and surface engineering of iron oxide nanoparticles for biomedical applications. *Biomaterials* **2005**, *26*, 3995-4021.

(5) Kim, D. K.; Zhang, Y.; Voit, W.; Rao, K. V.; Muhammed, M. Synthesis and characterization of surfactant-coated superparamagnetic monodispersed iron oxide nanoparticles. *Journal of Magnetism and Magnetic Materials* **2001**, *225*, 30-36.

(6) Corot, C.; Robert, P.; Idée, J.-M.; Port, M. Recent advances in iron oxide nanocrystal technology for medical imaging. *Advanced Drug Delivery Reviews* **2006**, *58*, 1471-1504.

(7) Na, H. B.; Song, I. C.; Hyeon, T. Inorganic Nanoparticles for MRI Contrast Agents. *Advanced Materials* **2009**, *21*, 2133-2148.

(8) Park, J.; An, K.; Hwang, Y.; Park, J.-G.; Noh, H.-J.; Kim, J.-Y.; Park, J.-H.; Hwang, N.-M.; Hyeon, T. Ultra-large-scale syntheses of monodisperse nanocrystals. *Nat Mater* **2004**, *3*, 891-895.

(9) Zhao, Z.; Zhou, Z.; Bao, J.; Wang, Z.; Hu, J.; Chi, X.; Ni, K.; Wang, R.; Chen, X.; Chen, Z.; Gao, J. Octapod iron oxide nanoparticles as high-performance T2 contrast agents for magnetic resonance imaging. *Nat Commun* **2013**, *4*.

(10) Wei, W.; Zhaohui, W.; Taekyung, Y.; Changzhong, J.; Woo-Sik, K. Recent progress on magnetic iron oxide nanoparticles: synthesis, surface functional strategies and biomedical applications. *Science and Technology of Advanced Materials* **2015**, *16*, 023501.

(11) Cho, E. J.; Holback, H.; Liu, K. C.; Abouelmagd, S. A.; Park, J.; Yeo, Y. Nanoparticle Characterization: State of the Art, Challenges, and Emerging Technologies. *Molecular Pharmaceutics* **2013**, *10*, 2093-2110.

(12) Siew, A.; Le, H.; Thiovolet, M.; Gellert, P.; Schatzlein, A.; Uchegbu, I. Enhanced Oral Absorption of Hydrophobic and Hydrophilic Drugs Using Quaternary Ammonium Palmitoyl Glycol Chitosan Nanoparticles. *Molecular Pharmaceutics* **2012**, *9*, 14-28.

(13) Kim, B. H.; Lee, N.; Kim, H.; An, K.; Park, Y. I.; Choi, Y.; Shin, K.; Lee, Y.; Kwon, S. G.; Na, H. B.; Park, J.-G.; Ahn, T.-Y.; Kim, Y.-W.; Moon, W. K.; Choi, S. H.; Hyeon, T. Large-Scale Synthesis of Uniform and Extremely Small-Sized Iron Oxide Nanoparticles for High-Resolution T1 Magnetic Resonance Imaging Contrast Agents. *Journal of the American Chemical Society* **2011**, *133*, 12624-12631.

(14) Palma, S. I. C. J.; Marciello, M.; Carvalho, A.; Veintemillas-Verdaguer, S.; Morales, M. d. P.; Roque, A. C. A. Effects of phase transfer ligands on monodisperse iron oxide magnetic nanoparticles. *Journal of Colloid and Interface Science* **2015**, *437*, 147-155.

(15) Ahmad, Z.; Shah, A.; Siddiq, M.; Kraatz, H.-B. Polymeric micelles as drug delivery vehicles. *RSC Advances* **2014**, *4*, 17028-17038.

(16) Lim, J.; Yeap, S. P.; Che, H. X.; Low, S. C. Characterization of magnetic nanoparticle by dynamic light scattering. *Nanoscale Research Letters* **2013**, *8*, 1-14.

(17) Lin, Y.; Wang, S.; Zhang, Y.; Gao, J.; Hong, L.; Wang, X.; Wu, W.; Jiang, X. Ultra-high relaxivity iron oxide nanoparticles confined in polymer nanospheres for tumor MR imaging. *Journal of Materials Chemistry B* **2015**, *3*, 5702-5710.

(18) Moghimi, S. M.; Hunter, A. C.; Murray, J. C. Long-Circulating and Target-Specific Nanoparticles: Theory to Practice. *Pharmacological Reviews* **2001**, *53*, 283-318.

(19) Mahmoudi, M.; Sant, S.; Wang, B.; Laurent, S.; Sen, T. Superparamagnetic iron oxide nanoparticles (SPIONs): Development, surface modification and applications in chemotherapy. *Advanced Drug Delivery Reviews* **2011**, *63*, 24-46.

(20) Clogston, J. D.; Patri, A. K.: Zeta Potential Measurement. In *Characterization of Nanoparticles Intended for Drug Delivery*; McNeil, E. S., Ed.; Humana Press: Totowa, NJ, 2011; pp 63-70.

(21) Pfeiffer, C.; Rehbock, C.; Hühn, D.; Carrillo-Carrion, C.; de Aberasturi, D. J.; Merk, V.; Barcikowski, S.; Parak, W. J. Interaction of colloidal nanoparticles with their local environment: the (ionic) nanoenvironment around nanoparticles is different from bulk and determines the physico-chemical properties of the nanoparticles. *Journal of The Royal Society Interface* **2014**, *11*.

(22) Chooi, K. W.; Simão Carlos, M. I.; Soundararajan, R.; Gaisford, S.; Arifin, N.; Schätzlein, A. G.; Uchegbu, I. F. Physical Characterisation and Long-Term Stability Studies on Quaternary Ammonium Palmitoyl Glycol Chitosan

(GCPQ)—A New Drug Delivery Polymer. *Journal of Pharmaceutical Sciences* **2014**, *103*, 2296-2306.

(23) Mahmoudi, M.; Sheibani, S.; Milani, A. S.; Rezaee, F.; Gauberti, M.; Dinarvand, R.; Vali, H. Crucial role of the protein corona for the specific targeting of nanoparticles. *Nanomedicine* **2015**, *10*, 215-226.

(24) Sakulkhu, U.; Mahmoudi, M.; Maurizi, L.; Coullerez, G.; Hofmann-Amtenbrink, M.; Vries, M.; Motazacker, M.; Rezaee, F.; Hofmann, H. Significance of surface charge and shell material of superparamagnetic iron oxide nanoparticle (SPION) based core/shell nanoparticles on the composition of the protein corona. *Biomaterials Science* **2015**, *3*, 265-278.

(25) Verma, A.; Stellacci, F. Effect of Surface Properties on Nanoparticle–Cell Interactions. *Small* **2010**, *6*, 12-21.

(26) Kobayashi, K.; Wei, J.; Iida, R.; Ijiro, K.; Niikura, K. Surface engineering of nanoparticles for therapeutic applications. *Polym J* **2014**, *46*, 460-468.

(27) Jiang, X.; Musyanovych, A.; Rocker, C.; Landfester, K.; Mailander, V.; Nienhaus, G. U. Specific effects of surface carboxyl groups on anionic polystyrene particles in their interactions with mesenchymal stem cells. *Nanoscale* **2011**, *3*, 2028-2035.

(28) Jiang, X.; Dausend, J.; Hafner, M.; Musyanovych, A.; Röcker, C.; Landfester, K.; Mailänder, V.; Nienhaus, G. U. Specific Effects of Surface Amines on Polystyrene Nanoparticles in their Interactions with Mesenchymal Stem Cells. *Biomacromolecules* **2010**, *11*, 748-753.

(29) Angeles, V.; Magdalena, C.; Alejandro, G. R.; Macarena, C.; Sabino, V.-V.; Carlos, J. S.; María del Puerto, M.; Rodolfo, M. The influence of surface functionalization on the enhanced internalization of magnetic nanoparticles in cancer cells. *Nanotechnology* **2009**, *20*, 115103.

(30) Albanese, A.; Tang, P. S.; Chan, W. C. W. The Effect of Nanoparticle Size, Shape, and Surface Chemistry on Biological Systems. *Annual Review of Biomedical Engineering* **2012**, *14*, 1-16.

(31) Alexis, F.; Pridgen, E.; Molnar, L. K.; Farokhzad, O. C. Factors Affecting the Clearance and Biodistribution of Polymeric Nanoparticles. *Molecular Pharmaceutics* **2008**, *5*, 505-515.

(32) Jun, Y.-w.; Huh, Y.-M.; Choi, J.-s.; Lee, J.-H.; Song, H.-T.; KimKim; Yoon, S.; Kim, K.-S.; Shin, J.-S.; Suh, J.-S.; Cheon, J. Nanoscale Size Effect of Magnetic Nanocrystals and Their Utilization for Cancer Diagnosis via Magnetic Resonance Imaging. *Journal of the American Chemical Society* **2005**, *127*, 5732-5733.

(33) Roca, A. G.; Morales, M. P.; O'Grady, K.; Serna, C. J. Structural and magnetic properties of uniform magnetite nanoparticles prepared by high temperature decomposition of organic precursors. *Nanotechnology* **2006**, *17*, 2783.

(34) Baaziz, W.; Pichon, B. P.; Fleutot, S.; Liu, Y.; Lefevre, C.; Greneche, J.-M.; Toumi, M.; Mhiri, T.; Begin-Colin, S. Magnetic Iron Oxide Nanoparticles: Reproducible Tuning of the Size and Nanosized-Dependent Composition, Defects, and Spin Canting. *The Journal of Physical Chemistry C* **2014**, *118*, 3795-3810.

(35) Tromsdorf, U. I.; Bruns, O. T.; Salmen, S. C.; Beisiegel, U.; Weller, H. A Highly Effective, Nontoxic T1 MR Contrast Agent Based on Ultrasmall PEGylated Iron Oxide Nanoparticles. *Nano Letters* **2009**, *9*, 4434-4440.

(36) Rohrer, M.; Bauer, H.; Mintorovitch, J.; Requardt, M.; Weinmann, H.-J. Comparison of Magnetic Properties of MRI Contrast Media Solutions at

Different Magnetic Field Strengths. *Investigative Radiology* **2005**, *40*, 715-724.

(37) Larsen, B. A.; Haag, M. A.; Serkova, N. J.; Shroyer, K. R.; Stoldt, C. R. Controlled aggregation of superparamagnetic iron oxide nanoparticles for the development of molecular magnetic resonance imaging probes. *Nanotechnology* **2008**, *19*, 265102.

(38) Vuong, Q. L.; Gillis, P.; Gossuin, Y. Monte Carlo simulation and theory of proton NMR transverse relaxation induced by aggregation of magnetic particles used as MRI contrast agents. *Journal of Magnetic Resonance* **2011**, *212*, 139-148.

(39) Guang Choo, E. S.; Tang, X.; Sheng, Y.; Shuter, B.; Xue, J. Controlled loading of superparamagnetic nanoparticles in fluorescent nanogels as effective T2-weighted MRI contrast agents. *Journal of Materials Chemistry* **2011**, *21*, 2310-2319.

(40) Senpan, A.; Caruthers, S. D.; Rhee, I.; Mauro, N. A.; Pan, D.; Hu, G.; Scott, M. J.; Fuhrhop, R. W.; Gaffney, P. J.; Wickline, S. A.; Lanza, G. M. Conquering the Dark Side: Colloidal Iron Oxide Nanoparticles. *ACS Nano* **2009**, *3*, 3917-3926.

(41) Caravan, P.; Ellison, J. J.; McMurry, T. J.; Lauffer, R. B. Gadolinium(III) Chelates as MRI Contrast Agents: Structure, Dynamics, and Applications. *Chemical Reviews* **1999**, *99*, 2293-2352.

Chapter 3

The *In vivo* Evaluation of Micellar Iron Oxide ‘Raspberry’ Nanoparticles for use as a Negative MRI Contrast Agent for Specific Cancer Diagnostics

3.1 Introduction

Animal research has long been key to the development of new medicines and is widely considered a prerequisite before clinical studies may be performed in humans.[1] In recent years, *in vitro* methods have become increasingly more sophisticated, but to get a complete understanding of complex interactions between chemical species in biological systems, an intact biological organism is often needed. This chapter explores a number of key biomedical questions that arise from using the iron oxide raspberry nanoparticles, as described in chapter 2, as a negative MRI contrast agent for *in vivo* applications by using animal tissues and fluids as a surrogate for their human counterparts. This chapter specifically evaluates the iron oxide raspberry nanoparticles and does not cover the blackberry nanoparticles. As covered in previous chapters, other attempts to encapsulate IONPs within a polymeric micelle have been attempted. Previous studies have often yielded impressive *in vitro* results but many have limited or no information regarding their biological stability or *in vivo* pharmacokinetic/pharmacodynamic characteristics.[2-8] These kinds of studies can often be challenging as polymeric surfactant nanoparticles can be highly sensitive to pH, salts and protein adsorption leading to instability in biological environments.[9] *In vitro* stability testing in bio-relevant environments should be evaluated before animal work is conducted and these types of investigations will be covered in this chapter.

Animal models can largely be divided into two categories; *pharmacokinetics* and *pharmacodynamics*.[1] Pharmacokinetics is often conducted in animals to observe the absorption, distribution, metabolism, and excretion of medicines in the body (ADME).[10] Through studying these processes one can gather information with regards to the raspberry nanoparticle's regions of potential imaging interest and toxicity. Pharmacodynamic animal models can further be divided into the *primary*

effects of the medicine/diagnostic, which in this project will focus on the ability of the raspberry nanoparticles to act as a contrast agent and, the *secondary effects* or side effects of which, are usually the undesired toxic effects of the agent. This chapter will focus on evaluating the pharmacokinetics and the primary pharmacodynamics effects (MR imaging capability) of the raspberry nanoparticles.

To fully evaluate their biomedical potential the iron oxide raspberry nanoparticles will also be tested against a cancer model. *In vivo* tumour models have been key to evaluating chemotherapeutic entities and over the years they have become increasingly advanced.[11] *In vitro* testing allows one to understand the mechanisms and the specific nature of a new chemical entity and is preferred where possible but, as of yet, these *in vitro* experiments are an over simplification of the chemical biology of a tumour environment and do not act as an effective surrogate for a human response to a treatment. Flank tumour models are a widely used cancer model.[12] A small amount of cancerous tissue is transplanted subcutaneously into a specific region, usually the flank, of a rodent. With the correct technique and the appropriate conditions the cancer cells will grow into full tumours within days or weeks. Flank tumours protrude from the surface of the host and so can easily be monitored throughout the experiment. Compared to alternative cancer models, flank tumour models are also relatively inexpensive and so are widely considered a good model to initially test the effectiveness of a cancer treatment.

A tumour is typically characterised by the defective architecture of its vasculature, primarily to meet the nutrient and oxygen demands of the rapidly growing cells. This defective vasculature is comprised of irregularly shaped, poorly aligned epithelial cells that form ‘leaky’ fenestrations in the newly formed blood vessels.[13] As a consequence it was soon discovered that macromolecules of appreciable size displayed preferential accumulation at tumour sites that exhibited this leaky vasculature.[14] This

phenomenon was termed the *enhanced permeation and retention* (EPR) effect and since its discovery nanomedicines have aimed to exploit this feature to favourably deliver nanoparticles to the sites of malignant growth. *Maeda et al,* amongst others*,* conducted many of the early studies using this principle to preferentially deliver chemotherapeutic agents and over the years this theory has become a gold standard in cancer research with a number of widely used clinically available non-targeted nano drug products, Doxil® and DaunoXome®, rationalising their mechanism of action using the EPR effect.[15-17] It is hypothesised in this project that the iron oxide raspberry nanoparticles will also display preferential tumour distribution and accumulation because of their nanosized nature. In this chapter a murine 4T1 breast cancer cell line was selected as they are widely regarded as an effective model to produce fast growing reproducible tumours on immunocompetent BALB/c mice.[18]

This chapter will aim to evaluate a number of key areas concerned with the biomedical investigation of the iron oxide raspberry nanoparticles. *In vitro* stability experiments will continue on from chapter 2 and will now be studied in biologically relevant solutions. Pharmacokinetics will be investigated in a number of major organs including; blood, liver, spleen, brain, lungs, heart and kidneys. *In vivo* MRI imaging will be conducted and will be compared with a commercially available product in order to assess the raspberry nanoparticle's imaging capability. Finally, *in vivo* investigations will be performed in a 4T1 sub-cutaneous flank tumour model in order to monitor their distribution, accumulation and imaging potential.

3.2 Materials

Chemical	Purity	Supplier
1,10-phenanthroline	>99.5%	Sigma-Aldrich
4T1 ATCC CRL-2539 cells		ATTC
BALB/c mice	Female	Harlem/ Charles River
Dextrose	20%	Martindale
EDTA microtainer		BD
Ferucarbotran® (Resovist®)	52.2 mg/mL	Meito Sangyo Co
Fetal bovine serum		Gibco
Hydrochloric acid	32%	Fisher
Hydroxylamine hydrochloride	>99%	Sigma-Aldrich
Iron standard for ICP	1000 ppm	Sigma-Aldrich
$FeCl_2.4H_2O$	98%	Sigma-Aldrich
Isoflurane		Vetone
Pentoject™ (pentobarbitone)	20% w/v	Animalcare
Phosphate buffer saline	10X	Gibco
RPMI 1640 medium		Gibco

Chemical	Purity	Supplier
Sodium acetate	>99%	Sigma-Aldrich
Sodium chloride	>99.8%	Fisher
Sodium hydroxide	>99%	Sigma-Aldrich
Trypan blue	0.4%	Gibco
Trypsin-EDTA	0.25%	Sigma-Aldrich
Wister rats	Male	Harlem
Yttrium standard for ICP	1000 ppm	Sigma-Aldrich

3.3 Methods

3.3.1 Stability in biologically relevant solutions

The iron oxide raspberry nanoparticle's obtained from methods described in *section 2.3.5* were investigated for stability in; H_2O, 0.9% NaCl, 1X PBS and 5% dextrose. Iron oxide raspberry nanoparticles were frozen and lyophilised to obtain a dry product and then dispersed in MilliQ water. Following this, the raspberry nanoparticles (2.5 mL) were added to; H_2O (2.5 mL), 1.8% NaCl (2.5 mL), 2X PBS (2.5 mL), 10% dextrose (2.5 mL), diluting each of the buffers by a factor of 2, and were incubated at 37 ^{O}C. At various time points aliquots were removed, centrifuged (224 rcf, 10 min) and then the supernatant was analysed for iron content via the 1,10-phenanthroline iron quantification assay. Briefly; The supernatant (200 µL) was added to 4 M HCl (200 µL) and digested at 70 ^{O}C. In a sample vial; sodium acetate (450 µL, 125 mg/mL) and hydroxylamine hydrochloride (50 µL, 10 mg/mL) were added to the supernatant (200 µL) followed by the 1,10-phenanthroline (300 µL, 10 mg/mL) turning the sample bright red if iron was present. Sample vials were protect from light for 1 h and then measured using UV/VIS at 510 nm. The iron concentrations were determined based on a calibration curve made from iron(II) chloride tetrahydrate.

3.3.2 Plasma stability

Plasma stability was monitored by ICP-AES (Varian 720-ES, Agilent, UK) paired with an automatic sample preparation system (Varian SPS 3, Agilent, UK). Blood was obtained from male Wister rats (400-450 g, Harlem, UK), collected into microtainer tubes coated in EDTA (K3E Vacutainer, BD Biosciences, UK) and maintained on ice. Plasma was obtained as the supernatant after centrifugation of blood samples (252 rcf, 10 min, 4 ^{O}C) and stored at -20 ^{O}C until used. Raspberry nanoparticles (2.5 mL) were added to rat plasma (2.5 mL), diluting the plasma by a factor of 2, and were

incubated at 37 ^{O}C. At various time points, aliquots were removed, centrifuged (224 rcf, 10 min) and then the supernatant was analysed for iron content via ICP-AES. Briefly; the supernatant (300 µL) was added to 70 % HNO_3 (300 µL) digested at 70 ^{O}C. The digestant was diluted by a factor of 35 and then measured on an ICP-AES. The iron concentrations were determined based on a calibration curve made from an iron standard for ICP (TraceCERT, Fluka).

3.3.3 Pharmacokinetics and biodistribution

Female BALB/c mice were used (20-25 g, Harlem, UK). All experiments were performed under a UK Home Office Animal License and in accordance with local ethics committee rules. A suspension of the iron oxide polymeric raspberry nanoparticles (6.5 mg Fe/mL) were prepared in 5% dextrose, titrated to pH 6 using 0.1 M NaOH and filtered through a 0.22 µm filter. The formulation was intravenously administrated via the tail vein (32.5 mg Fe/kg). At various time points animals were euthanized with Pentoject™ (pentobarbitone sodium 20% w/v, 150 mg/kg) via intraperitoneal injection. Blood was immediately collected via cardiac puncture and collected into microtainer tubes coated in EDTA (K2E Vacutainer, BD Biosciences, UK). Various tissues were collected (liver, spleen, brain, heart, lungs and kidneys) and were thoroughly rinsed in 0.9% NaCl (50 mL) and then stored at -80 ^{O}C until they could be further analysed. The tissues were lyophilised, the dry weight was determined and an yttrium standard for ICP was added (50 µL, 1000 ppm, TraceCERT, Fluka). Dry tissue samples were degraded in HNO_3 (70 %, 250 µL) for 1 h at 70 ^{O}C, this was followed by the addition of H_2O_2 (200 µL) and the tissues were degraded for a further 1 h at 70 ^{O}C. The digestant was cooled, diluted 35 times and centrifuged (4032 rcf, 10 min) to remove any fatty residue. Samples were analysed using ICP-AES (Varian 720, Agilent, UK). The iron concentrations were determined

based on a calibration curve made from an iron standard for ICP (TraceCERT, Fluka) in 2% HNO_3.

3.3.4 In vivo MRI measurements

T2 weighted MR images were collected using a 1T benchtop MRI scanner (ICON™, Bruker, UK) at 37 ^{O}C. Iron oxide raspberry nanoparticles (5 mg Fe/kg) were administered via the tail vein and images were collected pre-treatment and 1 h post administration of the contrast agent. A multi-slice spin-echo pulse sequence with the following parameters; TE: 6-100 ms, TR: 1845 ms was used to collect axial and coronal images. Animals were anesthetised using isoflurane while the animal's temperature was controlled via a heated bed and its respiration was monitored. All experiments were non-recovery and animals were euthanized via an overdose of isoflurane and death was confirmed via neck dislocation. The T2 relaxation was determined by curve fitting the echo times (TE) of each pixel in the image using MATLAB (Mathworks, UK). Commercially available Ferucarbotran (Resovist®) was also administrated and measured under the same conditions.

3.3.5 4T1 cell culture

4T1 (ATCC® CRL-2539™) were maintained in RPMI 1640 medium (GlutaMAX™, Gibco), supplemented with 10% fetal bovine serum incubated in a 5% CO_2 atmosphere at 37.5 ^{O}C. Fresh media was added every other day and cells were passaged (1/10) when they had reached 80-90% confluency using 0.25% trypsin-EDTA (sigma, UK) as the dissociation reagent. A 4T1 cell growth curve was conducted as follows; once the cells had reached 80% confluency, they were detached and counted using a haemocytometer and trypan blue dye (Gibco, UK). The cells were then seeded into wells with a total surface area of 9.6 cm^2 at a density of 20,000 cells per well. At various time points the cells would be detached and counted using a haemocytometer.

3.3.6 4T1 flank tumour model

4T1 cells were cultured in RPMI 1640 medium (GlutaMAX™, Gibco), supplemented with 10% fetal bovine serum (FBS). 3-4 h before harvesting, the cell medium was replaced to remove any dead cells. To harvest the cells the medium was removed and the cells washed with 1X PBS before adding 0.25% trypsin-EDTA (Sigma, UK) to dissociate the cells from then plate. After incubating the cells for 4 min at 37 ^{O}C the cell suspension was diluted 10:1 with complete medium and the cells counted using a haemocytometer. The cells were then placed in a centrifuge (214 rcf, 4 min) to pellet the cells, the medium was discarded and the cells were washed twice with PBS (214 rcf, 4 min). The cells were then suspended in FBS free medium at a density of 10 x10^6 cells/mL and kept on ice. Female BALB/c mice were used (20-25 g, Charles River, UK). All experiments were performed under a UK Home Office Animal License and in accordance with local ethics committee rules. The animals were shaved using hair clippers around the site of injection. Tumour cells were allowed to warm to room temperature and injected (1 x 10^6 cells, 100 µL) into the lower flank of the mouse. Tumour size and mouse weight was continually monitored through-out the duration of the experiment. Experiments were conducted when the tumour had reached at least 100 mm^3 which was measured using digital callipers and calculated using the formula; volume = $(width)^2$ x length/2.

3.3.7 Pharmacokinetic tumour study

For the pharmacokinetic study A suspension of the iron oxide polymeric raspberry nanoparticles (6.5 mg Fe/mL) were prepared in 5% dextrose, titrated to pH 6 using 0.1 M NaOH and filtered through a 0.22 µm filter. The formulation was intravenously administrated via the tail vein (32.5 mg Fe/kg). At various time points animals were euthanized with Pentoject™ (pentobarbitone sodium 20% w/v, 150 mg/kg) via intraperitoneal injection. The tumour tissue and tissue from the opposite flank was

removed, thoroughly rinsed in 0.9% NaCl (50 mL) and then stored at -80 ^{O}C until further analysed via ICP-AES as described previously.

3.3.8 In vivo MRI tumour study

T2 weighted MR images were collected using a 1T benchtop MRI scanner (ICON^{TM}, Bruker, UK) at 37 ^{O}C. Iron oxide raspberry nanoparticles (5 mg Fe/kg) were administered via the tail vein, images were collected pre-treatment and at various time points post administration of the contrast agent. A commercially available Ferucarbotran® was also administrated and measured under the same conditions.

3.3.9 Statistical analysis

Statistical analysis was performed via a one-way ANOVA test using IBM SPSS Statistics (IBM corp, Released 2016. IBM SPSS Statistics for Windows, Version 24.0) followed by an appropriate post-hoc test where necessary.

3.4 Results

3.4.1 Stability in biologically relevant solutions

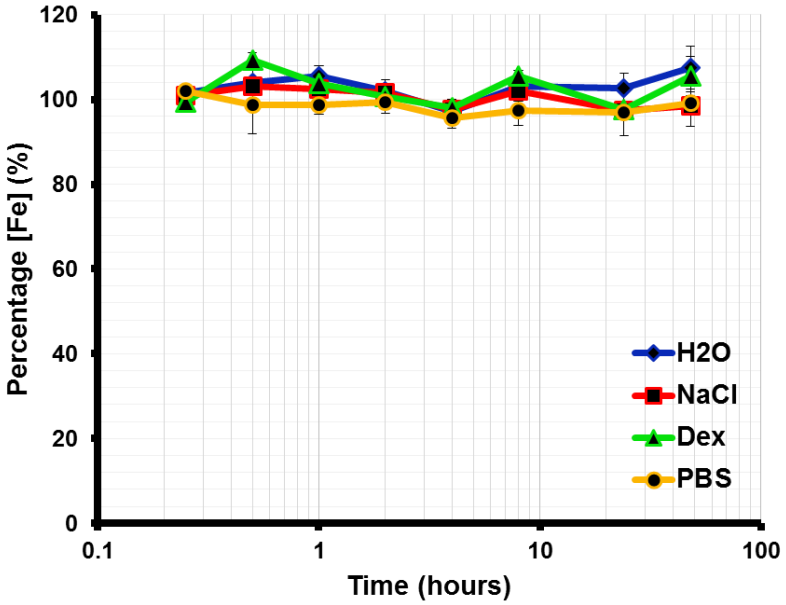

Figure 3.4.1.1. Raspberry nanoparticle stability was investigated in various biologically relevant solutions at 37 ^{O}C (H_2O, 1X PBS, 5% Dextrose, 0.9% NaCl). The iron content was monitored using the 1,10-iron phenanthroline assay. No significant difference to the controls was observed in any of the media tested suggesting good raspberry nanoparticle stability over the time period. Data are means ± s.d., n=3, (p <0.05, 1-way ANOVA, Tukey post hoc test).

3.4.2 Plasma stability

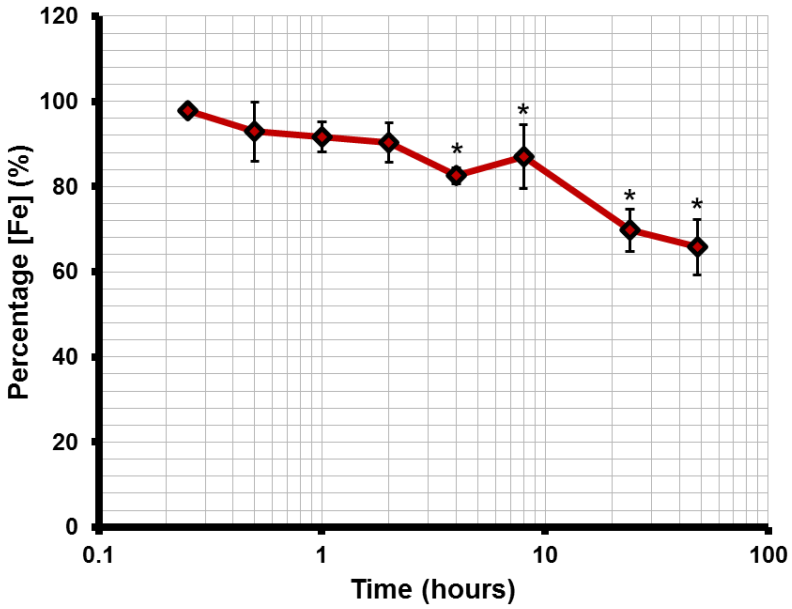

Figure 3.4.2.2. Raspberry nanoparticle stability was investigated in 50% rat plasma at 37 ^{O}C. The iron content was monitored using ICP-AES. A significant change in iron content was observed over the time period indicating a slight nanoparticle instability in plasma. Results suggest that while the raspberry nanoparticles are not fully stable in plasma, retaining a colloidal stability of 66% over a 48 h period should be satisfactory for most biomedical applications. Data are means ± s.d., n=3, (p <0.05, 1-way ANOVA, Tukey post hoc test).

3.4.3 Pharmacokinetics and biodistribution

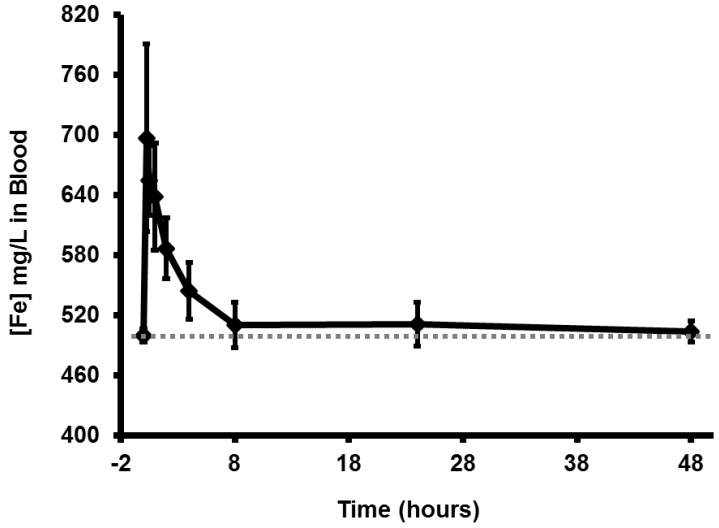

Figure 3.4.3.1. Total iron concentration in the blood following the i.v. administration of iron oxide raspberry nanoparticles (32.5 mg/kg) via the tail vein in female BALB/c mice. Background levels of iron are indicated via the dashed line. Plasma half-life ($t_{1/2}$) was 28.3 min. Data are means ± s.d., n=5.

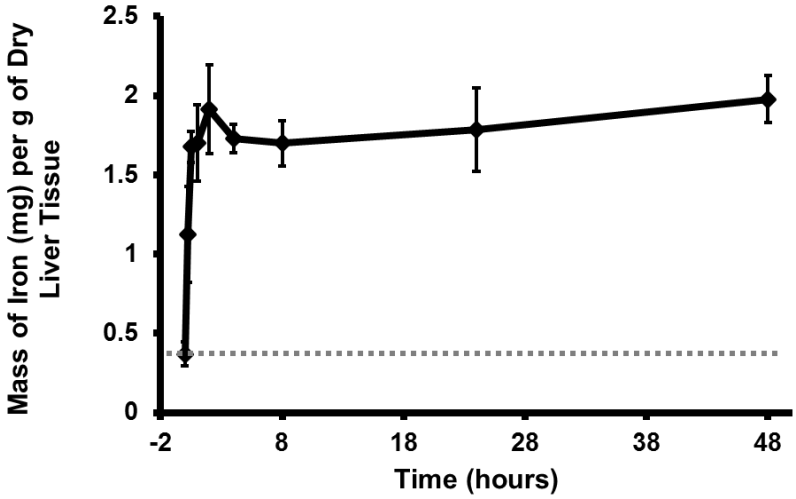

Figure 3.4.3.2. Total iron levels in the liver at various time points following the i.v. administration of iron oxide raspberry nanoparticles (32.5 mg/kg) via the tail vein in female BALB/c mice. Background levels of iron are indicated via the dashed line. Data are means ± s.d., n=5.

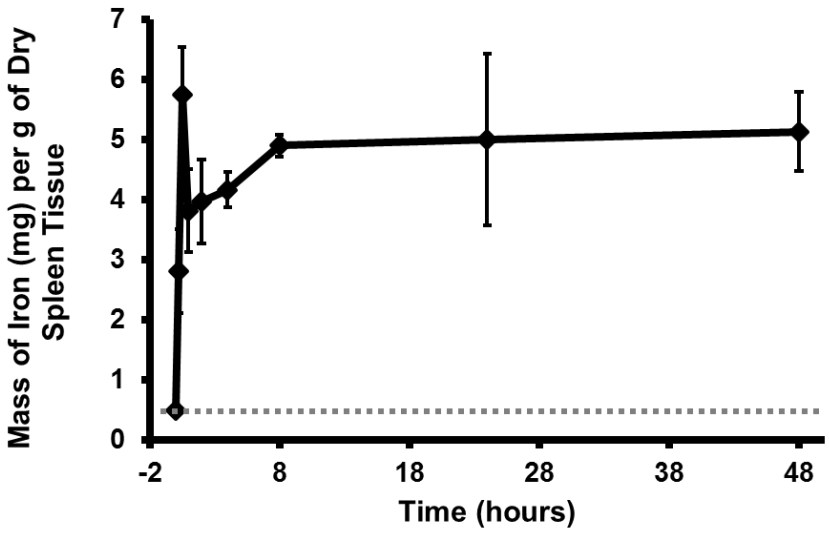

Figure 3.4.3.3. Total iron levels in the spleen at various time points following the i.v. administration of iron oxide raspberry nanoparticles (32.5 mg/kg) via the tail vein in female BALB/c mice. Background levels of iron are indicated via the dashed line. Data are means ± s.d., n=5.

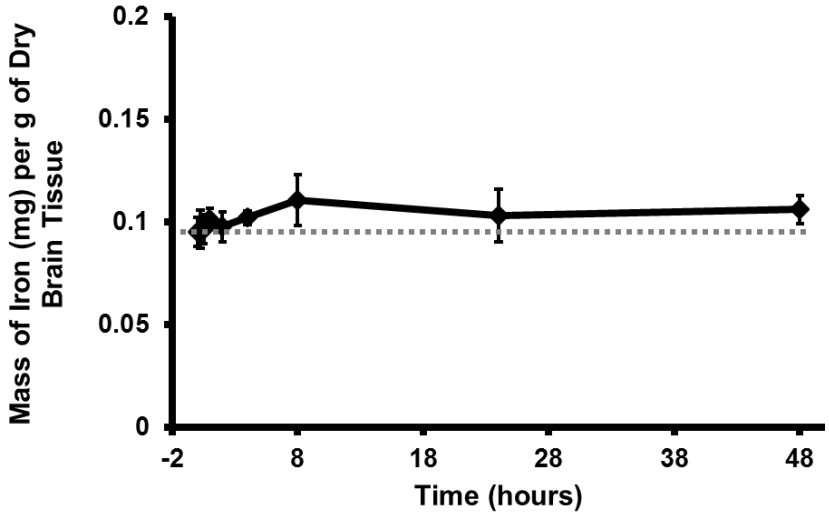

Figure 3.4.3.4. Total iron levels in the brain at various time points following the i.v. administration of iron oxide raspberry nanoparticles (32.5 mg/kg) via the tail vein in female BALB/c mice. Background levels of iron are indicated via the dashed line. Data are means ± s.d., n=5.

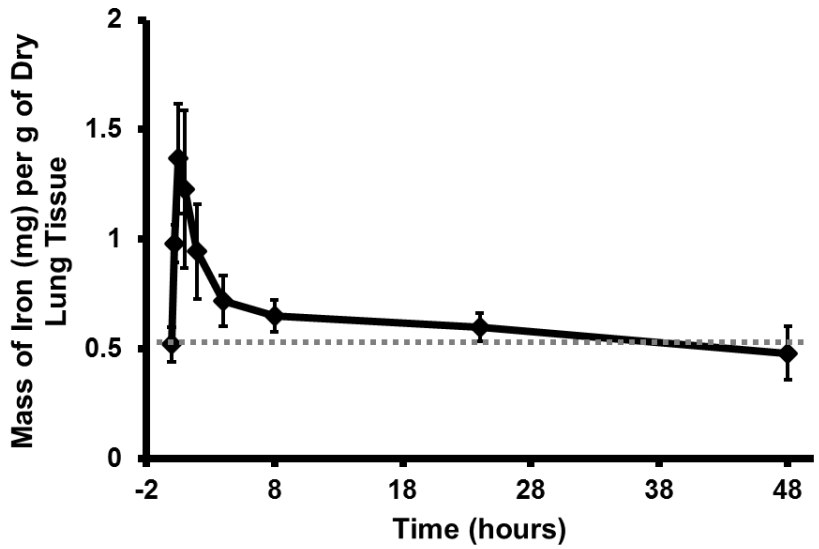

Figure 3.4.3.5. Total iron levels in the lung at various time points following the i.v. administration of iron oxide raspberry nanoparticles (32.5 mg/kg) via the tail vein in female BALB/c mice. Background levels of iron are indicated via the dashed line. Data are means ± s.d., n=5.

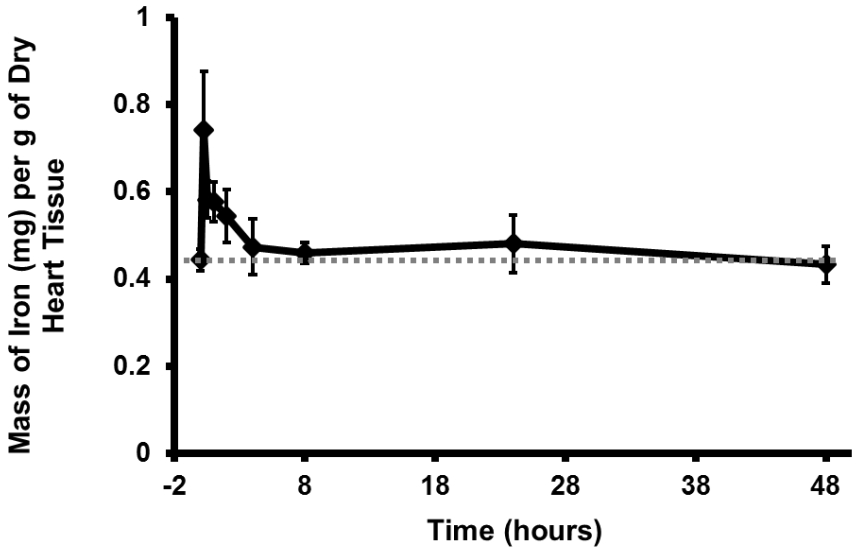

Figure 3.4.3.6. Total iron levels in the heart at various time points following the i.v. administration of iron oxide raspberry nanoparticles (32.5 mg/kg) via the tail vein in female BALB/c mice. Background levels of iron are indicated via the dashed line. Data are means ± s.d., n=5.

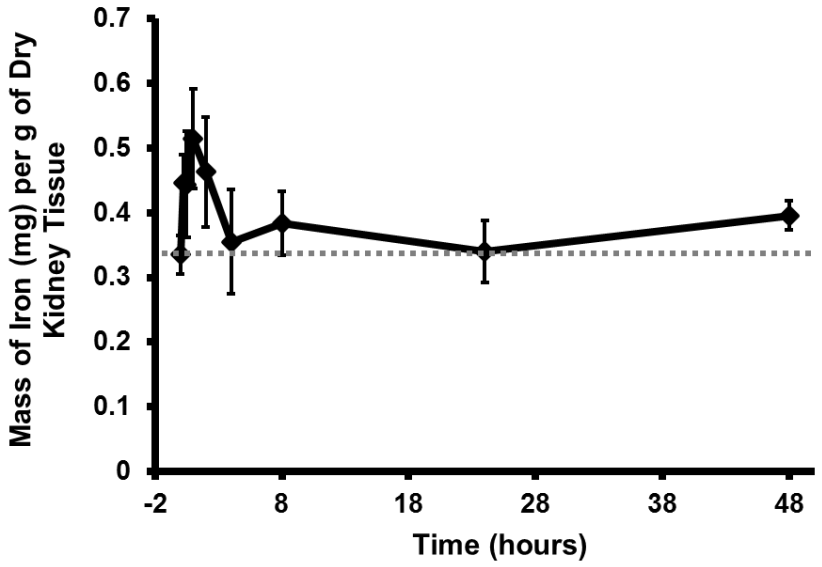

Figure 3.4.3.7. Total iron levels in the kidney at various time points following the i.v. administration of iron oxide raspberry nanoparticles (32.5 mg/kg) via the tail vein in female BALB/c mice. Background levels of iron are indicated via the dashed line. Data are means ± s.d., n=5.

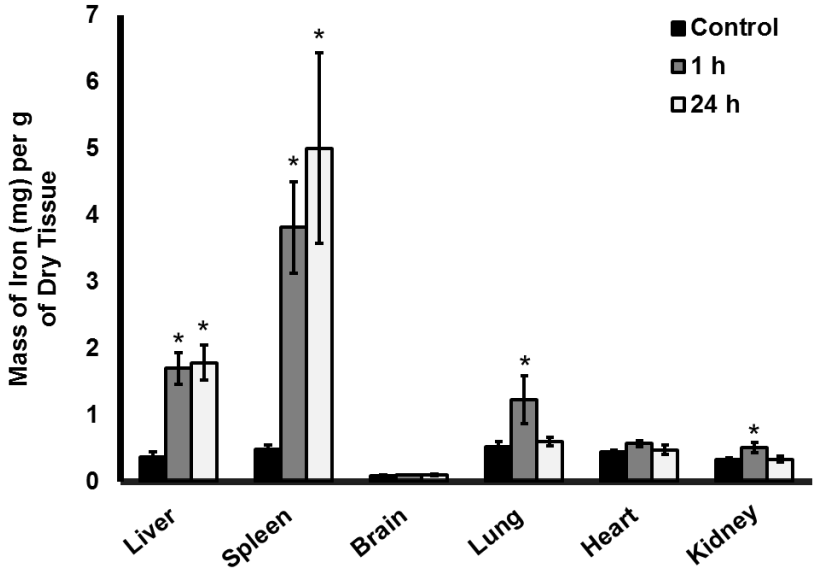

Figure 3.4.3.8. A summary comparing 1 h and 24 h iron levels to control levels in various organs following the i.v. administration of iron oxide raspberry nanoparticles (32.5 mg/kg) via the tail vein in female BALB/c mice. Data are means ± s.d., n=5 (significance = p <0.05, 1-way ANOVA, Tukey post hoc test).

3.4.4 In vivo MRI

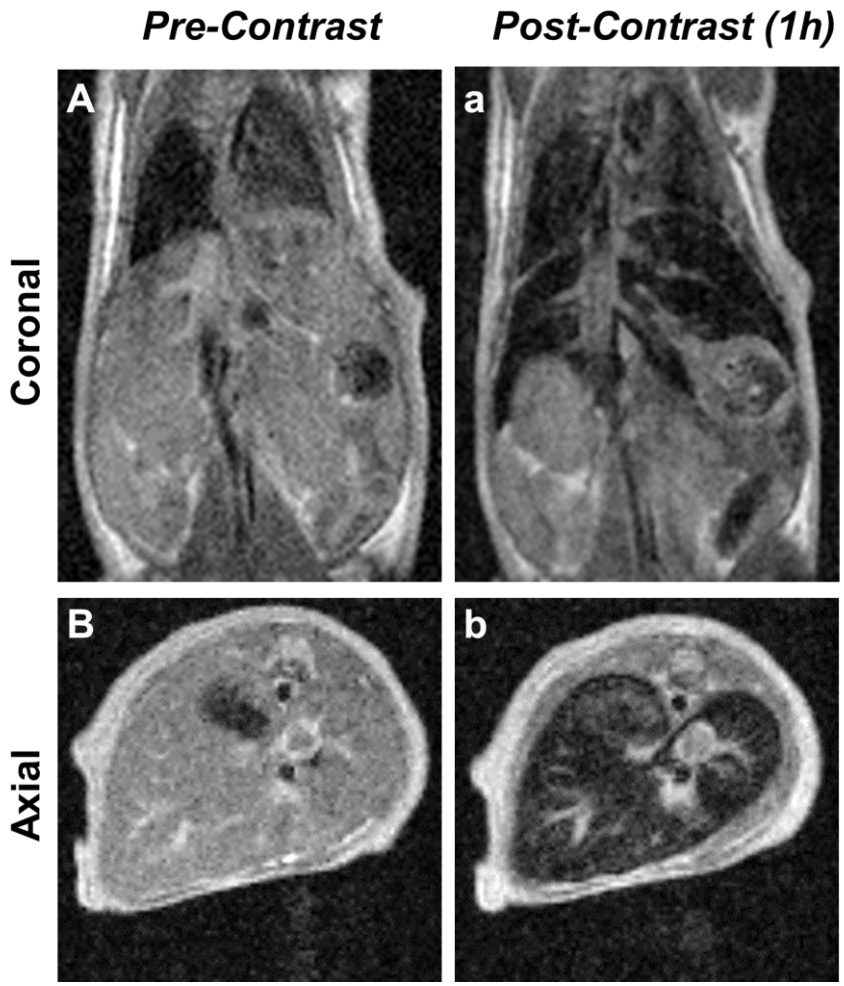

Figure 3.4.4.1. T2 weighted axial and coronal MRI images using the raspberry nanoparticles taken pre administration of the contrast agent (A and B) and 1 h after the administration of the contrast agent (a and b). Raspberry nanoparticles show distinct hypocontrast in the liver. Fine tissue structure of the liver, as well as, greater definition of the surrounding organs can be seen in the post contrast images using the raspberry nanoparticles.

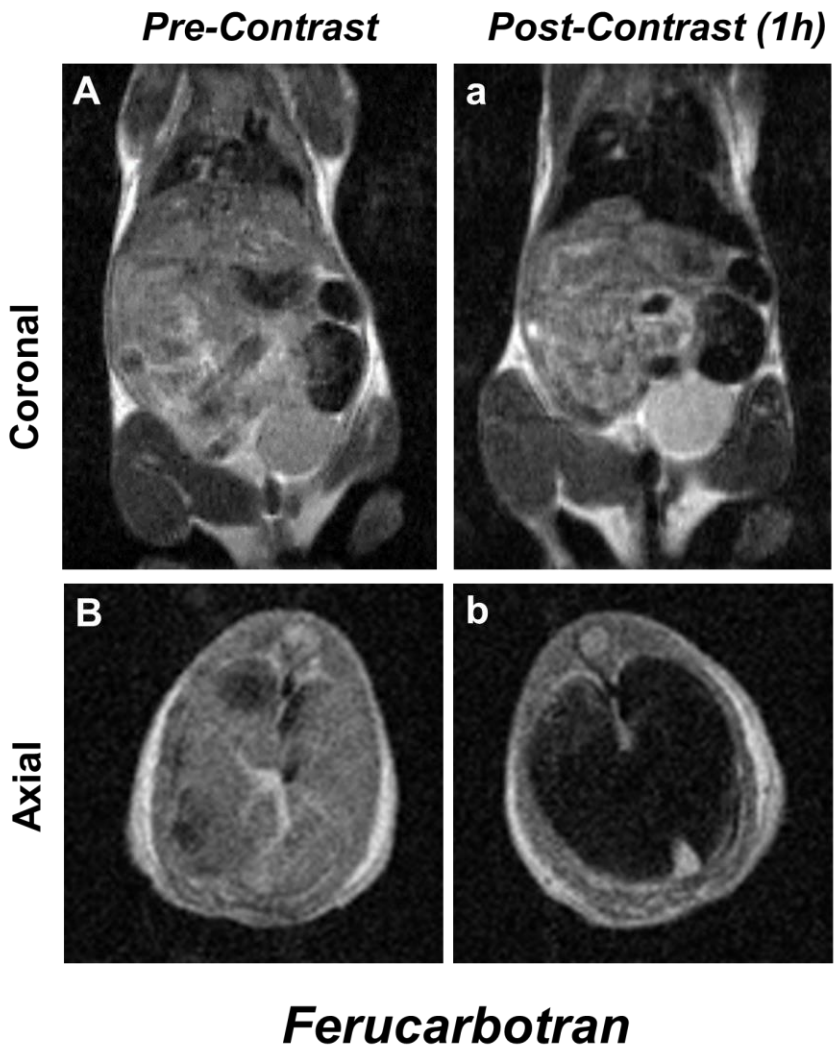

Figure 3.4.4.2. T2 weighted axial and coronal MRI images using the commercially available Ferucarbotran® (Resovist®, Meito Sangyo Co) taken pre administration of the contrast agent (A and B) and 1 h after the administration of the contrast agent (a and b). Distinct hypocontrast effect is observed in the liver, spleen and the lungs.

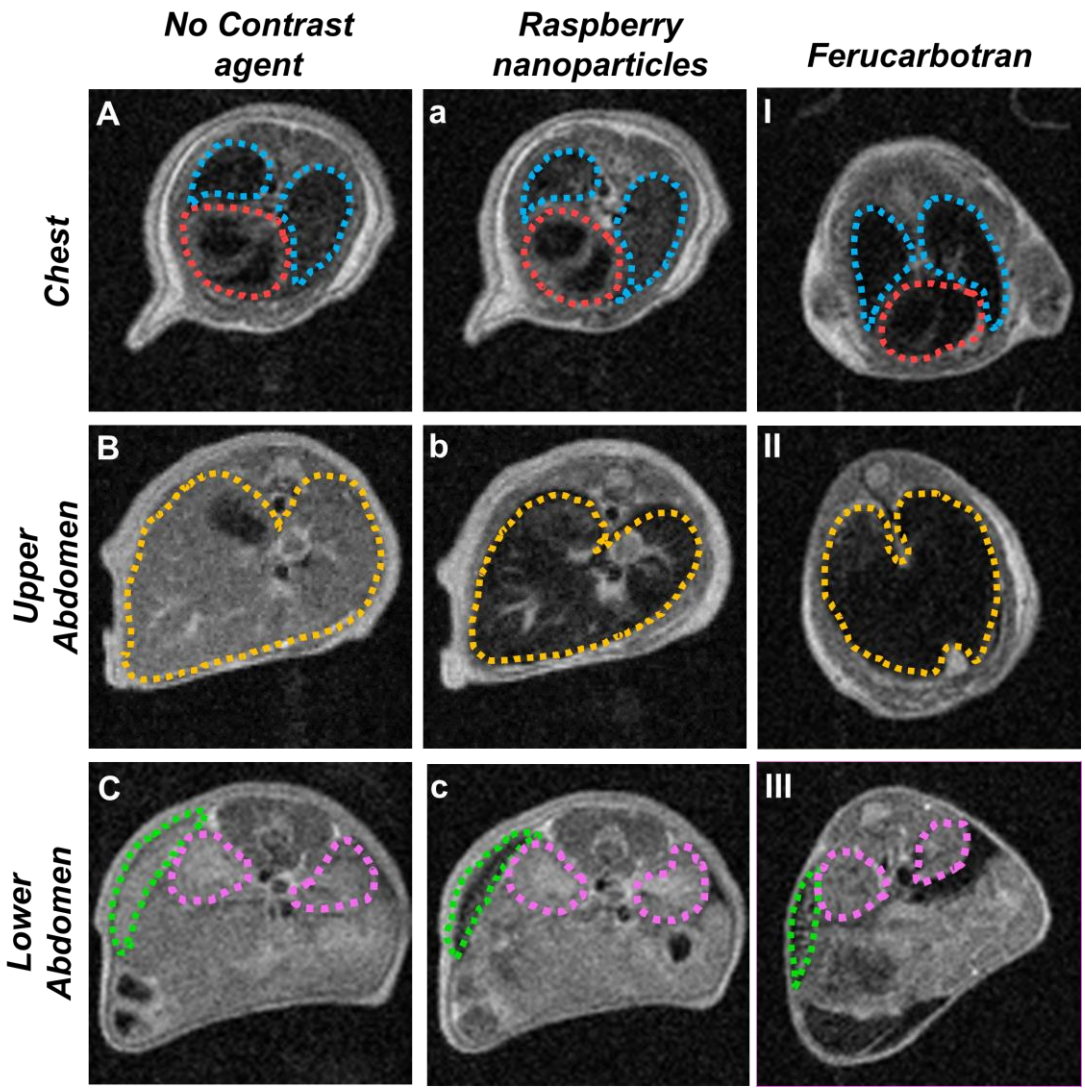

Figure 3.4.4.3. A collection of T2 weighted MRI axial images comparing the contrast effect of the raspberry nanoparticles to the commercially available Ferucarbotran® in the chest, upper abdomen and the lower abdomen regions. Organs of interest are highlighted as follows; heart (red), lungs (blue), liver (yellow), spleen (green) and kidneys (pink). The raspberry nanoparticles and Ferucarbotran® gave hypointense contrast in the liver (b and II) and spleen (c and III) while, signal darkening was only intensely observed in the lungs with the Ferucarbotran® (I).

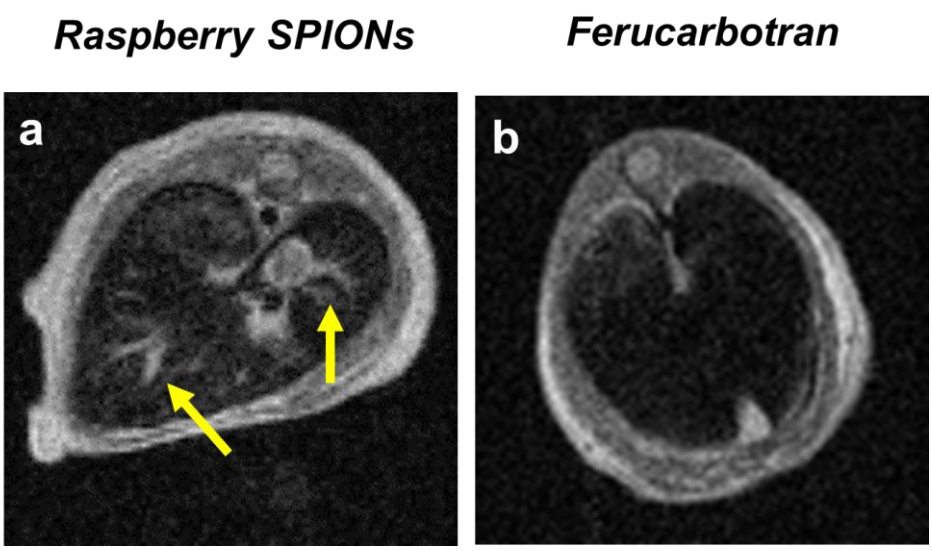

Figure 3.4.4.4. Comparison of the T2 weighted axial MRI images of the liver cross section using; (a), the raspberry nanoparticles and; (b), the commercially available Ferucarbotran®. Images were collected 1 h after the administration of the contrast agent. Both contrast agents display considerable darkening of the liver however, hepatic liver vessels can be seen in the post contrast images using the raspberry nanoparticles (arrowed).

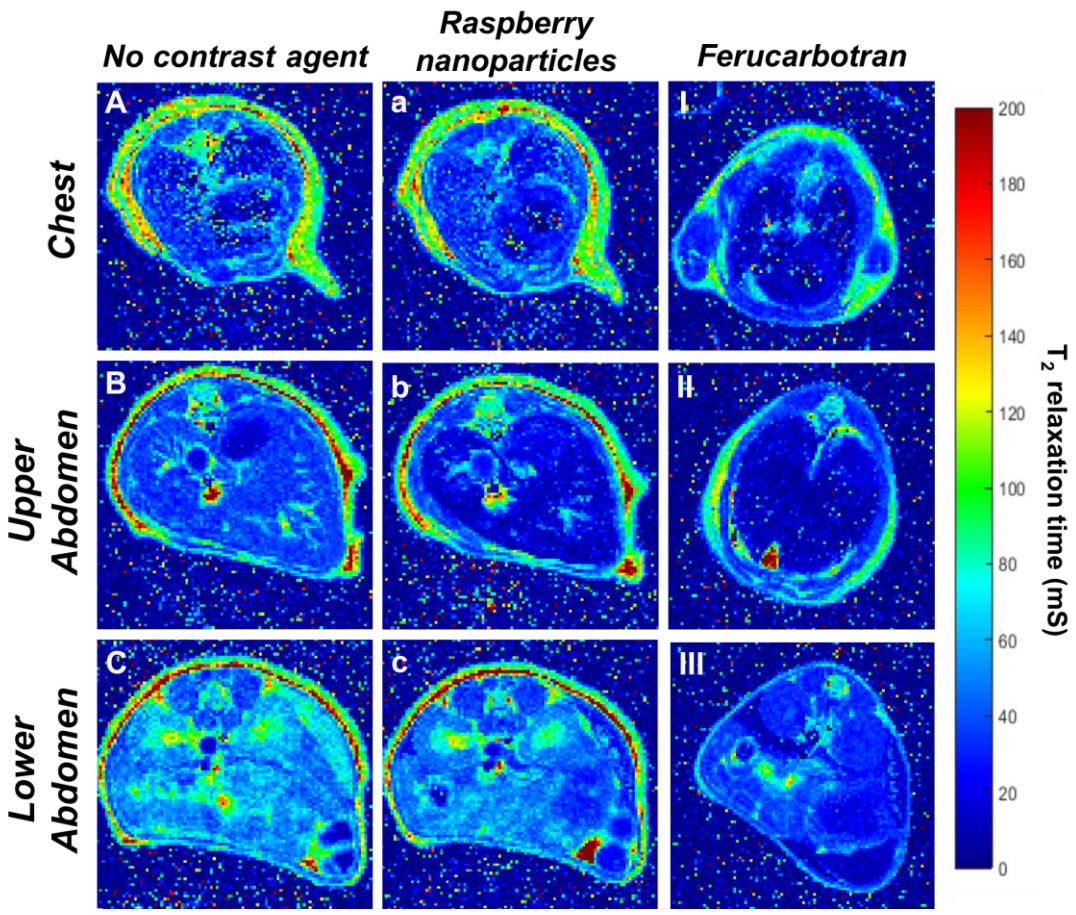

Figure 3.4.4.5. T2 relaxation maps of; no contrast agent (A-C), raspberry nanoparticles (a-c) and Ferucarbotran® (I-III) in the chest, upper abdomen and the lower abdomen regions. Maps were collected 1 hour post administration with the contrast agent. The T2 relaxation was determined by curve fitting the echo times (TE) of each pixel in the image using MATLAB (Mathworks, UK). T2 mapping allows one to visualise and quantify the effect a contrast agent has on the relaxation of the protons in an MR experiment.

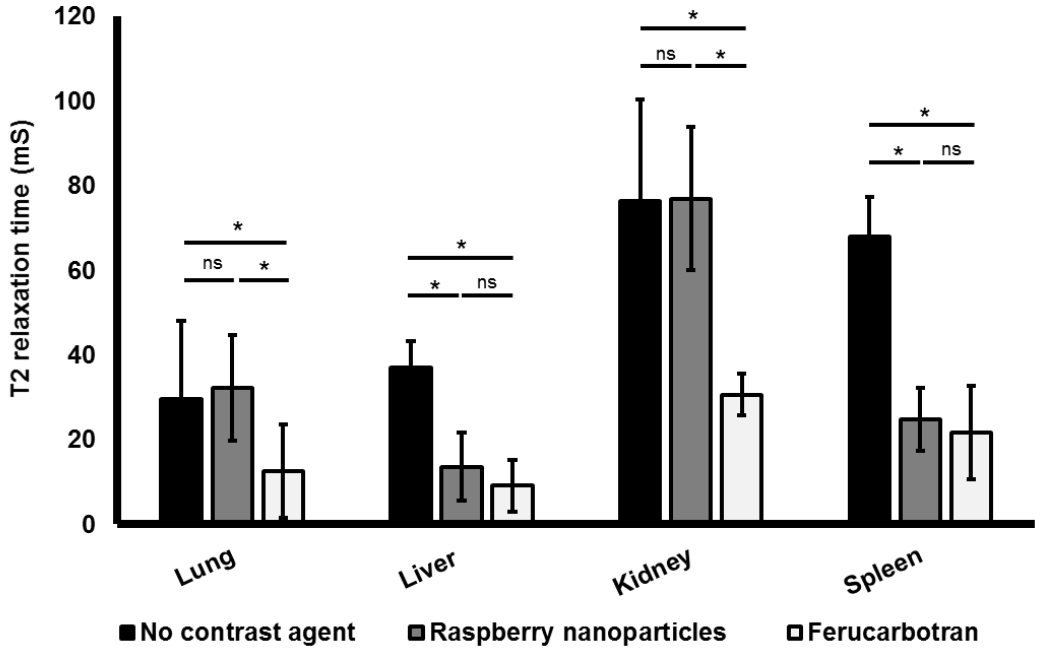

Figure 3.4.4.6. A summary of the effect on T2 relaxation times in various organs when using the raspberry nanoparticles compared to no contrast agent and the commercially available product Ferucarbotran®. Maps were collected 1 hour post administration with the contrast agents. The heart was unable to be mapped most likely due to movement from the beating heart during the experiment. Respiration was accounted for by gating the experimental procedure and as a result, show that the raspberry nanoparticles had no significant effect on the lungs unlike Ferucarbotran®, which did display a significant contrast effect in the region, the same relationship was observed in the kidneys. Both the raspberry nanoparticles and Ferucarbotran® gave significant signal reduction in the liver and spleen to a similar extent. Data are means ± s.d., (significance = p <0.05, 1-way ANOVA, Games-Howell post hoc test).

3.4.5 4T1 flank tumour model

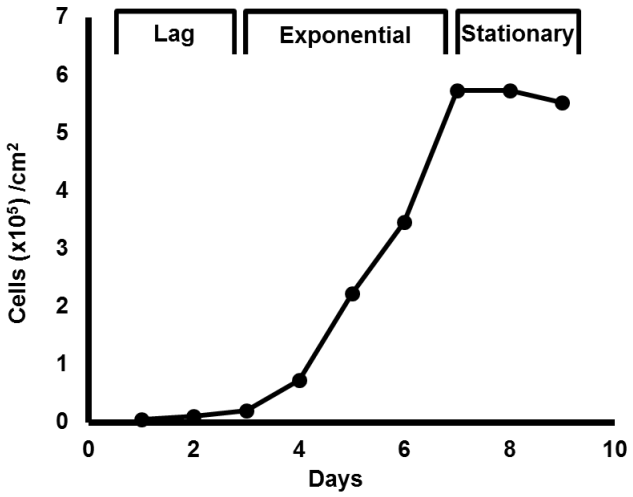

Figure 3.4.5.1. 4T1 growth dynamics, a typical sigmoidal curve is observed, which is composed of latency phase, exponential growth phase and a stationary phase. 4T1 cells have a doubling time of 1.8 days.

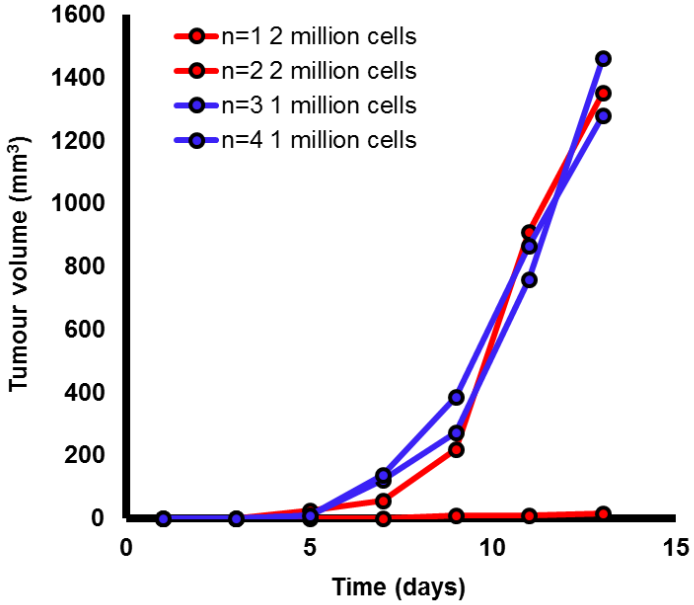

Figure 3.4.5.2. Pilot study for 4T1 flank tumour. Female BALB/c mice were injected with cancer cells in the right lower flank via a subcutaneous injection. The size of the tumour was monitored over the duration of experiment. Fully grown tumours (100 mm^3) could be grown within 7 days. The tumour associated with n=1 failed to take.

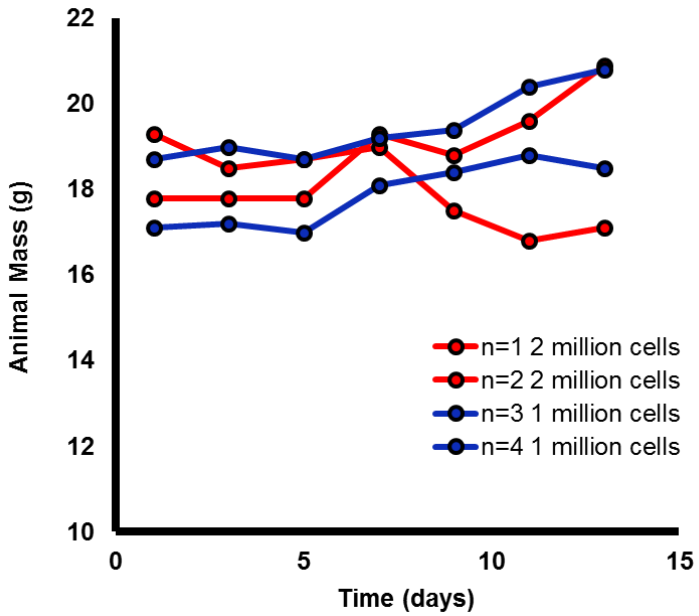

Figure 3.4.5.3. Pilot study for 4T1 flank tumour. Weight was monitored over the experiment as an indication of health.

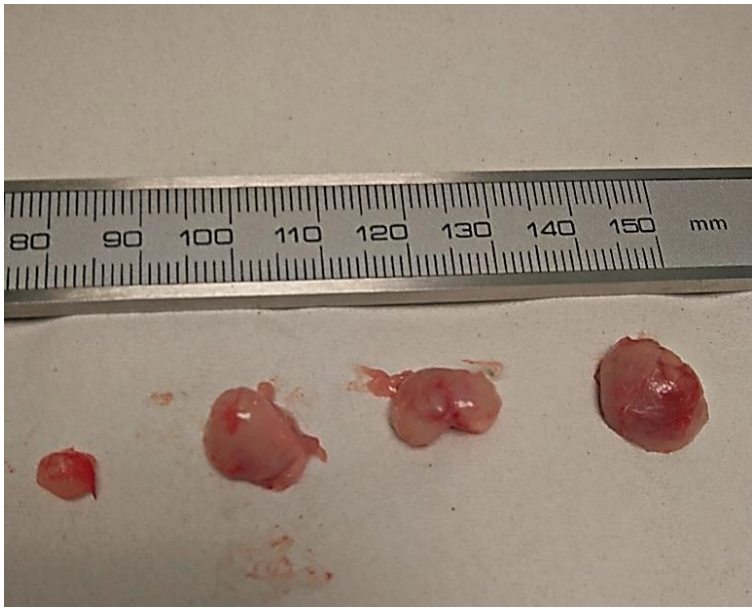

Figure 3.4.5.4. Pilot study for 4T1 flank tumour. Macro images of excised tumours.

3.4.6 In vivo tumour biodistribution

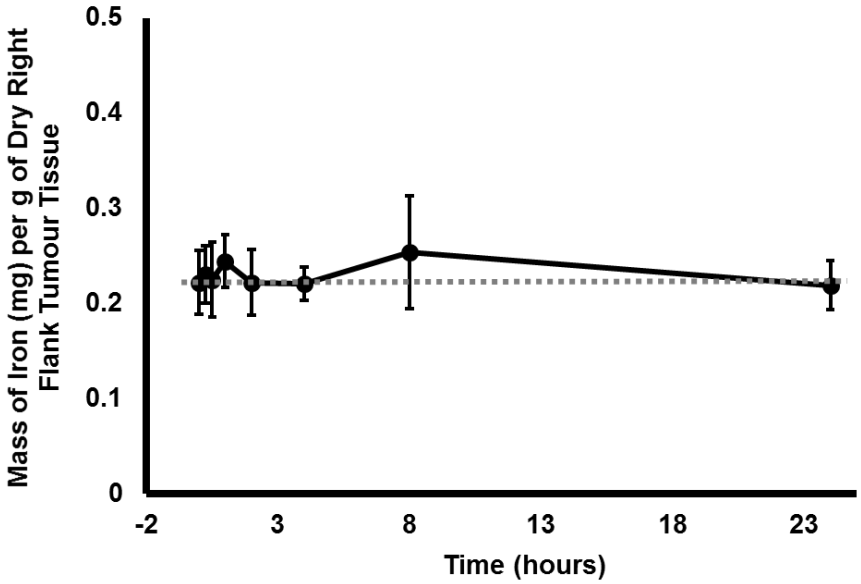

Figure 3.4.6.1. *In vivo* 4T1 flank tumour distribution for the raspberry nanoparticles. Total iron levels in the tumour were measured by ICP-AES at various time points following the i.v. administration of iron oxide raspberry nanoparticles (32.5 mg/kg) via the tail vein in female BALB/c mice. Background levels of iron are indicated via the dashed line. No significant increase in iron levels was observed over the time period, indicating that no raspberry nanoparticles were being distributed or accumulated in the tumour tissue. Data are means ± s.d., n=5 (p <0.05, 1-way ANOVA).

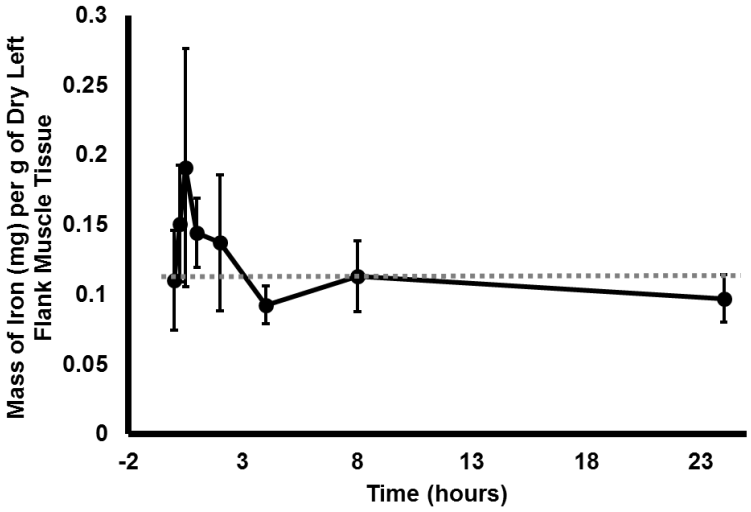

Figure 3.4.6.2. Total iron levels were measured in muscle tissue from the opposing flank as a negative control. A small trend increase in iron concentration was observed in the early time points however, this small increase was not statistically significant. Data are means ± s.d., n=5 (p <0.05, 1-way ANOVA).

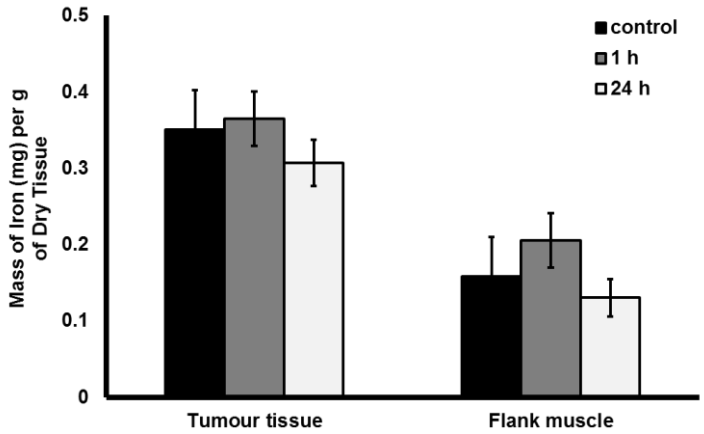

Figure 3.4.6.3. Summary of the iron distribution levels in a flank tumour and the surrounding muscle tissue compared to their control levels following the i.v. administration of iron oxide raspberry nanoparticles (32.5 mg/kg) via the tail vein in female BALB/c mice. No significant amounts of raspberry nanoparticles entered the tumour tissue. Data are means ± s.d., n=5 (significance = p <0.05, 1-way ANOVA, Tukey post hoc test).

3.4.7 In vivo MRI tumour study

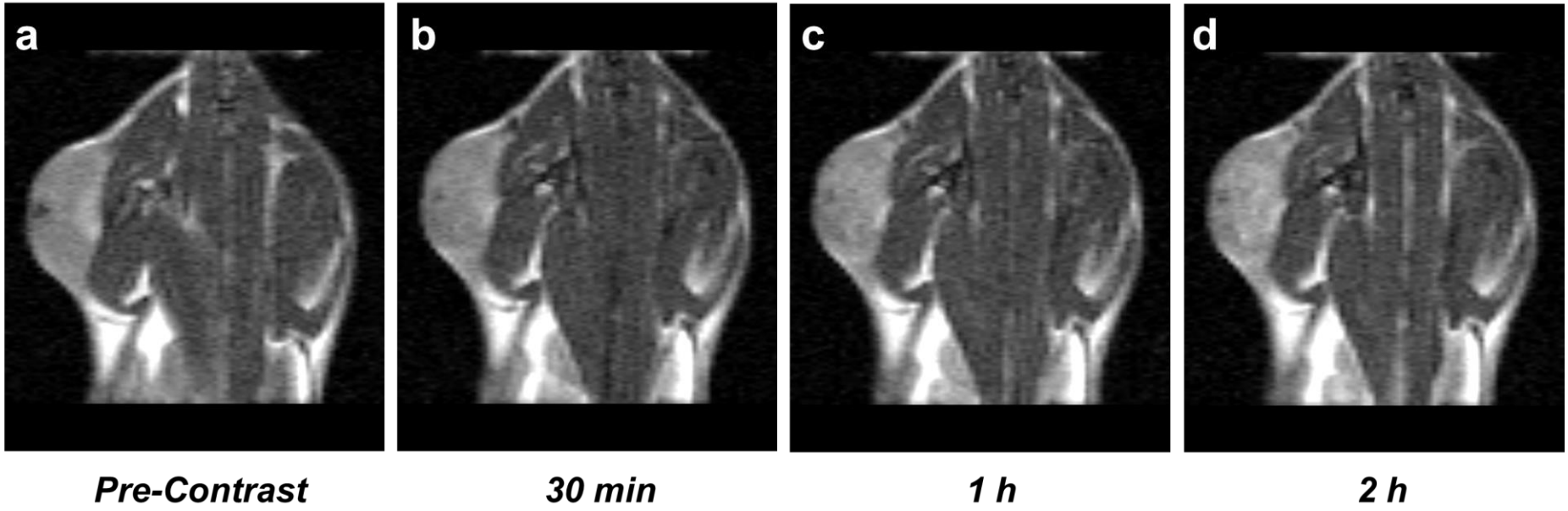

Figure 3.4.7.1. T2 weighted MR images of a flank tumour over a 2 hour period after i.v. administration of the Ferucarbotran® (Resovist®, 5 mg Fe/kg); (a), pre-contrast image; (b), 30 min; (c), 1 h and (d), 2 h. No distinctive hypointense contrast was observed in the tumour tissue at any time during the experiment.

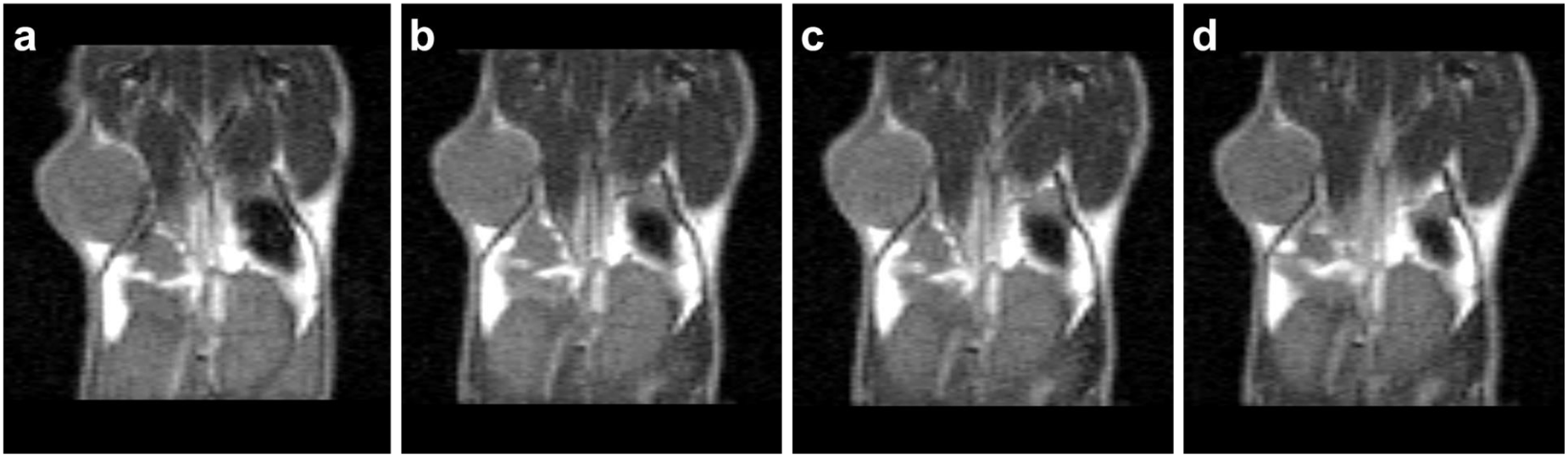

Figure 3.4.7.2. T2 weighted MR images of a flank tumour over a 2 hour period following the i.v. administration of the raspberry nanoparticles (5 mg Fe/kg); (a), pre-contrast image; (b), 30 min; (c), 1 h and (d), 2 h. As with the commercially available Ferucarbotran®, the raspberry nanoparticles gave no distinct hypointense contrast in the tumour tissue over the time period suggesting the raspberry nanoparticles do not act as an effective MRI contrast agent for this type of disease model.

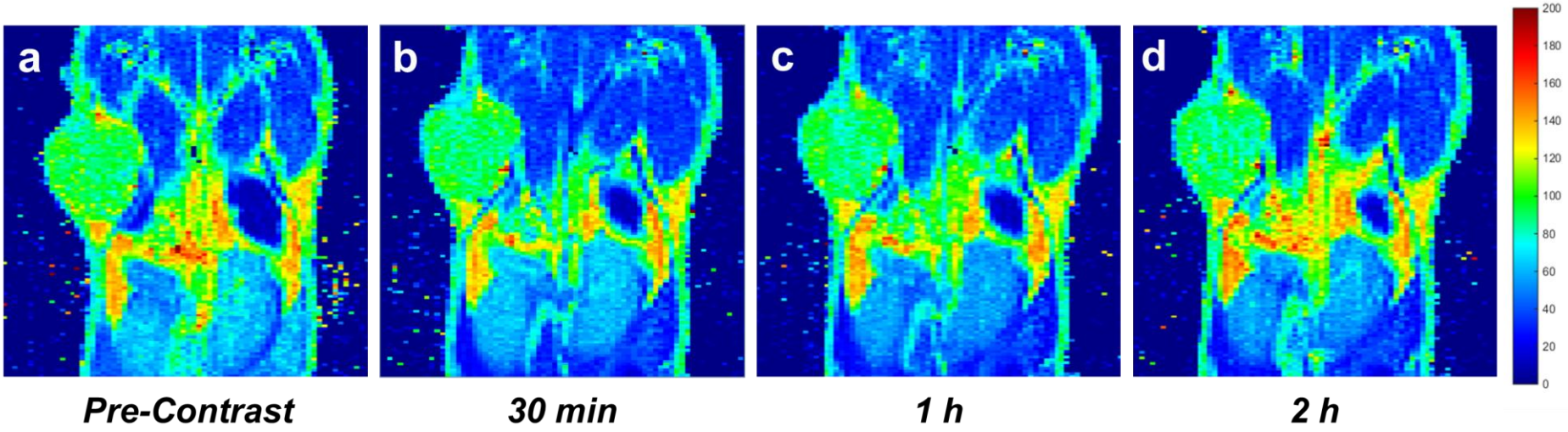

Figure 3.4.7.3. T2 relaxation maps of a flank tumour over a 2 hour period following the i.v. administration of the raspberry nanoparticles (5 mg Fe/kg); (a), pre-contrast image; (b), 30 min; (c), 1 h and (d), 2 h. The T2 relaxation was determined by curve fitting the echo times (TE) of each pixel in the image using MATLAB (Mathworks, UK).

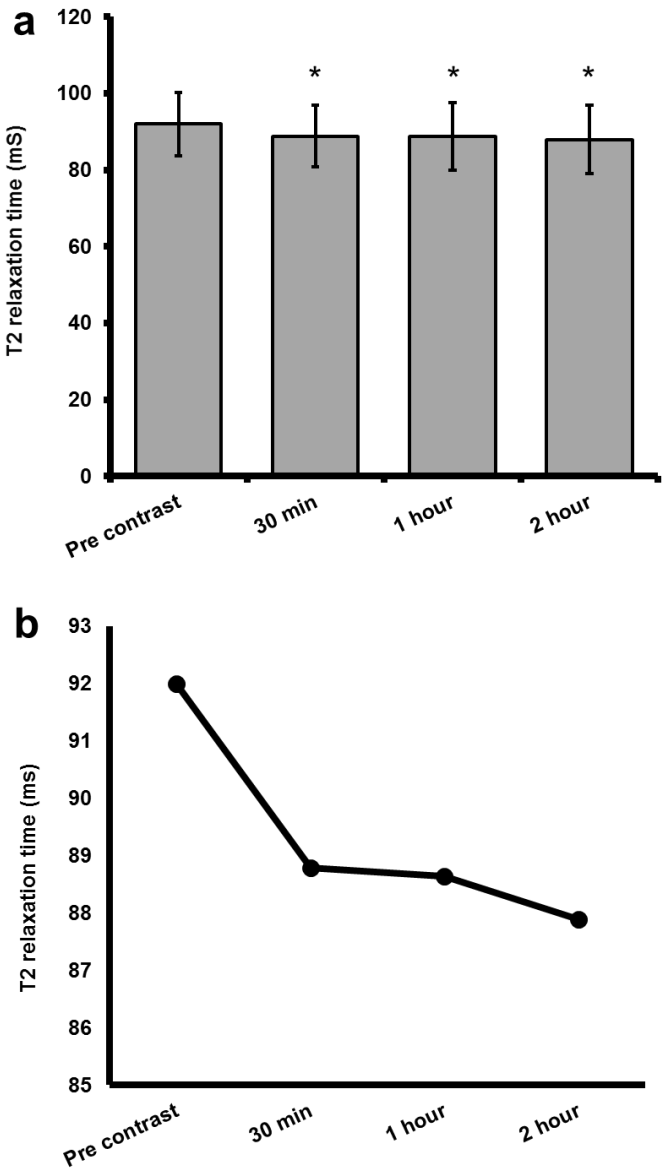

Figure 3.4.7.4. (a), A summary of the effect on T2 relaxation times in a flank tumour over a 2 hour period following an i.v. administration of the raspberry nanoparticles and (b), increased scale to highlight the significant change in relaxation time over the time period. A significant change in relaxation time was observed between the pre-contrast and post-contrast maps. This could be evidence for small levels of raspberry nanoparticles accumulating in the tumour tissue, however this difference was so small it had no effect on the overall contrast in an MR image to a human observer. Data are means ± s.d. (significance = p <0.05, 1-way ANOVA, Tukey post hoc test).

3.5 Discussion

3.5.1 Stability in biologically relevant solutions

Colloidal stability remains a critical parameter for nanoparticle systems that are to be used within a biological environment. In the previous chapter it was established that the iron oxide raspberry nanoparticles did have suitable colloidal properties in pure water conditions over 90 days, however the chemical environment of the human body is far more complex than merely a pure water system.[19] Where possible, *in vitro* stability testing should be performed to establish the suitability of a nanoparticle under more specific conditions. Unfortunately, studies like these can be challenging as polymeric surfactant based nanoparticles can often be highly sensitive to pH, salts and protein adsorption leading to stability issues within biological environments.[9,20] Not only could stability issues diminish the quality and effectiveness of the product, it could also lead to unexpected side effects; for example intravenously administered suspensions that contain particles >5 μm could lead to capillary blockage, reduced blood flow and result in embolism.[21,22] Colloidal stability was monitored in various biological relevant solutions at 37 ^{O}C and analysed by measuring the iron concentrations in the formulations using the 1,10-phenanthroline iron quantification assay (Figure 3.4.1.1). The 1,10-phenanthroline iron quantification assay is a method used to determine iron concentration. In the presence of iron in its +2 oxidation state, the 1,10-phenanthroline ligand is able to form the complex $[Fe(phen)_3]^{2+}$, more commonly known as *ferroin*, and upon complexation a bright red colour is observed that can easily be measured using UV/VIS spectroscopy.[23] Formation of ferroin is highly dependent on its chemical environment especially, oxidation state, pH and competitive binding ligands. The 1,10-phenanthroline ligand does not form the brightly coloured ferroin complex with iron in the commonly found +3 oxidation state and so a reducing agent such as hydroxylamine hydrochloride is used to confirm that

iron is only present in its reduced form. All assays were performed using a sodium acetate buffer in order to control pH. One must appreciate that measuring iron present in the supernatant does not directly indicate the presence of intact iron oxide raspberry nanoparticles, however when evaluating colloidal stability, it is widely considered that nanoparticles that are not stable have a strong tendency to flocculate increasing their mass considerably and in turn, causing sedimentation or creaming.[22] This understood, measuring iron concentration in the supernatant (after a centrifugation process) is a good indication that the nanoparticles are colloidally stable in their environment. Water was selected as a positive control, physiological concentration of isotonic saline (0.9% NaCl (w/v), 5% dextrose and phosphate buffer saline (1X PBS, pH 7.4) were believed to be a good selection of media to test the effects of salt screening, pH and osmotic pressures on the stability of the nanoparticles. It can be seen form Figure 3.4.1.1 that the raspberry nanoparticle formulations retain their colloidal stability over the 48 h period in all solutions. This strongly indicates that the raspberry nanoparticles should be suitably robust under physiological conditions.

3.5.2 Plasma stability

Although the biologically relevant solutions can give a good indication to the stability of the raspberry nanoparticles in biological environments, they are an over simplification and do not fully represent the complexity of biological fluids. The blood and blood vasculature is important for the delivery of drugs and diagnostic contrast agents and as the raspberry nanoparticles will most likely be intravenously administrated, it was thought necessary to measure their stability in blood plasma. Blood plasma is the liquid component of the blood which makes up about half of the blood volume. Plasma is devoid of the red and white cellular material and contains an array of proteins and electrolytes that are critical for healthy human function. Plasma

protein adsorption and charge screening from electrolytes pose considerable stability challenges when formulating a polymeric nanoparticle for biomedical purposes.[24] In this study the stability of the raspberry nanoparticles was investigated in 50% rat plasma via *inductively coupled plasma – atomic emission spectroscopy* (ICP-AES) as the 1,10-phenanthroline iron quantification assay did not work with biological samples (Figure 3.4.2.2.). A reasonable hypothesise is that ions or proteins within the blood samples may have competitively bound with the iron(II) or 1,10-phenanthroline ligands rendering the assay completely useless. ICP-AES is an analytical technique used for the detection of trace elements. A superheated gas cloud of charged particles is used to dissociate the sample into its constituent atoms or ions, exciting them to a higher energy level. As they return to their ground state they emit photons of a characteristic wavelength depending on the element present. This technique was found to be the most appropriate method for measuring iron content in the biological samples. Naturally, plasma samples do contain endogenous levels of iron and so background levels were always carefully monitored and subtracted from any data collected. The iron oxide raspberry nanoparticles had satisfactory plasma stability retaining stabilities of; 92%, 70% and 66% after 1 h, 24 h and 48 h, respectively. Overall, this was an extremely favourable result for a polymeric nanoparticle system in plasma and should be suitable for most biomedical applications.

3.5.3 Pharmacokinetics and biodistribution

To determine the *in vivo* biodistribution of the raspberry nanoparticles, various tissues (blood, liver, spleen, brain, lung, kidney and heart) were collected at various time points and the iron content measured using ICP-AES following tail vein injection into female BALB/c mice. A large dose at 32.5 mg Fe/kg was administrated in order to distinguish IONP iron levels from endogenous iron levels found in the blood and organs. By taking the average blood volume in a 20 g mouse to be 2 mL it can be

calculated that by the first 15 min time point 61% of the injected dose was present in the blood (Figure 3.4.3.1). After this point iron levels continued to decay and by the 1 h time point 43% of the injected dose was present in the blood. By the 8 h time point iron levels had reached background concentrations. Overall, the raspberry nanoparticles have a blood half-life ($t_{1/2}$) of 28.3 min. Literature findings report considerably varied IONP blood half-lives, typically ranging from several minutes to several hours, although some have been detected in the blood for longer.[25] This high variation in IONP half-life is often attributed to the engineered parameters of size, charge and surface coating of each IONP system under examination. As expected, the longer half-lives are often observed for PEGylated systems ($t_{1/2}$, 61–91 min in mice species), however the raspberry nanoparticles seem to compare quite favourable to a number of the dextran IONPs ($t_{1/2}$, 5–60 min in mice species).[26,27] The large dose administrated must also be considered, this was carried out in order to distinguish between endogenous levels of iron and the iron from the IONPs. However one study by *Levy et al* concluded that they may have observed IONP saturation within the spleen and, if this is the case, then one might expect to see longer blood circulation times of the nanoparticles under investigation.[28] A comprehensive summary of IONP blood half-lives can be found in a review by *Arami et al.*[25]

Over time, the data suggests that raspberry nanoparticles accumulate in the liver and spleen (Figure 3.4.3.2 and 3.4.3.3). By taking the average dry liver weight in a 20 g mouse to be 0.2 g and its dry spleen to be 30 mg it can be calculated that by the first 15 min time point, 23% of the injected dose is present in the liver and 11% of the injected dose is present in the spleen. By the 1 h time point this increases to; 41% in the liver and 15% in the spleen. Accumulation in the liver and spleen is widely considered the most common elimination pathway for IONP systems and is most likely as a result of the *first pass effect* in which the nanoparticles accumulate in the macrophage rich filter like tissues of these organs. The liver is comprised of sinusoidal

endothelial cells which have a sieve like nature and contain fenestrations that range between 100-200 nm.[29] This fenestrated tissue can easily filter out macromolecules of appreciable size and is a major challenge when designing long circulating nanoparticles. As the raspberry nanoparticles have an average hydrodynamic diameter of 190 nm many of these particles could simply be mechanically filtered out by the liver organ. The tissue of the liver is also lined with kupffer cells. These cells are highly effective at quickly phagocytizing the nearby IONPs from the blood.[30,31] Due to the high rate of IONP accumulation in the liver, past research has focused on using IONP as a negative MRI contrast agent for the detection of liver diseases with the majority of early clinical trials and commercially available products focusing in this area. The spleen can be divided into three key tissue types: The *white pulp* which, is responsible for the production of B and T lymphocytes; the *red pulp* which, is comprised of highly porous sinusoids which mechanically filter the blood as it enters the spleen and, the *marginal zone* which is lined with macrophage rich tissue.[32] Not surprisingly, studies have reported that IONPs often rapidly accumulate in the red pulp and the marginal zones of the spleen as the nanoparticles are filtered out by fenestrated venules and collected by the macrophages.[33,34] Several animal and clinical experiments have been performed predominantly focusing on the detection of spleen lesions using IONP contrast agents.[35] The iron oxide raspberry nanoparticles appear to adhere to the standard model and quickly accumulate in the liver and spleen reaching saturation in these organs by the 30 min time point. The iron concentrations stay at elevated levels throughout the duration of the 48 h experiment which is consistent with other studies that have reported increased levels of iron up to several days to weeks after treatment.[28,36-38]

There was no increase in iron concentration in the brain (Figure 3.4.3.4). This is most likely due to the highly effective *blood brain barrier* (BBB), a naturally occurring defence system which is made up of tightly packed endothelial cells that form highly

restrictive tight junctions designed to keep macromolecular toxins from entering the brain.[39] Studies showing IONPs reaching the brain tissue via parenteral administration do exist for example some recent studies include: *Kim et al* who found their silica coated nanoparticles were distributed to the brain while keeping the BBB intact and *Raut et al* learnt that by placing a magnetic field near the brain they could obtain preferential accumulation at the site.[40,41] Furthermore, *Veiseh et al* managed to deliver their protein targeted polyethylene glycol–grafted chitosan copolymer IONP to brain tumours while also keeping the BBB intact.[42] Although these seem like promising examples of IONP brain delivery, these discoveries are not common and their mechanism of transport through the BBB still needs to be investigated. A key advantage of IONPs not accumulating in the brain is that in recent years, scientists have found links between increased deposits of iron in the brain and neurodegenerative diseases such as Alzheimer's.[43,44] The causative link still needs investigating, however the case could be made that there is very little risk of these types of adverse effect with the raspberry nanoparticles.

A considerable iron increase was detected in the lungs however this was cleared after 4 h (Figure 3.4.3.5). In this case the increase in iron is most likely due to the raspberry nanoparticles being present in the blood at these moments. In other studies, IONPs have been found in the lungs and this is often attributed to the lung's large vasculature combined with the presence of macrophage rich tissue in the alveoli.[45,46] Although there is a severe need to treat and identify chronic obstructive pulmonary diseases, their detection using a T2 weighted IONP enhanced MRI images does pose a challenge due to lungs often being characterised by their distinct lack of an MRI signal. This said, it would still be an effective route for therapeutic intervention if drug loaded IONPs did display preferential accumulation in the lung tissue.[47]

The heart did exhibit an increase in iron in the early time points and this is probably due to the raspberry nanoparticles being present in the blood at these moments (Figure 3.4.3.6). Creating agents that target the heart is of high importance as myocardial infarction remains a leading cause of death and disability. In a study by *Chapon et al* they found that their dextran-IONPs did show higher contrast between healthy and ischemic myocardium and since then, two clinical studies have also shown Ferumoxytol® (Feraheme®) to produce hypo-enhancement in infarcted left ventricular walls.[48,49] Mechanistically, it is understood that ischemic injury in the heart triggers a release of macrophages to aid with the wound healing process and it is these extra macrophages that are responsible for the accumulation of IONPs in the damaged heart tissue.[25]

The kidneys also revealed a small increase in iron concentration in the early time points and this is also probably due to the raspberry nanoparticles being present in the blood at these time points (Figure 3.4.3.7). Like the liver and spleen, the kidneys are also reported to have filter like properties however, its filtering capacity is usually reserved for particles that are much smaller (<10 nm), as a result the raspberry nanoparticles are probably too big to demonstrate any renal filtration.[50] No adverse effects were observed in any of the animals in this experiment, even, when the administered dose was several fold higher than that needed for MR imaging. Overall from the findings presented here, one could speculate that shorter MRI scan times using this contrast agent would best serve to image whole body pathological conditions, whereas longer scan times would be preferential for imaging organs of the reticuloendothelial system such as the liver and spleen.

3.5.4 In vivo MRI

To evaluate the imaging potential of the raspberry nanoparticles, *in vivo* MR imaging was conducted using a 1T bench top MRI scanner (ICON™, Bruker, UK). Raspberry

nanoparticles (5 mg Fe/kg) were injected into the tail vein of female BALB/c mice. Pre-treatment and 1 hour post injection T2 weighted coronal and axial maps were collected (Figure 3.4.4.1). Noticeable hypointense contrast was observed in the liver to the extent where hepatic liver vessels became apparent.[51] The portal vein also was clearly visible in post contrast images. The benefit of having large contrast in the liver region is that many of the surrounding organs became easy to identify, most notably the kidneys which were often hard to distinguish from the liver in the pre-treatment images. Negative contrast was also observed in the spleen region. The data presented here corresponds nicely to the data collected from the pharmacokinetic data with most of the image darkening being observed in the liver and spleen. To assess the raspberry nanoparticle's clinical relevance, a commercially available IONP negative contrast agent Ferucarbotran® (Resovist®) was also measured (Figure 3.4.4.2). As predicted, darkening of the liver was also observed, however many of the hepatic liver vessels witnessed with the raspberry nanoparticles were not seen with Ferucarbotran®. Additionally, Ferucarbotran® displayed considerably more image darkening in the lungs which was not observed with the raspberry nanoparticles (Figure 3.4.4.3). Overall, the data presented here shows that the raspberry nanoparticles are more effective at highlighting fine vessel structure of the liver when compared to the commercial system (Figure 3.4.4.4). The reason why these hepatic liver veins are visualised with the raspberry nanoparticles and not the commercially available Ferucarbotran® could be associated with the size of the nanoparticle under investigation. The raspberry nanoparticles and Ferucarbotran® have average hydrodynamic sizes of 190 nm and 50 nm, respectively. After injection into the blood vasculature system, smaller sized Ferucarbotran® nanoparticles have the ability to penetrate and infiltrate the fenestrated sieve like tissue of the liver to a greater extent than the larger raspberry nanoparticles. The leaves areas surrounded by densely packed endothelial cells protected from the raspberry nanoparticles and therefore do

not appear hypointense in the resulting MR image, unlike Ferucarbotran® which is small enough to penetrate these areas.

To be able to quantify the effect the raspberry nanoparticles had on the T2 relaxivity in the various tissues, T2 relaxivity maps were collected and compared to experiments using no contrast agent and Ferucarbotran® (Figure 3.4.4.5). Maps were collected 1 hour post administration with the contrast agent. The T2 relaxation was determined by curve fitting the echo times (TE) of each pixel in the image using MATLAB (Mathworks, UK). A summary of the T2 relaxation times of specific regions of interest (lungs, liver, kidney and spleen) can be seen in Figure 3.4.4.6. The heart could not be mapped accurately as it gave a large variation in the results collected, this was most likely due to movement from the beating heart during the experiment which would have taken several seconds to acquire for each slice. Respiration was accounted for by gating the experimental procedure and as a result, show that the raspberry nanoparticles had no significant effect on the lungs unlike Ferucarbotran®, which did display a significant effect on relaxation time in the region. The same relationship was observed in the kidneys. Both the raspberry nanoparticles and Ferucarbotran® gave significant effects on relaxivity in the liver and spleen to a similar extent. Overall this data signifies an overall difference between the raspberry nanoparticles and the commercially available Ferucarbotran®; at the 1 hour time point both species can be used to give hypointense MRI contrast in healthy liver and spleen tissue, however the raspberry nanoparticles do not affect other organs such as the lungs and kidneys making them somewhat more selective in their organ imaging. IONPs have been used to image organs of the reticuloendothelial system for a number of years, however their popularity has decreased considerable with many of the original IONP MRI liver imaging contrast agents having been withdrawn from the market. This has largely been attributed to their lack of specificity to a disease target. The work presented here shows that the iron oxide raspberry nanoparticles can be

used for imaging in biological environments, especially in the liver and spleen without any of the other regions or organs being involved. However their true success will be measured upon their specificity towards a disease target and the extent to which they are useful for the diagnosis of liver and spleen diseases, such as liver cirrhosis, splenic rupture and cancer.

3.5.5 Tumour modelling

In this project a tumour study was established to investigate the iron oxide raspberry nanoparticles' ability to distribute and accumulate into tumour tissue. The experimental hypothesis was that distribution and accumulation of non-targeted nanoparticles would be driven by the *enhanced permeability and retention* (EPR) effect. This is a well-documented effect where particles of appreciable size display preferential accumulation in tumour tissue by exploiting the leaky vasculature of the rapidly growing mass of cells. In this study a murine 4T1 breast cancer cell line was selected as it is widely regarded as one of the best models to produce fast growing reproducible breast tissue tumours in immunocompetent BALB/c mice.[52] When inoculated into breast tissue, 4T1 cells are known to rapidly progress into a lethal disease quickly spreading to the liver, lungs, bone and brain, making this cell line a good model for late stage metastatic breast cancer.[53] Unlike many other flank tumour models, 4T1 cells can be implemented into non-immunocompromised BALB/c mice. Finding cells lines that can be used on immunocompetent species is considered significant as the immune system is often a key defence mechanism in the body's fight against a foreign species like a drug or imaging agent. Most tumour models are conducted in immune deficient nude mice in order to allow human tissues to be grown, however removing the immune system may introduce a significant discrepancy into the model that does not translate to typical cancer patients who often will have immune function. In this project it was found that 4T1 cell cultures grew rapidly and aggressively giving a doubling time of 1.8 days (Figure 3.4.5.1). 4T1

growth dynamics followed a typical sigmoidal curve, which is composed of latency phase, exponential growth phase and a stationary phase. *In vivo* pilot studies were conducted in order to establish a reasonable protocol and understand the growth progress of the 4T1 tumour cells. Female BALB/c mice were injected with cancer cells in the right lower flank via a subcutaneous injection. The size of the tumour was monitored over the duration of the experiment using digital callipers (Figure 3.4.5.2).[54] Fully grown tumours (100 mm^3) could be grown within 7 days. Injecting 2 $x10^6$ cells displayed more variation than injecting 1 $x10^6$ cells as, n=1 failed to take in the same manner. There appears to be little difference between the growth rate of injecting 2 $x10^6$ cells and 1 $x10^6$ cells (excluding n=1). Weight was monitored over the experiment as an indication of health (Figure 3.4.5.3). n=1 in the group that was inoculated with 2 $x10^6$ cells was the only animal to lose weight over the experiment however, it was still within the 15% deviation from initial weight. All other animals gained weight over the experiment indicating satisfactory health. Tumours were excised at the end of the pilot experiment revealing that solid tumours had developed at the site of injection that were spherical and homogenous in nature (Figure 3.4.5.4). In conclusion to the pilot study, 1 $x10^6$ cells were used to inoculate mice in further studies as this produced good tumours and had a higher take rate than using 2 $x10^6$ cells.

3.5.6 In vivo tumour biodistribution and MRI

The raspberry nanoparticles were evaluated for their specificity towards a disease target by performing an *in vivo* biodistribution experiment. 4T1 flank tumours were developed by subcutaneously injecting 1 $x10^6$ cells into the lower right flank of BALB/c female mice. All the mice developed homogenous tumours as expected confirming the robustness of the 4T1 model. As previously used, a large dose at 32.5 mg Fe/kg was administrated and at various time points tissues were collected and analysed via

ICP-AES (Figure 3.4.6.1). Tissue was collected from muscle in the left flank to act as a negative control (Figure 3.4.6.2). It was found that no increase in iron levels was observed in the tumour tissue at any time point. Although a disappointing result it was thought that investigating this result further could be beneficial.

In vivo MRI tumour investigations were conducted on the raspberry nanoparticles using Ferucarbotran® as a control. As predicted Ferucarbotran® did not accumulate in the tumour over a 2 h duration (Figure 3.4.7.1). Resovist® has been used to diagnose liver carcinoma, however it does so by accumulating in healthy liver tissue consequently, reducing its signal and highlighting the regions of disease. Using the Molecular Envelope Technology (GCPQ) to create a positively charged nanoparticle it was predicted that the raspberry nanoparticles would overcome the challenges faced by the mononuclear phagocyte system (predominantly the liver and spleen) and accumulate in the tumour tissue as a result of the EPR effect. Raspberry nanoparticles were injected into BALB/c mice at a concentration of 5 mg Fe/kg and monitored over 2 h via MRI (Figure 3.4.7.2). Results show that no signal darkening was observed in the flank tumour over the 2 h period. These results correlate well with the ICP-AES tumour biodistribution data. T2 relaxation maps of a flank tumour were also collected over a 2 hour period (Figure 3.4.7.3 and Figure 3.4.7.4). The results indicate there was a small significant reduction in relaxation time between the pre-contrast and post-contrast experiments. This could be evidence that small amounts of raspberry nanoparticles are accumulating in the tumour tissue and overall slightly reducing its relaxation time, however in conclusion, this effect is so small it has no effect on the overall MR image to a human observer. These results suggest that in this 4T1 flank tumour model the raspberry nanoparticles do not act as a good diagnostic agent for the detection of tumour tissue.

When considering results such as the ones above, evaluating the limitations of these complex experiments should be discussed. The Alliance for Nanotechnology in Cancer recently published that to evaluate the EPR effect, sub-cutaneous flank tumour xenografts were thought to offer limited value as these types of tumours did not often translate well into human diseases.[55] In addition to this, the National Cancer Institute (NCI) screening programme has stated, the activity of an agent *in vitro* did not predict the activity in subcutaneous flank xenograft models, which in turn did not predict for the activity against clinical cancer.[56,57] The use of flank tumour animal models as a predictive tool for the performance of cancer treatments in patients has been extensively debated in recent years. Defining the optimal cancer model to evaluate the activity of a drug or imaging agent still remains an elusive goal for oncologists to this day. This said, it is still widely considered that the flank tumour model is a useful experiment and its success can be significantly increased by selecting and culturing a tumour with similar factors that resemble the disease that one aims to mimic. Factors that have considerable effects on the tumour model include: tumour volume, type of tumour, location, nature of the vasculature and the surrounding stroma and macrophage infiltration. The 4T1 cell line may model the effect of late stage breast cancer very well however, its microenvironment may not be suitable to study the EPR effect with this type of nanoparticle. In future it would be wise to understand the micro environment of the 4T1 flank tumour; physically, using microscopy, histochemical procedures and size exclusion experimentation using high molecular weight dyes and; chemically, by evaluating and quantifying the biochemistry at the tumour site. When considering the above result one should also reflect on the blood half-life ($t_{1/2}$). In the seminal work of *Matsumura and Maeda* they claimed that a nanoparticle must be in systemic circulation for several hours before nanoparticle can be influenced by the EPR effect.[14,15] Upon reflection the raspberry nanoparticle's $t_{1/2}$ of 28.3 min may not be long enough for it to take advantage of the EPR effect and hence, provides evidence to support the standard theory.

On all accounts a number of passively targeted IONP entities have been shown to accumulate in tumour tissues for example; *Moore et al* was successfully able to obtain contrast in their gliosarcoma rodent model using a dextran-IONP.[58] Laresen et al showed tumour uptake in their silane anchored PEGylated IONP in a flank tumour model while *Park et al* have had success delivering their non-targeted dextran based IONP nanoworms.[59,60] A number of other examples exist however, relative to the magnitude of IONP research, the author believes that evidence of passively targeted tumour nanoparticles is not overly abundant with the majority relying on dextran and PEGylated systems to provide the stealth surface coating needed to evade the reticuloendothelial system.[61,62] In recent years, one strategy used to increase the specificity and delivery of a nanoparticle to a diseased site is by a practise known as *active targeting*. It is widely known that cancers often display an overexpression of biological markers and receptors and so by anchoring a targeting ligand to the outer sphere of the nanoparticle one may improve its affinity to a specific target.[63,64] Many innovative methods have been used to target IONPs to disease sites including the surface modification using; folate like molecules, peptides, proteins, antibodies and aptamers. A comprehensive summary of active targeted IONPs can be found in a recent review by *Rosen et al.*[65] This said however, one cannot simply rely on active targeting as there are a number of examples in the literature where active targeting has had little to no effect on IONP tumour accumulation. *NDong et al* found their monoclonal antibody targeted IONP showed great promise through extensive *in vitro* testing, however failed to display any significant tumour uptake in their animal models.[66] This is because the biological environment of an animal is incredibly complex and nanoparticles are often subjected to a range of biochemical processes.

3.6 Conclusions

In conclusion, this chapter has conducted a number of pre-clinical experiments to evaluate the effectiveness of the iron oxide raspberry nanoparticles as an MRI contrast agent. Results demonstrate that the iron oxide raspberry nanoparticles have good colloidal stability in a range of biologically relevant solutions (H2O, 0.9% NaCl, 5% dextrose and 1X PBS) and display adequate stability in blood plasma. Pharmacokinetic studies have shown that the nanoparticles have a blood half-life of 28.3 min and quickly accumulate in the liver and spleen. The raspberry nanoparticles are also distributed to the lungs, heart and kidneys, however they do not accumulate in these organ tissues, no nanoparticle distribution or accumulation was observed in the brain. *In vivo* MRI studies show that these nanoparticles do act as effective MRI contrast agent in the liver and spleen and when compared to the commercially available product, they appear to make it easier to visualise the fine vesical structure of the liver and its surrounding organs. To evaluate the iron oxide raspberry's specificity towards a disease target an *in vivo* tumour model was conducted. A murine 4T1 breast cancer cell line was cultured and subcutaneously injected into the lower flank of BALB/c mice at a concentration of 1 $x10^6$ cells per animal. Fully grown flank tumours (100 mm^3) could be grown on healthy mice within 7 days. Iron oxide raspberry nanoparticles were injected into tumour bearing mice, however a pharmacokinetic study showed no nanoparticle accumulation at the tumour site. This result was later confirmed by conducting *in vivo* MRI experiments which also gave no observable hypointense contrast at the tumour site. T2 relaxation maps may have indicated a small change in relaxivity after contrast agent administration however, it was not large enough to produce any meaningful contrast effect in an MR image. Using a 4T1 sub-cutaneous flank tumour, the raspberry nanoparticles do not appear to be a good candidate for MRI tumour diagnostics. Future work would be to evaluate

the raspberry nanoparticles on alternative tumour models to validate these results and in addition to this, consider strategies to PEGylate or anchor an active targeting ligand to the outer sphere of the nanoparticle to improved tumour distribution and penetration. Overall, the iron oxide raspberry nanoparticles proved to give good contrast in the liver but their true success will rely on their specificity towards a disease target.

(1) Hau, J.; Schapiro, S. J.: *Handbook of Laboratory Animal Science, Second Edition: Essential Principles and Practices*; CRC Press, 2002.

(2) Ai, H.; Flask, C.; Weinberg, B.; Shuai, X. T.; Pagel, M. D.; Farrell, D.; Duerk, J.; Gao, J. Magnetite-Loaded Polymeric Micelles as Ultrasensitive Magnetic-Resonance Probes. *Advanced Materials* **2005**, *17*, 1949-1952.

(3) Berret, J.-F.; Schonbeck, N.; Gazeau, F.; El Kharrat, D.; Sandre, O.; Vacher, A.; Airiau, M. Controlled Clustering of Superparamagnetic Nanoparticles Using Block Copolymers: Design of New Contrast Agents for Magnetic Resonance Imaging. *Journal of the American Chemical Society* **2006**, *128*, 1755-1761.

(4) Kim, J.; Lee, J. E.; Lee, S. H.; Yu, J. H.; Lee, J. H.; Park, T. G.; Hyeon, T. Designed Fabrication of a Multifunctional Polymer Nanomedical Platform for Simultaneous Cancer- Targeted Imaging and Magnetically Guided Drug Delivery. *Advanced Materials* **2008**, *20*, 478-483.

(5) Pöselt, E.; Kloust, H.; Tromsdorf, U.; Janschel, M.; Hahn, C.; Maßlo, C.; Weller, H. Relaxivity Optimization of a PEGylated Iron-Oxide-Based Negative Magnetic Resonance Contrast Agent for T2-Weighted Spin–Echo Imaging. *ACS Nano* **2012**, *6*, 1619-1624.

(6) Su, H.; Liu, Y.; Wang, D.; Wu, C.; Xia, C.; Gong, Q.; Song, B.; Ai, H. Amphiphilic starlike dextran wrapped superparamagnetic iron oxide nanoparticle clsuters as effective magnetic resonance imaging probes. *Biomaterials* **2013**, *34*, 1193-1203.

(7) Su, H.-Y.; Wu, C.-Q.; Li, D.-Y.; Ai, H. Self-assembled superparamagnetic nanoparticles as MRI contrast agents— A review. *Chinese Physics B* **2015**, *24*, 127506.

(8) Lin, Y.; Wang, S.; Zhang, Y.; Gao, J.; Hong, L.; Wang, X.; Wu, W.; Jiang, X. Ultra-high relaxivity iron oxide nanoparticles confined in polymer nanospheres for tumor MR imaging. *Journal of Materials Chemistry B* **2015**, *3*, 5702-5710.

(9) Lazzari, S.; Moscatelli, D.; Codari, F.; Salmona, M.; Morbidelli, M.; Diomede, L. Colloidal stability of polymeric nanoparticles in biological fluids. *Journal of Nanoparticle Research* **2012**, *14*, 1-10.

(10) Jambhekar, S.; Breen, P. J.: *Basic Pharmacokinetics*; Pharmaceutical Press, 2009.

(11) Conn, P. M.: *Animal Models for the Study of Human Disease*; Elsevier Science, 2013.

(12) Cekanova, M.; Rathore, K. Animal models and therapeutic molecular targets of cancer: utility and limitations. *Drug design, development and therapy* **2014**, *8*, 1911-1921.

(13) Iyer, A. K.; Khaled, G.; Fang, J.; Maeda, H. Exploiting the enhanced permeability and retention effect for tumor targeting. *Drug Discovery Today* **2006**, *11*, 812-818.

(14) Matsumura, Y.; Maeda, H. A New Concept for Macromolecular Therapeutics in Cancer Chemotherapy: Mechanism of Tumoritropic Accumulation of Proteins and the Antitumor Agent Smancs. *Cancer Research* **1986**, *46*, 6387-6392.

(15) Maeda, H. The enhanced permeability and retention (EPR) effect in tumor vasculature: the key role of tumor-selective macromolecular drug targeting. *Advances in Enzyme Regulation* **2001**, *41*, 189-207.

(16) Maeda, H. Modified Therapeutic Proteins SMANCS and polymer-conjugated macromolecular drugs: advantages in cancer chemotherapy. *Advanced Drug Delivery Reviews* **1991**, *6*, 181-202.

(17) Maeda, H.; Seymour, L. W.; Miyamoto, Y. Conjugates of anticancer agents and polymers: advantages of macromolecular therapeutics in vivo. *Bioconjugate Chemistry* **1992**, *3*, 351-362.

(18) Tao, K.; Fang, M.; Alroy, J.; Sahagian, G. G. Imagable 4T1 model for the study of late stage breast cancer. *BMC cancer* **2008**, *8*, 228.

(19) Loftsson, T.: *Drug Stability for Pharmaceutical Scientists*; Elsevier Science, 2014.

(20) Elsabahy, M.; Wooley, K. L. Design of polymeric nanoparticles for biomedical delivery applications. *Chemical Society Reviews* **2012**, *41*, 2545-2561.

(21) Patravale, V. B.; Date, A. A.; Kulkarni, R. M. Nanosuspensions: a promising drug delivery strategy. *Journal of Pharmacy and Pharmacology* **2004**, *56*, 827-840.

(22) Wu, L.; Zhang, J.; Watanabe, W. Physical and chemical stability of drug nanoparticles. *Advanced Drug Delivery Reviews* **2011**, *63*, 456-469.

(23) Walczak, M. M.; Flynn, N. T. Spectroelectrochemical study of the generation of tris-(1,10-phenanthroline) iron(II/III) from μ-oxo-bis[aquabis(1,10-phenanthroline) iron(III)]. *Journal of Electroanalytical Chemistry* **1998**, *441*, 43-49.

(24) Yang, W.; Zhang, L.; Wang, S.; White, A. D.; Jiang, S. Functionalizable and ultra stable nanoparticles coated with zwitterionic poly(carboxybetaine) in undiluted blood serum. *Biomaterials* **2009**, *30*, 5617-5621.

(25) Arami, H.; Khandhar, A.; Liggitt, D.; Krishnan, K. M. In vivo delivery, pharmacokinetics, biodistribution and toxicity of iron oxide nanoparticles. *Chemical Society Reviews* **2015**, *44*, 8576-8607.

(26) Chambon, C.; Clement, O.; Le Blanche, A.; Schouman-Claeys, E.; Frija, G. Superparamagnetic iron oxides as positive MR contrast agents: In vitro and in vivo evidence. *Magnetic Resonance Imaging* **1993**, *11*, 509-519.

(27) Bengele, H. H.; Palmacci, S.; Rogers, J.; Jung, C. W.; Crenshaw, J.; Josphson, L. Biodistribution of an ultrasmall superparamagnetic iron oxide colloid, BMS 180549, by different routes of administration. *Magnetic Resonance Imaging* **1994**, *12*, 433-442.

(28) Levy, M.; Luciani, N.; Alloyeau, D.; Elgrabli, D.; Deveaux, V.; Pechoux, C.; Chat, S.; Wang, G.; Vats, N.; Gendron, F.; Factor, C.; Lotersztajn, S.; Luciani, A.; Wilhelm, C.; Gazeau, F. Long term in vivo biotransformation of iron oxide nanoparticles. *Biomaterials* **2011**, *32*, 3988-3999.

(29) Braet, F.; Wisse, E. Structural and functional aspects of liver sinusoidal endothelial cell fenestrae: a review. *Comparative Hepatology* **2002**, *1*, 1-1.

(30) Dupas, B.; Berreur, M.; Rohanizadeh, R.; Bonnemain, B.; Meflah, K.; Pradal, G. Electron microscopy study of intrahepatic ultrasmall superparamagnetic iron oxide kinetics in the rat. Relation with magnetic resonance imaging. *Biology of the Cell* **1999**, *91*, 195-208.

(31) Briley-Saebo, K.; Bjørnerud, A.; Grant, D.; Ahlstrom, H.; Berg, T.; Kindberg, G. M. Hepatic cellular distribution and degradation of iron oxide nanoparticles following single intravenous injection in rats: implications for magnetic resonance imaging. *Cell and Tissue Research* **2004**, *316*, 315-323.

(32) Tarantino, G.; Savastano, S.; Capone, D.; Colao, A. Spleen: A new role for an old player? *World journal of gastroenterology* **2011**, *17*, 3776-3784.

(33) Arami, H.; Khandhar, A. P.; Tomitaka, A.; Yu, E.; Goodwill, P. W.; Conolly, S. M.; Krishnan, K. M. In vivo multimodal magnetic particle imaging (MPI) with tailored magneto/optical contrast agents. *Biomaterials* **2015**, *52*, 251-261.

(34) Demoy, M.; Andreux, J.-P.; Weingarten, C.; Gouritin, B.; Guilloux, V.; Couvreur, P. Spleen Capture of Nanoparticles: Influence of Animal Species and Surface Characteristics. *Pharmaceutical Research* **1999**, *16*, 37-41.

(35) Ferrucci, J. T.; Stark, D. D. Iron oxide-enhanced MR imaging of the liver and spleen: review of the first 5 years. *American Journal of Roentgenology* **1990**, *155*, 943-950.

(36) Gu, L.; Fang, R. H.; Sailor, M. J.; Park, J.-H. In Vivo Clearance and Toxicity of Monodisperse Iron Oxide Nanocrystals. *ACS Nano* **2012**, *6*, 4947-4954.

(37) Weissleder, R.; Bogdanov, A.; Neuwelt, E. A.; Papisov, M. Long-circulating Drug Delivery SystemsLong-circulating iron oxides for MR imaging. *Advanced Drug Delivery Reviews* **1995**, *16*, 321-334.

(38) Jain, T. K.; Reddy, M. K.; Morales, M. A.; Leslie-Pelecky, D. L.; Labhasetwar, V. Biodistribution, Clearance, and Biocompatibility of Iron Oxide Magnetic Nanoparticles in Rats. *Molecular Pharmaceutics* **2008**, *5*, 316-327.

(39) Chen, Y.; Liu, L. Modern methods for delivery of drugs across the blood–brain barrier. *Advanced Drug Delivery Reviews* **2012**, *64*, 640-665.

(40) Kim, J. S.; Yoon, T.-J.; Yu, K. N.; Kim, B. G.; Park, S. J.; Kim, H. W.; Lee, K. H.; Park, S. B.; Lee, J.-K.; Cho, M. H. Toxicity and Tissue Distribution of Magnetic Nanoparticles in Mice. *Toxicological Sciences* **2006**, *89*, 338-347.

(41) Raut, S. L.; Kirthivasan, B.; Bommana, M. M.; Squillante, E.; Sadoqi, M. The formulation, characterization and in vivo evaluation of a magnetic carrier for brain delivery of NIR dye. *Nanotechnology* **2010**, *21*, 395102.

(42) Veiseh, O.; Sun, C.; Fang, C.; Bhattarai, N.; Gunn, J.; Kievit, F.; Du, K.; Pullar, B.; Lee, D.; Ellenbogen, R. G.; Olson, J.; Zhang, M. Specific Targeting of Brain Tumors with an Optical/Magnetic Resonance Imaging Nanoprobe across the Blood-Brain Barrier. *Cancer Research* **2009**, *69*, 6200-6207.

(43) Honda, K.; Casadesus, G.; Petersen, R. B.; Perry, G.; Smith, M. A. Oxidative Stress and Redox-Active Iron in Alzheimer's Disease. *Annals of the New York Academy of Sciences* **2004**, *1012*, 179-182.

(44) Ke, Y.; Qian, Z. M. Iron misregulation in the brain: a primary cause of neurodegenerative disorders. *The Lancet Neurology* **2003**, *2*, 246-253.

(45) Xu, H.; Cheng, L.; Wang, C.; Ma, X.; Li, Y.; Liu, Z. Polymer encapsulated upconversion nanoparticle/iron oxide nanocomposites for multimodal imaging and magnetic targeted drug delivery. *Biomaterials* **2011**, *32*, 9364-9373.

(46) Kievit, F. M.; Stephen, Z. R.; Veiseh, O.; Arami, H.; Wang, T.; Lai, V. P.; Park, J. O.; Ellenbogen, R. G.; Disis, M. L.; Zhang, M. Targeting of Primary Breast Cancers and Metastases in a Transgenic Mouse Model Using Rationally Designed Multifunctional SPIONs. *ACS Nano* **2012**, *6*, 2591-2601.

(47) Bailey, M. M.; Berkland, C. J. Nanoparticle formulations in pulmonary drug delivery. *Medicinal Research Reviews* **2009**, *29*, 196-212.

(48) Chapon, C.; Franconi, F.; Lemaire, L.; Marescaux, L.; Legras, P.; Saint-Andre, J. P.; Denizot, B.; Le Jeune, J. J. High field magnetic resonance imaging evaluation of superparamagnetic iron oxide nanoparticles in a permanent rat myocardial infarction. *Invest Radiol* **2003**, *38*, 141-146.

(49) Bietenbeck, M.; Florian, A.; Sechtem, U.; Yilmaz, A. The diagnostic value of iron oxide nanoparticles for imaging of myocardial inflammation--quo vadis? *Journal of cardiovascular magnetic resonance : official journal of the Society for Cardiovascular Magnetic Resonance* **2015**, *17*, 54.

(50) Longmire, M.; Choyke, P. L.; Kobayashi, H. Clearance properties of nano-sized particles and molecules as imaging agents: considerations and caveats. *Nanomedicine* **2008**, *3*, 703-717.

(51) Gandhi, S. N.; Brown, M. A.; Wong, J. G.; Aguirre, D. A.; Sirlin, C. B. MR Contrast Agents for Liver Imaging: What, When, How. *RadioGraphics* **2006**, *26*, 1621-1636.

(52) Pulaski, B. A.; Ostrand-Rosenberg, S. Mouse 4T1 breast tumor model. *Current protocols in immunology / edited by John E. Coligan ... [et al.]* **2001**, *Chapter 20*, Unit 20.22.

(53) DuPre, S. A.; Redelman, D.; Hunter, K. W., Jr. The mouse mammary carcinoma 4T1: characterization of the cellular landscape of primary tumours and metastatic tumour foci. *International journal of experimental pathology* **2007**, *88*, 351-360.

(54) Carlsson, G.; Gullberg, B.; Hafstrom, L. Estimation of liver tumor volume using different formulas - an experimental study in rats. *Journal of cancer research and clinical oncology* **1983**, *105*, 20-23.

(55) Prabhakar, U.; Maeda, H.; Jain, R. K.; Sevick-Muraca, E. M.; Zamboni, W.; Farokhzad, O. C.; Barry, S. T.; Gabizon, A.; Grodzinski, P.; Blakey, D. C. Challenges and key considerations of the enhanced permeability and retention effect for nanomedicine drug delivery in oncology. *Cancer Res* **2013**, *73*, 2412-2417.

(56) Morton, C. L.; Houghton, P. J. Establishment of human tumor xenografts in immunodeficient mice. *Nat. Protocols* **2007**, *2*, 247-250.

(57) Johnson, J. I.; Decker, S.; Zaharevitz, D.; Rubinstein, L. V.; Venditti, J. M.; Schepartz, S.; Kalyandrug, S.; Christian, M.; Arbuck, S.; Hollingshead, M.; Sausville, E. A. Relationships between drug activity in NCI preclinical in vitro and in vivo models and early clinical trials. *Br J Cancer* **2001**, *84*, 1424-1431.

(58) Moore, A.; Marecos, E.; Alexei Bogdanov, J.; Weissleder, R. Tumoral Distribution of Long-circulating Dextran-coated Iron Oxide Nanoparticles in a Rodent Model. *Radiology* **2000**, *214*, 568-574.

(59) Larsen, B. A.; Haag, M. A.; Serkova, N. J.; Shroyer, K. R.; Stoldt, C. R. Controlled aggregation of superparamagnetic iron oxide nanoparticles for the development of molecular magnetic resonance imaging probes. *Nanotechnology* **2008**, *19*, 265102.

(60) Park, J.-H.; von Maltzahn, G.; Zhang, L.; Schwartz, M. P.; Ruoslahti, E.; Bhatia, S. N.; Sailor, M. J. Magnetic Iron Oxide Nanoworms for Tumor Targeting and Imaging. *Advanced Materials* **2008**, *20*, 1630-1635.

(61) Lee, H.; Lee, E.; Kim, D. K.; Jang, N. K.; Jeong, Y. Y.; Jon, S. Antibiofouling Polymer-Coated Superparamagnetic Iron Oxide Nanoparticles as Potential Magnetic Resonance Contrast Agents for in Vivo Cancer Imaging. *Journal of the American Chemical Society* **2006**, *128*, 7383-7389.

(62) Yu, M. K.; Jeong, Y. Y.; Park, J.; Park, S.; Kim, J. W.; Min, J. J.; Kim, K.; Jon, S. Drug-Loaded Superparamagnetic Iron Oxide Nanoparticles for Combined Cancer Imaging and Therapy In Vivo. *Angewandte Chemie* **2008**, *120*, 5442-5445.

(63) Ulbrich, K.; Holá, K.; Šubr, V.; Bakandritsos, A.; Tuček, J.; Zbořil, R. Targeted Drug Delivery with Polymers and Magnetic Nanoparticles: Covalent and Noncovalent Approaches, Release Control, and Clinical Studies. *Chemical Reviews* **2016**, *116*, 5338-5431.

(64) Yu, M. K.; Park, J.; Jon, S. Targeting Strategies for Multifunctional Nanoparticles in Cancer Imaging and Therapy. *Theranostics* **2012**, *2*, 3-44.

(65) Rosen, J. E.; Chan, L.; Shieh, D.-B.; Gu, F. X. Iron oxide nanoparticles for targeted cancer imaging and diagnostics. *Nanomedicine: Nanotechnology, Biology and Medicine* **2012**, *8*, 275-290.

(66) Ndong, C.; Tate, J. A.; Kett, W. C.; Batra, J.; Demidenko, E.; Lewis, L. D.; Hoopes, P. J.; Gerngross, T. U.; Griswold, K. E. Tumor Cell Targeting by Iron Oxide Nanoparticles Is Dominated by Different Factors In Vitro versus In Vivo. *PLoS ONE* **2015**, *10*, e0115636.

Chapter 4

Encapsulation Strategies for Poorly Soluble Anticancer Drugs within Micellar Iron Oxide Nanoparticles

4.1 Introduction

A key challenge in this project was to design a theranostic nanoparticle platform to investigate if the simultaneous visualisation and treatment of a medicine would improve the effectiveness of a cancer treatment. The previous chapters have focused on the imaging element of the nanoparticle platform. This chapter outlines the efforts to investigate the therapeutic element. Chemotherapy using small molecule drugs has been considered a front line strategy for the treatment of cancer since the 1950s.[1] These small molecule entities are highly effective at providing a lethal package to cancer cells, however they are often limited by; poor solubility in aqueous environments, low bioavailability and a lack of disease specificity usually leading to off target side effects.[2,3] Scientists have attempted to overcome many of these challenges by incorporating anticancer drugs within a polymer matrix. It was envisaged from the conception of this project that the GCPQ technology would provide a good strategy for encapsulation of IONPs and a hydrophobic drug. By adding a magnetic component to an anticancer drug one can open the therapeutic to several pathways that may prove to be advantageous in the treatment of cancer: Firstly, one now has the ability to visualise the drug *in vivo* using the non-invasive technique of MRI, a strategy extensively studied in this body of work. Secondly, an element of specificity may be added, as the drug may now be magnetically guided to the site of disease by an external magnetic field and lastly, local heating may be induced by applying an alternating magnetic field. This chapter will explore methods for small molecule drug encapsulation within the magnetic iron oxide raspberry nanoparticles.

In this chapter three drugs were investigated:

Lomustine is a highly hydrophobic nitrosourea alkylating agent (<0.5 mg/mL at 25 ^{O}C) which has traditionally been used to treat glioblastoma.[4] Under physiological conditions lomustine decomposes into several intermediates, the most significant being a 2-chloroethyl carbonium ion, a highly reactive species that readily undergoes DNA alkylation and crosslinking, a lethal process that inevitably results in cell death.[5-7] Lomustine is sold under the tradename CeeNU® and has been approved for use to treat glioblastoma since 1976.

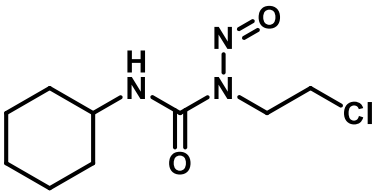

Figure 4.1.1. Chemical structure of lomustine: M_w, 233.7 g/mol

Paclitaxel is a diterpenoid first isolated from the bark of the Pacific Yew (Taxus brevifolia) and was found to stabilise microtubule assemblies within the cell, in turn inhibiting mitosis and triggering an apoptotic cell death pathway.[8] Paclitaxel is sold under the tradenames Taxol™ and Abraxane™ and has been found to have anticancer effects against a wide variety of cancers including, breast, colon, ovarian, neck and lung.[9] Paclitaxel is however a hydrophobic drug and is limited by its poor aqueous solubility (<0.3 µg/mL at 25 ^{O}C).[10] In the commercially available Taxol™ formulation, paclitaxel is administrated as an infusion formulated with ethanol and polyethoxylated caster oil (Cremphor EL®) (1:1, v/v). Cremphor EL® is not an inert excipient and has been associated with a number of adverse effects.[11,12] Paclitaxel is also available in a Cremphor EL® free formulation in the form of an albumin-paclitaxel nanoparticle suspension sold under the name of Abraxane™.

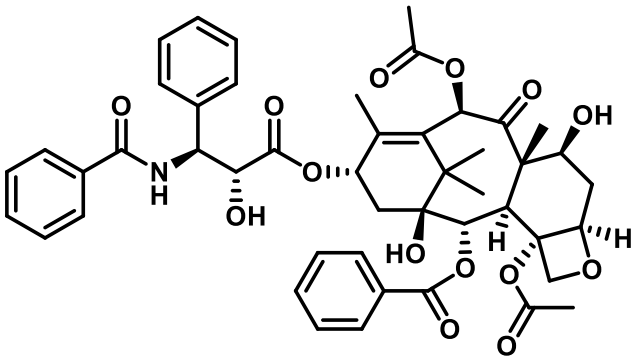

Figure 4.1.2. Chemical structure of paclitaxel: M_w, 853.9 g/mol

Methotrexate is classified as an antifolate chemotherapeutic which acts by suppressing the activity of the dihydrofolate reductase enzyme, in turn, interrupting the folate cycle which is a key mechanism needed for cell proliferation.[13] Methotrexate was one of the earliest small molecule anti-cancer drugs to be approved and has been used to treat a wide variety of cancers including; acute lymphocytic leukemia, non-Hodgkin's lymphoma, osteosarcoma, choriocarcinoma, head and neck cancer, and breast cancer.[14] Although methotrexate has been at the forefront of cancer treatment for decades it is limited by its poor water soluble at physiological pH (<0.01 mg/mL at 20 ^{O}C) and has a low bioavailability leading patients to require high doses or frequent administrations.[15] This kind of regime leads to off target side effects in the bone marrow, liver, kidney and gastrointestinal tract and drug resistance.[16,17] To overcome these challenges a number of publications have conjugated methotrexate to larger macromolecules, including PEG and albumin, to increase the plasma half-life and provide some targeting as a result of the EPR effect.[18,19]

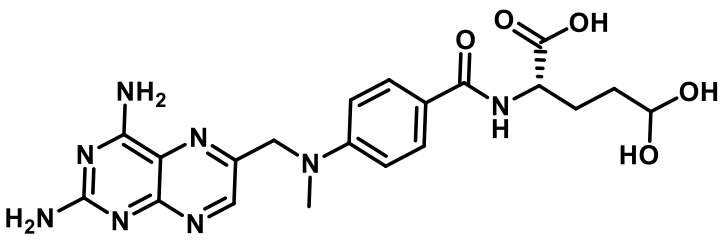

Figure 4.1.2. Chemical structure of methotrexate: M_w, 454.4 g/mol

4.2 Materials

Chemical	Purity	Supplier
Acetonitrile	>99.9%	Fisher
Chloroform	>99.9%	Sigma-Aldrich
Dimethyl sulfoxide	>99.7%	Sigma-Aldrich
Hexane	>99.5%	Sigma-Aldrich
Lomustine	>98%	Sigma-Aldrich
Methanol	>99.9%	Fisher
Methotrexate	>98%	Sigma-Aldrich
Nitrogen	>99.99%	BOC
Disodium phosphate (Na_2HPO_4)	>99%	Sigma-Aldrich
Monosodium phosphate (NaH_2PO4)	>99%	Sigma-Aldrich
Paclitaxel	99.5%	LC Laboratories
Toluene	>99.5%	Fisher

4.3 Methods

4.3.1 Lomustine HPLC procedure

High performance liquid chromatography (HPLC) was conducted using an Agilent Technologies 1200 series HPLC system, which comprised of a vacuum degasser, quaternary pump, auto-sampler, column compartment with thermostat and a variable wavelength UV detector.

Lomustine analysis was measured using in a procedure outlined by *Fisusi et al.*[20] Chromatograms were acquired using a C18 reverse phase monolithic column (Onyx, 5 µm, 100 x 4.6 mm, Phenomenex, UK) fitted with a guard column (Onyx monolithic C18 guard cartridge, 5 x 4.6 mm, Phenomenex, UK). The mobile phase consisted of methanol:water (50:50) and a flow rate of 1.5 mL/min. The column temperature was maintained at 40 ^{O}C and the detection wavelength was set at 230 nm. Formulations were diluted in methanol (1:10) and centrifuged (224 rcf, 5 min) before analysis.

4.3.2 Lomustine encapsulation via the emulsification-evaporation method

In a vial, iron oxide nanoparticles (20 mg/mL) prepared as described in *section 2.3.4* and Lomustine (5 mg/mL) were suspended in hexane (0.8 mL) and were added to a GCPQ solution (2 mL, 15 mg/mL). The solution was sonicated using probe sonication (2 x 5 min, 7 micron amplitude, Soni Prep 150, MSE, UK) at the interface between the organic and aqueous phases, creating a brown emulsion. This emulsion was left to separate over 48 h. The aqueous layer was then extracted and any residual hexane was allowed to evaporate overnight. The product was frozen and lyophilised to obtain a dry product which was then reconstituted in water (2 mL).

4.3.3 Lomustine encapsulation via the solvent free method

In a vial, 4 mg of powdered lomustine was added to a solution of raspberry nanoparticles (2 mL), prepared as described in *section 2.3.5*, with an iron content of 10 mg Fe/mL and a GCPQ content of 15 mg/mL. The solution was sonicated in an ice bath using probe sonication (2 x 5 min, Soni Prep 150, MSE, UK).

4.3.4 Lomustine encapsulation via the ethanoic co-solvent method

An ethanoic solution of lomustine (0.2 mL, 20 mg/mL) was added to an aqueous solution raspberry nanoparticles (1.8 mL) with an iron content of 11 mg Fe/mL and a GCPQ content of 16.5 mg/mL and immediately sonicated in an ice bath using probe sonication (2 x 5 min). The addition of the ethanoic solution diluted the formulation by a factor of 1.1 overall giving a final formulation with a drug concentration of 2 mg/mL, iron content of 10 mg Fe/mL and a GCPQ content of 15 mg/mL.

4.3.5 Lomustine encapsulation via the thin-film method

Raspberry nanoparticles were suspended in methanol (2 mL) with a resulting iron content of 10 mg Fe/mL and a GCPQ content of 15 mg/mL. This solution was then added to 4 mg of lomustine and vortexed until fully dissolved. The methanol was evaporated under a gentle stream of N_2 and then suspended in 2 mL of water.

4.3.6 Paclitaxel HPLC procedure

Paclitaxel chromatograms were acquired using a C18 reverse phase monolithic column (Onyx, 5 µm, 100 x 4.6 mm, Phenomenex, UK) fitted with a guard column (Onyx monolithic C18 guard cartridge, 5 x 4.6 mm, Phenomenex, UK). The mobile phase consisted of acetonitrile:water (50:50) and a flow rate of 1.0 mL/min. The column temperature was maintained at 40 ^{O}C and the detection wavelength was set

at 227 nm. Formulations were diluted in methanol (1:10) and centrifuged (2000 rpm, 5 min) before analysis.

4.3.7 Paclitaxel encapsulation via the emulsification-evaporation method

In a vial, iron oxide nanoparticles (20 mg/mL) prepared as described in *section 2.3.4* and paclitaxel (3 mg/mL) were suspended in chloroform (2 mL) and were added to a GCPQ solution (5 mL, 15 mg/mL). The solution was then sonicated using probe sonication (2 x 5 min, Soni Prep 150, MSE, UK) at the interface between the organic and aqueous phases, creating a brown emulsion. This emulsion was left to separate over 48 h. The aqueous layer was then extracted and any residual chloroform was allowed to evaporate overnight. The product was frozen and lyophilised to obtain a dry product which was then reconstituted in water (5 mL).

4.3.8 Paclitaxel encapsulation ethanoic co-solvent method

An ethanoic solution of paclitaxel (0.25 mL, 12 mg/mL) was added to an aqueous solution of pre-prepared raspberry nanoparticles (2.25 mL), prepared as described in *section 2.3.5,* with an iron content of 11 mg Fe/mL and a GCPQ content of 16.5 mg/mL and immediately sonicated in an ice bath using probe sonication (2 x 5 min). The addition of the ethanoic solution diluted the formulation by a factor of 1.1 overall giving a final formulation with a drug concentration of 2 mg/mL, iron content of 10 mg Fe/mL and a GCPQ content of 15 mg/mL. This formulation was then measured for drug content via HPLC.

4.3.9 Methotrexate HPLC procedure

Methotrexate chromatograms were acquired using a C18 reverse phase monolithic column (Onyx, 5 µm, 100 x 4.6 mm, Phenomenex, UK) fitted with a guard column (Onyx monolithic C18 guard cartridge, 5 x 4.6 mm, Phenomenex, UK). The mobile

phase consisted of sodium phosphate buffer pH 8:acetonitrile (92:8) and a flow rate of 1.0 mL/min. The column temperature was maintained at 30 ^{O}C and the detection wavelength was set at 305 nm. Formulations were diluted in mobile phase (1:10).

4.3.10 Ligand exchange of hydrophobic iron oxide nanoparticles with methotrexate

Briefly, iron oxide nanoparticles (20 mg) were precipitated from hexane (1 mL) by the addition of ethanol and were collected via centrifugation (5436 rcf, 10 min), the supernatant was discarded and replaced with ethanol and this procedure was repeated twice. The final precipitate was re-dispersed in toluene. MTX (36 mg) in DMSO (2 mL) was added to the toluene mixture and the reaction was bath sonicated (10 min) and left to stir at room temperature for 48 h. After 48 h a sediment was observed, this was collected via centrifugation (5436 rcf, 10 min), the supernatant was discarded and replaced with ethanol and this procedure was repeated twice and then dried under vacuum. The final precipitate was collected as a red solid.

4.4 Results

4.4.1 Method 1: In situ emulsification-evaporation method

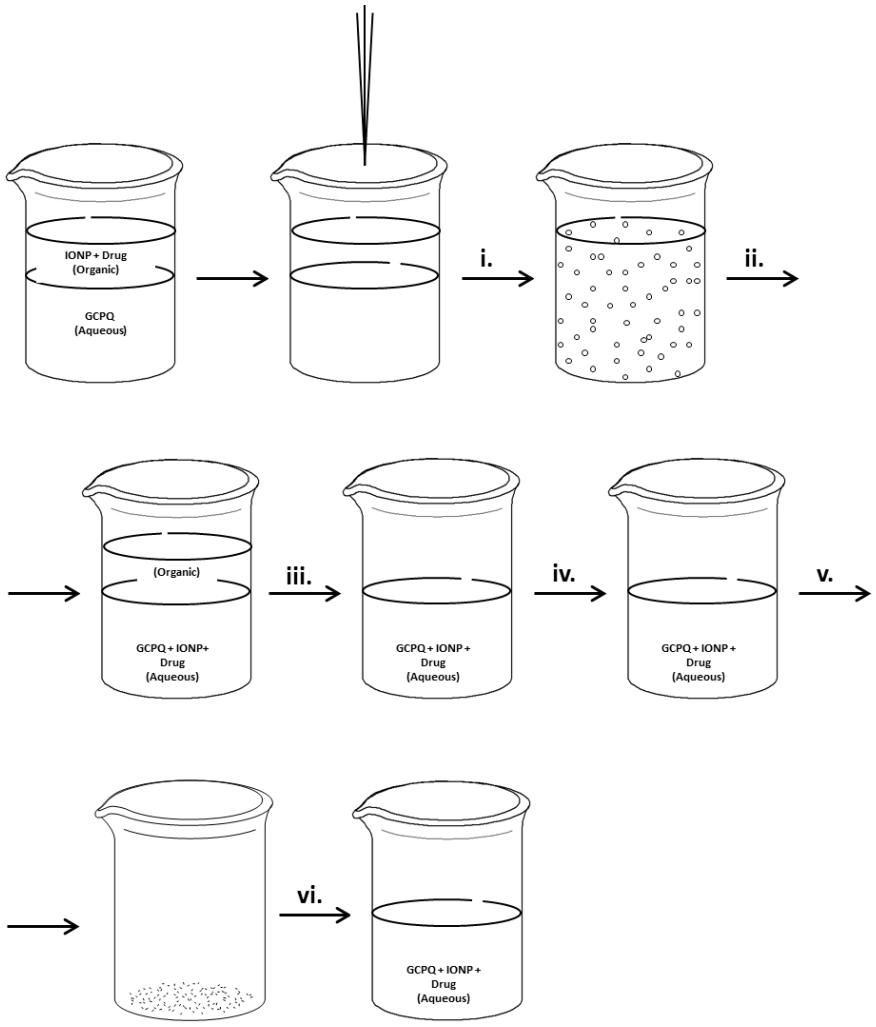

Scheme 4.4.1.1. The preparation of drug loaded iron oxide raspberry nanoparticles via the in situ emulsification and evaporation method. The drug and iron oxide nanoparticles are suspended in the organic layer (hexane or dichloromethane) while the polymer micelles are in an aqueous layer (water). The formulation then undergoes: **i**, emulsification via probe sonication; **ii**, separation; **iii**, extraction; **iv**, evaporation; **v**, lyophilisation; **vi**, reconstitution in aqueous medium.

4.4.2 Method 2: Solvent free method

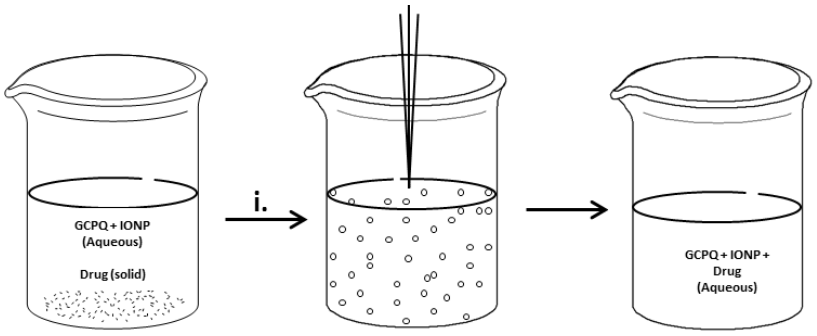

Scheme 4.4.2.1. The preparation of drug loaded iron oxide raspberry nanoparticles via the solvent free method. The drug was added in powder form to an aqueous solution of pre-prepared raspberry nanoparticles. The procedure involves: **i**, probe sonication.

4.4.3 Method 3: Ethanoic co-solvent method

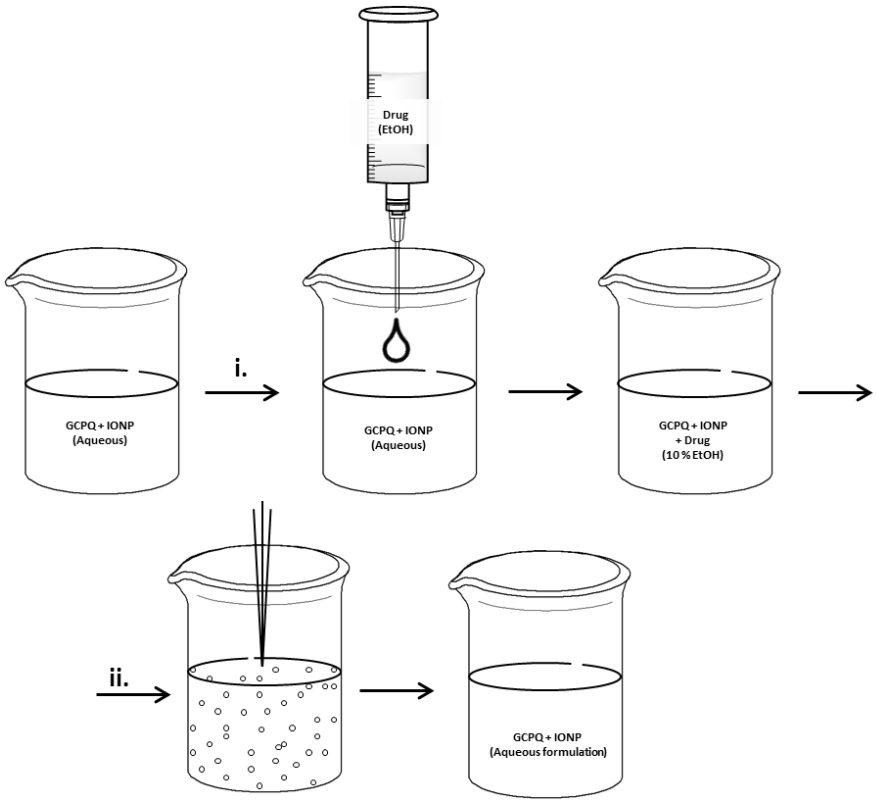

Scheme 4.4.3.1. The preparation of drug loaded iron oxide raspberry nanoparticles via the ethanoic co-solvent method. The drug was dissolved in an ethanoic solution and then added to an aqueous solution of pre-prepared raspberry nanoparticles. The procedure involves: **i**, addition of drug in ethanoic solution; **ii**, probe sonication.

4.4.4 Method 4: Thin-film method

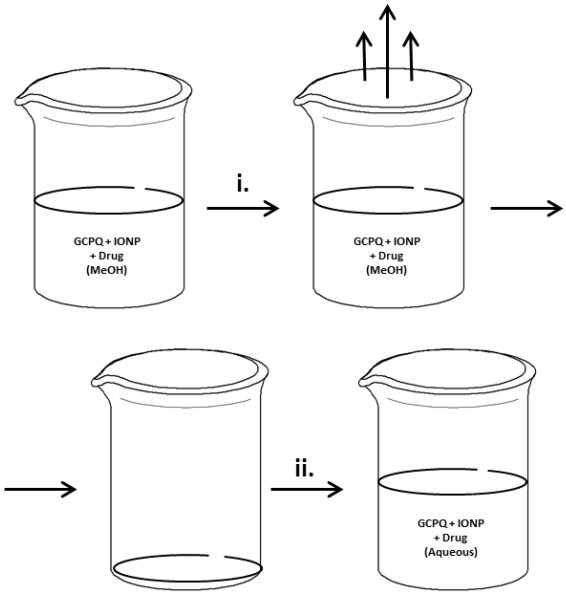

Scheme 4.4.4.1. The preparation of drug loaded iron oxide raspberry nanoparticles via the thin film method. The procedure involves; mixing the drug and pre-prepared iron oxide raspberry nanoparticles in methanol and then **i**, evaporation of solvent followed by **ii**, reconstitution in aqueous medium.

4.4.5 Lomustine encapsulation

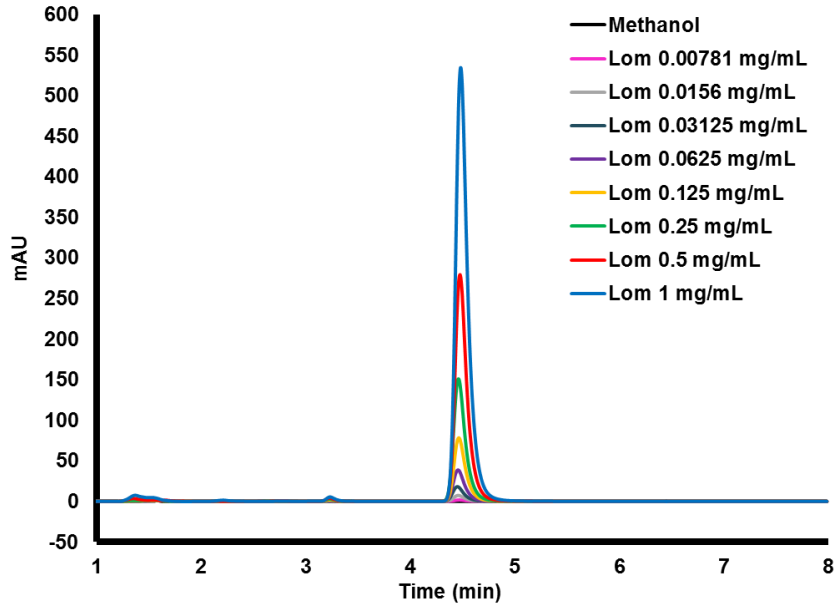

Figure 4.4.5.1. HPLC chromatogram of lomustine (Lom) using an isocratic procedure of H_2O: MeOH (1:1) at 40 ^{O}C, UV/Vis wavelength = 230 nm. Lomustine had a retention time of 4.6 min and a LOD of 0.00781 mg/mL.

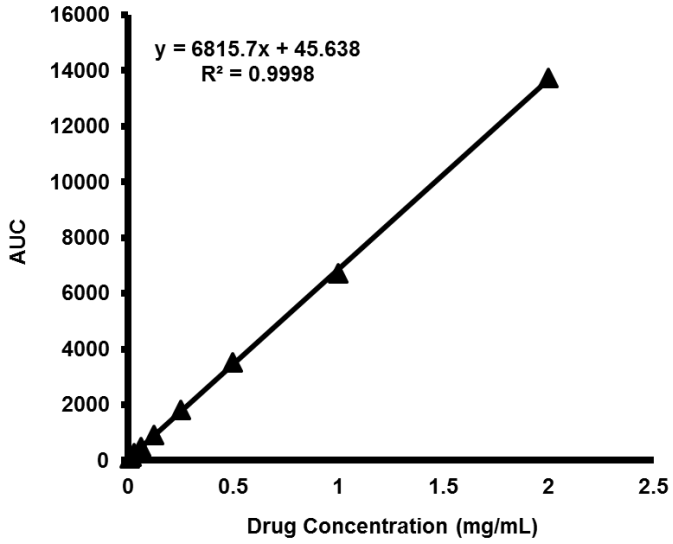

Figure 4.4.5.2. Lomustine calibration curve: y = 6816x +45.6, r^2 = 0.9998.

	Lomustine (mg/mL)	Encapsulation Efficiency (%)
Method 1 *(emulsification-evaporation method)*	0.18 ± 0.01	7.79 ± 0.29
Method 2 *(solvent free method)*	0.07 ± 0.002	3.65 ± 0.11
Method 3 *(ethanoic co-solvent method)*	0.04 ± 0.001	2.43 ± 0.48
Method 4 *(thin-film)*	0.13 ± 0.001	4.5 ± 0.11

Table 4.4.5.1. HPLC Summary of various raspberry nanoparticle encapsulation methods for lomustine. Target drug content was 2 mg/mL. The results suggest that no method gave suitable encapsulation efficiencies. The emulsification-evaporation method 1 gave the highest drug encapsulation, however this was still <10% and cannot be considered an efficient strategy. Data are means ± s.d., n =3.

4.4.6 Paclitaxel encapsulation

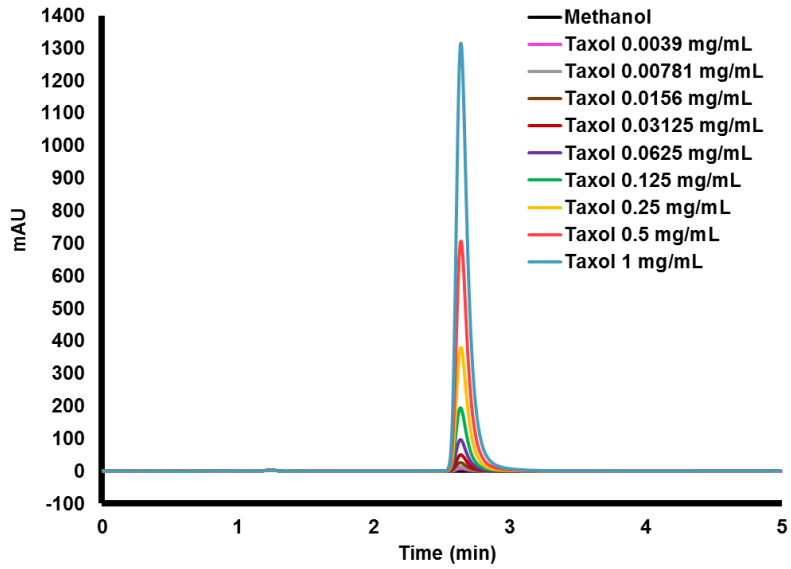

Figure 4.4.6.1. HPLC chromatogram of paclitaxel (Taxol) using an isocratic procedure of [H_2O: ACN (1:1)] at 40 ^{O}C, UV/Vis wavelength = 227 nm. Paclitaxel had a retention time of 2.7 min and a LOD of 0.0039 mg/mL.

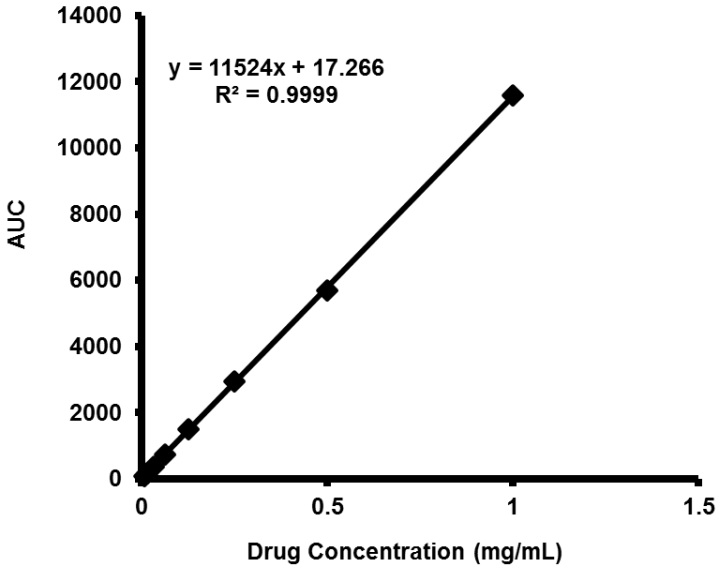

Figure 4.4.6.2. Paclitaxel calibration curve: y = 11524x +17.3, r^2 = 0.9999.

	Paclitaxel (mg/mL)	Encapsulation Efficiency (%)
Method 1 *(emulsification-evaporation method)*	0.03 ± 0.01	2.3 ± 1.0
Method 3 *(ethanoic co-solvent method)*	1.06 ± 0.04	96.6 ± 4.8

Table 4.4.6.1. HPLC Summary of various raspberry nanoparticle encapsulation methods for Paclitaxel. Target drug content was 1.2 mg/mL. The HPLC data confirmed that the ethanoic co-solvent method 3 produced a formulation that contained a suitable drug content and encapsulation efficiency. Data are means ± s.d., n =3.

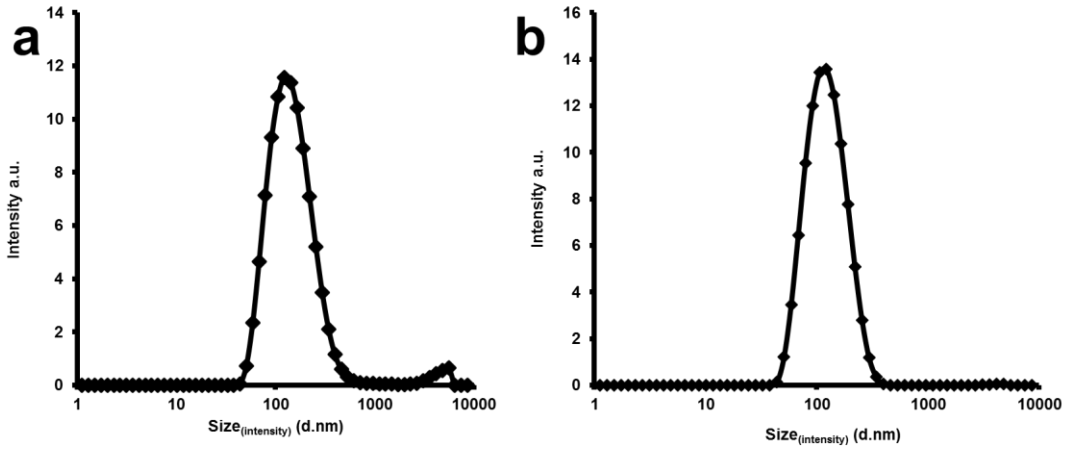

Figure 4.4.6.3. (a), DLS measurement of the paclitaxel iron oxide raspberry nanoparticle formulation. Average size by Intensity was 256 nm, PdI; 0.22 and gave an encapsulation efficiency of (96.4 ± 1.9)% measured by HPLC. A second peak several microns in size can also be seen. This could be caused by a small amount of unencapsulated drug. (b), These larger particulates were removed via filtration (1.2 µM). The filtered formulation gave an average size by Intensity of 143.0 nm, PdI; 0.14. n=3. EE% (101.5 ± 3.6). Data are means ± s.d., n=3.

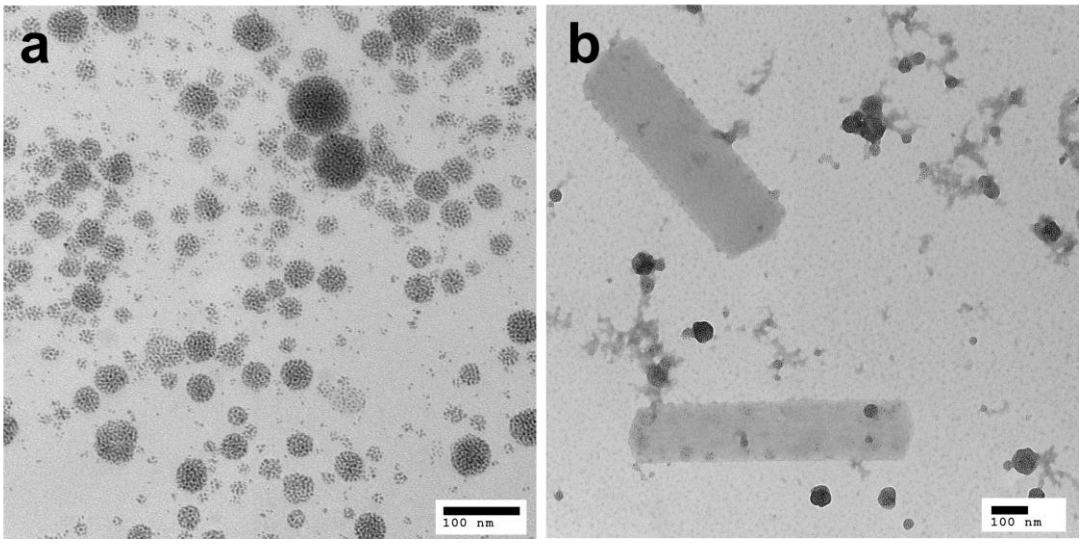

Figure 4.4.6.4. TEM of the paclitaxel iron oxide raspberry nanoparticle formulation; (a), no stain and (b), with a 1% uranyl acetate stain. TEM images with no stain clearly show the typical iron oxide raspberry nanoparticles, however when the stain is added nanocrystals of paclitaxel can be visualised as large nano-rods (700 nm x 200 nm). This result could be evidence that paclitaxel has been stabilised in the formulation in a nanocrystal form, however it has not been encapsulated within the micellar raspberry nanoparticle.

4.4.7 Methotrexate encapsulation

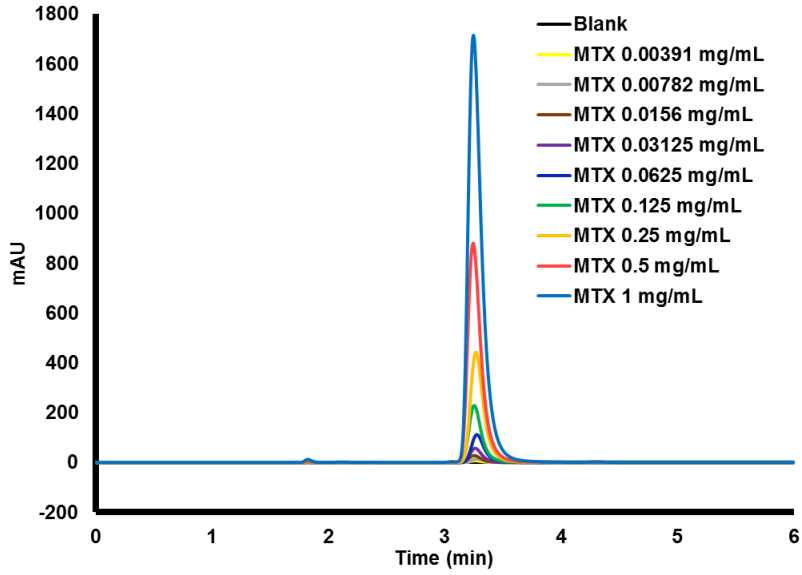

Figure 4.4.7.1. HPLC chromatogram of methotrexate (MTX) using an isocratic procedure of [sodium phosphate buffer pH 8: ACN (92:8)] at 30 ^{O}C, UV/Vis wavelength = 305 nm. Methotrexate had a retention time of 3.2 min and a LOD of 0.0039 mg/mL.

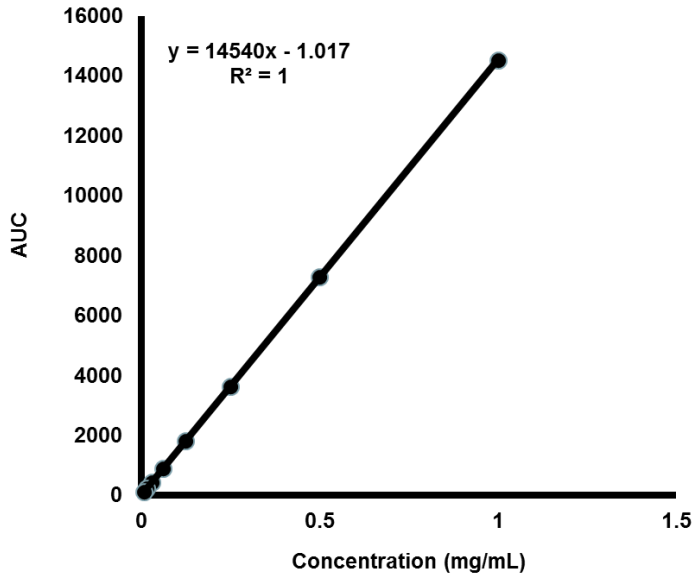

Figure 4.4.7.2. Methotrexate calibration curve: y = 14540x -1.0, r^2 = 1.

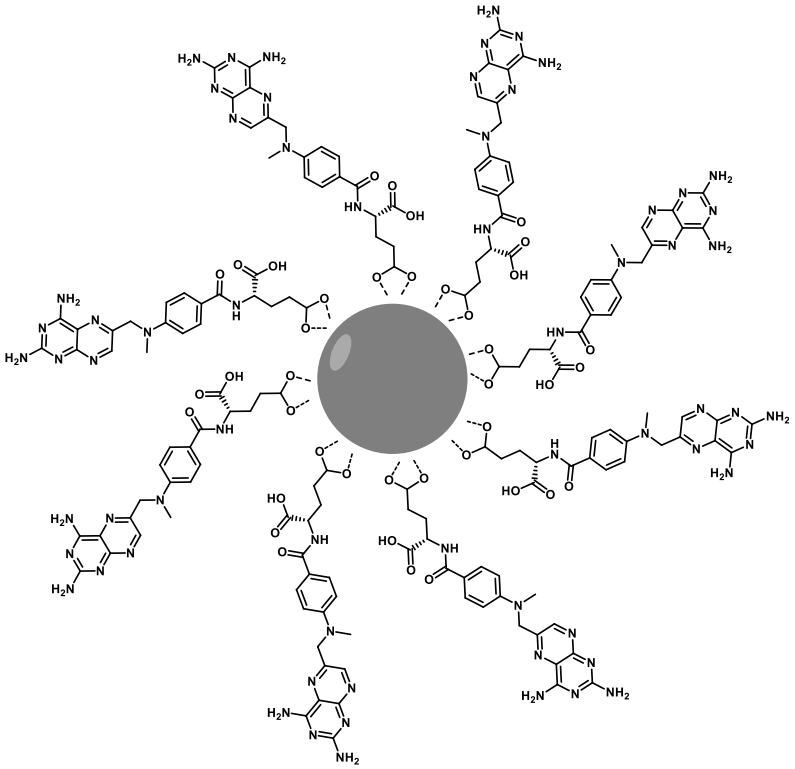

Figure 4.4.7.3. Schematic of the resulting MTX.IONP produced via ligand exchange.

Figure 4.4.7.4. Macro image of the resulting MTX.IONP produced via ligand exchange in water. The resulting material was insoluble in a range of organic and polar solvents making it unsuitable for downstream applications.

4.5 Discussion

The thermodynamic equilibrium between the drug and polymer is often not sufficient enough to overcome the activation energy needed for spontaneous drug encapsulated micellisation.[21] A preparation method is usually required to facilitate high drug loading within the polymeric nanoparticle. The encapsulation of lomustine within the GCPQ polymeric nanoparticle was first investigated via an in situ emulsification-evaporation method, where the lomustine and the hydrophobic IONPs were suspended in a hexane layer while the GCPQ nanoparticles were suspended in an aqueous layer. Probe sonication was used to provide the energy needed to emulsify the formulation. The resulting emulsion was allowed to separate over 48 h and the aqueous layer was extracted, frozen and then lyophilised to obtain a dry product that could then be reconstituted in water at the desired concentration. This technique was deemed the most suitable as the drug could be loaded together with the hydrophobic IONPs in a one-step procedure. The lomustine content of the formulation was measured via HPLC and gave a drug content of (0.18 ± 0.010) mg/mL and an EE% of (7.79 ± 0.29) %. Overall this was not considered an efficient method for drug loading. Following this, a solvent-free method was investigated for lomustine encapsulation. Lomustine in powder form was added to a suspension of raspberry nanoparticles and sonicated. This type of procedure is classified as a *top-down* strategy where large crystals of the drug, several microns in size, are subjected to a high energy environment via sonication in an attempt to break the drug crystals into nano-sized particulates that could then be incorporated within the nano-sized micelles. Analysis via HPLC gave a drug content of (0.07 ± 0.002) mg/mL and an EE% of (3.65 ± 0.11) % concluding that this was not a suitable method for drug encapsulation. A *bottom-up* strategy was investigated and this came in the form of an ethanoic co-solvent method. The miscibility of ethanol and water allows for this formulation to exist as a singly phase while according to EMA and FDA guidelines

ethanol may be present in an injectable formulation up to 20% v/v. Lomustine readily dissolves in ethanol (47 mg/mL at 25 ^{O}C) and therefore an ethanoic solution of lomustine was added to a solution of raspberry nanoparticles under sonication. It was hypothesised that the GCPQ polymer would control the precipitation of lomustine in the aqueous environment in order to facilitate micelle encapsulation. HPLC analysis gave a drug content of (0.04 ± 0.001) mg/mL and an EE% of (2.43 ± 0.45) %, overall concluding that this was a poor strategy for drug encapsulation. The *thin-film or solution casting* technique is a widely known technique often used for drug encapsulation within liposomes. The method involved suspending both the raspberry nanoparticles and lomustine in methanol. Once thoroughly dispersed the methanol was removed via a stream of N_2 and gentle heating in order to obtain a thin-film on the surface of the vessel. The thin-film was then hydrated with water to obtain the formulation at the desired concentration. HPLC analysis gave a drug content of (0.13 ± 0.001) mg/mL and an EE% of (4.50 ± 0.11) %, suggesting this was not a good lomustine encapsulation procedure. In conclusion, several method for lomustine encapsulation within the raspberry nanoparticles were investigated resulting in the identification of no effective drug loading methods. When considering a result such as this, it should be considered that a lomustine loaded raspberry nanoparticle may not be a thermodynamically favoured structure. The Flory-Huggins theory attempts to describe the interaction between a drug and a polymeric matrix thermodynamically through an entropy component and an enthalpy component. The theory is based on the principle that chemical entities that are similar in nature interact favourably. It can therefore be hypothesised that the hydrophobic core of the polymeric GCPQ micelle and the lomustine molecule are not similar enough in nature to undergo a favourable interaction. Future experiments could involve measuring the Flory-Huggins parameter to see if the palmitic core of the GCPQ micelle and lomustine have a favourable thermodynamic interaction. The difficulty with loading lomustine into a nanoparticle may be reflected by the limited number of attempts to encapsulate this drug within a

nanoparticle. To the authors knowledge, only two lomustine encapsulated nanoparticles exist: *Mehrotra et al* adopted an emulsion-evaporation procedure using chitosan as their nanoparticle forming polymer.[22] To produce a stable nanoparticle they had to use a crosslinking agent to chemically entrap the drug within the nanoparticle. The second method published was by our own group *Fisusi et al*, where lomustine was encapsulated by producing a stable oil-in-water emulsion.[20] Although both strategies were effective at loading lomustine into a polymeric nanoparticle, in this project they were considered undesirable strategies as it was believed that the oil-in-water emulsion would have a significant effect on the contrast ability of the raspberry nanoparticle and the crosslinking may produce a nanoparticle that does not effectively release the drug pay load. Lomustine is still a promising candidate however, a suitable method for simple drug loading into the raspberry nanoparticles was not identified in this body of work.

Paclitaxel was chosen as the next drug candidate to be investigated as the theranostic therapeutic. Paclitaxel is a widely used chemotherapeutic drug and it is active against a broad range of cancers. The use of paclitaxel is limited by its poor aqueous solubility and is often formulated in a mixture of Cremophor® (polyoxyethylated castor oil) and ethanol (c.a. 50:50 v/v). To increase the efficiency of paclitaxel many nanoparticle formulations have been developed which has even lead to a commercially available product in the form of Abraxane®, approved by the FDA in 2005 for the treatment of breast cancer. In this project the preferred in situ emulsion and evaporation method was initially investigated. In this circumstance, paclitaxel was not soluble in hexane and so the organic solvent was substituted for chloroform. Both the paclitaxel and hydrophobic IONPs were suspended in a chloroform layer and the GCPQ polymer was suspended in a water layer. Sonication was used to provide the energy for emulsification and the resulting product was worked up as previously described. HPLC analysis gave a drug content of (0.03 ±

0.01) mg/mL and an EE% of (2.31 ± 1.0) %, indicating this is a poor method for encapsulation. It was predicted that an ethanoic co-solvent may provide improved encapsulation results as paclitaxel has good solubility in ethanol (40 mg/mL at 25 ^{O}C) and ethanol is a major excipient in the Taxol® formulation. Paclitaxel was suspended in ethanol and was added to the raspberry nanoparticles under sonication. The formulation was measured for drug content by HPLC and gave a loading of (1.06 ± 0.04) mg/mL and an EE% of (96.6 ± 4.8) % which was a particularly good result. The formulation was measured for size by DLS resulting in a distribution with two distinct peaks and an average size by intensity of 256 nm, PDI; 0.22 (Figure 4.4.6.3.a). The larger peak measured several microns in size and is most likely a result of a small number of drug aggregates in the formulation. These aggregates were removed via filtration through a 1.2 µm syringe filter. Upon removal of the paclitaxel aggregates the DLS distribution gave a single peak with an average size by intensity of 143.0 nm, PDI; 0.14 and HPLC confirmed that there was no significant change in drug concentration after filtration. Electron microscopy was used to investigate the morphology of the paclitaxel-raspberry nanoparticle formulation. Typical iron oxide raspberry nanoparticles were imaged however, when a 1% uranyl acetate stain was used, large rod like nanocrystals were observed (c.a. 700 nm x 200 nm). This could be evidence that paclitaxel had not been encapsulated within the polymer micelle but instead, small nanocrystals of paclitaxel have been stabilised within the conditions of the formulation. A control formulation with just paclitaxel and no raspberry nanoparticles was prepared in the same manner and when measured by HPLC gave no drug encapsulation, suggesting that the polymeric raspberry nanoparticles are having an effect on the paclitaxel. A reasonable hypothesis for the structures observed is that the energy provided by sonication was enough to disintegrate large micron sized crystals into much smaller nano crystals, their high surface energies could then be stabilised by free GCPQ polymer and in doing so reduce their tendency to re-aggregate. Although the formation of paclitaxel nanocrystals is quite interesting,

it nevertheless, does not meet the criteria for a theranostic nanoparticle. One could imagine when administered into the body the paclitaxel nanocrystals and the raspberry nanoparticles could undergo mechanisms completely independently of each other and would therefore not make for a useful duel functional nanoparticle. An alternative hypothesis is that the uranyl acetate stain may have a competitive interaction with the paclitaxel in the drug-GCPQ complex, causing the paclitaxel to crystallise out of the aqueous formulation to form the observed nano-rods. It is also, possible that the nano-rod crystals observed are formed from the crystallisation of the uranyl acetate salt itself, however this premise is unlikely, as uranyl acetate crystallisation was never observed in previous imaging experiments conducted under similar conditions (use of the uranyl acetate stain at concentration of 1% w/w in water, pH 4-5). The correct hypothesis was determined by a simple magnetic separation procedure. A strong magnet was used to collect the raspberry nanoparticles from the formulation which were then dispersed into fresh media. HPLC gave a drug encapsulation of (0.01 ± 0.002) mg/mL and an EE% of (0.66 ± 0.23) % concluding that the paclitaxel was not bound to the magnetic raspberry nanoparticles. Overall, with the techniques employed here it can be concluded that paclitaxel was not encapsulated within the raspberry nanoparticles.

Interestingly, the conditions from the ethanoic co-solvent method did yield rod like nanocrystals of paclitaxel which could have some significance. Nanocrystals are considered sub-micron particles of the pure compound in its crystalline form. These formulations require no carrier nanoparticle but frequently need some stabilising agents to prevent agglomeration. Nanocrystals have gained considerable attention for the oral administration of drugs as they often have significantly improved dissolution profiles compared to their micron sized counterparts.[23] Their success has led to a number of chemotherapeutic compounds now available as a nanocrystal formulation including; Rapamune®, Emend®, TriCor®, Megace® ES, Triglide®,

Avinza®, Focalin® XR, Ritalin® LA and Zanaflex Capsules.[24] Alternatively, high concentrations of hydrophobic drug nanocrystals can be injected intravenously as there is little risk of capillary blockage and embolism. Both strategies discussed would overcome the toxic effects of administering paclitaxel with Cremophor EL® in the Taxol formulation® and the expense associated with the albumin nanoparticle carrier in Abraxane®. Currently there are 12 published studies where paclitaxel nanocrystals have been reported. The first was by *Lui et al* in 2010, using D-α-tocopheryl polyethylene glycol 1000 succinate (TPGS) as the stabilising agent.[25] Comparable to GCPQ, TPGS is a long chained amphiphilic polymer and may account for the similar structures seen. The methods reported for paclitaxel nanocrystal synthesis can largely be divided into two strategies; the use of a co-solvent (bottom up strategy)[26-31] and the mechanical disintegration (top down strategy)[24,32-34] with many of the studies using a variety of stabilizers and excipients to achieve the desired nanoparticles. A number of relevant studies include; *Wei et al*,[26] *Hollis et al*,[28] *Gao et al*,[29] and *Zhao et al*,[31] who all used an ethanoic co-solvent to produce their paclitaxel nanocrystals and *Lv et al*, who used a chitosan and a quaternized chitosan as the stabilising agent for their paclitaxel nanocrystals which when administered as a treatment to tumour bearing mice gave a significant increase in mean survival rates.[30] Paclitaxel still remains a promising drug and so other methods could still be investigated in order to achieve appreciable drug loading. Alternatively as discussed previously, perhaps the hydrophobic core of the GCPQ nanoparticle is not a suitable environment to stabilise the paclitaxel molecules.

The third drug investigated was Methotrexate. An attempt was made to encapsulate methotrexate by anchoring the drug to the surface of the IONPs, via a ligand exchange procedure, prior to encapsulation within the GCPQ polymeric micelle. Methotrexate is classified as an antifolate chemotherapeutic and is characterised by its structural similarity to folic acid. The structure of methotrexate is comprised of a

multi-ring pteridine group linked to para-aminobenzoic acid, which in turn connects with a terminal glutamic acid residue.[13] This molecular structure presents itself with two carboxylic acid groups and it was predicted that, via a ligand exchange procedure, methotrexate could be anchored to the surface of the iron oxide via these two electron dense groups. A HPLC procedure was developed for the detection of methotrexate using a C-18 reverse phase column with a mobile phase of sodium phosphate buffer, pH 8:aceonitrile (92:8). The ligand exchange procedure was conducted in a similar manner to that described by the DMSA ligand exchange procedure performed in Chapter 2. Methotrexate was solubilised in DMSO and was added to a dispersion of hydrophobic IONPs in toluene and vigorously mixed. After 48 h a precipitate had formed indicating a change in composition, however the resulting product was not soluble in a range of polar and non-polar solvents rendering, the newly formed species difficult to use in downstream applications. There have been 12 reported attempts to formulate methotrexate with IONPs: 7 of the studies involve methotrexate being chemically conjugated to the surface of an IONP via an anchoring group.[18,35-40] 4 studies use emulsification[41-44] and one study uses electrostatic interactions[45]. There are no reported studies where methotrexate have been bound to the surface of iron oxide via a ligand exchange procedure. This is a surprise as co-ordinating methotrexate to the surface of an IONP via its carboxylic acid groups appears to be an obvious strategy, however with the lack of published data supporting this, perhaps it is not actually possible obtain a product that can be used for biological applications. Overall one attempt was made to load methotrexate into the iron oxide raspberry nanoparticle and so future work could seek to explore several other strategies.

4.6 Conclusion

In conclusion, this chapter aimed to encapsulate three chemotherapeutic drugs into the iron oxide raspberry nanoparticles in order to act as the therapeutic element in the proposed theranostic nano-platform. The drug loading of lomustine was attempted via four individual methods; emulsion-evaporation, solvent-free, ethanoic co-solvent and thin-film, yielding encapsulation efficiencies of (7.79 ± 0.29) %, (3.65 ± 0.11) %, (2.43 ± 0.45) % and (4.50 ± 0.11) %, respectively. No method yielded an effective or efficient encapsulation method for lomustine within the formulation.

The loading of paclitaxel was attempted via two individual methods; emulsion-evaporation and ethanoic co-solvent, yielding encapsulation efficiencies of (2.31 ± 1.0) % and (96.6 ± 4.8) %, respectively. The ethanoic co-solvent method gave apparently good encapsulation results, however when further analysed via TEM, it was revealed that the paclitaxel had not been encapsulated within the raspberry nanoparticles, but instead had formed stabilised nanocrystals of the drug in the formulation. Although an interesting result, this type of formulation did not meet the criteria for a theranostic platform.

The loading of methotrexate directly onto the IONPs was attempted via a ligand exchange procedure taking advantage of the free carboxylic acid groups within methotrexates' chemical structure. Although there was an indication that a new species had formed it did not disperse in a range of polar and non-polar solvents making downstream characterisation and formulation difficult.

Overall, no drug was encapsulated within the raspberry nanoparticles effectively or efficiently. Future work could focus on measuring the Flory-Huggins parameter of the hydrophobic core of the micelle in order to narrow the selection of drug candidates

down to molecules that might have thermodynamically favourable interactions. Secondly, other strategies for drug encapsulation within a polymeric nanoparticle do exist including acid-base titrations and oil-in-water emulsions. Alternatively, one could chemically conjugate the drug to the nanoparticle through a suitable linker.

(1) DeVita, V. T.; Chu, E. A History of Cancer Chemotherapy. *Cancer Research* **2008**, *68*, 8643-8653.

(2) Savjani, K. T.; Gajjar, A. K.; Savjani, J. K. Drug Solubility: Importance and Enhancement Techniques. *ISRN Pharmaceutics* **2012**, *2012*, 195727.

(3) Widakowich, C.; de Castro, G.; de Azambuja, E.; Dinh, P.; Awada, A. Review: Side Effects of Approved Molecular Targeted Therapies in Solid Cancers. *The Oncologist* **2007**, *12*, 1443-1455.

(4) Weiss, R. B.; Issell, B. F. The nitrosoureas: carmustine (BCNU) and lomustine (CCNU). *Cancer treatment reviews* **1982**, *9*, 313-330.

(5) Reed, D. J.; May, H. E.; Boose, R. B.; Gregory, K. M.; Beilstein, M. A. 2-Chloroethanol Formation as Evidence for a 2-Chloroethyl Alkylating Intermediate during Chemical Degradation of 1-(2-Chloroethyl)-3-cyclohexyl-1-nitrosourea and 1-(2-Chloroethyl)-3-(trans-4-methylcyclohexyl)-1-nitrosourea. *Cancer Research* **1975**, *35*, 568-576.

(6) Kohn, K. W. Interstrand cross-linking of DNA by 1,3-bis(2-chloroethyl)-1-nitrosourea and other 1-(2-haloethyl)-1-nitrosoureas. *Cancer Res* **1977**, *37*, 1450-1454.

(7) Middleton, M. R.; Margison, G. P. Improvement of chemotherapy efficacy by inactivation of a DNA-repair pathway. *The Lancet Oncology* **2003**, *4*, 37-44.

(8) Rowinsky , E. K.; Donehower , R. C. Paclitaxel (Taxol). *New England Journal of Medicine* **1995**, *332*, 1004-1014.

(9) Singla, A. K.; Garg, A.; Aggarwal, D. Paclitaxel and its formulations. *International Journal of Pharmaceutics* **2002**, *235*, 179-192.

(10) Konno, T.; Watanabe, J.; Ishihara, K. Enhanced solubility of paclitaxel using water-soluble and biocompatible 2-methacryloyloxyethyl

phosphorylcholine polymers. *Journal of Biomedical Materials Research Part A* **2003**, *65A*, 209-214.

(11) Gelderblom, H.; Verweij, J.; Nooter, K.; Sparreboom, A. Cremophor EL: the drawbacks and advantages of vehicle selection for drug formulation. *European Journal of Cancer* **2001**, *37*, 1590-1598.

(12) Weiss, R. B.; Donehower, R. C.; Wiernik, P. H.; Ohnuma, T.; Gralla, R. J.; Trump, D. L.; Baker, J. R.; Van Echo, D. A.; Von Hoff, D. D.; Leyland-Jones, B. Hypersensitivity reactions from taxol. *Journal of Clinical Oncology* **1990**, *8*, 1263-1268.

(13) Jolivet , J.; Cowan , K. H.; Curt , G. A.; Clendeninn , N. J.; Chabner , B. A. The Pharmacology and Clinical Use of Methotrexate. *New England Journal of Medicine* **1983**, *309*, 1094-1104.

(14) Chabner, B. A.; Roberts, T. G. Chemotherapy and the war on cancer. *Nat Rev Cancer* **2005**, *5*, 65-72.

(15) Abolmaali, S. S.; Tamaddon, A. M.; Dinarvand, R. A review of therapeutic challenges and achievements of methotrexate delivery systems for treatment of cancer and rheumatoid arthritis. *Cancer Chemotherapy and Pharmacology* **2013**, *71*, 1115-1130.

(16) Banerjee, D.; Mayer-Kuckuk, P.; Capiaux, G.; Budak-Alpdogan, T.; Gorlick, R.; Bertino, J. R. Novel aspects of resistance to drugs targeted to dihydrofolate reductase and thymidylate synthase. *Biochimica et Biophysica Acta (BBA) - Molecular Basis of Disease* **2002**, *1587*, 164-173.

(17) Vezmar, S.; Becker, A.; Bode, U.; Jaehde, U. Biochemical and clinical aspects of methotrexate neurotoxicity. *Chemotherapy* **2003**, *49*, 92-104.

(18) Lin, J.; Li, Y.; Li, Y.; Wu, H.; Yu, F.; Zhou, S.; Xie, L.; Luo, F.; Lin, C.; Hou, Z. Drug/Dye-Loaded, Multifunctional PEG–Chitosan–Iron Oxide

Nanocomposites for Methotraxate Synergistically Self-Targeted Cancer Therapy and Dual Model Imaging. *ACS Applied Materials & Interfaces* **2015**, *7*, 11908-11920.

(19) Wunder, A.; Stehle, G.; Schrenk, H. H.; Hartung, G.; Heene, D. L.; Maier-Borst, W.; Sinn, H. Antitumor activity of methotrexate-albumin conjugates in rats bearing a Walker-256 carcinoma. *International journal of cancer* **1998**, *76*, 884-890.

(20) Fisusi, F. A.; Siew, A.; Chooi, K. W.; Okubanjo, O.; Garrett, N.; Lalatsa, K.; Serrano, D.; Summers, I.; Moger, J.; Stapleton, P.; Satchi-Fainaro, R.; Schatzlein, A. G.; Uchegbu, I. F. Lomustine Nanoparticles Enable Both Bone Marrow Sparing and High Brain Drug Levels - A Strategy for Brain Cancer Treatments. *Pharm Res* **2016**, *33*, 1289-1303.

(21) Biswas, S.; Vaze, O. S.; Movassaghian, S.; Torchilin, V. P.: Polymeric Micelles for the Delivery of Poorly Soluble Drugs. In *Drug Delivery Strategies for Poorly Water-Soluble Drugs*; John Wiley & Sons Ltd, 2013; pp 411-476.

(22) Mehrotra, A.; Nagarwal, R. C.; Pandit, J. K. Lomustine Loaded Chitosan Nanoparticles: Characterization and in-Vitro Cytotoxicity on Human Lung Cancer Cell Line L132. *Chemical and Pharmaceutical Bulletin* **2011**, *59*, 315-320.

(23) Dizaj, S. M.; Vazifehasl, Z.; Salatin, S.; Adibkia, K.; Javadzadeh, Y. Nanosizing of drugs: Effect on dissolution rate. *Research in Pharmaceutical Sciences* **2015**, *10*, 95-108.

(24) Sharma, S.; Verma, A.; Teja, B. V.; Shukla, P.; Mishra, P. R. Development of stabilized Paclitaxel nanocrystals: In-vitro and in-vivo efficacy studies. *European Journal of Pharmaceutical Sciences* **2015**, *69*, 51-60.

(25) Liu, Y.; Huang, L.; Liu, F. Paclitaxel Nanocrystals for Overcoming Multidrug Resistance in Cancer. *Molecular pharmaceutics* **2010**, *7*, 863-869.

(26) Wei, L.; Ji, Y.; Gong, W.; Kang, Z.; Meng, M.; Zheng, A.; Zhang, X.; Sun, J. Preparation, physical characterization and pharmacokinetic study of paclitaxel nanocrystals. *Drug Development and Industrial Pharmacy* **2015**, *41*, 1343-1352.

(27) Zhang, H.; Hu, H.; Zhang, H.; Dai, W.; Wang, X.; Wang, X.; Zhang, Q. Effects of PEGylated paclitaxel nanocrystals on breast cancer and its lung metastasis. *Nanoscale* **2015**, *7*, 10790-10800.

(28) Hollis, C. P.; Weiss, H. L.; Evers, B. M.; Gemeinhart, R. A.; Li, T. In Vivo Investigation of Hybrid Paclitaxel Nanocrystals with Dual Fluorescent Probes for Cancer Theranostics. *Pharmaceutical Research* **2014**, *31*, 1450-1459.

(29) Gao, L.; Liu, G.; Kang, J.; Niu, M.; Wang, Z.; Wang, H.; Ma, J.; Wang, X. Paclitaxel nanosuspensions coated with P-gp inhibitory surfactants: I. Acute toxicity and pharmacokinetics studies. *Colloids and Surfaces B: Biointerfaces* **2013**, *111*, 277-281.

(30) Lv, P.-P.; Wei, W.; Yue, H.; Yang, T.-Y.; Wang, L.-Y.; Ma, G.-H. Porous Quaternized Chitosan Nanoparticles Containing Paclitaxel Nanocrystals Improved Therapeutic Efficacy in Non-Small-Cell Lung Cancer after Oral Administration. *Biomacromolecules* **2011**, *12*, 4230-4239.

(31) Zhao, R.; Hollis, C. P.; Zhang, H.; Sun, L.; Gemeinhart, R. A.; Li, T. Hybrid Nanocrystals: Achieving Concurrent Therapeutic and Bioimaging Functionalities toward Solid Tumors. *Molecular Pharmaceutics* **2011**, *8*, 1985-1991.

(32) Patel, K.; Patil, A.; Mehta, M.; Gota, V.; Vavia, P. Oral delivery of paclitaxel nanocrystal (PNC) with a dual Pgp-CYP3A4 inhibitor: Preparation,

characterization and antitumor activity. *International Journal of Pharmaceutics* **2014**, *472*, 214-223.

(33) De Smet, L.; Colin, P.; Ceelen, W.; Bracke, M.; Van Bocxlaer, J.; Remon, J. P.; Vervaet, C. Development of a Nanocrystalline Paclitaxel Formulation for Hipec Treatment. *Pharmaceutical Research* **2012**, *29*, 2398-2406.

(34) Kenth, S.; Sylvestre, J.-P.; Fuhrmann, K.; Meunier, M.; Leroux, J.-C. Fabrication of Paclitaxel Nanocrystals by Femtosecond Laser Ablation and Fragmentation. *Journal of Pharmaceutical Sciences* **2011**, *100*, 1022-1030.

(35) Gupta, J.; Bhargava, P.; Bahadur, D. Methotrexate conjugated magnetic nanoparticle for targeted drug delivery and thermal therapy. *Journal of Applied Physics* **2014**, *115*, 17B516.

(36) Kohler, N.; Sun, C.; Wang, J.; Zhang, M. Methotrexate-Modified Superparamagnetic Nanoparticles and Their Intracellular Uptake into Human Cancer Cells. *Langmuir* **2005**, *21*, 8858-8864.

(37) Das, M.; Mishra, D.; Dhak, P.; Gupta, S.; Maiti, T. K.; Basak, A.; Pramanik, P. Biofunctionalized, phosphonate-grafted, ultrasmall iron oxide nanoparticles for combined targeted cancer therapy and multimodal imaging. *Small* **2009**, *5*, 2883-2893.

(38) Gao, F.; Yan, Z.; Zhou, J.; Cai, Y.; Tang, J. Methotrexate-conjugated magnetic nanoparticles for thermochemotherapy and magnetic resonance imaging of tumor. *Journal of Nanoparticle Research* **2012**, *14*, 1-10.

(39) Li, M.; Neoh, K.-G.; Wang, R.; Zong, B.-Y.; Tan, J. Y.; Kang, E.-T. Methotrexate-conjugated and hyperbranched polyglycerol-grafted Fe3O4 magnetic nanoparticles for targeted anticancer effects. *European Journal of Pharmaceutical Sciences* **2013**, *48*, 111-120.

(40) Liu, Y.; Xie, M.; Wang, S.; Zheng, Q.; Chen, A.; Deng, Q. Facile fabrication of high performances MTX nanocomposites with natural biomembrane bacterial nanoparticles using GP. *Materials Letters* **2013**, *100*, 248-251.

(41) Ragheb, R. R. T.; Kim, D.; Bandyopadhyay, A.; Chahboune, H.; Bulutoglu, B.; Ezaldein, H.; Criscione, J. M.; Fahmy, T. M. Induced clustered nanoconfinement of superparamagnetic iron oxide in biodegradable nanoparticles enhances transverse relaxivity for targeted theranostics. *Magnetic Resonance in Medicine* **2013**, *70*, 1748-1760.

(42) Likhitkar, S.; Bajpai, A. K. An In Vitro Experimental Approach to Study Magnetically Targeted Release of Methotrexate From Superparamagnetic Starch Nanocarriers. *International Journal of Polymeric Materials and Polymeric Biomaterials* **2014**, *63*, 941-950.

(43) Moura, C. C.; Segundo, M. A.; Neves, J.; Reis, S.; Sarmento, B. Co-association of methotrexate and SPIONs into anti-CD64 antibody-conjugated PLGA nanoparticles for theranostic application. *International journal of nanomedicine* **2014**, *9*, 4911-4922.

(44) Albuquerque, J.; Moura, C. C.; Sarmento, B.; Reis, S. Solid Lipid Nanoparticles: A Potential Multifunctional Approach towards Rheumatoid Arthritis Theranostics. *Molecules (Basel, Switzerland)* **2015**, *20*, 11103-11118.

(45) Pandya, S. R.; Singh, M. Preparation and characterization of magnetic nanoparticles and their impact on anticancer drug binding and release processes moderated through a 1st tier dendrimer. *RSC Advances* **2016**, *6*, 37391-37402.

Chapter 5

Outlook and Future work

5.1 Thesis Overview

This project has introduced an amphiphilic chitosan based polymer, named GCPQ, as a potential biocompatible vector for the simultaneous delivery of a diagnostic probe and a chemotherapeutic agent. The GCPQ polymer was successfully synthesised via a three-step reaction from the starting material, glycol chitosan. Acid hydrolysis was used to reduce the molecular weight of the glycol chitosan from c.a. 120 kDa to c.a. 7 kDa measured by GPC-MALLS. Hydrophobic alkyl pendent chains were introduced via a palmitoylation step using palmitic acid N-hydrosuccinimide (PNS). Palmitoylated glycol chitosan (PGC) was further functionalised with trimethyl, dimethyl and monomethyl amine groups using methyl iodide, overall yielding N-palmitoyl-N-monomethyl-N,N-dimethyl-N,N,N-trimethyl-6-O-glycolchitosan (GCPQ). Polymer structures were confirmed by NMR and gave a palmitoyl functionalisation of (13.4 ± 2.9)% and a trimethyl functionalisation of (15.6 ± 4.7)%.

The co-precipitation method using iron(II/III) chloride salts and ammonium hydroxide was used to make naked IONPs. Purification was performed via a magnetic separation and wash procedure. The naked IONPs had an average diameter of (8.4 ± 2.1) nm, but would agglomerate into micron sized particles causing sedimentation in aqueous conditions. The naked IONPs were made colloidally stable via sonochemical treatment in the presence of GCPQ, only when the IONP:polymer ratio was >1:0.04. The structures formed were termed blackberry nanoparticles. The blackberry nanoparticles had an average size of 156 nm by DLS and remained colloidally stable in water for at least 30 days at 5 ^{O}C. The blackberry nanoparticles had a positive surface charge of (+22.5 ± 6.1) mV in neutral conditions (pH 7.1) confirmed by electrophoretic light scattering. XRD confirmed the presence of magnetic iron oxide while SQUID experimentation confirmed that the blackberry nanoparticles were superparamagnetic making them a suitable candidate for MRI

contrast applications. Relaxometry found that the blackberry nanoparticles had a high r_2 value of 294.8 μM^{-1} S^{-1} and an r_2/r_1 of 21.1 giving it a comparable relaxivity profile to a number of known commercially available IONP based negative MRI contrast agents.

Hydrophobic IONPs were synthesised via the high temperature thermal decomposition of an iron-oleate complex. The hydrophobic IONPs had an average diameter of (4.8 ± 0.8) nm and would only disperse in organic solvents such as hexane, chloroform and THF. The hydrophobic IONPs could be made colloidally stable in aqueous environments by incorporating them within a GCPQ micelle using an emulsification-evaporation procedure. The resulting nanoparticles formed ordered nanostructures and were termed raspberry nanoparticles. Colloidal stability was only achieved when the IONP:polymer ratio was >1:0.25 and the raspberry nanoparticles were found to be colloidally stable in water for at least 90 days at 5 ^{O}C. Raspberry nanoparticle size could also be controlled (120-230 nm by DLS) by varying the IONP:polymer ratio. Raspberry nanoparticles had a positive charge of (+24.4 ± 1.5) mV in neutral conditions (pH 7.1) and were not stable in strongly alkaline conditions (pH >8). XRD confirmed the presence of magnetic iron oxide and SQUID experimentation confirmed that the raspberry nanoparticles were superparamagnetic and that IONP encapsulation within the micelle did not diminish their magnetic properties. Relaxometry experimentation found that the raspberry nanoparticles had an r_2 value of 51.8 μM^{-1} S^{-1} and an r_2/r_1 of 79.1, giving it a relaxivity profile unlike any other commercially available product. Essentially, the same materials were used in both GCPQ IONP formulations, however differences in synthesis methods and formulation procedures produced two nanoparticle species with different magnetic and MRI contrast properties.

Preclinical animal studies were performed using the raspberry nanoparticles. The raspberry nanoparticle had favourable colloidal stabilities in a range of biologically relevant solutions (H_2O, 0.9% NaCl, 5% dextrose, 1X PBS and 50% rat plasma). Raspberry nanoparticle pharmacokinetics were evaluated in female BALB/c mice by ICP-AES following intravenous administration. The raspberry nanoparticles had a blood half-life of 28.3 min and accumulated in the liver and spleen over time. The raspberry nanoparticles were also distributed to the heart, lungs and kidneys, however no accumulation in these tissues was observed. No raspberry nanoparticles were observed in the brain at any time point. The *in vivo* MRI properties of the raspberry nanoparticles were evaluated using a 1T bench top MRI scanner (ICON^{TM}, Bruker, UK). Significant contrast was observed in the liver and spleen. Liver contrast produced clear visualisation of hepatic liver veins, which were not observed when compared to the commercially available product. For a conclusive comparison this result should be replicated several more times, however it could indicate a significant clinical advantage for using the raspberry nanoparticles as an MRI probe. The raspberry nanoparticles were evaluated in a cancer disease model. 4T1 tumours were successfully established on female BALB/c mice. A pharmacokinetic study indicated no significant amounts of raspberry nanoparticles were accumulating in the tumour tissue. MRI studies indicate a small reduction in signal, however this was not large enough to create a contrast effect for a human observer. Overall, the raspberry nanoparticles did provide good *in vivo* contrast in the liver and spleen, however using a 4T1 tumour model no contrast was observed in the diseased site. This result could be a result of an unsuitable tumour model, or alternatively, the blood half-life of the raspberry nanoparticles may not have been long enough to take advantage of the EPR effect. Future work should validate this result in an alternative tumour model.

Addition of a therapeutic component was investigated using several drug molecules and several encapsulation procedures. Lomustine was made available in the

formulation at a drug concentration of (0.18 ± 0.010) mg/mL and an EE% of (7.79 ± 0.29)%. Paclitaxel was made available in the formulation at a drug concentration of (1.06 ± 0.04) mg/mL and an EE% of (96.6 ± 4.8)%, however upon further investigation it was found that the paclitaxel was not encapsulated within the raspberry nanoparticles, but was in fact present as nanocrystals. An interesting result, but cannot be considered a nanotheranostic. Methotrexate was briefly investigated, as it was predicted that the drug would have an affinity to the IONPs via its terminal carboxylic acid groups. An MTX.IONP complex may have been produced via a ligand exchange procedure, however the product was insoluble in a range of solvents making it challenging to characterise and difficult to use for downstream formulations. In all, no effective drug encapsulation was discovered in this body of work within the given time.

5.2 Future work

A major challenge to address was that no effective drug encapsulation was discovered within the project. A number of chemotherapeutic agents were investigated, however satisfactory conditions for drug encapsulation were not met. Methotrexate was only briefly investigated and so alternative encapsulation strategies could be used. At physiological pH, methotrexate has a poor aqueous solubility (<1 mg/mL at 19 ^{O}C), however its solubility increases significantly when placed in weakly alkaline conditions (~ pH 8.5). As a result an interesting strategy could be to titrate a weakly basic solution of methotrexate with a weakly acid solution of the raspberry nanoparticles. Alternatively, a hydrophilic drug could be considered, for example doxorubicin or cisplatin, although their mechanism of drug loading would be unknown and as it is unlikely that they would be compatible within the hydrophobic core of the GCPQ micelle. An interesting strategy may be to use the raspberry nanoparticle as a delivery vector for gene therapies, most notably small interfering RNA (siRNA).[1] siRNA is a class of small double stranded RNA that is used to inhibit upstream

mechanisms used for protein synthesis. Specific types of siRNA molecules can be used to suppress the expression of disease promoting proteins and therefore have wide applications as a therapeutic agent. Although promising, siRNA has to overcome several biological barriers, most notably the blood, which rapidly degrades naked siRNA before it reaches its therapeutic target.[2] The delivery of siRNA may be promoted by using vectors such as polymers, liposomes and viruses.[3,4] As siRNA has a negative charge and the raspberry nanoparticles have a positive charge, it could therefore be hypothesised that an electrostatic complex may be formed. This could help protect the siRNA and provide the therapeutic element to the nanotheranostic.

Another crucial aspect was that the raspberry nanoparticle did not accumulate at the site of the 4T1 tumour. To be considered a good delivery vector the raspberry nanoparticles must accumulate at the diseased site. Future work should investigate their distribution in alternative tumour models, preferably ones that have been validated for the EPR effect. Cell lines that have been used to demonstrate the EPR effect include; B16F10 melanoma, Sarcoma 180 (S-180), Meth-A sarcoma and Colon 38 in mice. Walker 256 and Yoshida AH136B in rats and VX-II in rabbits.[5] Alternative tumours can be used, however their microenvironment should be validated for nanoparticle permeation. This can be performed using the Evan's blue-albumin complex. This large macromolecular dye should accumulate in tumour tissue that has poor architecture and leaky fenestrations.

Accumulation may also be improved by exploiting the magnetic nature of the raspberry nanoparticles. The raspberry nanoparticles are superparamagnetic in nature and will become magnetised in the presence of an external magnetic field, however will be rendered inactive when the field is removed. Medicine can exploit this feature, as when the superparamagnetic delivery vector is administrated into systemic absorption it is free to circulate, depicted by its pharmacokinetic profile,

however it may be separated from the blood by passing through a magnetic field. As long as the magnetic forces overcome the drag forces of the blood, then it can allow for the accumulation of superparamagnetic species at the site of the external magnetic field.[6] Increasing the accumulation of the drug at the site using magnetic guidance would reduce the amount of drug in systemic distribution and reduce the amount of drug required in each dose. Overall, leading to a more efficient treatment with less off target side effects. Very quickly it can be seen how magnetic targeting can be used to improve the specificity of a treatment, this topic has been discussed in *section 1.4.3* where a number of studies have investigated the clinical relevance of this strategy. It is not hard to imagine that the raspberry nanoparticle could be used in this manner.

Additionally another strategy that could improve the accumulation of the raspberry nanoparticles at the tumour site is a practise known as active targeting.[7] To be an effective delivery vector the raspberry nanoparticles must accumulate in the tumour tissue and avoid healthy tissue. Cancers cells often display an overexpression of biological markers and receptors associated with their rapid growth. Decorating the nanoparticle with ligands that have an affinity with these overexpressed receptors can provide the nanoparticle with an enhanced disposition for a cancer target. This process has been adopted for drug delivery with varying degrees of success using; folate like molecules, peptides, proteins, antibodies, antibody fragments and aptamers. Active targeting alone is not a solution to nanoparticle accumulation in a cancer target, as distribution to the tumour must first occur. However, when nanoparticle distribution is observed at the diseased site, active targeting may be used to increase the efficiency of the treatment.

It is also worth discussing how the nanotheranostic could be evaluated for its clinical relevance. It is of the author's opinion that the clinical relevance of a nanotheranostic

has not yet clearly been demonstrated in the literature. As reviewed, tumour efficiency studies of drug loaded IONPs have been conducted with reasonably successful outcomes at reducing tumour volume and growth rate *(section 1.4.2)*. This however, does not indicate a tangible clinical benefit as these tumour efficiency studies do not take advantage of the diagnostic probe. However, using a drug filled nanotheranostic as a diagnostic probe would not be appropriate either, as this could lead to the drug dosing of potentially healthy patients. When considering the nature of a diagnostic and the nature of a therapeutic an interesting discussion emerges. The key point being made is that diagnostics and therapeutics often have very different requirements. For example, a diagnostic should be reasonably non-toxic and should have a short half-life in a patient, whereas, a drug may be toxic and should have maximum residence time at the site of disease. These points have been largely unaddressed in the nanotheranostic community and pose considerable challenges when trying to determine clinical relevance.

The main advantage of a nanotheranostic is that via a simple diagnostic procedure one can map the therapeutic distribution within a patient. The benefit being, that one now has the ability to determine if the drug is being delivered to the diseased site. This kind of advantage is difficult to model in an *in vivo* experiment. One possible experiment that could highlight this advantage would be to have a large subject population with a large variation in disease type. In one half of the population you would blanket dose the group with the nanotheranostic (therapeutic group). In the second population you would perform a diagnostic procedure following administration of the nanotheranostic (nanotheranostic group). If the nanotheranostic was found to accumulate at the diseased site, then the treatment could be continued in that individual. Of course, treating patients in this manner would actually lead to the same number of successful treatment cases in both groups, however the efficiency of treatment would be much higher in the nanotheranostic group due to the initial

screening procedure. Attempting to find clinical significance using smaller sample groups may seem counter intuitive but, it could lead to increased treatment efficiencies. This ultimately leads to an interesting situation, where, as the specificity of a treatment increases, the number of patients in a trial would ultimately have to decrease. Designing studies which show the relevance of nanotheranostics is challenging and is worth some considerable thought.

The author also believes it would be worth investigating the effect that IONP core size has on the properties of the raspberry nanoparticles. Increasing the IONP core size should increase the magnetic properties of the raspberry nanoparticles. Increased magnetic properties would lead to the development of a more potent T2 contrast agent and would increase the raspberry nanoparticle's applicability in magnetic targeting and hyperthermia applications. High temperature thermal decomposition methods to yield larger crystal sizes (~10 nm) were investigated in the early stages of this project. TEM confirmed that they had been successfully synthesised, but their purification from the reaction solvent was troublesome making them unsuitable for downstream applications. Organic phase dialysis using polycarbonate membranes is a purification method that was not investigated and could perhaps be used to separate the high b.p. organic solvents from the nanoparticles.

As mentioned, a superparamagnetic nanoparticle can also be used to provide localised magnetic heating by placing them in the vicinity of an alternating magnetic field *(section 1.4.3)*.[8] Hyperthermia treatment using IONPs is perhaps one of the most exciting new areas for magnetic nanoparticle research. Cancer cells are more sensitive to heat than healthy cells and if the localised magnetic heating is controlled between 42-46 ^{O}C for between 10-30 mins then the cancer cells can be killed with minimal damage to the healthy tissue.[8] Additionally, a number of studies have also reported that the hyperthermia tumour kill efficiency can be greatly enhanced while

the patient is undergoing a chemotherapeutic regime.[9] It can therefore be hypothesised that a chemotherapeutic IONP could provide the same effects but in a localised packet, reducing off target side effects caused by the drug being in systemic distribution. This area is relatively new and a drug encapsulation raspberry nanoparticle has all the components to qualify as a candidate for this type of treatment.

5.3 Scientific impact

Nanotheranostics allow for disease visualisation, treatment and real time monitoring in a single package. In theory, they have the ability to vastly increase the efficiency of a treatment, however in practice their clinical relevance has yet to be demonstrated. Nanotheranostic success lies with engineering particles that are specific in design and function. In this project it was hoped that micelle technology could be used to simultaneously encapsulate an IONP imaging probe and a chemotherapeutic drug. Overall, the formulation of a nanotheranostic was not discovered in this body of work within the given time frame, however the experimentation leading up to its formation have led to some interesting scientific results that may have some impact on the scientific community. Firstly, IONPs themselves are not biocompatible. Naked IONPs agglomerate to reduce their high surface energies, while IONPs made from organic solvent reactions are highly hydrophobic. New strategies to make biocompatible IONPs are important and this project addressed these issues by using the amphiphilic GCPQ polymer. In the project two new colloidally stable IONP products were created; the blackberry nanoparticles and the raspberry nanoparticles. Comprehensive characterisation and analysis was performed on both nanostructures leading to a set of experiments that any researcher could follow for their own engineered IONPs. The most unique structure created was the raspberry nanoparticle. By comparing these structures to single crystal DMSA.IONPs it was found that the raspberry nanoparticles

enhanced r_2 relaxivity, while supressing r_1 relaxivity, ultimately leading to a technology that can provide improved T2 "negative" contrast agents. This project also described the stability of IONPs in biorelevant solutions using DLS, the iron phenanthroline quantification assay and ICP-AES. These studies are often overlooked in the literature and hopefully the stability studies conducted here will provide a template that can be followed by scientists in the field. One of the most impressive results was the development of the ICP-AES protocol for the analysis of *in vivo* tissue samples used to evaluate the pharmacokinetics and biodistribution of the raspberry nanoparticles. In the past, the pharmacokinetics and biodistribution were usually performed using radioactive isotopes, however these studies have become unfashionable due to the considerable risks to the researchers involved. Alternatively, MRI can be used to monitor the biodistribution of the IONPs, however these studies do not give quantitative data in relation to IONP accumulation. The ICP-AES is a relatively straight forward procedure, which gave quantitative data at minimum risk to the user. To the author's knowledge the pharmacokinetic studies performed in this body of work, are the first to evaluate a positively charged micellar IONP *in vivo*. In vivo MRI studies were also performed which actually validated the pharmacokinetic and biodistribution data. Raspberry nanoparticles accumulated in the spleen and liver and so validating the standard model for IONP clearance in a biological system. Raspberry nanoparticle did not show a significant effect on the lungs or kidneys, unlike the commercially available product Ferucarbotran® (Resovist®) possibly indicating a more organ specific contrast agent. In an addition to this, the raspberry nanoparticles highlighted the hepatic veins to a much larger extent than the commercially available product. This could give the raspberry nanoparticle a significant clinical advantage for their use as a diagnostic device for liver imaging. The raspberry nanoparticles were also evaluated for their tumour accumulation in a 4T1 BALB/c model. Tumour studies suggested that the raspberry nanoparticles had a small effect in the tumour site, however this was not large enough to produce any

meaningful contrast to a human observer. This project has highlighted that the 4T1 model is simple to establish, however may not be appropriate for the investigation of nanoparticle accumulation and other researchers should use it with caution. This body of work has also investigated the drug loading capacity of the micellar raspberry nanoparticles. It has shown that simply being hydrophobic is often not enough of a driving force to yield drug encapsulation within micelle nanoparticles and great care should be taken when selecting a drug candidate. Lastly this project has openly discussed the clinical relevance of a nanotheranostic and strategies that demonstrate their advantage to a patient. Although multifunctional nanotheranostics are impressive constructions of nanoengineering, their application for improving patient health is largely not discussed in the nanoscale community. Importantly, this thesis has led to an open discussion with regards to the application of nanotheranostics in disease treatment.

(1) Dorsett, Y.; Tuschl, T. siRNAs: applications in functional genomics and potential as therapeutics. *Nat Rev Drug Discov* **2004**, *3*, 318-329.

(2) Kanasty, R.; Dorkin, J. R.; Vegas, A.; Anderson, D. Delivery materials for siRNA therapeutics. *Nat Mater* **2013**, *12*, 967-977.

(3) Gavrilov, K.; Saltzman, W. M. Therapeutic siRNA: Principles, Challenges, and Strategies. *The Yale Journal of Biology and Medicine* **2012**, *85*, 187-200.

(4) Xia, H.; Mao, Q.; Paulson, H. L.; Davidson, B. L. siRNA-mediated gene silencing in vitro and in vivo. *Nat Biotech* **2002**, *20*, 1006-1010.

(5) Maeda, H.; Wu, J.; Sawa, T.; Matsumura, Y.; Hori, K. Tumor vascular permeability and the EPR effect in macromolecular therapeutics: a review. *J Control Release* **2000**, *65*, 271-284.

(6) Pankhurst, Q. A.; Connolly, J.; Jones, S. K.; Dobson, J. Applications of magnetic nanoparticles in biomedicine. *Journal of Physics D: Applied Physics* **2003**, *36*, R167.

(7) Yu, M. K.; Park, J.; Jon, S. Targeting Strategies for Multifunctional Nanoparticles in Cancer Imaging and Therapy. *Theranostics* **2012**, *2*, 3-44.

(8) Hervault, A.; Thanh, N. T. K. Magnetic nanoparticle-based therapeutic agents for thermo-chemotherapy treatment of cancer. *Nanoscale* **2014**, *6*, 11553-11573.

(9) Urano, M. Invited Review: For the clinical application of thermochemotherapy given at mild temperatures. *International Journal of Hyperthermia* **1999**, *15*, 79-107.